Pyrometallurgical Oxide-Sulfide Anion Exchange for Improved Material Separation and Metal Production

by

Caspar R. Stinn

B.Sc. in Chemical Engineering
Massachusetts Institute of Technology, 2018

Submitted to the Department of Materials Science and Engineering in Partial Fulfillment of the Requirements for the Degree of

Doctor of Philosophy

at the

Massachusetts Institute of Technology

June 2023

Authored by:	Caspar R. Stinn Department of Materials Science and Engineering 1 May 2023
Certified by:	Antoine Allanore Professor of Metallurgy, Thesis Supervisor
Accepted by:	Robert J. Macfarlane Chair, Departmental Committee on Graduate Studies

Pyrometallurgical Oxide-Sulfide Anion Exchange for Improved Material Separation and Metal Production

by

Caspar R. Stinn

Submitted to the Department of Materials Science and Engineering on 1 May 2023, in partial fulfillment of the requirements for the degree of Doctor of Philosophy

Abstract

Efforts to decarbonize, reduce water consumption, and respond to increasing feedstock complexity motivate the search for new processing pathways in mining, recycling, and metal production. Currently, environmentally tedious and economically burdensome chemical separations are required to produce pure compounds amenable to materials manufacturing and metal production. An alternative approach is the development of chemical pretreatments that enable low cost, environmentally sustainable physical separations instead. This can be accomplished via pyrometallurgical anion exchange chemistry. Revisiting separation pathways provides an added benefit; new separation chemistries can enable improved downstream processes for metal production without direct greenhouse gas emissions. Sulfur-based routes are expected to be particularly versatile. However, kinetic and thermodynamic unknowns currently hinder the deployment of sulfur-based separation chemistries.

Herein, thermodynamic modelling and oxide sulfidation kinetic measurements enable for the first time the establishment of an integrated thermodynamic, kinetic, and mass transport framework for pyrometallurgical oxide-sulfide anion exchange. Selective sulfidation via this methodology is established to be a low cost, sustainable pretreatment that enables high performance, environmentally friendly physical separations in place of legacy chemical approaches. This approach is shown to be effective across a range of modern materials processing challenges, including rare earth separation, lithium ion battery recycling, metal slag recycling, and commodity mineral processing. Separation metrics achieved through pyrometallurgical selective sulfidation exhibit order of magnitude improvements over state of the art hydrometallurgical pathways. Life cycle and technoeconomic assessments reveal these benefits also come at a fraction of the cost and environmental impact.

Furthermore, novel sulfide products from pyrometallurgical oxide-sulfide anion exchange are found to be amenable to metal production via simple vacuum thermal treatments. Aluminothermic reduction via reactive vacuum distillation is shown to enable manufacturing of a range of alloys from sulfide feedstocks without direct greenhouse gas emissions, including aluminum-manganese, aluminum-scandium, ferronickel, ferrochromium, and iron-rare earth alloys. Together, sulfide-based processing pathways are found to unlock new synergies in metal separation and reduction for a sustainable materials future.

Thesis Supervisor: Antoine Allanore
Title: Professor of Metallurgy

Acknowledgments

Through the course of my studies, I have been incredibly fortunate to benefit from the presence of many wonderful, kind people. I would first and foremost like to thank my parents, Terri Stinn and Dean Stinn, and my sister, Lucille Stinn, for their unwavering love and support through my childhood, academic, and life adventures. They were crucial in helping instill within me a love for learning and making things with my own hands. I would also like to thank Jingyi (Monica) Wen and Bonbon for their care and encouragement as I completed graduate school.

Academically, I would first like to thank the Undergraduate Research Opportunities Program (UROP) students I worked with, including Alena Culbertson, Carolina Gutierrez, Vasu Kaker, Lucas Marden, Helena Merker, and Spencer Toll. I would also like to thank my direct research collaborators, including Zachary Kenneth Adams, Ethan Benderly-Kremen, Charles Boury, Andrew Caldwell, Brian Chmielowiec, Katrin Daehn, Katsu Nose, Toru Okabe, Lucas Rush, Mary Elizabeth Wagner, and Ryohei (Hachi) Yagi. I would like to thank Jonathan Paras for his assistance in learning the core curriculum of materials science and preparing for the written qualifying exam, as well as for driving me home after long days in lab. In addition, I appreciate all of the other current and former Allanore Research Group members who I have had the privilege to learn from and work with during both my undergraduate and graduate studies. I would like to thank Grace Kim, Hilary Sheldon, and Vaciane Simeon for their administrative support and the USA Department of Energy, the USA Defense Advanced Research Projects Agency, the MIT UROP Office, and the MIT Deshpande Center for their financial support.

I would also like to thank the members of my thesis committee, Elsa Olivetti and Donald R. Sadoway, for their time, wisdom, and perspective through the course of my graduate studies. Finally, I would like to thank my thesis advisor and mentor, Antoine Allanore, who has been a constant source of insight, guidance, support, encouragement, and patience during my time as both a UROP student and a graduate student in his research group.

Contents

List of Figures

Chapter 4

Chapter 7

List of Tables

Chapter 7

Nomenclature

Fundamental Physical Constants

R	Ideal gas constant

Symbols

a	Thermodynamic activity
a_{BM}	Design/engineering/contingency capital cost scaling factor
a_c	Capital cost preexponential factor
a_{FOB}	Free on board capital cost preexponential factor
a_{LF}	Location capital cost scaling factor
a_{LM}	Instruments and buildings capital cost preexponential factor
a_{PM}	Physical module capital cost preexponential factor
a_{TM}	Offsites/indirect/field expense capital cost preexponential factor
β	Beta, stoichiometric factor
β^{sep}	Separation factor
c	Concentration
C_{FC}	Total fixed module capital cost
C_{FOB}	Free on board capital cost
C_{ISBL}	Inside battery limits capital cost
C_{PM}	Physical module capital cost
C_T	Total fixed module capital cost of a process block
γ	Gamma, stoichiometric factor
D	Distribution coefficient

δ	Delta, stoichiometric factor
$\Delta_{\mathrm{f}}G°$	Standard Gibbs energy of formation
$\Delta_{\mathrm{r}}G°$	Standard Gibbs energy of reaction
$\Delta_r H°$	Standard enthalpy of reaction
$\Delta \mathrm{r}_{\mathrm{S}}$	Difference in ionic (Shannon) radii
$\Delta_r S°$	Standard entropy of reaction
$\Delta\chi$	Difference in electronegativity (Pauling)
$E°$	Standard decomposition potential
ϵ	Epsilon, stoichiometric factor
ϵ_p	Pellet porosity
f	Fugacity
ζ	Zeta, stoichiometric factor
η	Eta, stoichiometric factor
η_k	Kinetic effectiveness factor
θ	Theta, stoichiometric factor
I_y	Cost index for a given year
I_R	Cost index for a reference year
ι	Iota, stoichiometric factor
k	Intrinsic chemical reaction rate constant
κ	Kappa, stoichiometric factor
λ	Lambda, stoichiometric factor
Λ	Optical basicity
m	Mass
m^*	Molar mass
M_1	Metallic element
M_1^{n+}	Metallic cation
M_2	Metallic element that is different from M_1
M_2^{n+}	Metallic cation that is different from M_1^{n+}
$M_\gamma O_\delta S_\epsilon$	Condensed metal-oxygen-sulfur reactant compound
$M_\iota O_\kappa S_\lambda$	Condensed metal-oxygen-sulfur product compound

$M_\eta S_\theta$	Condensed metal sulfide compound
$M_\gamma X_\delta$	Condensed metal oxide, selenide, telluride, arsenide, or antimonide reactant compound
μ	Mu, stoichiometric factor
n	Economy of scale exponent
n_k	Reaction order
ν	Nu, stoichiometric factor
v_{space}^{min}	Critical gas space velocity in a reactor
$P_{Al_2S_3}$	Aluminum sulfide partial pressure
$\left[P_{Al_2S_3}\right]_{crit}$	Critical aluminum sulfide partial pressure for aluminothermic reduction of a sulfide via reactive vacuum distillation
P_c	Relevant scaling metric for capital cost
P_{Cl_2}	Chlorine partial pressure
P_{CS}	Carbon monosulfide partial pressure
P_{CS_2}	Carbon disulfide partial pressure
P_{F_2}	Fluorine partial pressure
P_{O_2}	Oxygen partial pressure
P_{S_2}	Sulfur partial pressure
$\left[P_{S_2}\right]_{crit}$	Critical sulfur partial pressure for direct vacuum thermal decomposition
$\left[P_{S_2}/P_{SeS}\right]_{crit}$	Critical sulfur to selenium sulfide ratio required for selenide-sulfide anion exchange
$\left[P_{S_2}/P_{SO_2}\right]_{crit}$	Critical sulfur to sulfur dioxide ratio required for oxide-sulfide anion exchange
$\left[P_{S_2}/P_{SO_2}\right]_{rx}$	Sulfur to sulfur dioxide ration within a reactor
$\left[P_{S_2}/P_{TeS}\right]_{crit}$	Critical sulfur to tellurium sulfide ratio required for telluride-sulfide anion exchange
P_{SeS}	Selenium sulfide partial pressure

P_{TeS}	Tellurium sulfide partial pressure
P_{vap}	Vapor pressure
$P_{X_\kappa S_\lambda}$	$X_\kappa S_\lambda$ partial pressure
$\left[P_{S_2}/P_{X_\kappa S_\lambda}\right]_{crit}$	Critical sulfur to $X_\kappa S_\lambda$ ratio required for anion exchange between X and sulfur
r'	Reaction rate (mass basis)
${R_{PD}}'$	Modified Pilling-Bedworth Ratio
$\overline{r_S}$	Average ionic (Shannon) radius across all oxide and sulfide compounds of all coordination numbers for a given metal cation valency
ρ	Density
T	Absolute temperature
T_B	Boiling point temperature
τ_{space}^{max}	Critical gas space time in a reactor
x	Stoichiometric factor
X	Oxygen, selenium, tellurium, arsenic, or antimony
$X_\kappa S_\lambda$	Sulfide gas containing oxygen, selenium, tellurium, arsenic, or antimony
χ	Electronegativity (Pauling)
ψ	Stoichiometry dependent sulfur to sulfur dioxide partial pressure ratio
$\psi_{rxn_{\Delta G}}$	Standard Gibbs energy of reaction contribution to the stoichiometry dependent sulfur to sulfur dioxide partial pressure ratio (ψ)
$\psi_{rxn_{\Delta H}}$	Enthalpic contribution to the stoichiometry dependent sulfur to sulfur dioxide partial pressure ratio (ψ)
$\psi_{rxn_{\Delta S}}$	Entropic contribution to the stoichiometry dependent sulfur to sulfur dioxide partial pressure ratio (ψ)
ψ_{sol}	Solution effect contribution to the stoichiometry dependent sulfur to sulfur dioxide partial pressure ratio (ψ)

Chemical Formulas in Text and Tables[i]

Ag	Silver, element or metal
Al	Aluminum, element or metal
Al_4C_4	Aluminum carbide, compound
Al_2O_3	Alumina or aluminum oxide, compound
Al_2S_3	Aluminum sulfide, compound
$Al_2Si_2O_5(OH)_4$	Kaolinite, mineral
Ar	Argon, element
As	Arsenic, element or metal
As_4S_4	Arsenic sulfide, compound
Au	Gold, element or metal
B	Boron, element
BN	Boron nitride, compound
Ba	Barium, element or metal
$BaSO_4$	Barium sulfate, compound
BaS	Barium sulfide, compound
Bi	Bismuth, element or metal
C	Carbon, element
Ca	Calcium, element or metal
$CaCO_3$	Calcium carbonate, compound
$Ca_3(PO_4)_2$	Calcium phosphate, compound
CaS	Calcium sulfide, compound
Ce	Cerium, compound or metal
CeO_2	Cerium oxide, compound
Cl	Chlorine, element
Cl_2	Chlorine, compound
Cr	Chromium, element or metal
Cr_2O_3	Chromium oxide, compound

[i] Element atomic symbols shown in figures but not listed here are as defined in the periodic table of elements.

CrS	Chromium sulfide, compound
$(Ca, Mg)S$	Oldhamite (Old), chondrite meteorite mineral
Co	Cobalt, element or metal
Co_9S_8	Cobalt sulfide, compound
$Co_3Ni_6S_8$	Nickel-cobalt sulfide, compound
CO	Carbon monoxide, compound
CO_2	Carbon dioxide, compound
CS	Carbon monosulfide, compound
CS_2	Carbon disulfide, compound
Cs	Cesium, element or metal
Cu	Copper, element or metal
Cu_3As	Copper arsenide
Cu_3AsS_4	Enargite, mineral
(Cu, Fe, S)	Iron-depleted copper-iron sulfide matte
$CuFeS_2$	Chalcopyrite, mineral
Cu_xO	Copper oxide, compound
Cu_2O	Copper(I) oxide, compound
Cu_2S	Copper sulfide, compound
$Cu_{12}Sb_{0.6}As_{3.4}S_{13}$	Tennantite, mineral
Cu_3SbS_4	Famatinite, mineral
Cu_xSO_4	Copper sulfate, compound
Di	Neodymium-praseodymium, mixture of elements or metal alloy
Dy	Dysprosium, element or metal
Dy_2O_3	Dysprosium oxide, compound
Dy_2O_2S	Dysprosium oxysulfide, compound
Er	Erbium, element or metal
Eu	Europium, element or metal
F	Fluorine, element
Fe	Iron, element or metal
$FeCr_2O_4$	Chromite, mineral

$((Fe,Cr)S$	Iron-chromium sulfide, nonstoichiometric compound
$Fe(Fe,Ti)_2O_4$	Titanomagnetite, mineral
(Fe,Ln,B)	Iron-lanthanide-boron, compound
$(Fe,Mn)(Nb,Ta)_2O_6$	Columbite-tantalite, mineral
$Fe_{1-\beta}\ Ni_\beta MgSiO_4$	Olivine, compound
$Fe_{1-\beta}\ MgSiO_{4-\beta}$	Nickel-depleted olivine, compound
$(Fe,Ni,Mg)_2SiO_4$	Olivine, mineral
FeO	Iron monoxide, compound
Fe_3O_4	Iron oxide, compound
Fe_2O_3	Iron sesquioxide, compound
FeS	Iron sulfide, compound
FeS_2	Iron disulfide, compound
	Pyrite, mineral
$Fe_2(SO_4)_3$	Ferric sulfate, compound
$FeScO_3$	Iron-scandium oxide, compound
$Fe_3(Al_{0.3}Si_{0.7})$	Iron-aluminum-silicon intermetallic, compound
Fe_2SiO_4	Fayalite, mineral or compound
$FeTiO_3$	Ilmenite, mineral
Gd	Gadolinium, element or compound
HCl	Hydrochloric acid
Hf	Hafnium, element or metal
Hg	Mercury, element or metal
Ho	Holmium, element or metal
H_2S	Hydrogen sulfide, compound
I	Iodine, element
Ir	Iridium, element or metal
K	Potassium, element or metal
$KAl_2(AlSi_3O_{10})(F,OH)_2$	Muscovite, mineral
LaF_3	Lanthanum fluoride, compound
La_2O_3	Lanthanum oxide or lanthanum sesquioxide, compound

$LaOF$	Lanthanum oxyfluoride, compound
La_2O_2S	Lanthanum oxysulfide, compound
$La_{10}OS_{14}$	"Higher" lanthanum oxysulfide, compound
$LaPO_4$	Lanthanum phosphate, compound
$LaPO_4 * xH_2O$	Lanthanum phosphate hydrate, compound
LaS_2	Lanthanum disulfide, compound
La_2S_3	Lanthanum sulfide or lanthanum sesquisulfide, compound
La_3S_4	"Intermediate" lanthanum sulfide, compound
Li	Lithium, element or metal
$LiAlO_2$	Lithium aluminate, compound
$LiAl_5O_8$	Lithium aluminate, compound
$(Li, Mn)Al_2O_4$	Lithium-manganese-aluminum oxide, compound
$LiSO_4$	Lithium sulfide, compound
Ln	Lanthanide, element or metal
$LnCO_3F$	Bastnaesite, mineral
Ln_2O_2S	Lanthanide oxysulfide, compound
$Ln_{10}OS_{14}$	"Higher" lanthanide oxysulfide, compound
$LnPO_4$	Monazite, mineral
	Xenotime, mineral
	Mixed rare earth element phosphate, compound
LnS_2	Lanthanide disulfide, compound
Ln_2S_3	Lanthanide sulfide, compound
Ln_3S_4	"Intermediate" lanthanide sulfide, compound
M	Metal, element or metal
M_2O_3	Metal sesquioxide, compound
Mg	Magnesium, element or metal
$MgCO_3$	Magnesium carbonate, compound
MgO	Magnesia or magnesium oxide, compound
MgS	Magnesium sulfide, compound
	Niningerite (Nng), chondrite meteorite mineral
$MgSiO_3$	Enstatite (En), chondrite meteorite mineral

Mn	Manganese, element or metal
$MnAl_{4.17}$	Aluminum-manganese intermetallic, compound
$MnAl_6$	Aluminum-manganese intermetallic, compound
MnS	Manganese sulfide, compound
Mo	Molybdenum, element or metals
MoS_2	Molybdenum sulfide, compound
	Molybdenite, mineral
Na	Sodium, element or metal
Na_2CO_3	Sodium carbonate, compound
NaF	Sodium fluoride, compound
Nb	Niobium, element or metal
Nd	Neodymium, element or metal
Nd_2O_3	Neodymium oxide, compound
Nd_2O_2S	Neodymium oxysulfide, compound
$Nd_{10}OS_{14}$	"Higher" neodymium oxysulfide, compound
NdS_2	Neodymium disulfide, compound
Nd_2S_3	Neodumium sulfide, compound
Nd_3S_4	"Intermediate" neodymium sulfide, compound
Ni	Nickel, element or metal
NiO	Nickel oxide, compound
NiS	Nickel sulfide, compound
Ni_3S_2	Nickel subsulfide, compound
O	Oxygen, element
O_2	Oxygen, compound
P	Phosphorous, element
Pb	Lead, element or metal
P_4O_{10}	Phosphorous pentoxide
P_4S_{10}	Phosphorous pentasulfide
Pr	Praseodymium, element or metal
Pr_6O_{11}	Praseodymium oxide, compound
Pr_2O_2S	Praseodymium oxysulfide, compound

Pt	Platinum, element or metal
Rb	Rubidium, element or metal
Re	Rhenium, element or metal
S	Sulfur, element
S_2	Sulfur, compound
S_8	Sulfur, compound
S_X	Sulfur, compound
Sb	Antimony, element or metal
Sb_2S_3	Antimony sulfide, compound
Sc	Scandium, element or metal
$ScAl_3$	Scandium-aluminum intermetallic, compound
Sc_2O_3	Scandium oxide or scandium sesquioxide, compound
Sc_2O_2S	Scandium oxysulfide, compound
Sc_2S_3	Scandium sulfide or scandium sesquisulfide, compound
Sc_3S_4	Intermediate scandium sulfide, compound
Se	Selenium, element
SeS	Selenium sulfide, compound
SF_6	Sulfur hexafluoride, compound
Si	Silicon, element or metal
SiO_2	Silica or silicon oxide, compound
	Quartz, mineral
$SiCl_4$	Silicon tetrachloride, compound
SiS	Silicon sulfide, compound
Sm	Samarium, element or metal
SO_2	Sulfur dioxide, compound
Sr	Strontium, element or metal
$SrCO_3$	Strontium carbonate, compound
SrO	Strontium oxide, compound
SrS	Strontium sulfide, compound
Ta	Tantalum, element or metal
Tb	Terbium, element or metal

Te	Tellurium, element
TeS	Tellurium sulfide, compound
Th	Thorium, element or metal
Ti	Titanium, element or metal
TiO_2	Titanium dioxide, compound
Tm	Thulium, metal
U	Uranium, element or metal
W	Tungsten, element or metal
WO_3	Tungsten oxide, compound
Zn	Zinc, element or metal
ZnS	Zinc sulfide, compound
Zr	Zirconium, element or metal
$(Zr,Hf)Cl_4$	Zirconium-hafnium chloride, compound
$(Zr,Hf)O_2$	Zirconium-hafnium oxide, compound
$(Zr,Hf)SiO_4$	Zircon, mineral
ZrO_2	Zirconium oxide, compound
$ZrOS$	Zirconium oxysulfide, compound
ZrS_2	Zirconium sulfide or zirconium disulfide, compound
$Zr_{1-x}S_2$	Zirconium deficient sulfide, compound

Abbreviations

AACE	American Associate of Cost Engineers
AISI	American Iron and Steel Institute
AlMn	Aluminum manganese alloy
AlMn10	Aluminum manganese master alloy with 10 wt% manganese
AlSc	Aluminum scandium alloy
Aq	Aqueous phase
A^*	Chemical phase
atm	atmospheres of pressure
B^*	Chemical phase that is different than A^*

cm	Centimeter
CALPHAD	CALculation of PHAse Diagrams
CAPEX	Capital cost
CEPCI	Chemical engineering plant cost index
CDSR	Carbothermically driven sulfur reflux
e^-	Electron
En	Enstatite (chondrite meteorite mineral)
eq	Equivalent
eV	Electron volts
EW	Electrowinning
FeB	Ferroboron alloy
FeCr	Ferrochromium alloy
FeDy	Ferrodysprosium alloy
FeNdB	Iron-neodymium-boron (magnet)
FeNi	Ferronickel alloy
g	gram
GWP	Global warming potential
HDEHP	Di-(2-ethylhexyl)phosphoric acid
HPAL	High pressure acid leaching
HRC	Hot rolled coil
ICP-MS	Inductively-coupled plasma mass spectroscopy
ICP-AES	Inductively-coupled plasma atomic emission spectroscopy
ISBL	Inside battery limits
ISO	International Organization for Standardization
k	Kilo (thousand)
K	Kelvin, absolute temperature scale
KF	Kleinflansch (German)
kg	Kilogram
kta	Kilotonnes per year
kWh	Kilowatt-hour
LCA	Life cycle assessment

LCI	Life cycle inventory
LECO	Light element combustion analysis, also the acronym for Laboratory Equipment COrperation, the manufacturer of many combustion analysis instruments
LIB	Lithium ion battery
M	Molar
mm	Millimeters
mol	Moles
na	Not analyzed
ND	Not detected
nil	Below detection limit
NMC	Nickel-manganese-cobalt
$NMC111$	Cathode oxide with equal parts nickel, manganese, and cobalt
Nng	Niningerite (chondrite meteorite mineral)
NORM	Normally occurring radioactive material
OES	Optical emission spectroscopy
Old	Oldhamite (chondrite meteorite mineral)
OPEX	Operating cost
Or	Organic phase
$P_{\%}$	Percentile
PGM	Platinum group metal
pm	Picometers
ppb	Parts per billion
ppm	Parts per million
QXRD	X-ray diffraction analysis (quantitative)
rem	Remainder
REM	Rare earth metal
SEM-EDS	Scanning electron microscope energy dispersive x-ray spectroscopy
sccm	Standard cubic centimeters per minute

SX	Solvent extraction
TA	Terrestrial acidification
USD	United States dollars
WRD	Water resource depletion
XRD	X-ray diffraction analysis (qualitative)

Chapter 1

Introduction

The electrification of sectors ranging from transportation[1] to heavy industry[2] stimulates growing demand for the materials needed to establish infrastructure based on renewable technologies, spanning from base elements such as copper and nickel[3] to specialty elements such as the rare earths[4]. Meeting growing demand for these critical metallic elements motivates strategies for expanding production from both natural minerals and recycled sources[5,6]. Innovation in mining requires designing processes to profitably handle lower mineral and concentrate grades[7], while continuing to tackle the high emissions and energy usage characteristic of both conventional pyrometallurgy and hydrometallurgy[8]. Meanwhile, recycling of materials from secondary feedstocks requires the reprocessing of complex materials with different impurities than natural minerals[9–11]. In practice, metal production from minerals and waste sources are often intertwined due to the role primary smelters play in recycling both base and rare elements[12,13].

There is a critical need for a paradigm shift in the types of technologies and chemistries utilized for metals mining and production, driven by global desires to decarbonize and conserve water. Presently, production of metals directly accounts for over 8% of global carbon dioxide (CO_2) emissions[14], with mining accounting for an additional 4-7% of total global greenhouse gas emissions[15]. Current best-practice metal production and mining processes remain carbon-intensive due to the need for process heat and electricity from the burning fossil fuels. Carbon sources are also used as chemical reagents. Concurrently, materials separations in mining and

metal production are highly water-intensive processes, with up to 50% of commodity scale metal production conducted in regions already plagued by water scarcity[15]. By 2040, production of many metals will be conducted entirely in highly arid and water stressed regions, with droughts already causing yearly closures of facilities in regions ranging from Brazil to Germany, resulting in multimillion-dollar losses in daily productivity[15]. Challenges with water and carbon usage are compounded by the fact that mineral and metal production are becoming more energy intensive, almost double for some commodity metals since 2000, due to the global depletion of high-purity and easy to mine metal ore reserves[16]. Clearly, novel chemistries and materials-based solutions are necessary to economically meet sustainability goals in metals and minerals processing.

The conventional supply chain and processing pathway for metal extraction and production from natural ores can be broken into several key steps that each increase the purity of the metallic element in the material: mining and crushing of the metal-containing ore, beneficiation processes for purification of the mined minerals to form an intermediate "concentrate" compound via physical or chemical separation, and finally subsequent reduction of the concentrate to produce a metal product. Intermediate products along this pathway are often traded as commodities themselves; therefore, an effective price of the metallic element can be determined along each stage of its production, from rock to pure metal. Figure 1.1 illustrates market values and greenhouse gas emissions of some commodity metals through their production process[17–27]. For some products such as nickel (Ni) and rare earth metals (REM), large increases in value are found early in the supply chain during mineral processing due to the need for energy intensive chemical separations. For others such as iron (Fe), the bulk of the value is derived during reduction of concentrate to metal. As shown in Figure 1.2, across the supply chain, the processing steps responsible for the largest contributions to metal value are also generally the largest contributors to greenhouse emissions, providing both economic and environmental incentive to innovate those extraction technologies and chemistries. Minimization of costs and environmental impacts in turn requires co-optimization of material separation and metal reduction processes.

High value processing stages early in the metal production supply chain arise from the need for challenging chemical separations of individual metallic elements from mixed metal oxide, phosphate, silicate, or sulfide minerals. The geologic formation of mixed metal cation minerals was thermodynamically driven[28], and therefore large energy inputs and high capital

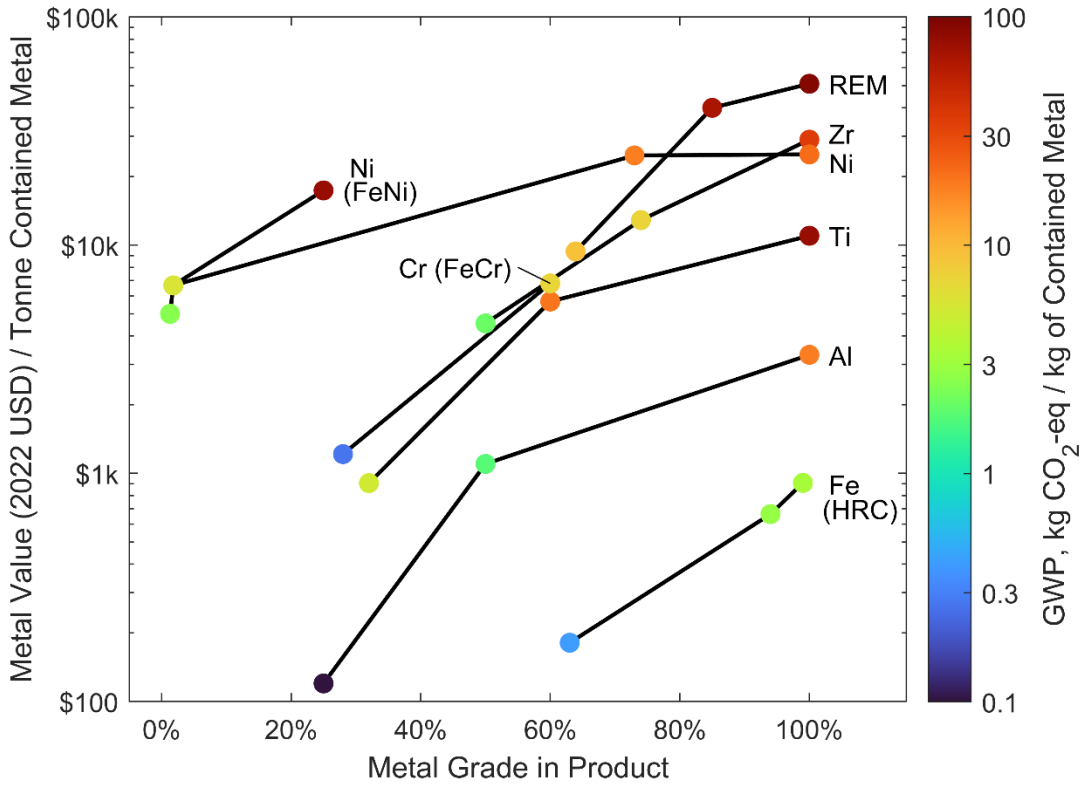

Figure 1.1: Effective metal value (2022 USD) and global warming potential (GWP) versus metal product grade for metals along their production pathway. For rare earth metal (REM) mineral beneficiation, separation into pure oxides, and production of pure metals, values are reported as an average of all rare elements weighted based on their relative abundance in bastnaesite concentrate from Bayan Obo in Inner Mongolia. For ferronickel (FeNi), ferrochromium (FeCr), and all intermediate products, no allocation of value or environmental impact is attempted between components; all monetary values and environmental impacts are attributed to the denoted metal.

expenses are required to overcome the favorable mixing thermodynamics of these metallic elements within the compound. Meanwhile, high value processing steps later in the production pathway arise from challenges in metal reduction or refining. These burdens originate from the chemistry of the metal feedstock compound, itself dictated by natural geochemistry and the processing techniques employed during beneficiation and materials separation.

Recycling is a promising approach to sustainably supplement metal markets with secondary sources of critical materials and alleviate environmental and technoeconomic problems in mining and mineral processing. In many end of life products or manufacturing

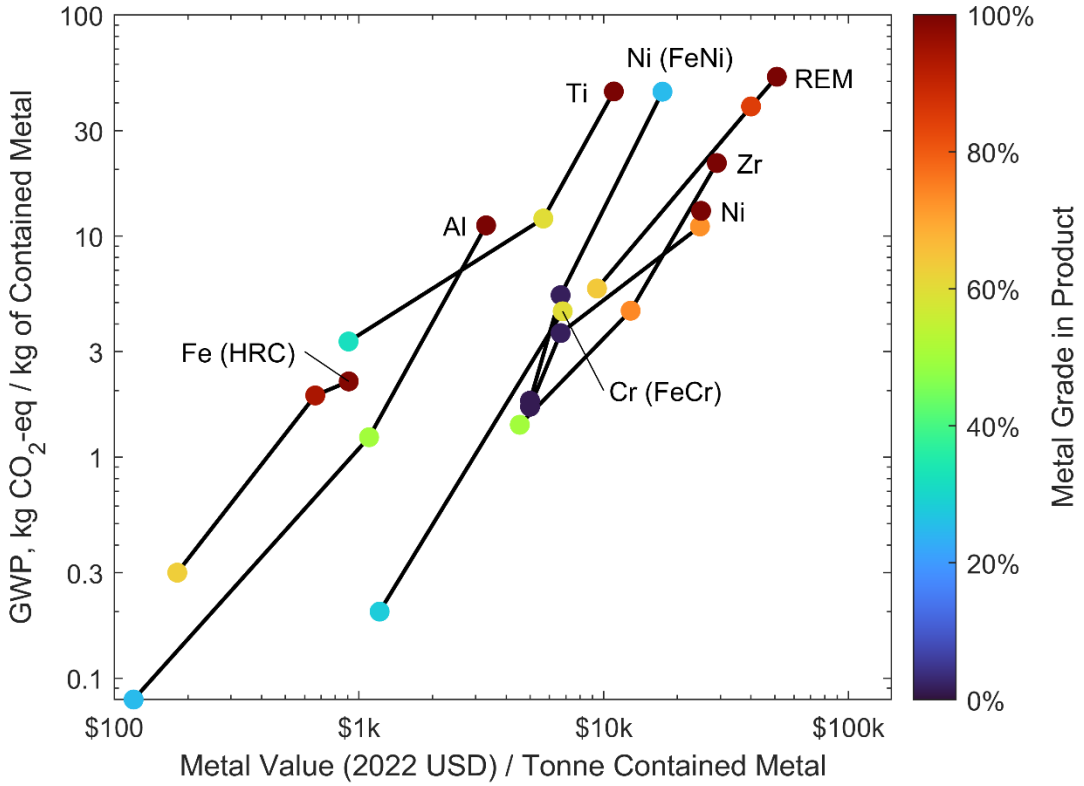

Figure 1.2: Correlation between global warming potential (GWP) and effective metal value (2022 USD) for metals along their production pathway. For rare earth metal (REM) mineral beneficiation, separation into pure oxides, and production of pure metals, values are reported as an average of all elements weighted based on their relative abundance in bastnaesite concentrate from Bayan Obo in Inner Mongolia. For ferronickel (FeNi), ferrochromium (FeCr), and all intermediate products, no allocation of value or environmental impact is attempted between components; all monetary values and environmental impacts are attributed to the denoted metal.

waste, valuable elements exist at much higher grades than in natural ores[1,10]. Extraction from these secondary sources can potentially reduce costs and impacts of production[29]. However, recycled feedstocks often exhibit higher degrees of chemical complexity than their mineral corollaries, potentially increasing the intensity of remaining separations prior to remanufacturing or hindering recovery entirely[4,30]. As for primary production of metals, separation methods employed during recycling must be compatible with approaches available in subsequent processing steps if they are going to rely on existing downstream processing infrastructure[12,13].

The realities of separations for metal production from natural and recycled feedstocks converge to one central theme: optimization of separation chemistries is critical for environmental and economic sustainability across materials supply webs. The choice between chemical and physical separation is practically made based on bulk processing realities such as energy usage and cost. Herein, materials separation is contextualized as an anion exchange process. This ultimately enables the establishment of a new chemical framework for sustainable materials separation and production using sulfur-based processes.

1.1 Chemical Separations as Anion Exchange Processes

The isolation of an element or compound from its surrounding medium relies on exploitable chemical or physical distinctions between components of the system. Physical separation processes are enabled by physical property differences, such as gravimetric separation (density), froth flotation (hydrophobicity), magnetic separation (magnetic susceptibility), electrostatic separation (electrical conductivity), and distillation (vapor pressure). Meanwhile, chemical separation processes are enabled by differences in reactivity between components when in a given environment, as are leveraged for example during acid leaching, aqueous-organic solvent extraction, alkali fusion, matte smelting, or selective reduction.

Often, the natural chemistry of metal ores is not the most conducive to metal separation. When the metals coexist in a single compound or as a solid solution within the mineral matrix, as is often the case for industrially-relevant oxide and other chalcogenide minerals, the individual metal elements cannot be liberated from one another via comminution alone. Notable examples include zirconium (Zr), hafnium (Hf), and silicon (Si) separation from zircon ($(Zr, Hf)SiO_4$)[30], copper (Cu) and Fe separation from chalcopyrite ($CuFeS_2$)[12], niobium (Nb) and tantalum (Ta) separation from columbite-tantalite ($(Fe, Mn)(Nb, Ta)_2O_6$)[31], titanium (Ti) and Fe separation from titanomagnetite ($Fe(Fe, Ti)_2O_4$)[32], and rare earth elements from any of their mineral sources[33]. Therefore, compounds or solid solutions are conventionally broken up (cracked) early in the separation process by chemical treatments such as acid roasting[34] or halogenation[32], or their components separated later using liquid-state methods such as matte smelting[12], electrowinning (EW)[35–38], or solvent extraction (SX)[31,33,39]. All of these chemical approaches

can be viewed in the context of anion exchange, with examples of both selective and complete anion exchange presently conducted in industry.

For halogenation, a common approach is carbochlorination of metal components from an oxide, shown below for the cracking of $(Zr, Hf)SiO_4$ using carbon (C) and chlorine gas (Cl_2) at 1100 °C[40].

$$(Zr, Hf)SiO_4\ (s) + 4C(s) + 4Cl_2\ (g) = (Zr, Hf)Cl_4(g) + SiCl_4\ (g) + 4CO(g) \quad (1.1)$$

Upon complete chlorination of the $(Zr, Hf)SiO_4$ in a fluidized bed, the oxide anions have been exchanged with chloride anions. The differences in vaporization temperature between zirconium-hafnium chloride ($(Zr, Hf)Cl_4$, ~ 300 °C) and silicon tetrachloride ($SiCl_4$, 58 °C) allow for selective condensation of the $(Zr, Hf)Cl_4$, effectively cracking the $(Zr, Hf)SiO_4$ and removing Si due to this oxide-chloride anion exchange. Halogenation for anion exchange can also be performed selectively when reaction kinetics are controlled, as Sohn studied for the carbochlorination of Fe from ilmenite ($FeTiO_3$) to produce titanium dioxide (TiO_2)[32].

$$FeTiO_3(s) + C(s) + Cl_2(g) = FeCl_2(g) + TiO_2(s) + CO(g) \quad (1.2)$$

Similar halogenation schemes to Eqns. 1.1 and 1.2 are commonplace in the treatment of transition metal oxides[41–43], and have also been extensively studied for rare earth elements[33]. Due to the difference in aqueous solubility between oxides and chlorides, carbochlorination can also facilitate selective leaching of metal chlorides from unreacted oxides.

Hydrometallurgical separations such as aqueous-organic solvent extraction may also be viewed in the context of anion exchange. In the initial aqueous feed for liquid-liquid hydrometallurgical separation, the cations of both metals (M_1^{n+} and M_2^{n+}) are solvated of chelated in the acidic aqueous phase (Aq) that is then contacted with an immiscible organic phase (Or). One metal cation is then selectively solvated or chelated in, then extracted by, the organic phase[33].

$$(M_1^{n+}, M_2^{n+}) \times \mathrm{Aq} + \mathrm{Or} = M_1^{n+} \times \mathrm{Aq} + M_2^{n+} \times \mathrm{Or} \quad (1.3)$$

While the aqueous and organic solvating or chelating phases may not be anions per say, they still reflect that by changing the species or environment to which the metal cation binds, separation of metals trapped together in compounds and solid solutions becomes possible. This approach is often employed to leverage solvation and chelating behavior to accentuate minute chemical differences between elements for separation. Notable examples include rare earth elements[33], Nb from Ta[31], Zr from Hf[39], platinum group metals[13], Cu from Fe[12], and nickel (Ni) from cobalt (Co)[13].

For separation of metal sulfides, matte smelting is an approach that can also be thought of in the framework of anion exchange. For the case of Cu production from $CuFeS_2$, Fe separation is conducted in part via in situ oxidation of Fe with oxygen gas (O_2) in the presence of silica (SiO_2) to form a slag containing fayalite (Fe_2SiO_4), a Fe-depleted copper-iron sulfide matte (Cu, Fe, S), and sulfur dioxide (SO_2)[12], where β, γ, δ, ϵ, ζ are stoichiometric factors:

$$CuFeS_2(l) + \beta O_2(g) + \gamma SiO_2(s) = \delta(Cu, Fe, S)(l) + \epsilon Fe_2SiO_4(l) + \zeta SO_2(g) \quad (1.4)$$

The selective desulfidation of Fe in matte smelting is manifested as an oxide-sulfide anion exchange reaction. The conversion of Fe from a sulfide to an oxide allows it to be separated from Cu, leveraging the solution thermodynamics of oxide solubility in the sulfide matte and sulfide solubility in the oxide slag, as well as physical property differences between the two phases such as surface tension and viscosity.

While matte smelting is often used for selective desulfidation, anion exchange by selective sulfidation of an oxide has also been explored in the context of ore cracking and upgrading. Oxides and sulfides are readily separated via conventional froth flotation due to differences in surface hydrophobicity[44,45], suggesting that anion exchange via selective sulfidation would facilitate metal separation techniques with immediate industrial relevance. Selective sulfidation has been explored by the author and others for recovery of a variety of metals[46–68]. The anion exchange between oxygen (O) and sulfur (S) for the selective sulfidation with gaseous elemental sulfur (S_2) of Ni from olivine ($(Fe, Ni, Mg)_2SiO_4$), a component of

nickeliferous lateritic ore, to form nickel sulfide (NiS)is described by the following reaction, where β is a stoichiometric factor:

$$Fe_{1-\beta}\, Ni_{\beta} MgSiO_4(s) + \frac{3\beta}{4} S_2\,(g) =$$
$$Fe_{1-\beta}\, MgSiO_{4-\beta}\,(s) + \beta NiS(s) + \frac{\beta}{2} SO_2(g) \qquad (1.5)$$

The prospect of isolating otherwise difficult to separate oxides by selective sulfidation followed by flotation is promising from environmental, economic, and technological readiness standpoints. However, effective anion exchange from oxides to sulfides is presently hindered by ill-informed reaction kinetics and thermodynamic trends. Sulfidizing agents that are gaseous at or near room temperature, such as hydrogen sulfide (H_2S) and carbon disulfide (CS_2), are known to be non-selective sulfidizing agents[69], leaving pyrite (FeS_2) and elemental sulfur[ii] (S_X) as the main candidates for a S source in selective sulfidation. Therefore, selective sulfidation has thus far either employed FeS_2 mixed with the oxide to be sulfidized, or S pressed in a briquette with the oxide, both of which mask the reaction kinetics and mass transport understanding necessary to design highly-selective anion exchange between oxides and sulfides[55]. Anion exchanges leveraging S chemistry will be the focus of later chapters herein.

Holistically, metal separation technologies ranging from halogenation to matte smelting to solvent extraction can all be viewed in this context of anion exchange. Many other possible anion exchange processes can be imagined, employing chemistries ranging from low temperature aqueous and organic systems up to high temperature pnictogens, chalcogenide, or halides. When informed by the materials science and chemistry of the system, novel anion exchange methods can embody a step change in relevant technoeconomic metrics for metals separation, including purity, efficiency, sustainability, and cost. In the following section, anion exchange chemical processes are considered as pretreatments to enable physical separation.

[ii] Gaseous elemental sulfur (S_X) contains a range of allotropes from monatomic S to S_8. Diatomic sulfur (S_2) is the dominant species in the gas phase at a pressure of 1 atm and temperatures between 800 °C and 2000 °C[77].

1.2 Anion Exchange as a Pretreatment for Physical Separation and the Mineralogical Barrier

In primary production, metallic element sources can be grouped into two categories: those that exist as the dominant cationic species in a single mineral or phase, and those that exist as minor components in phases or minerals via atomic substitution. This distinction between physical and chemical mixtures of natural minerals is termed the "mineralogical barrier"[70]. Across the mineralogical barrier, energy requirements and costs are higher for chemical separation of elements versus physical separation[71]. Secondary sources of materials likewise exhibit their own "mineralogical barrier" between systems where target elements exist as physically-separable entities – such as cathode separation from casing materials in batteries – and systems where target elements are engineered to be in solid solution or mixed metal compounds[59]. The latter requires chemical separations – such as Co separation from manganese in nickel-manganese-cobalt (NMC) oxide battery cathode chemistries[29]. While study of the mineralogical barrier does not replace detailed life cycle assessment with well-defined system boundaries tailored to individual processes or materials, it serves as a useful generalization of energy use trends in materials extraction.

Theoretical and practical mineralogical barriers[59] are compared in Figure 1.3 as a function of product grade in the material feedstock, with the grades of critical elements from recycled magnet, battery, and slag sources noted[72–74]. The theoretical mineralogical barrier for a target element grade in a material feedstock may be determined by the difference in the minimum energy required to chemically extract that component from a single-phase mixture, derived from the ideal Gibbs energy of mixing at a temperature of 25 °C, and the minimum energy required for physical liberation[iii]. Meanwhile, a practical mineralogical barrier may be determined by comparing the actual energy input for comminution and physical separations in mineral concentrate production to that of leaching and solvent extraction in chemical separations. For physical separation processes, energy for grinding using high intensity stirred mills and physical separation via froth flotation as a function of liberated particle size is sometimes

[iii] The minimum practical energy for liberation can be assessed for one spherical grouping of particles from the bulk material, derived using crack resistance energy[78] and the King liberation model[79,80].

available[75]. Here it is taken from zinc sulfide (ZnS) concentrate production data[76], chosen as a model system due to the wide range of liberation sizes practiced in the industry. Energy requirements[8] for high pressure acid leaching (HPAL), SX, and EW for Cu and Ni are used as model systems for simple hydrometallurgical chemical separations. They provide a fair proxy due to the limited number of solvent extraction stages required for separation[12,13]. Energy requirements for lanthanide (Ln) mineral acid roasting, leaching, SX, and compound precipitation to produce cerium oxide (CeO_2), lanthanum oxide (La_2O_3), neodymium oxide (Nd_2O_3), and praseodymium oxide (Pr_6O_{11}) are used as a model system for chemical separations requiring numerous hydrometallurgical separation stages[33].

The practical mineralogical barrier between physical and simple chemical separations is observed to decrease in relative magnitude with decreasing material grade. At a grade of approximately 0.1 wt%, the difference in energy requirements for material separation via physical and simple hydrometallurgical methods becomes negligible. This correlation is consistent with the conventional wisdom that when minerals become too fine-grained or low grade, leaching and hydrometallurgical processing is necessary for product recovery due to decreasing comminution efficiency at decreasing liberation sizes. Meanwhile, with increasing material grade, the energy reduction of physical separations over chemical separations is readily apparent. For example, at feedstock grades of 0.5 wt%, 3 wt%, 10 wt%, and 30 wt%, corresponding to Cu recycling from slag, lithium (Li) recycling from lithium ion batteries, Ni or Co recycling from lithium ion batteries, and Ln recycling from iron-lanthanide-boron (Fe,Ln,B) magnets respectively, the practical barrier is approximately 45,000 kWh, 19,000 kWh, 11,000 kWh, and 6,000 kWh respectively per tonne of product, or 225 kWh, 570 kWh, 1100 kWh, and 1800 kWh respectively per tonne of feed[59]. For pretreatment processes that enable physical separation, this can be viewed as their energy budget. For reference, the energy burden of Cu slag cleaning in a flash furnace is approximately 100 kWh per tonne of feed[12], and Ni smelting in an electric arc furnace is approximately 500 kWh per tonne of feed[13]. Therefore, for both mineralogical and end of life recycling feedstocks where target elements are trapped in solid solutions, a simple pyrometallurgical chemical pretreatment is attractive to enable subsequent physical separation. As discussed in Section 1.1, this pretreatment will likely take the form of a high temperature, pyrometallurgical anion exchange process.

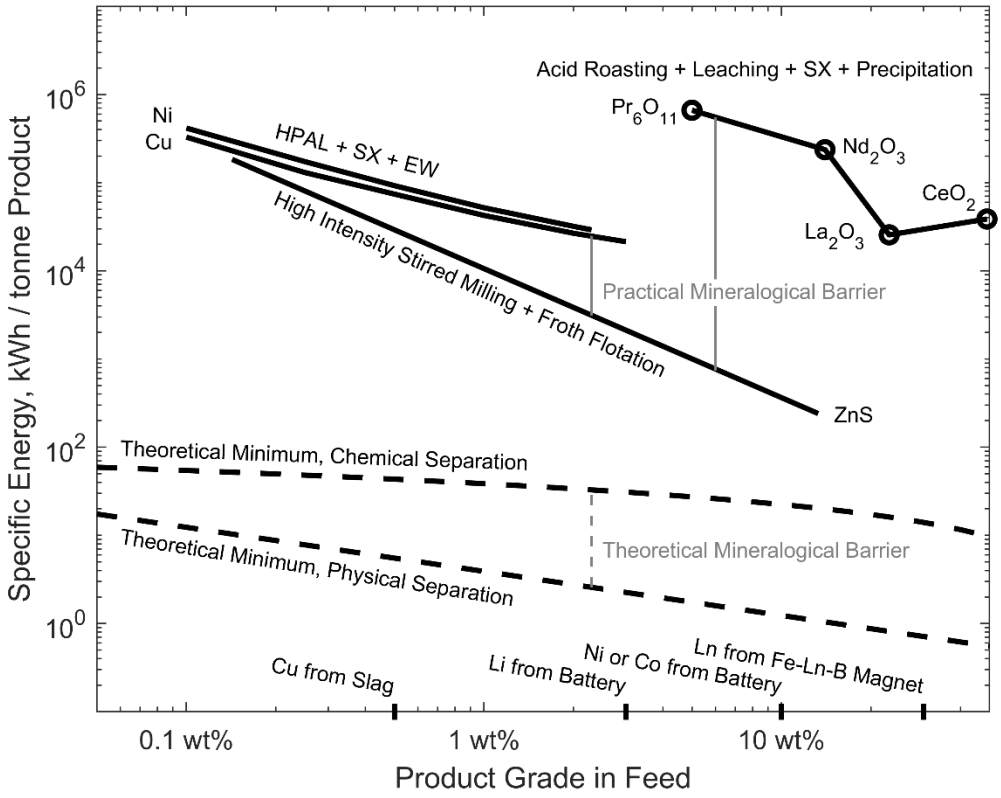

Figure 1.3: Calculated theoretical and practical mineralogical barriers between physical and chemical separations. If the burden of selectivity can be shifted from chemical to physical separation processes via a suitable, energy efficient pretreatment, significant energy savings in materials separation are possible at grades relevant for recovery of critical elements from recycled magnet, battery, and slag sources.

1.3 Focus of the Present Work

From the preceding sections, materials separations can be conducted using physical or chemical methods. Physical separations are energetically preferred for isolating components from physical mixture of distinct phases. Meanwhile, chemical separations are necessary when target elements are mixed with impurities at an atomic level. Regardless of the approach, the separation chemistry employed influences the sustainability and cost of subsequent processing steps, such as metal reduction. This work will focus on the establishment of pyrometallurgical anion exchange chemical pretreatments that enable economically competitive decarbonization in materials processing. In the following chapter, arguments will be made that pyrometallurgical

oxide-sulfide anion exchange chemistry is a promising candidate for separations. Later in Chapter 3, an integrated thermodynamic, kinetic, and mass transport framework will be established for oxide-sulfide anion exchange process design. In Chapters 4 and 5, the separation efficacy of oxide-sulfide anion exchange processes will be explored experimentally. In Chapter 6, technoeconomic evaluation and life cycle assessment will establish the competitiveness of this new approach with legacy processing pathways. Finally in Chapter 7, carbon-free metal product production from sulfide feedstocks produced via oxide-sulfide anion exchange will be demonstrated.

1.4 Summary

Efforts to reduce environmental impacts in metals processing and mining come at a time of falling ore grades and increasing mineralogical complexity. The duality of this challenge motivates the search for new process chemistries that enable reductions in greenhouse gas emissions, water usage, and cost. Across materials processing supply webs, optimizations in separation chemistries are necessary to both reduce the burden of impurity management and facilitate energy efficient, low carbon methods of metal reduction. Separations can be grouped into physical and chemical methods.

Physical approaches leverage comminution to liberate distinct phases from one another which are then isolated using methods such as gravimetric separation, magnetic separation, or froth flotation. Chemical separations are required when target elements and impurities are mixed at the atomic level. They generally require significantly more energy than physical methods; this energy gap is termed the “mineralogical barrier”.

An attractive avenue to reduce the energy burden of chemical separations is to develop a chemical pretreatment that enables subsequent physical separation in place of chemical separation. Energy use trends suggest this pretreatment can be accomplished pyrometallurgically. Such approaches can be envisioned utilizing anion exchange chemistry. In the following chapters, pyrometallurgical oxide-sulfide anion exchange chemistry will be established as pathway to economically decarbonize materials processing and metal reduction for a sustainable future.

1.5 References

1. Harper, G. *et al.* Recycling lithium-ion batteries from electric vehicles. *Nature* vol. 575 75–86 (2019).
2. Allanore, A. Electrochemical engineering for commodity metals extraction. *Electrochem. Soc. Interface* **26**, 63–68 (2017).
3. Nguyen, R. T., Eggert, R. G., Severson, M. H. & Anderson, C. G. Global Electrification of Vehicles and Intertwined Material Supply Chains of Cobalt, Copper and Nickel. *Resour. Conserv. Recycl.* **167**, 105198 (2021).
4. Cheisson, T. & Schelter, E. J. Rare earth elements: Mendeleev's bane, modern marvels. *Science (80-.).* **363**, 489–493 (2019).
5. Binnemans, K., Jones, P. T., Müller, T. & Yurramendi, L. Rare Earths and the Balance Problem: How to Deal with Changing Markets? *Journal of Sustainable Metallurgy* vol. 4 126–146 (2018).
6. Olivetti, E. A., Ceder, G., Gaustad, G. G. & Fu, X. Lithium-Ion Battery Supply Chain Considerations: Analysis of Potential Bottlenecks in Critical Metals. *Joule* vol. 1 229–243 (2017).
7. Rötzer, N. & Schmidt, M. Decreasing Metal Ore Grades—Is the Fear of Resource Depletion Justified? *Resources* **7**, 88 (2018).
8. Norgate, T. & Jahanshahi, S. Low grade ores – smelt, leach or concentrate? *Miner. Eng.* **23**, 65–73 (2010).
9. Chang, K., Hallstedt, B. & Music, D. Thermodynamic and Electrochemical Properties of the Li−Co−O and Li−Ni−O Systems. *Chem. Mater.* **24**, 97–105 (2011).
10. Wagner, M.-E. & Allanore, A. Chemical Thermodynamic Insights on Rare-Earth Magnet Sludge Recycling. *ISIJ Int.* **60**, 2339–2349 (2020).
11. Wang, M. Enthalpy of formation of LiNiO2, LiCoO2 and their solid solution, LiNi1−xCoxO2. *Solid State Ionics* **166**, 167–173 (2004).
12. Schlesinger, M. E., King, M. J., Sole, K. C. & Davenport, W. G. *Extractive Metallurgy of Copper*. (2011). doi:10.1017/CBO9781107415324.004.
13. Crundwell, F. K., Moats, M. S., Ramachandran, V., Robinson, T. G. & Davenport, W. G. *Extractive Metallurgy of Nickel, Cobalt, and Platinum-Group Metals*. (Elsevier, 2011).

14. Hoffmann, C., Hoey, M. Van & Zeumer, B. *Decarbonization challenge for steel*. (2020).
15. Delevingne, L., Glazener, W., Grégoir, L. & Henderson, K. *Climate risk and decarbonization: What every mining CEO needs to know*. (2020).
16. Azadi, M., Northey, S. A., Ali, S. H. & Edraki, M. Transparency on greenhouse gas emissions from mining to enable climate change mitigation. *Nat. Geosci.* **13**, (2020).
17. Guberman, D. Nickel in Indonesia: A Story of Trade Restraints and Emerging Technologies. in *Executive Briefings on Trade, May 2021* (2021).
18. Fan, Z. & Friedmann, S. J. Low-carbon production of iron and steel: Technology options, economic assessment, and policy. *Joule* **5**, 829–862 (2021).
19. Nuss, P. & Eckelman, M. J. Life cycle assessment of metals: a scientific synthesis. *PLoS One* **9**, e101298 (2014).
20. ISE. *Current prices of rare earths*. (2019).
21. Sphera. *Nickel Institute Life Cylce Data*. (2023).
22. Farjana, S. H., Huda, N. & Mahmud, M. A. P. Impacts of aluminum production: A cradle to gate investigation using life-cycle assessment. *Sci. Total Environ.* **663**, 958–970 (2019).
23. K Lee, J. C. & Wen, Z. Pathways for greening the supply of rare earth elements in China. *Nat. Sustain.* **1**, 598–605 (2018).
24. MCI. *World steel prices - flat & long products*. https://www.steelonthenet.com/steel-prices.html (2023).
25. USGS. *Mineral commodity summaries 2023*. http://pubs.er.usgs.gov/publication/mcs2023 (2023) doi:10.3133/mcs2023.
26. SMM. *Metal Spot Prices*. www.metal.com.
27. Outokumpu. Environmental Product Declaration. (2019).
28. Goldschmidt, V. M. The principles of distribution of chemical elements in minerals and rocks. The seventh Hugo Müller Lecture, delivered before the Chemical Society on March 17th, 1937. *J. Chem. Soc.* 655–673 (1937) doi:10.1039/JR9370000655.
29. Ciez, R. E. & Whitacre, J. F. Examining different recycling processes for lithium-ion batteries. *Nat. Sustain.* **2**, 148–156 (2019).
30. Reck, B. K. & Graedel, T. E. Challenges in Metal Recycling. *Science (80-.).* **337**, 690–696 (2012).
31. Flett, D. S. Solvent extraction in hydrometallurgy: the role of organophosphorus

extractants. *J. Organomet. Chem.* **690**, 2426–2438 (2005).

32. Rhee, K. I. & Sohn, H. Y. The selective carbochlorination of iron from titanlferous magnetite ore in a fluidized bed. *Metall. Trans. B* **21**, 341–347 (1990).
33. Zhao, B., Zhang, J. & Schreiner, B. *Separation Hydrometallurgy of Rare Earth Elements*. (Springer International Publishing AG Switzerland, 2016).
34. Narayanan, R. P., Kazantzis, N. K. & Emmert, M. H. Selective Process Steps for the Recovery of Scandium from Jamaican Bauxite Residue (Red Mud). *ACS Sustain. Chem. Eng.* **6**, 1478–1488 (2018).
35. McCoy, H. N. The Electrolysis of Rare Earth Acetates and the Separation of Europium as Amalgam from Other Rare Earths. *J. Am. Chem. Soc.* **63**, 3432–3433 (1941).
36. Kolesov, G. M. & Pankratova, L. N. Separation of Rare-earth Elements by Electrolysis at a Mercury Cathode. *Russ. Chem. Rev.* **37**, 701–710 (1968).
37. Sahu, S. K., Chmielowiec, B. & Allanore, A. Electrolytic Extraction of Copper, Molybdenum and Rhenium from Molten Sulfide Electrolyte. *Electrochim. Acta* **243**, 382–389 (2017).
38. Daehn, K. E. *et al.* Liquid Copper and Iron Production from Chalcopyrite, in the Absence of Oxygen. *Metals (Basel).* **12**, 1440 (2022).
39. Taghizadeh, M., Ghanadi, M. & Zolfonoun, E. Separation of zirconium and hafnium by solvent extraction using mixture of TBP and Cyanex 923. *J. Nucl. Mater.* **412**, 334–337 (2011).
40. Neilsen, R. H. Hafnium and Hafnium Compounds. in *Encyclopedia of Chemical Technology* (2013). doi:10.1002/14356007.a12.
41. Gaballah, I. & Djona, M. Recovery of Co, Ni, Mo, and V from unroasted spent hydrorefining catalysts by selective chlorination. *Metall. Mater. Trans. B* **26**, 41–50 (1995).
42. González, J., Bohé, A., Pasquevich, D. & Ruiz, M. D. C. β-Ta2O5 Carbochlorination with Different Types of Carbon. *Can. Metall. Q.* **41**, 29–40 (2002).
43. Sohn, H. Y. & Zhou, L. The kinetics of carbochlorination of titania slag. *Can. J. Chem. Eng.* **76**, 1078–1082 (1998).
44. Kyzas, G. Z., Lazaridis, N. K. & Matis, K. A. Flotation: Recent innovations in an interesting and effective separation process. in *Advanced Low-Cost Separation Techniques*

in Interface Science vol. 30 15–42 (Elsevier B.V., 2019).

45. Gallios, G. P., Kyzas, G. Z. & Matis, K. A. Flotation in the 2010s: Focus on mineral processing. in *Advanced Low-Cost Separation Techniques in Interface Science* vol. 30 43–68 (Elsevier B.V., 2019).
46. Ahmad, S., Rhamdhani, M. A., Pownceby, M. I. & Bruckard, W. J. Sulfidation Kinetics of Natural Chromite Ore Using H2S Gas. *Metall. Mater. Trans. B Process Metall. Mater. Process. Sci.* **46**, 557–567 (2015).
47. Ahmad, S., Rhamdhani, M. A., Pownceby, M. I. & Bruckard, W. J. Thermodynamic assessment and experimental study of sulphidation of ilmenite and chromite. *Trans. Institutions Min. Metall. Sect. C Miner. Process. Extr. Metall.* **123**, 165–177 (2014).
48. Ke, Y. *et al.* Behavior and effect of calcium during hydrothermal sulfidation and flotation of zinc-calcium-based neutralization sludge. *Miner. Eng.* **74**, 68–78 (2015).
49. Ke, Y. *et al.* Sulfidation behavior and mechanism of zinc silicate roasted with pyrite. *Appl. Surf. Sci.* **435**, 1011–1019 (2018).
50. Liang, Y. J. *et al.* Hydrothermal sulfidation and floatation treatment of heavy-metal-containing sludge for recovery and stabilization. *J. Hazard. Mater.* **217**–**218**, 307–314 (2012).
51. Liu, W., Zhu, L., Han, J., Jiao, F. & Qin, W. Sulfidation mechanism of ZnO roasted with pyrite. *Sci. Rep.* **8**, 1–12 (2018).
52. Merritt, R. R. High Temperature Methods for Processing Monazite: II. Reaction with Sodium Carbonate. *J. Less-Common Met.* **166**, 211–219 (1990).
53. Rhamdhani, M. A., Ahmad, S., Pownceby, M. I., Bruckard, W. J. & Harjanto, S. Selective sulphidation of impurities in weathered ilmenite. Part 1 – Applicability to different ilmenite deposits and simulated Becher kiln conditions. *Miner. Eng.* **121**, 55–65 (2018).
54. Stinn, C. & Allanore, A. Ferronickel Production from Nickel Laterite via Sulfide Chemistry. in *Advances in Pyrometallurgy* (ed. Fleuriault, C.) 1–17 (The Minerals, Metals & Materials Society, 2023).
55. Stinn, C. & Allanore, A. Selective sulfidation of metal compounds. *Nature* **602**, 78–83 (2022).
56. Stinn, C. & Allanore, A. Selective Sulfidation and Electrowinning of Nickel and Cobalt for Lithium Ion Battery Recycling. in *Ni-Co 2021: The 5th International Symposium on*

Nickel and Cobalt (eds. Anderson, C. et al.) 99–110 (Springer Nature Switzerland AG, 2021). doi:10.1007/978-3-030-65647-8_7.

57. Stinn, C. & Allanore, A. Selective Sulfidation for Rare Earth Element Separation. in *Rare Metal Technology 2022* (ed. Ouchi, T.) 259–278 (The Minerals, Metals & Materials Society, 2022). doi:10.1007/978-3-030-92662-5_25.
58. Allanore, A. & Stinn, C. Selective Sulfidation and Desulfidation (Patent US20210277531A1). (2021).
59. Stinn, C. & Allanore, A. Shifting the Burden of Selectivity from Chemical to Physical Separation Processes via Selective Sulfidation. in *REWAS 2022: Developing Tomorrow's Technical Cycles* (ed. Lazou, A.) 119–136 (The Minerals, Metals & Materials Society, 2022).
60. Stinn, C., Gutierrez, C., Daehn, K. & Allanore, A. Sulfidation for Copper Mineral Processing and Impurity Management. in *The Igo Wilkomirsky Symposium on Pyrometallurgy* (ed. IIMCh) 785–796 (Copper 2022, 2022).
61. Stinn, C., Kaker, V., Adams, Z. K. & Allanore, A. Separation of Rare Earth Elements from Monazite Via Sulfidation. in *Rare Metal Technology 2023* (ed. Ouchi, T.) (The Minerals, Metals & Materials Society, 2023). doi:10.2472/jsms.12.559.
62. Allanore, A. & Stinn, C. Sulfide Reactive Vacuum Distillation, Absorption, Stripping, and Extraction for Metal Alloy Production. (2023).
63. Godoy, R. & Krasuk, J. H. Thermic Sulphidization and Copper Recovery from Basic Copper Oxide Ores with Limestone Gangue. *Lat. Am. J. Chem. Eng. Appl. Chem.* **4**, 13–30 (1974).
64. Han, J., Liu, W., Wang, D., Jiao, F. & Qin, W. Selective Sulfidation of Lead Smelter Slag with Sulfur. *Metall. Mater. Trans. B* **47**, 344–354 (2015).
65. Han, J. *et al.* Selective Sulfidation of Lead Smelter Slag with Pyrite and Flotation Behavior of Synthetic ZnS. *Metall. Mater. Trans. B* **47B**, 2400–2410 (2016).
66. Han, J. *et al.* Mechanism study on the sulfidation of ZnO with sulfur and iron oxide at high temperature. *Sci. Rep.* **7**, 42536 (2017).
67. Harris, C. T., Peacey, J. G. & Pickles, C. A. Selective sulphidation and flotation of nickel from a nickeliferous laterite ore. *Miner. Eng.* **54**, 21–31 (2013).
68. Harris, C. T., Peacey, J. G. & Pickles, C. A. Selective sulphidation of a nickeliferous

lateritic ore. *Miner. Eng.* **24**, 651–660 (2011).

69. Afanasiev, P. *et al.* Preparation of the mixed sulfide Nb2Mo3S10 catalyst from the mixed oxide precursor. *Catal. Letters* **64**, 59–63 (2000).
70. Skinner, B. J. A Second Iron Age Ahead? The distribution of chemical elements in the earth's crust sets natural limits to man's supply of metals that are much more important to the future of society than limits on energy. *Am. Sci.* **64**, 258–269 (1976).
71. Skinner, B. J. Earth resources (minerals/metals/ores/geochemistry/mining). *Proc. Natl. Acad. Sci. USA* **76**, 4212–4217 (1979).
72. Ahmed, S., Nelson, P. A., Gallagher, K. G., Susarla, N. & Dees, D. W. Cost and energy demand of producing nickel manganese cobalt cathode material for lithium ion batteries. *J. Power Sources* **342**, 733–740 (2017).
73. Gorai, B., Jana, R. K. & Premchand. Characteristics and utilisation of copper slag - A review. *Resour. Conserv. Recycl.* **39**, 299–313 (2003).
74. Zhang, Y. *et al.* Hydrometallurgical Recovery of Rare Earth Elements from NdFeB Permanent Magnet Scrap: A Review. *Met. 2020, Vol. 10, Page 841* **10**, 841 (2020).
75. Taylor, L., Skuse, D., Blackburn, S. & Greenwood, R. Stirred media mills in the mining industry: Material grindability, energy-size relationships, and operating conditions. *Powder Technol.* **369**, 1–16 (2020).
76. de Bakker, J. Energy Use of Fine Grinding in Mineral Processing. *Metall. Mater. Trans. E* **1**, 8–19 (2014).
77. Meyer, B. Elemental sulfur. *Chem. Rev.* **76**, 367–388 (1976).
78. Fuerstenau, D. & Abouzeid, A.-Z. The energy efficiency of ball milling in comminution. *Int. J. Miner. Process.* **67**, 161–185 (2002).
79. Finch, J. A. & Petruk, W. Testing a solution to the King liberation model. *Int. J. Miner. Process.* **12**, 305–311 (1984).
80. King, R. P. A model for the quantitative estimation of mineral liberation by grinding. *Int. J. Miner. Process.* **6**, 207–220 (1979).

Chapter 2

Hypothesis

Success in economical decarbonization of metal production from natural and recycled sources requires the deployment of improved material separation processes that unlock new sustainability synergies across the supply chain. The separation of an element or compound from its surrounding medium relies on exploitable chemical or physical variations between components of the system. Physical separation processes, which isolate distinct phases from one another, are enabled by physical property differences between those phases. Examples include gravimetric separation (density), froth flotation (hydrophobicity), magnetic separation (magnetic susceptibility), electrostatic separation (electrical conductivity), and distillation (vapor pressure). Meanwhile, chemical separation processes accomplish isolation of components mixed at the atomic level by leveraging anion exchange chemistry. These are enabled by differences in reactivity between components when in a given anion environment. Examples include solvent extraction, alkali fusion, carbochlorination, matte smelting, sulfidation, or selective reduction. As discussed in Chapter 1, the choice between chemical and physical separation is practically made based on bulk processing realities such as energy usage and cost, and may be contextualized through the concept of the "mineralogical barrier". Low energy selective anion exchange processes that enable subsequent physical separation are a promising pathway to reduce the energy and environmental burden of material enrichment and improve downstream metal reduction.

Herein oxide-sulfide anion exchange chemistry is established as a promising pathway to shift the burden of selectivity from tedious chemical separation processes to more economically and environmentally benign physical methods. Hypotheses surrounding the efficacy and implementation of this approach are constructed. An analytical pathway is proposed to test these hypotheses.

2.1 The Case for Oxide-Sulfide Anion Exchange Chemistry

Differences in a given chemical or physical property within a system must be as large as possible in order to maximize the effectiveness of materials separation based on that property. Distinctions in physical and chemical properties between one compound and another at the atomic scale are related to their bonding behaviors (polarity) and arrangement (ex: ligancy and ionic radius)[1]. Likewise, according to Hume Rothery[2] and Goldschmidt[3] Rules, the solubility or precipitation of an element or compound in the bulk matrix and its partitioning between phases is determined by similar phenomena. The optimal anion exchange chemistry to enable improved material separations is that which maximizes differences in bonding and atomic arrangement to enable pragmatically exploitable chemical and physical property differences. Concurrently, new anion exchange separation chemistries must be consistent with technoeconomic and supply web realities. For a new separation framework to be broadly applicable, its feedstocks must exhibit low costs and environmental impacts. Separation products must be amenable to end product manufacture. A balance must be struck between performance, cost, and price.

To identify promising anion exchange chemistries for separation, the following main criteria are proposed:

- Anion exchange reagent abundance / cost
- Likelihood of anion exchange reagent to form immiscible product compounds
- Amenability to subsequent physical separation and reduction to metal

- Anticipated performance improvements versus deployed methods

Oxide materials are chosen as starting feedstocks for treatment via anion exchange. Oxygen-based minerals (silicates, carbonates, etc.) are among the most prevalent in nature[3]. Meanwhile, sulfide and end of life recycled materials are readily calcined to form oxides[4].

In Table 2.1, the crustal abundance,[5] sources[6], costs[6], and reserves[6] of some different anion elements are reported. Phosphorous (P), sulfur (S), fluorine (F), and chlorine (Cl) are geologically abundant, with feedstocks for their production currently processed at commodity scales. Of these, S is the most readily and economically available in its pure elemental form. While specialty separation applications could be imagined for less abundant anion elements, current supply chains and market dynamics do not motivate their adoption as platform feedstocks for anion exchange treatments across broad sectors of extractive metallurgy.

The potential efficacy of oxide anion exchange using P, S, F, and Cl to produce distinct phases for physical separation may be considered using principles from Hume Rothery[2] and modified[7] Goldschmidt[3] criteria for bonding and miscibility. Species with larger differences in size or electronegativity are more likely to form distinct phases, herein aiding in their separation. Differences in Pauling electronegativity[8] ($\Delta\chi$) and ionic (Shannon) radius[9] (Δr_S) between anion exchange candidates and oxygen (O) are compared in Table 2.2, with larger differences predicted to better facilitate phase immiscibility. While the generation of immiscible compounds is probable during all oxide anion exchanges considered, anion exchange with phosphorous and sulfur maximize differences in $\Delta\chi$ and Δr_S. This suggests that oxide-sulfide or oxide-phosphorous anion exchange are the most amenable to compound precipitation. However, the amenability of different anion exchange pathways to subsequent physical separation and metal reduction must also be considered.

Separations of oxides, sulfides, halides, and phosphorous-containing compounds have all been considered extensively in mineral processing. In regards to enabling downstream physical separation using mature technologies, oxide-sulfide anion exchange is the most versatile. Sulfides are among the easiest materials to physically separate from oxides using methods ranging from gravimetric separation (density), froth flotation (hydrophobicity), magnetic separation (magnetic susceptibility), electrostatic separation (electrical conductivity), and volatility (vapor pressure)[10,11]. Halides may be separated using similar approaches; additional

Element	Crustal Abundance (ppm)[5]	Sources[6]	2022 Global Yearly Production and Reserves[6]	2022 USA Average Commodity Price[6]
Phosphorous (P)	1050	Phosphate rocks	Production: 220,000,000 tonnes of phosphate rock Reserves: 72,000,000,000 tonnes of phosphate rock	Phosphate rock: $90 / tonne
Arsenic (As)	1.8	Sulfide and sulfosalt minerals	Production: 45,000 tonnes of arsenic content, mostly as trioxide Reserves: > 900,000 tonnes of arsenic content	Pure element: $3,300 / tonne
Antimony (Sb)	0.02	Sulfide and sulfosalt minerals	Production: 110,000 tonnes of antimony content Reserves: >1,800,000 tonnes of antimony content	Pure element: $14,000 / tonne
Sulfur (S)	350	Native mineral, metal sulfides, natural gas, petroleum, tar sands, coal, gypsum	Production: 82,000,000 tonnes Reserves: >5,000,000,000 in mineral sources, natural gas, and petroleum >600,000,000,000 in coal and shale sources	Pure element: $150 / tonne
Selenium (Se)	0.05	Sulfide and sulfosalt minerals	Production: 3,200 tonnes Reserves: 81,000 tonnes	Pure element: $22,000 / tonne
Tellurium (Te)	0.001	Sulfide and sulfosalt minerals	Production: 640 tonnes Reserves: 32,000 tonnes	Pure element: $70,000 / tonne
Fluorine (F)	585	Fluorspar and phosphate minerals, sea water	Production: 8,300,000 tonnes of fluorspar rock Reserves: 260,000,000 tonnes of fluorspar rock, 5,000,000,000 tonnes of fluorspar equivalent in phosphate rocks	Fluorspar rock: $140 - $360 / tonne
Chlorine (Cl)	145	Brines, salt deposits, sea water	Production: 290,000,000 tonnes of salt Reserves: salt is virtually inexhaustible	Salt: $8 - $230 / tonne
Iodine (I)	0.45	Brine deposits, sea water	Production: 33,000 tonnes Reserves: 6,100,000 in brine deposits 90,000,000,000 in sea water	Pure element $41,000 / tonne

Table 2.1: Crustal abundances, sources, yearly production, reserves, and costs of some anion elements.

	P	S	F	Cl
$\Delta\chi$ / eV$^{1/2}$ [8]	1.25	0.86	-0.53	0.28
Δr_S / pm [9]	-72 (-3)	-44 (-2)	-0.07 (-1)	-41 (-1)

Table 2.2: Comparison of electronegativity (Pauling) and ionic (Shannon) radius differences ($\Delta\chi$ and Δr_S respectively) between different anions with oxygen. For Δr_S, anion charge is denoted in parenthesis. Oxide anions are taken to have a -2 charge.

care is required however to manage the solubilities of different salts during water-based separation processes such as flotation[12]. Separations of oxides and phosphates are also accomplished via froth flotation and other methods[13].

Oxides, sulfides, and halides are all amenable to a variety of methods of metal reduction. Oxides have historically been reduced carbothermically, yet carbon-free electrolytic, hydrogen, and metallothermic pathways exist[14–21]. Sulfides are readily reduced via oxidative[10,11] or electrolytic methods[22–30]; metallothermic approaches are also available[31–36] but have received less attention. Electrolytic pathways and metallothermic reduction are the norm for metal production from or in molten fluorides and chlorides[37]. Reduction of phosphates is challenging electrolytically[38] and they are generally converted to some other chemistry prior to metal production. This suggests that oxide-phosphate anion exchange is less conducive for enabling physical separation directly prior to reduction than other approaches.

Reduction series are compared between oxides, sulfides, fluorides, and chlorides at a temperature of 1000 °C and oxygen, sulfur, fluorine, and chlorine partial pressures (P_{O_2}, P_{S_2}, P_{F_2}, and P_{Cl_2} respectively) of 1 atm in Figures 2.1-2.3, calculated using the FactSage 8.0 FactPS database. In most instances, sulfide formation is predicted to exhibit less negative standard Gibbs energy of formation ($\Delta_f G°$) than other anion chemistries, indicating lower thermodynamic barriers to compound reduction and metal production. This approach could enable the use of lower energy reduction pathways with carbon-free reductants. More detailed technoeconomic and sustainability analysis is required however to determine if this oxide-sulfide anion exchange is sufficiently energy efficient to make lower reduction burdens worthwhile.

From trends in feedstock costs, separation versatility, and energy savings in reduction, oxide-sulfide anion exchange chemistry is the most promising from a technoeconomic perspective. However, technoeconomic advantages must be supported by separation

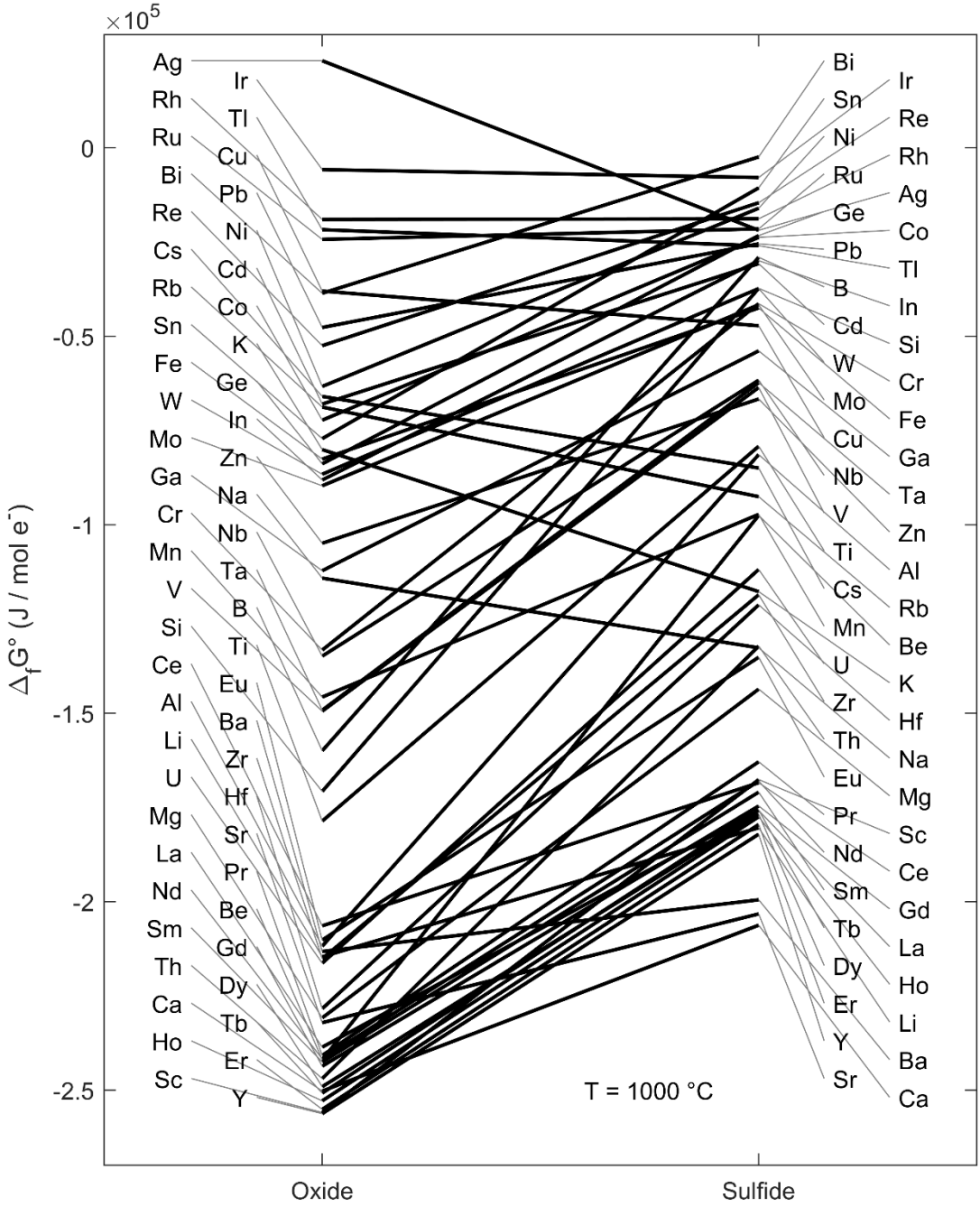

Figure 2.1: Comparison of the Gibbs energy of formation ($\Delta_f G°$) for oxide and sulfide compounds at 1000°C and oxygen or sulfur gas partial pressures of 1 atm. Less negative values correspond to lower thermodynamic barriers to metal reduction.

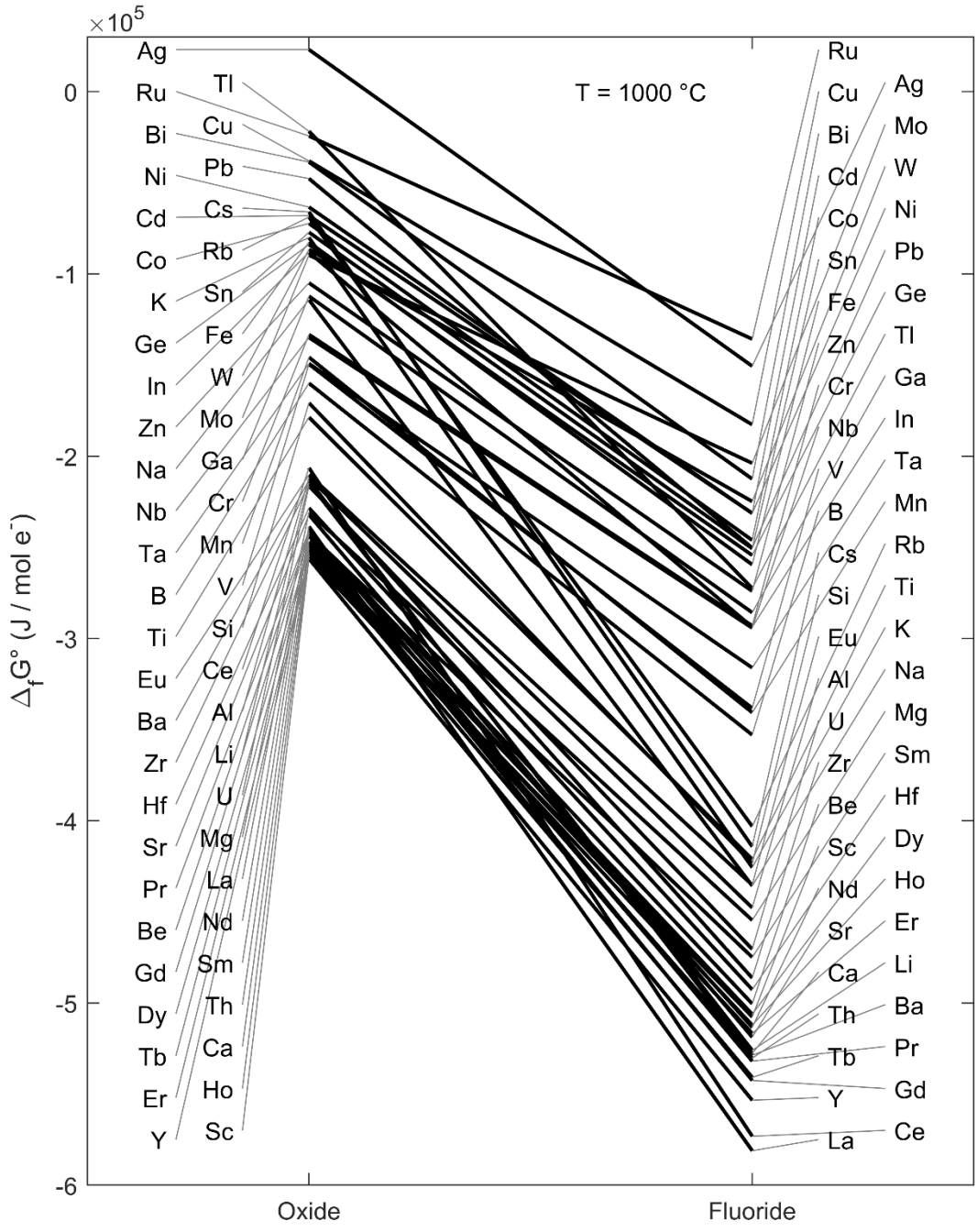

Figure 2.2: Comparison of the Gibbs energy of formation ($\Delta_f G°$) for oxide and fluoride compounds at 1000°C and oxygen or fluorine gas partial pressures of 1 atm. Less negative values correspond to lower thermodynamic barriers to metal reduction.

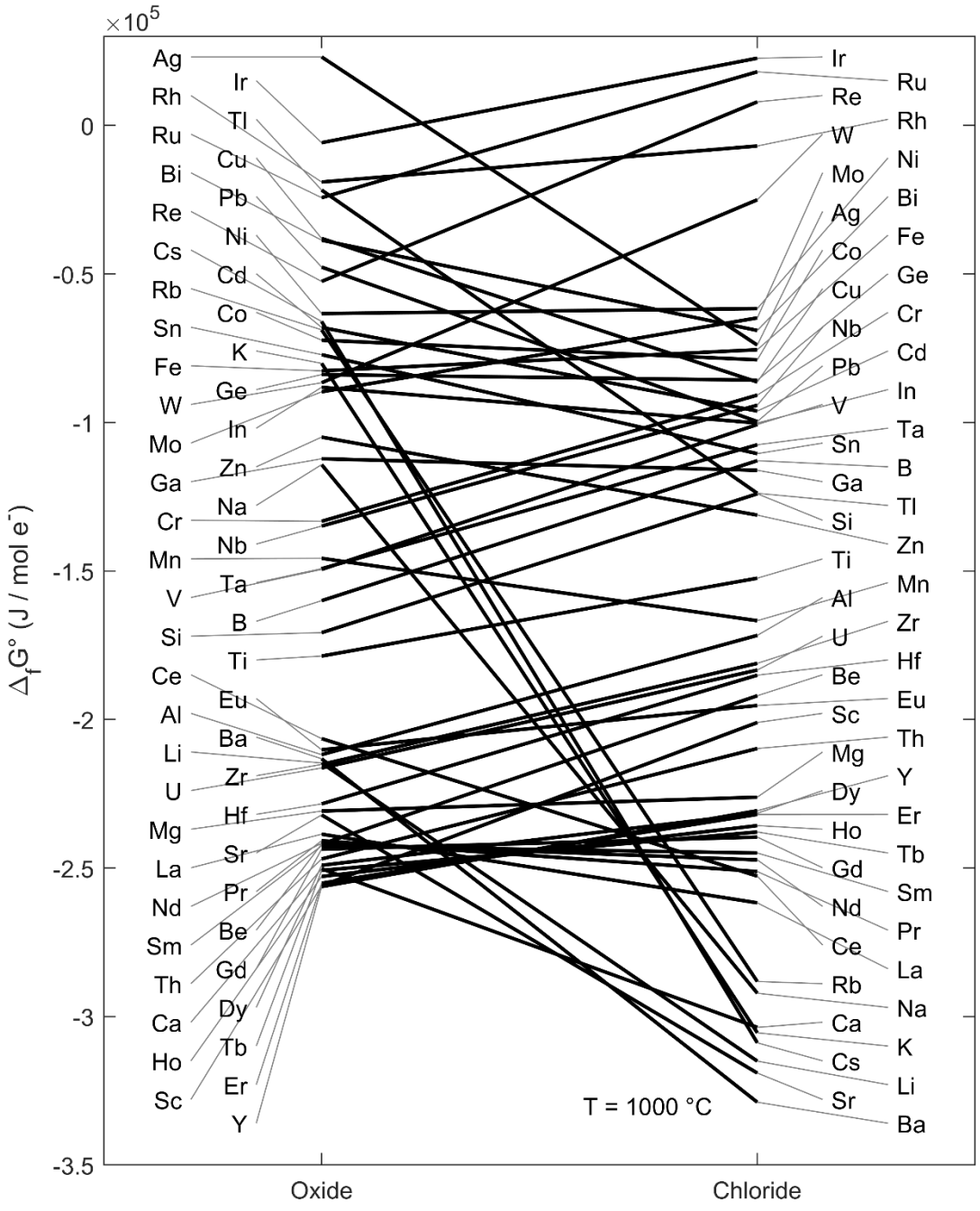

Figure 2.3: Comparison of the Gibbs energy of formation ($\Delta_f G°$) for oxide and chloride compounds at 1000°C and oxygen or chlorine gas partial pressures of 1 atm. Less negative values correspond to lower thermodynamic barriers to metal reduction.

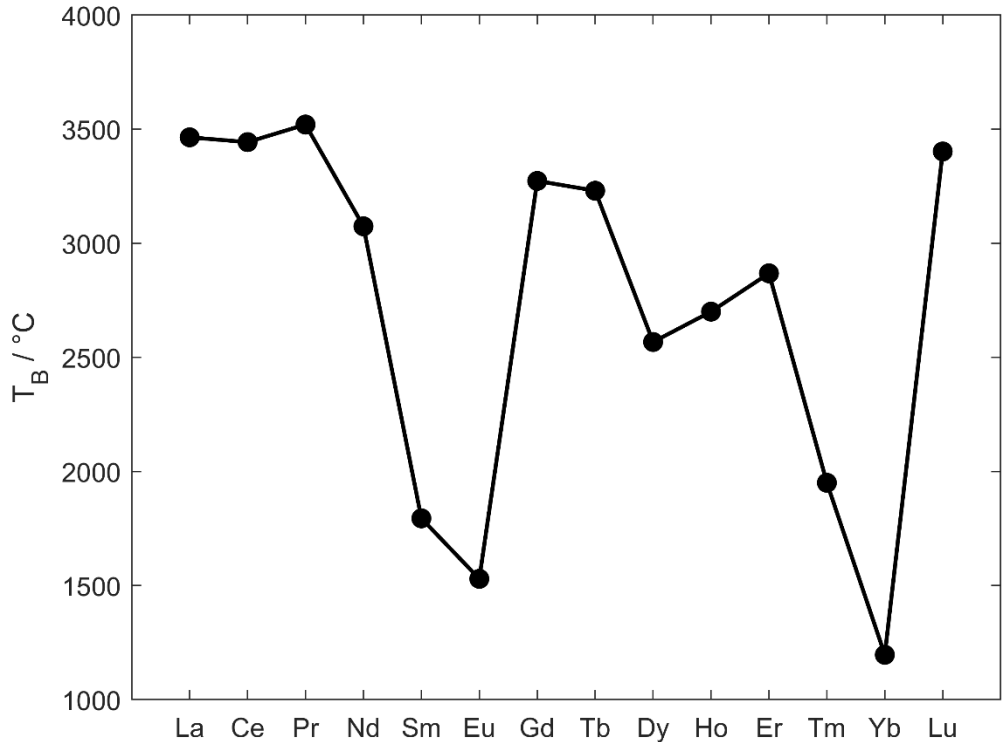

Figure 2.4: Boiling points (T_B) of lanthanide (Ln) elements.

performance. The lanthanide (Ln) elements are chosen as a case study for exploring the potential separation effectiveness of oxide-sulfide anion exchange. Currently, Ln are among the most challenging elements to chemically isolate, generally requiring up to a hundred or more hydrometallurgical separation stages to achieve a pure Ln compound. Ostensibly, this separation difficulty is due to the chemical similarities between the rare earth elements. However, even minute variations in valence and electronic structure can lead to notable differences in physical or chemical behavior. One example is found in the boiling point[iv] temperatures (T_B) of lanthanide elements[39], plotted in Figure 2.4. Large variations in vaporization behaviors between Ln highlight that minute deviations in ground state configurations and valence transitions can manifest into significant property differences[40]. Optimal anion exchange chemistries for

[iv] For quantitative insight into the electronic origins of variations in rare earth element vaporization behavior and valency, the reader is directed to work by Johansson[40,59] and Strange[60].

separation should similarly accentuate atomic scale differences and bonding behavior between elements into meaningful and exploitable properties for separation.

Preliminary insight into the potential effectiveness of novel oxide-sulfide anion exchange can be derived from the geologic partitioning of elements between oxide and sulfide phases. However, leveraging terrestrial sulfide mineral phases to inform potential oxide-sulfide anion exchange efficacy is challenging for several reasons. Accessible terrestrial sulfide phases have been subjected to weathering and hydrothermal forces. Furthermore, geologic sulfide phases on Earth generally formed under P_{O_2} that lead to a large number of elements being almost exclusively partitioned into oxide-based mineral phases (oxides, silicates, phosphates, etc.). This informed the notion of lithophilic (oxide or rock-loving) and chalcophilic (sulfur or chalcogenide-loving) elements[3]. However, other interstellar bodies, such as Enstatite- (En) chondrite meteorites, may have formed celestially under lower P_{O_2} than Earth, providing more neutral insight of elements' differing affinities toward oxide or sulfide formation[41].

En-chondrite meteorites are chosen as a case study to compare the separation effectiveness of rare earth elements between oxide and sulfide phases versus modern hydrometallurgical approaches. Generally, the separation effectiveness for two metallic elements (M_1 and M_2) achieved by a two-phase separation system (phases A* and B^*) is described by the separation factor[13] β^{sep}, where D is the distribution ratio of a metal between the two phases, and c is the concentration of the metallic element in the phase:

$$\beta^{sep}{}_{M_1/M_2} = \frac{D_{M_1}}{D_{M_2}} = \frac{\frac{c_{M_1}^{(A^*)}}{c_{M_1}^{(B^*)}}}{\frac{c_{M_2}^{(A^*)}}{c_{M_2}^{(B^*)}}} \tag{2.1}$$

β^{sep} is effectively a figure of merit for the separation purity. As defined in Eqn. 2.1, β^{sep} does not provide insight for the kinetics or mass transport of the separation chemistry.

Calculated D for Ln elements between major En oxide ($MgSiO_3$) and oldhamite (Old) or niningerite (Nng) sulfide phases ($(Ca, Mg)S$ and MgS respectively) in the Sahara 97072 chondrite meteorite[42] are reported in the top panel of Figure 2.5. Ln concentrations are on the order of 2-20 ppm, 1-400 ppb, and 0.1-2 ppm in Old, Nng, and En phases respectively[42].

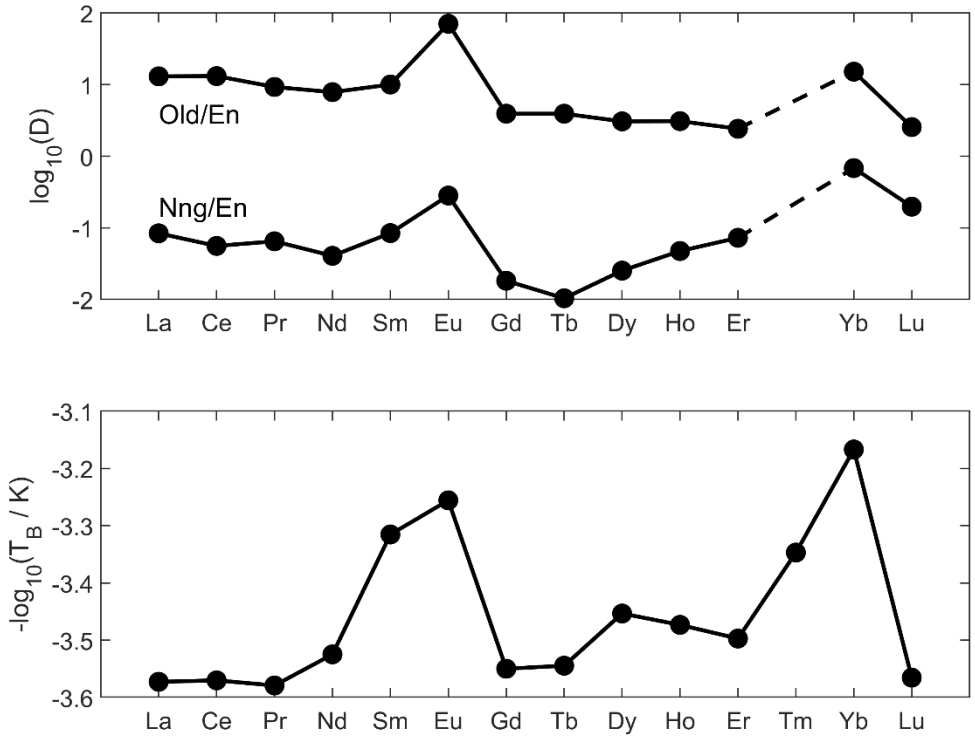

Figure 2.5: Correlation of lanthanide (Ln) element distribution ratios (D) between oxide (En) and sulfide (Old or Nng) phases in En-chondrite meteorites and the negative logarithm of the pure element boiling point (T_B). The upper panel corresponds to rare earth element D between oxide (En) and sulfide (Old or Nng). The lower panel illustrates the correlation between inverse $\log_{10}$ of T_B in Kelvin (K) and trends in D above.

$D_{\mathrm{Old/En}}$ and $D_{\mathrm{Nng/En}}$ exhibit different orders of magnitude but follow similar trends for individual rare earth elements. Trends between individual rare earth element partitioning directly correlate with the inverse $\log_{10}$ of T_B, shown in the lower panel of Figure 2.5. Previously, Johansson attributed trends in lanthanide vaporization with changing valency and a transition between metallic and insulating behavior in liquid and gaseous states respectively[40]. This suggests that oxide-sulfide anion exchange chemistry may leverage similar electronic structure variations between rare earth elements to accentuate their chemical differences, potentially enabling selective separation. These correlations motivate considerations surrounding the role of electronic, electrostatic, and electronegativity effects in describing a compound's affinity toward oxide-sulfide anion exchange, detailed in Chapter 3. Some other

elements found mixed in oxide phases on earth, such as niobium (Nb) and tantalum (Ta) also exhibit selective partitioning between chondrite oxide and sulfide phases[41]. Together, these findings challenge conventional wisdom[3] surrounding which elements are chalcophilic and lithophilic; surprises in element partitioning under less oxidizing conditions reveals that chalcophilic and lithophilic behavior are in fact dependent on the system environment. Meanwhile, variations in the divalent calcium (Ca) and magnesium (Mg) ratio in Nng and Old highlight that thermodynamic mixing and solution effects may further modulate oxide-sulfide anion exchange behavior, providing additional opportunities for selectivity in oxide-sulfide anion exchange. This suggests that siderophilic interactions with divalent iron may be a likely avenue to tune oxide-sulfide anion exchange selectivity. From Eqn. 2.1, β^{sep} may be calculated between Nng, Old, and En phases to quantify separation effectiveness.

Table 2.3 compares current industrial[13] hydrometallurgical β^{sep} with the partitioning of Ln between the En-chondrite oxide and sulfide phases for some challenging Ln separations. Partitioning of Ln between En-chondrite oxide and sulfide phases is found to be on par with or more selective than modern industrial hydrometallurgy[13]. These findings suggests that oxide-sulfide anion exchange may be a promising approach for achieving highly selective materials separation.

	Old / En	**Nng / En**	**P507-kerosene / HCl**	**HDEHP / HCl**	**Cyanex 923**
$\boldsymbol{Nd/Pr}$	1.2	1.6	1.1	1.9	1.2
$\boldsymbol{Nd/Sm}$	1.3	2.1	1.8	1.4	1.3
$\boldsymbol{Eu/Tb}$	18.0	15.5	1.4	1.2	1.0

Table 2.3: Comparison of natural En-chondrite and industrial hydrometallurgical separation factors for neodymium (Nd) / praseodymium (Pr), Nd / samarium (Sm), and europium (Eu) / terbium (Tb). P507 and Cyanex 923 refer to proprietary organic solvent extractants, HDEHP refers to di-(2-ethylhexyl)phosphoric acid, and HCl refers to hydrochloric acid.

2.2 Prior Art, Scientific Gaps, and Engineering Challenges

Industrial scale materials separations and metal production utilizing sulfide processing have previously been mostly limited to metals that occur naturally as sulfide minerals, such as copper (Cu), nickel (Ni), molybdenum (Mo), lead (Pb), zinc (Zn), mercury (Hg), Sb, and platinum group metals (PGMs). However, the idea of introducing S as a reactant in metallurgical processes has been around since the Middle Ages. Prior to the year 1200, it was discovered that S could be employed for dealloying gold (Au) and silver (Ag)[43]. By the year 1500, this approach[43] was also demonstrated for separation of Au from Cu. Around the same time, antimony sulfide (Sb_2S_3) was also shown to facilitate Au dealloying[43]. While constituting the pinnacle of industrial chemistry at the time, separation approaches based on sulfide chemistry did not receive wide scale application to metals beyond Au, Ag, Cu, Pb, Hg, and Sb until much later.

In the 19th and early 20th centuries, industrial scale processing of metals and materials using modern chemical frameworks began. Predominance area diagrams developed by Pourbaix[44] and later popularized by Kellogg[45] quantified approaches for sulfide roasting, enabling subsequent carbothermic or oxidative reduction. Oxide-sulfide anion exchange was employed industrially for processing oxides of Cu and nickel Ni in the second half of the twentieth century[10,46,47]. However, these approaches were not geared toward maximizing process selectivity, and again received limited attention for metals that did not also exist in significant sulfide-based mineral reserves with established sulfide reduction pathways.

Expansion of minerals processing operations using S today benefit from the ability to abate SO_2 emissions via the production of sulfuric acid[48]. For many Cu smelters, the acid and electricity produced via SO_2 abatement is a significant contributor to revenue[11]. Efforts to decarbonize and reduce water consumption have motivated the expansion of sulfide based processing to new minerals and chemistries. Oxide-sulfide anion exchange has been proposed to enable the selective sulfidation of metals from mixed compounds, including oxide and slag mineral sources[46,49–54]. However, no comparative thermodynamic or kinetic framework has been previously established to identify key trends in selectivity for material separations across a range of process chemistries, hindering insight into new separation opportunities[4].

Current experimental approaches have generally leveraged condensed S sources such as pyrite (FeS_2)[52,54,55], non-selective sulfidizing agents such as hydrogen sulfide (H_2S) or carbon disulfide (CS_2)[56–58], or briquettes containing S pressed and premixed with mineral feedstocks[49,50]. These approaches have collectively masked mass transport and kinetic phenomena within the system. This has hindered the ability to rationally design oxide-sulfide anion exchange processes geared toward controlling the solubility of target elements in feedstock oxides and their subsequent precipitation as physically separable sulfide compounds[4]. Together, this lack of integrated thermodynamic, kinetic, and mass transport insight hampers economic and sustainability evaluations needed for potential deployment. Finally, these unknown factors cascade into the design of downstream sulfide handling processes such as reduction to metal. For metal production from sulfides, experimental efforts have largely focused only on the sulfide feedstocks available naturally today[22,24,25,30]. Any novel sulfide product produced via oxide sulfide anion exchange will require thermodynamic and experimental confirmation of its feasibility as a feedstock for metal reduction.

Overall, unknown oxide-sulfide anion exchange kinetics, thermodynamic trends, and sulfide reduction behavior are key scientific gaps. These create engineering uncertainties by hindering economic and sustainability evaluation of oxide-sulfide anion exchange chemistries. Nevertheless as motivated in Chapter 1, Section 1.2 and here in Section 2.1, oxide-sulfide anion exchange is a promising pathway to enable low cost, environmentally benign physical separation in place of chemical methods. In the following sections, hypotheses for separation efficacy, cost and impact, and metal production via oxide-sulfide anion exchange are postulated. Frameworks for testing these hypotheses are subsequently proposed.

2.3 Hypotheses for Separation Efficacy, Cost and Impact, and Metal Production

In the preceding sections, pyrometallurgical oxide-sulfide anion exchange was established as a promising pretreatment to enable low cost, environmentally benign physical separations in place of expensive and unsustainable chemical methods. This in turn is predicted to unlock new pathways to low cost, decarbonized metal production via reduction of sulfides.

However, significant scientific and engineering unknowns remain. To elucidate these uncertainties, the following hypotheses are proposed:

- Selective oxide-sulfide anion exchange decreases the solubility of target cation elements in feedstock materials, supporting their selective extraction and physical separation.

- Increasing the selectivity of pyrometallurgical processes via oxide-sulfide anion exchange reduces the need for subsequent hydrometallurgical processing, lowering the cost and environmental impact of materials separations.

- Sulfidation of an oxide decreases the thermodynamic barrier to metal reduction, supporting the use of less reactive reductants or direct thermal decomposition for metal production.

If these hypotheses were to be validated, oxide-sulfide anion exchange would be a promising platform chemistry candidate for sustainable minerals processing, recycling, and metal production. Analytical frameworks and methodologies to test these hypotheses are introduced in the following section and detailed in Chapter 3.

2.4 Analytical Framework

Pyrometallurgical oxide-sulfide anion exchange is hypothesized to enable improved low carbon materials separation and metal production. To test the viability of this approach, oxide-sulfide anion exchange must be explored across chemical, economic, and sustainability parameters. Furthermore, the efficacy of reducing novel sulfide separation products to metal must be evaluated. In principle, this work may divide into three main tasks:

- Experimental demonstration of selective oxide-sulfide anion exchange for physical separation

- Technoeconomic and life cycle assessment of oxide-sulfide anion exchange

- Experimental demonstration of sulfide reduction

In the following chapters, these tasks are accomplished. Motivated by scientific and engineering unknowns, an integrated thermodynamic, kinetic, and transport framework is established in Chapter 3 to predict the selectivity of oxide-sulfide anion exchange processes. These insights motivate methods proposed to evaluate the chemical, technoeconomic, and sustainability performance of the chemistry. Pyrometallurgical oxide-sulfide anion exchange is explored experimentally in Chapters 4 and 5 for a variety of system chemistries and impurity landscapes. Based on experimentally verified separation performance, detailed technoeconomic and life cycle assessments are conducted in Chapter 6. Upon establishing the technoeconomic and environmental competitiveness of sulfide-based separation pathways, sulfide reduction is explored in Chapter 7. Perspectives and future work are concluded in Chapter 8.

2.5 Summary

Herein, pyrometallurgical oxide-sulfide anion exchange was identified as a promising approach to reduce the cost and environmental impact of material separations and metal production. However, past attempts at employing pyrometallurgical oxide-sulfide anion exchange were hindered by uncharacterized thermodynamic and kinetic behavior. Based on these insights and uncertainties, it was hypothesized that selective oxide-sulfide anion exchange decreases the solubility of target cation elements in feedstock materials to support their selective extraction and physical separation. Increasing the selectivity of pyrometallurgical processes via oxide-sulfide anion exchange was predicted to reduce the need for subsequent hydrometallurgy, lowering the cost and environmental impact of materials separations. Finally, sulfidation of an oxide was theorized to decrease the thermodynamic barrier to metal reduction, supporting the use of less reactive reductants or direct thermal decomposition for metal production. These hypotheses are evaluated in subsequent chapters.

2.6 References

1. Pauling, L. The Nature of the Chemical Bond. IV. The Energy of Single Bonds and the Relative Electronegativity of Atoms. *J. Am. Chem. Soc.* **54**, 3570–3582 (1932).
2. Hume-Rothery, W. & Raynor, G. V. The Structure of Metals and Alloys. in *The Institute of Metals Monograph and Report* 391 (Institute of Metals, 1956).
3. Goldschmidt, V. M. The principles of distribution of chemical elements in minerals and rocks. The seventh Hugo Müller Lecture, delivered before the Chemical Society on March 17th, 1937. *J. Chem. Soc.* 655–673 (1937) doi:10.1039/JR9370000655.
4. Stinn, C. & Allanore, A. Selective sulfidation of metal compounds. *Nature* **602**, 78–83 (2022).
5. Haynes, W. M. Abundance of elements in the earth's crust and in the sea. in *CRC Handbook of Chemistry and Physics* 14–17 (2017).
6. USGS. *Mineral commodity summaries 2023*. (2023).
7. Ringwood, A. E. The principles governing trace element distribution during magmatic crystallization Part I: The influence of electronegativity. *Geochim. Cosmochim. Acta* **7**, 189–202 (1955).
8. Allred, A. L. Electronegativity values from thermochemical data. *J. Inorg. Nucl. Chem.* **17**, 215–221 (1961).
9. Shannon, R. D. Revised effective ionic radii and systematic studies of interatomic distances in halides and chalcogenides. *Acta Crystallogr. Sect. A* **32**, 751–767 (1976).
10. Crundwell, F. K., Moats, M. S., Ramachandran, V., Robinson, T. G. & Davenport, W. G. *Extractive Metallurgy of Nickel, Cobalt, and Platinum-Group Metals*. (Elsevier, 2011).
11. Schlesinger, M. E., King, M. J., Sole, K. C. & Davenport, W. G. *Extractive Metallurgy of Copper*. (2011). doi:10.1017/CBO9781107415324.004.
12. Miller, J. D. & Yalamanchili, M. R. Fundamental aspects of soluble salt flotation. *Miner. Eng.* **7**, 305–317 (1994).
13. Zhao, B., Zhang, J. & Schreiner, B. *Separation Hydrometallurgy of Rare Earth Elements*. (Springer International Publishing AG Switzerland, 2016).
14. Rukini, A., Rhamdhani, M. A., Brooks, G. A. & Van den Bulck, A. Metals Production and Metal Oxides Reduction Using Hydrogen: A Review. *J. Sustain. Metall.* **8**, 1–24 (2022).

15. Nakanishi, B. R. & Allanore, A. Electrochemical Investigation of Molten Lanthanum-Yttrium Oxide for Selective Liquid Rare-Earth Metal Extraction. *J. Electrochem. Soc.* **166**, E420–E428 (2019).
16. Halmann, M., Frei, A. & Steinfeld, A. Magnesium production by the pidgeon process involving dolomite calcination and MgO silicothermic reduction: Thermodynamic and environmental analyses. *Ind. Eng. Chem. Res.* **47**, 2146–2154 (2008).
17. Gupta, C. K. & Krishnamurthy, N. Oxide reduction processes in the preparation of rare-earth metals. *Mining, Metall. Explor.* **30**, 38–44 (2013).
18. David Belitskus. Aluminothermic production of metals and alloys. *J. Met.* **24**, 30–34 (1972).
19. Brinkmann, F., Mazurek, C. & Friedrich, B. Metallothermic Al-Sc co-reduction by vacuum induction melting using Ca. *Metals (Basel).* **9**, (2019).
20. Allanore, A., Yin, L. & Sadoway, D. R. A new anode material for oxygen evolution in molten oxide electrolysis. *Nature* **497**, 353–6 (2013).
21. Allanore, A. Electrochemical engineering of anodic oxygen evolution in molten oxides. *Electrochim. Acta* **110**, 587–592 (2013).
22. Daehn, K. E. *et al.* Liquid Copper and Iron Production from Chalcopyrite, in the Absence of Oxygen. *Metals (Basel).* **12**, 1440 (2022).
23. Daehn, K. & Allanore, A. Electrolytic production of copper from chalcopyrite. *Curr. Opin. Electrochem.* **22**, 110–119 (2020).
24. Qu, J. *et al.* Anode electrolysis of sulfides. *Proc. Natl. Acad. Sci.* **119**, 1–7 (2022).
25. Sahu, S. K., Chmielowiec, B. & Allanore, A. Electrolytic Extraction of Copper, Molybdenum and Rhenium from Molten Sulfide Electrolyte. *Electrochim. Acta* **243**, 382–389 (2017).
26. Sokhanvaran, S., Lee, S.-K., Lambotte, G. & Allanore, A. Electrochemistry of Molten Sulfides: Copper Extraction from BaS-Cu2S. *J. Electrochem. Soc.* **163**, D115–D120 (2016).
27. Stinn, C. & Allanore, A. Selective Sulfidation and Electrowinning of Nickel and Cobalt for Lithium Ion Battery Recycling. in *Ni-Co 2021: The 5th International Symposium on Nickel and Cobalt* (eds. Anderson, C. et al.) 99–110 (Springer Nature Switzerland AG, 2021). doi:10.1007/978-3-030-65647-8_7.

28. Townsend, C. P. Process for the Reduction of Ores. (1906).
29. Yin, H., Chung, B. & Sadoway, D. R. Electrolysis of a molten semiconductor. *Nat. Commun.* **7**, 12584 (2016).
30. Wagner, M.-E. & Allanore, A. Electrochemical Separation of Ag 2 S and Cu 2 S from Molten Sulfide Electrolyte . *J. Electrochem. Soc.* **169**, 063511 (2022).
31. Akhgar, B. N. & Pourghahramani, P. Mechanochemical reduction of natural pyrite by aluminum and magnesium. *J. Alloys Compd.* **657**, 144–151 (2016).
32. Setoudeh, N. & Welham, N. J. Metallothermic reduction of zinc sulfide induced by ball milling. *J. Mater. Sci.* **52**, 6388–6400 (2017).
33. Stinn, C. & Allanore, A. Ferronickel Production from Nickel Laterite via Sulfide Chemistry. in *Advances in Pyrometallurgy* (ed. Fleuriault, C.) 281–297 (The Minerals, Metals & Materials Society, 2023). doi:10.1007/978-3-031-22634-2_25.
34. Stinn, C., Benderly-kremen, E. & Allanore, A. Scandium Master Alloy Production Via Sulfidation and Vacuum Aluminothermic Reduction. in *Light Metals 2023* (2023).
35. Stinn, C., Toll, S. & Allanore, A. Aluminothermic Reduction of Sulfides via Reactive Vacuum Distillation. in *Light Metals 2022* 681–688 (2022).
36. Venkataramani, R., Bose, D. K. & Jena, P. K. Alumino-thermic reduction of molybdenite concentrate under vacuum. *Trans. Indian Inst. Met.* **23**, 13–16 (1970).
37. Yan, X. Y. & Fray, D. J. Molten Salt Electrolysis for Sustainable Metals Extraction and Materials Processing - A Review. in *Electrolysis: Theory, Types and Applicaations* (eds. Kuai, S. & Meng, J.) (2010).
38. Winand, R. F. . Electrolysis of oxide melts. in *Proceedings Conference of Extractive Metallurgy* 20–33 (1981).
39. John R. Rumble. Melting, Boiling, Triple, and Critical Points and Densities of the Elements. in *CRC Handbook of Chemistry and Physics* (2022).
40. Johansson, B. The boiling points of the rare earth metals. *J. Phys. F Met. Phys.* **5**, 1241–1247 (1975).
41. Yoshizaki, T., Ash, R. D., Lipella, M. D., Yokoyama, T. & McDonough, W. F. Variable refractory lithophile element compositions of planetary building blocks: Insights from components of enstatite chondrites. *Geochim. Cosmochim. Acta* **308**, 173–187 (2021).
42. Gannoun, A., Boyet, M., El Goresy, A. & Devouard, B. REE and actinide

microdistribution in Sahara 97072 and ALHA77295 EH3 chondrites: A combined cosmochemical and petrologic investigation. *Geochim. Cosmochim. Acta* **75**, 3269–3289 (2011).

43. Agricola, G. *De re Metallica*. (1556).
44. Pourbaix, M. J. N. & Rorive-Bouté, M. C. M. Graphical study of metallurgical equilibria. *Discuss. Faraday Soc.* **4**, 139–154 (1948).
45. Kellogg, H. H. A Critical Review of Sulfation Equilibria. *Trans. Metall. Soc. AIME* **230**, 1622–1634 (1964).
46. Godoy, R. & Krasuk, J. H. Thermic Sulphidization and Copper Recovery from Basic Copper Oxide Ores with Limestone Gangue. *Lat. Am. J. Chem. Eng. Appl. Chem.* **4**, 13–30 (1974).
47. Diaz, C. M., Landolt, C. A., Vahed, A., Warner, A. E. M. & Taylor, J. C. A Review of Nickel Pyrometallurgical Operations. *JOM* **40**, 28–33 (1988).
48. King, M. J., Davenport, W. G. & Moats, M. S. *Sulfuric Acid Manufacture - Analysis, Control and Optimization*. (2013).
49. Harris, C. T., Peacey, J. G. & Pickles, C. A. Selective sulphidation of a nickeliferous lateritic ore. *Miner. Eng.* **24**, 651–660 (2011).
50. Harris, C. T., Peacey, J. G. & Pickles, C. A. Selective sulphidation and flotation of nickel from a nickeliferous laterite ore. *Miner. Eng.* **54**, 21–31 (2013).
51. Han, J., Liu, W., Wang, D., Jiao, F. & Qin, W. Selective Sulfidation of Lead Smelter Slag with Sulfur. *Metall. Mater. Trans. B* **47**, 344–354 (2015).
52. Han, J. *et al.* Selective Sulfidation of Lead Smelter Slag with Pyrite and Flotation Behavior of Synthetic ZnS. *Metall. Mater. Trans. B* **47B**, 2400–2410 (2016).
53. Han, J. *et al.* Mechanism study on the sulfidation of ZnO with sulfur and iron oxide at high temperature. *Sci. Rep.* **7**, 42536 (2017).
54. Liu, W., Zhu, L., Han, J., Jiao, F. & Qin, W. Sulfidation mechanism of ZnO roasted with pyrite. *Sci. Rep.* **8**, 1–12 (2018).
55. Ke, Y. *et al.* Sulfidation behavior and mechanism of zinc silicate roasted with pyrite. *Appl. Surf. Sci.* **435**, 1011–1019 (2018).
56. Ahmad, S., Rhamdhani, M. A., Pownceby, M. I. & Bruckard, W. J. Sulfidation Kinetics of Natural Chromite Ore Using H2S Gas. *Metall. Mater. Trans. B Process Metall. Mater.*

Process. Sci. **46**, 557–567 (2015).

57. Ahmad, S., Rhamdhani, M. A., Pownceby, M. I. & Bruckard, W. J. Thermodynamic assessment and experimental study of sulphidation of ilmenite and chromite. *Trans. Institutions Min. Metall. Sect. C Miner. Process. Extr. Metall.* **123**, 165–177 (2014).
58. Merritt, R. R. High Temperature Methods for Processing Monazite: II. Reaction with Sodium Carbonate. *J. Less-Common Met.* **166**, 211–219 (1990).
59. Johansson, B. Valence state at the surface of rare-earth metals. *Phys. Rev. B* **19**, 6615–6619 (1979).
60. Strange, P., Svane, A., Temmerman, W. M., Szotek, Z. & Winter, H. Understanding the valency of rare earths from first-principles theory. *Nature* **399**, 756–758 (1999).

Chapter 3

Oxide-Sulfidation Anion Exchange Methodology

In Chapters 1 and 2, pyrometallurgical oxide-sulfide anion exchange chemistry was presented as a promising avenue to reduce the environmental impact of materials separation and production. Three hypotheses were proposed:

- Selective oxide-sulfide anion exchange decreases the solubility of target cation elements in feedstock materials, supporting their selective extraction and physical separation.

- Increasing the selectivity of pyrometallurgical processes via oxide-sulfide anion exchange reduces the need for subsequent hydrometallurgical processing, lowering the cost and environmental impact of materials separations.

- Sulfidation of an oxide decreases the thermodynamic barrier to metal reduction, supporting the use of less reactive reductants or direct thermal decomposition for metal production.

Unknown trends in sulfidation thermodynamics and kinetics presently hinder the development of sustainable and economical oxide-sulfide anion processes for materials separation. In this chapter, an integrated thermodynamic, kinetic, and mass transport framework is constructed to design oxide-sulfide anion exchange processes that are selective for individual elements. An experimental and modelling methodology is proposed to test the first two hypotheses above and explore process levers that control selectivity in metal compound sulfidation for materials extraction and separation. Insights into operating conditions inform the development of capital cost, operating cost, and sustainability models to understand the environmental and economic competitiveness of pyrometallurgical oxide-sulfide anion exchange versus established hydrometallurgy processes. Results acquired following the methodologies described herein are subsequently presented in Chapters 4-6. These results inform the design and demonstration of new methods of metal sulfide reduction in Chapter 7.

3.1 Thermodynamic Framework for Selectivity in Oxide-Sulfide Anion Exchange

The pyrometallurgical sulfidation or desulfidation of a condensed reactant consisting of metal (M), oxygen (O), and sulfur (S) ($M_\gamma O_\delta S_\epsilon$) to form a new condensed $M-O-S$ product ($M_\iota O_\kappa S_\lambda$) in the presence of a gas atmosphere composed of sulfur and sulfur dioxide (S_2 and SO_2 respectively) is described below by Eqn. 3.1, where β, γ, δ, ϵ, ζ, η, θ, ι, κ, λ, μ, and ν are stoichiometric factors.

$$\beta M_\gamma O_\delta S_\epsilon + \zeta S_2 + \eta SO_2 = \theta M_\iota O_\kappa S_\lambda + \mu S_2 + \nu SO_2 \quad (3.1)$$

Herein, sulfidation refers to increasing the S to O ratio of the product metal compound versus the reactant, whereas desulfidation refers to decreasing the S to O ratio of the product metal compound. While S gas has allotropes ranging from monoatomic S to cyclic S_8, at temperatures between 800 °C and 3000 °C diatomic sulfur (S_2) is the dominant form[1]. From Le Chatelier's principle[2], the extent of reaction (as referenced to $M_\gamma O_\delta S_\epsilon$ or $M_\iota O_\kappa S_\lambda$) may be controlled through modulation of the ratio of S_2 and SO_2 gasses within the system. For a system at thermodynamic

equilibrium, the activities (a) of $M_\gamma O_\delta S_\epsilon$ and $M_\iota O_\kappa S_\lambda$, the fugacities ($f$) of S_2 and SO_2, and the standard Gibbs energy of reaction ($\Delta_r G°$) may be related using the law of mass action[3–5]. Gas phase behavior may be connected to condensed phase behavior as follows.

$$\log_{10}\left(e^{\frac{\Delta_r G^\circ}{RT}}\right) + \log_{10}\left(\frac{{a_{M_\iota O_\kappa S_\lambda}}^\theta}{{a_{M_\gamma O_\delta S_\epsilon}}^\beta}\right) = \log_{10}\left(\frac{{f_{S_2}}^{(\zeta-\mu)}}{{f_{SO_2}}^{(\nu-\eta)}}\right) \tag{3.2}$$

For an ideal gas phase, Eqn. 3.2 may be rewritten using partial pressures (P) in place of fugacities. ψ is defined as a stoichiometry dependent ratio of P_{S_2} to P_{SO_2}, with contributions from reaction ($\psi_{rxn_{\Delta G}}$) and solution (ψ_{sol}) effects[6].

$$\log_{10}\left(e^{\frac{\Delta_r G^\circ}{RT}}\right) + \log_{10}\left(\frac{{a_{M_\iota O_\kappa S_\lambda}}^\theta}{{a_{M_\gamma O_\delta S_\epsilon}}^\beta}\right) = \log_{10}\left(\frac{{P_{S_2}}^{(\zeta-\mu)}}{{P_{SO_2}}^{(\nu-\eta)}}\right) = \psi \tag{3.3}$$

$$\log_{10}\left(e^{\frac{\Delta_r G^\circ}{RT}}\right) = \psi_{rxn_{\Delta G}} \tag{3.4}$$

$$\log_{10}\left(\frac{{a_{M_\iota O_\kappa S_\lambda}}^\theta}{{a_{M_\gamma O_\delta S_\epsilon}}^\beta}\right) = \psi_{sol} \tag{3.5}$$

In the limit where $\zeta = 1$, $\eta = 0$, and $\mu = 0$, a full derivation of Eqn. 3.3-3.5 is included by the author elsewhere[6]. $\psi_{rxn_{\Delta G}}$ may be subdivided into enthalpic ($\psi_{rxn_{\Delta H}}$) and entropic ($\psi_{rxn_{\Delta S}}$) contributions as follows, where $\Delta_r H°$ and $\Delta_r S°$ correspond to the standard enthalpy and entropy of the reaction respectively.

$$\psi_{rxn_{\Delta G}} = \log_{10}\left(e^{\frac{\Delta_r H^\circ}{RT}}\right) + \log_{10}\left(e^{\frac{-\Delta_r S^\circ}{R}}\right) \tag{3.6}$$

$$\log_{10}\left(e^{\frac{\Delta_r H^\circ}{RT}}\right) = \psi_{rxn_{\Delta H}} \tag{3.7}$$

$$\log_{10}\left(e^{\frac{-\Delta_r S^\circ}{R}}\right) = \psi_{rxn_{\Delta S}} \tag{3.8}$$

Smaller values of ψ correspond to lower thermodynamic barriers to sulfidation via oxide-sulfide anion exchange. Therefore, compounds with lower ψ exhibit higher sulfidation affinities. $\psi_{rxn_{\Delta G}}$, $\psi_{rxn_{\Delta H}}$, and $\psi_{rxn_{\Delta S}}$ are tabulated in Figure 3.1 at 1000 °C for sulfidation and desulfidation reactions between solid oxides, oxysulfides, sulfates, and sulfides. Compound stoichiometries are detailed by the author elsewhere[6]. $\psi_{rxn_{\Delta G}}$ directly correlates with $\psi_{rxn_{\Delta H}}$, while the variation in $\psi_{rxn_{\Delta S}}$ within a class of materials is smaller than that of $\psi_{rxn_{\Delta H}}$. The origin of trends in $\psi_{rxn_{\Delta H}}$ and $\psi_{rxn_{\Delta S}}$ are addressed in Sections 3.1.1 and 3.1.2.

3.1.1 Enthalpic Contributions to Oxide-Sulfide Anion Exchange Thermodynamics

Previously, Goldschmidt reported that the diadochy between cations in ionic, semi-metallic, and metallic mineral crystals nucleated from magmatic phases in terrestrial and systems is governed by the cation's ionic radius and charge[7]. Later this framework was expanded by Ringwood[8], who accounted for exceptions to Goldschmidt's rules of distribution in magmatic minerals using Pauling's concept of electronegativity[9]. Similarly, for sulfidation of an oxide to form a new sulfide phase, $\psi_{rxn_{\Delta H}}$ is observed to be a function of the metallic element's ionic crystal (Shannon) radius[10,11], oxidation state, and electronegativity[12,13] as depicted in Figure 3.2. Trends with average Shannon radius ($\overline{r_S}$), oxidation state, and electronegativity (χ) described in the context of sulfidation below and in Section 2.4.2 may be reversed to describe desulfidation.

For a metal cation at a given oxidation state, as $\overline{r_S}$ increases, $\psi_{rxn_{\Delta H}}$ for sulfidation of an oxide decreases, corresponding to an increased enthalpic affinity for sulfidation. This phenomenon arises from Coulomb's inverse square law of electrostatic attraction as applied to ionic lattices[8], where for a given charge smaller cations are preferentially partitioned into an oxide's lattice site. Therefore, larger cations are relatively easier to nucleate into more covalent sulfide phases. For cations with similar $\overline{r_S}$, those with higher charges are preferentially partitioned into oxide lattice sites while those with lower charges require lower $\psi_{rxn_{\Delta H}}$ to sulfidize from the oxide. Therefore, cations with similar $\overline{r_S}$ and lower valencies also tend to have increased enthalpic affinities for sulfidation.

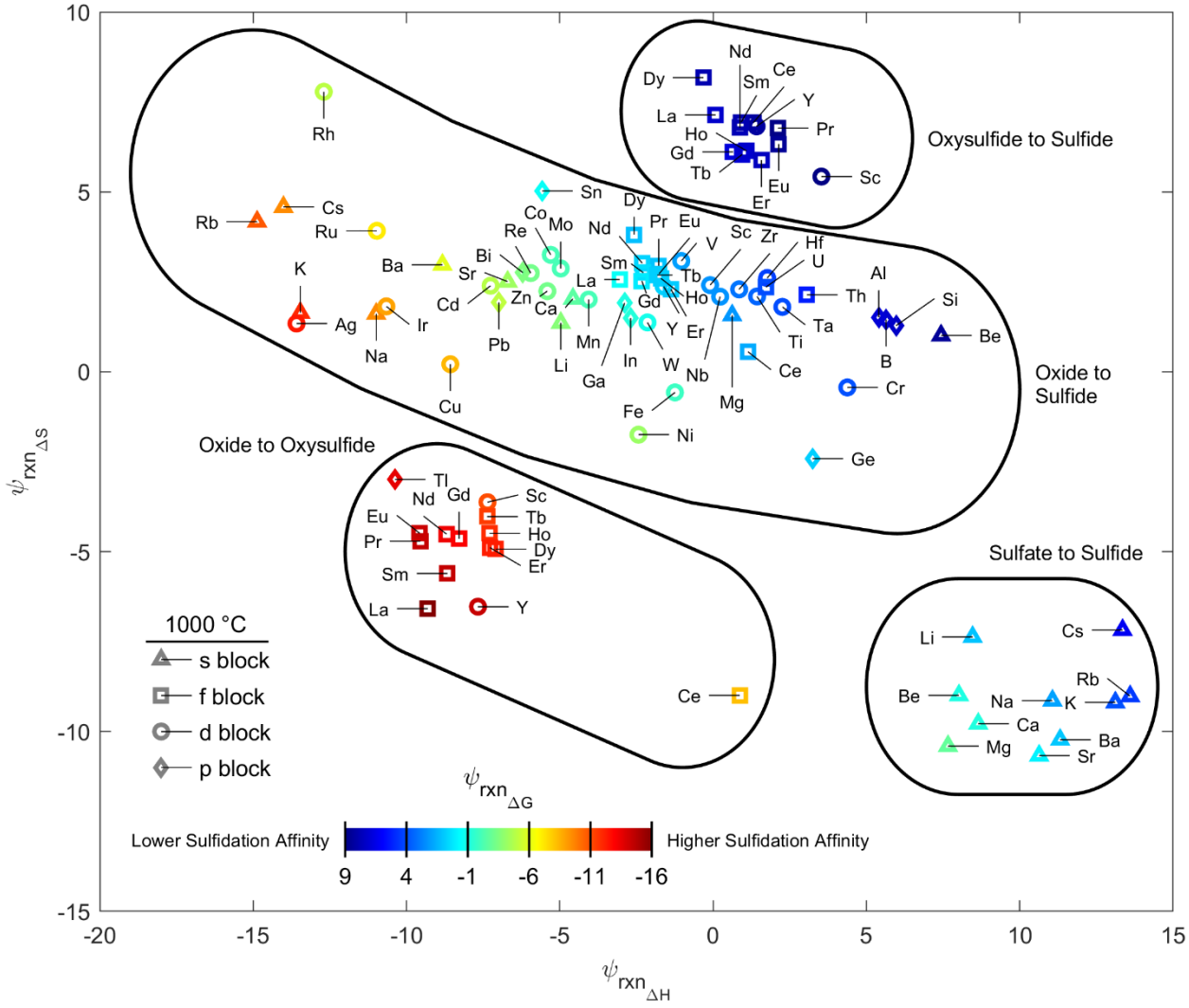

Figure 3.1: Relative contributions of enthalpic ($\psi_{rxn_{\Delta H}}$) and entropic ($\psi_{rxn_{\Delta S}}$) effects to the sulfidation affinity of solid oxides, oxysulfides, and sulfates to form solid sulfides at 1000 °C. Values are calculated using FactSage 8.0 supplemented with literature data. For compounds with a melting point below 1000 °C, thermodynamic data is extrapolated using that of the high temperature solid.

Meanwhile for a given $\overline{r_S}$ and cation charge, more electronegative metals generally require lower $\psi_{rxn_{\Delta H}}$ to sulfidize their oxides. As the χ of the metal decreases, the more ionic its bonding will be as both an oxide and a sulfide. For more electronegative metals, the increased covalent character of the bonding weakens the ionic structure of the host oxide lattice, lowers

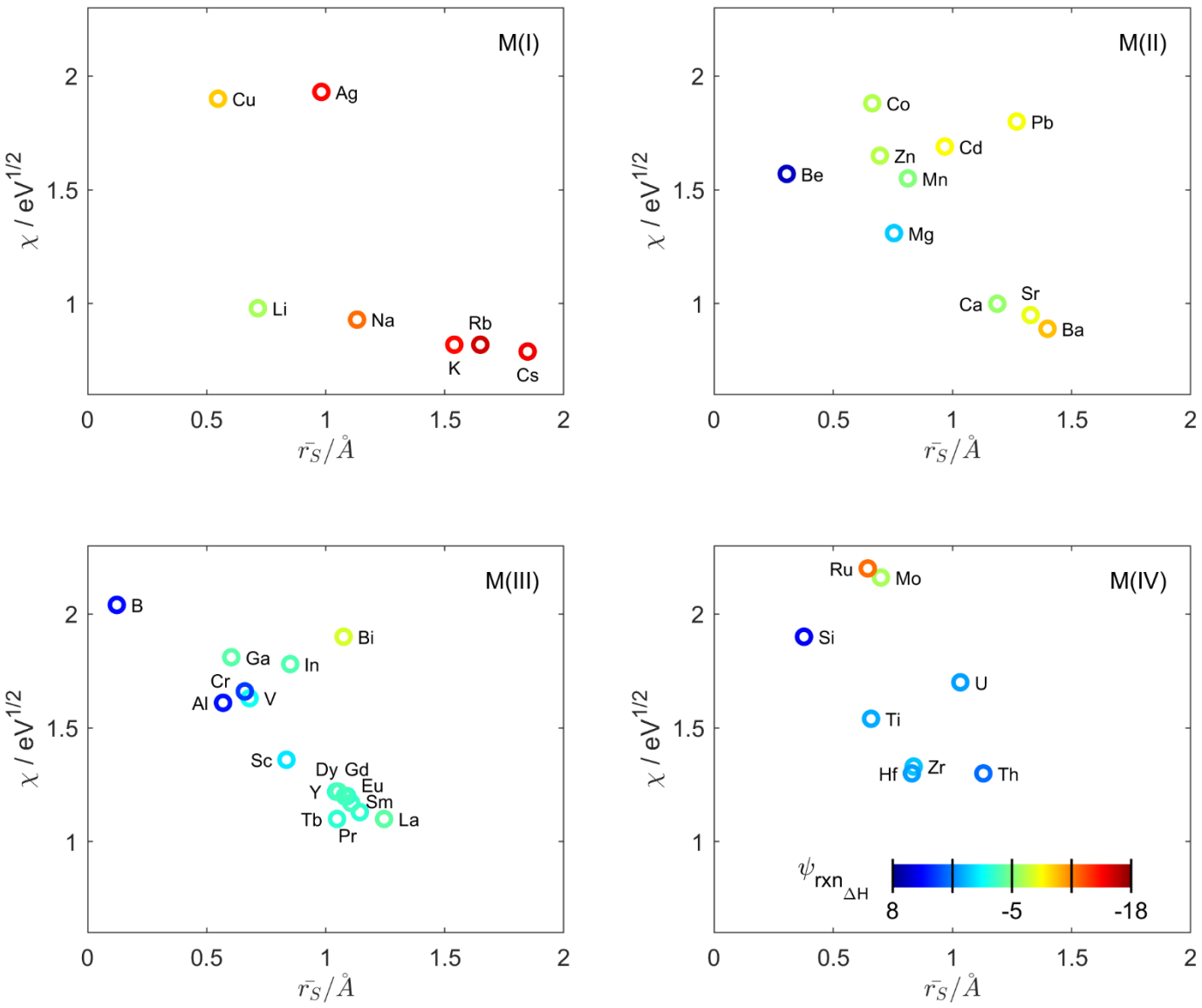

Figure 3.2: Variation in enthalpic sulfidation affinity ($\psi_{rxn_{\Delta H}}$) with the metallic element's Pauling electronegativity (χ) and average Shannon radius ($\overline{r_S}$), grouped by metal cation valency. $\overline{r_S}$ is an average across all oxide and sulfide compounds of all coordination numbers of the stated metal cation valency.

$\psi_{rxn_{\Delta H}}$ required for sulfidation and formation of the more covalent sulfide bond, and increases the oxide's enthalpic affinity for sulfidation. Consequently, the same chemical and bonding phenomena that drives diadochy and partitioning of metallic elements in terrestrial and meteoric mineral phases[7,8] also contributes to the observed sulfidation behavior in

pyrometallurgical anion exchange for the design of sustainable industrial materials separations.

3.1.2 Entropic Contributions to Oxide-Sulfide Anion Exchange Thermodynamics

Compared to the formation of a sulfide from an oxide, the formation of an oxysulfide from an oxide exhibits a lower $\psi_{rxn_{\Delta S}}$ due to an increase in the configurational entropy of the condensed solid arising from the new mixture of oxygen and sulfur anions in the lattice. The formation of a sulfide from an oxysulfide exhibits a higher $\psi_{rxn_{\Delta S}}$ due to the loss of anion configurational entropy upon sulfidation. Meanwhile, formation of a sulfide from a sulfate exhibits lower $\psi_{rxn_{\Delta S}}$ than from the oxide due to the decomposition of the sulfate polyatomic anion, leading to more molecules entering the higher entropy gas phase upon sulfidation.

For formation of a sulfide from an oxide or oxysulfide, there is a slight correlation between increasing $\psi_{rxn_{\Delta S}}$ and decreasing $\psi_{rxn_{\Delta H}}$. This may be due to a decrease in the configurational entropy of the sulfidation reaction for increasing $\bar{r}_S$ (and therefore lower $\psi_{rxn_{\Delta H}}$). However, this does not preclude the possibility that nonconfigurational entropic effects, such as electronic state entropy[14], may also contribute to trends in oxide sulfidation behavior, considering the difference in semiconducting and metallization behavior[15] between oxides and sulfides. However, individual contributions to reaction entropy will not be addressed further herein. For discussion of electronic contributions to entropy, the reader is directed to work by the author[16] and others[17,18].

3.1.3 Pourbaix-Kellogg Formalism for Selectivity in Oxide-Sulfide Anion Exchange

As derived in Eqn. 3.1-3.5, ψ is effectively a stoichiometry-dependent ratio of P_{S_2} to P_{SO_2} in the gas atmosphere that describes the extent of sulfidation or desulfidation of a $M-O-S$ compound $M_\gamma O_\delta S_\epsilon$ to $M_\iota O_\kappa S_\lambda$. However, to compare the partitioning of different metallic elements with distinct compound stoichiometries between $M_\gamma O_\delta S_\epsilon$ and $M_\iota O_\kappa S_\lambda$ phases, ψ must be related to the observable S_2 to SO_2 ratio of the system[6].

In the absence of solution effects ($\psi_{sol} = 0$) the predominance area diagram formulation developed by Pourbaix[19] and popularized by Kellogg[20] may be employed to relate the critical stoichiometric-independent ratio of S_2 to SO_2 required for sulfidation or desulfidation of a compound ($\left[P_{S_2}/P_{SO_2}\right]_{crit}$) to $\psi_{rxn_{\Delta G}}$. A predominance area diagram[6] calculated using the FactSage 8.0 FactPS database supplemented with literature data[21–30] is illustrated in Figures 3.3 for scandium-oxygen-sulfur ($Sc - O - S$) compounds with unit activities at a temperature of 1000 °C and a total pressure of 1 atm. Predominance area diagrams for other $M - O - S$ compounds are available in referenced works by the author[6,31,32]. $\left[P_{S_2}/P_{SO_2}\right]_{crit}$ for formation of a given compound is the P_{S_2} to P_{SO_2} ratio which occurs at the intersection of the phase domain boundary and the 1 atm total pressure isobar. Nongraphical methods using gas equilibrium data via the Gibbs phase rule may also be used to calculate $\left[P_{S_2}/P_{SO_2}\right]_{crit}$ from ψ for a given reaction[6].

The path of the total pressure isobar through the phase domain illustrates the thermodynamically preferred path of sulfidation or desulfidation through intermediate compounds. For example, during sulfidation of Sc compounds (Figure 3.3), scandium oxysulfide (Sc_2O_2S) exists as a thermodynamically stable intermediate between scandium oxide (Sc_2O_3) and scandium sulfide (Sc_2S_3). As shown for $\psi_{rxn_{\Delta G}}$ in Figure 3.1, the existence of Sc_2O_2S as a stable intermediate compound increases $\left[P_{S_2}/P_{SO_2}\right]_{crit}$ for Sc_2S_3 formation and decreases $\left[P_{S_2}/P_{SO_2}\right]_{crit}$ for Sc_2O_3 formation versus $\left[P_{S_2}/P_{SO_2}\right]_{crit}$ as calculated for a direct reaction between Sc_2O_3 and Sc_2S_3.

A sulfidation series may be determined to directly compare the relative ease of formation of a sulfide as a function of gas atmosphere and temperature. Stable oxide, oxysulfide, or sulfate precursors may be identified using the predominance area diagram formalism. $\left[P_{S_2}/P_{SO_2}\right]_{crit}$ for formation of a sulfide may be plotted versus temperature, shown in Figure 3.4 for some come oxide, oxysulfide, and sulfate precursors. All metal compounds are taken to be condensed species at unit activity. For plots of $\left[P_{S_2}/P_{SO_2}\right]_{crit}$ versus temperature for other compounds, the reader is directed to referenced works by the author[31,32]. This sulfidation series diagram takes a

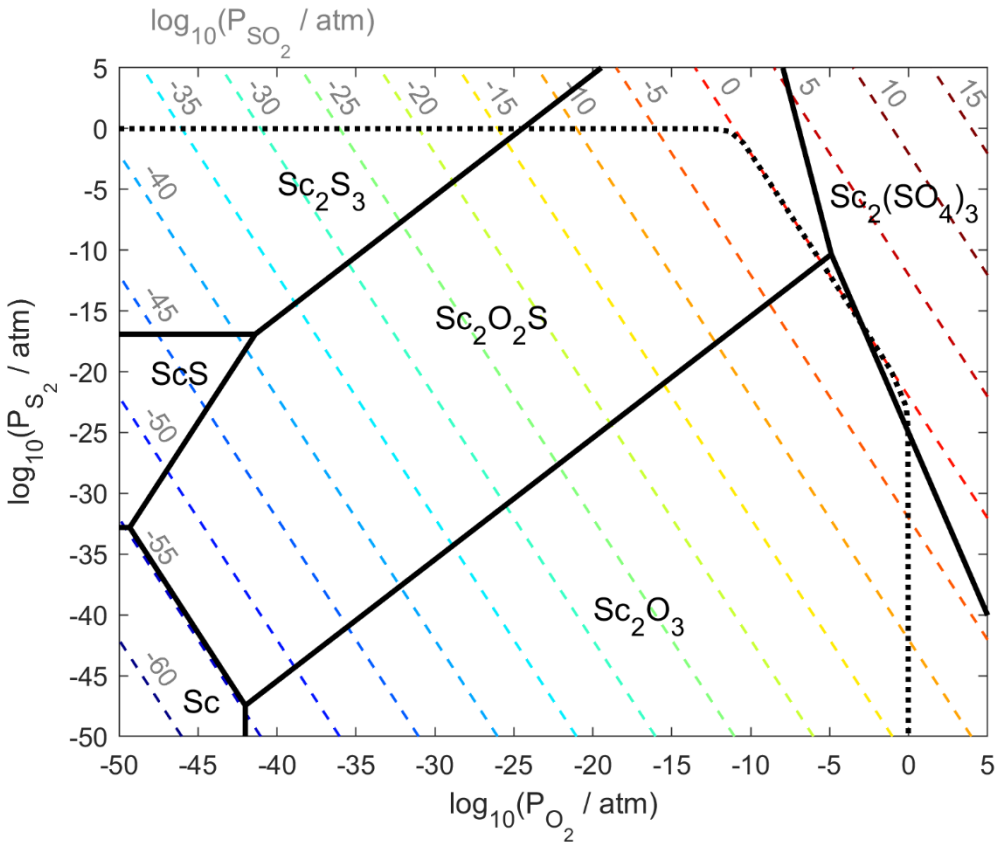

Figure 3.3: Predominance area diagram for scandium-oxygen-sulfur ($Sc - O - S$) compounds with unit activities at a temperature of 1000 °C and a total pressure of 1 atm. Solid lines correspond to phase domains, dashed lines to SO_2 partial pressure isobars, and the solid line to the 1 atm of total pressure isobar.

similar form both visually and functionally to a conventional Ellingham diagram[33], where the oxygen partial pressure (P_{O_2}) required for formation of an oxide compound at unit activity from a metal at unit activity ($a = 1$) is plotted versus temperature. The larger the relative spacing between elements, in principle the more selectively a reaction can be carried out with respect to graphically nearby chemistries, ignoring solution effects.

An isotherm at 1000 °C from the sulfidation series is compared to those of the Ellingham series for oxides and sulfides in Figure 3.5, determined graphically from predominance area diagrams for valencies and compounds reported by the author elsewhere[6]. Predominance area diagrams are generated using the FactSage 8.0 FactPS database supplemented with literature data[21–30]. Both the relative orders and spacing between elements are different for the sulfidation,

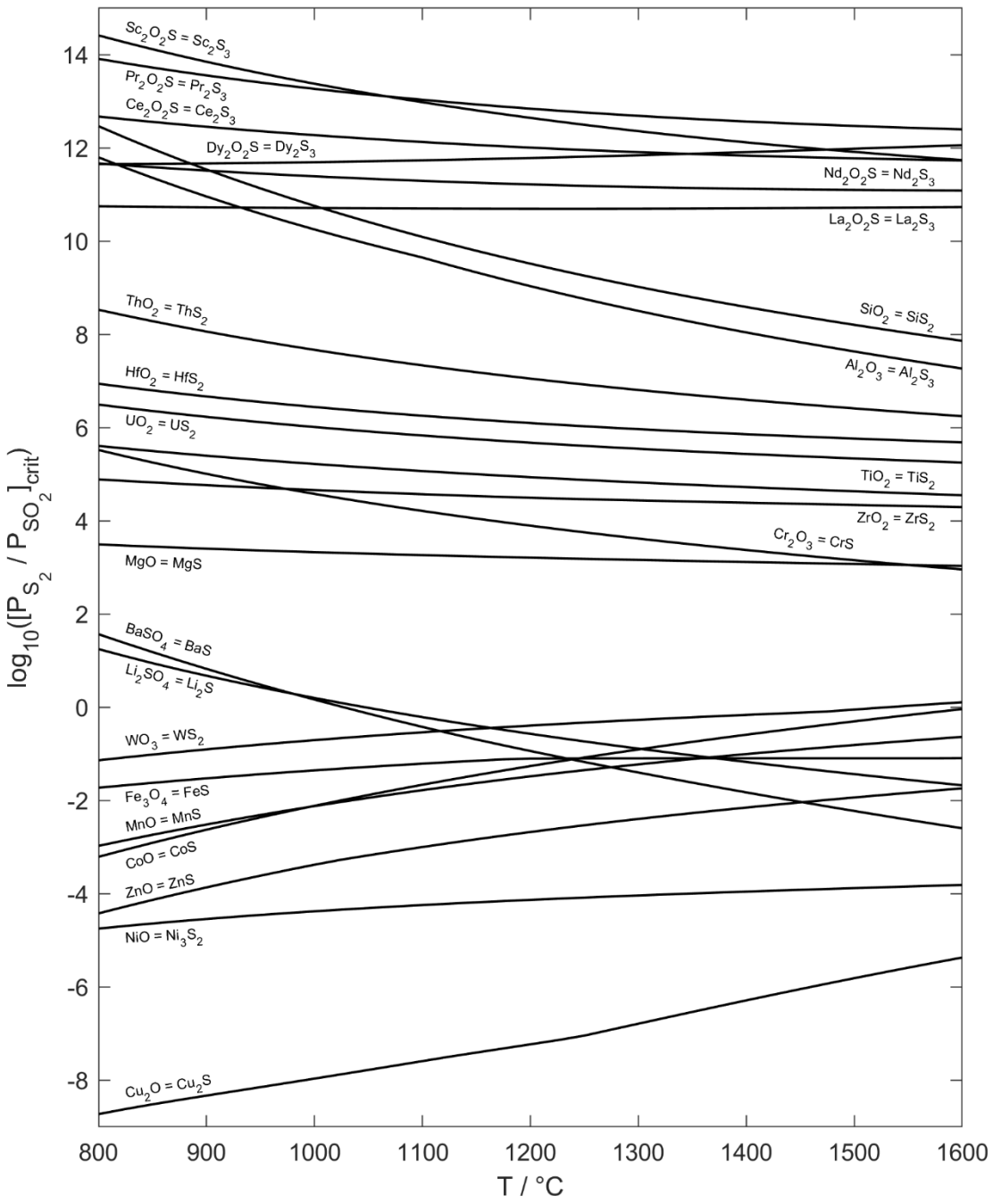

Figure 3.4: Sulfidation series depicting the critical sulfur to sulfur dioxide partial pressure ratio ($\left[P_{S_2}/P_{SO_2}\right]_{crit}$) of sulfide formation from some condensed metal oxide, oxysulfide, and sulfate precursors. $\left[P_{S_2}/P_{SO_2}\right]_{crit}$ is calculated numerically. All compounds are taken to be immiscible with unit activity. For compounds that boil in the temperature range depicted, condensed-phase thermodynamic data is extrapolated with temperature.

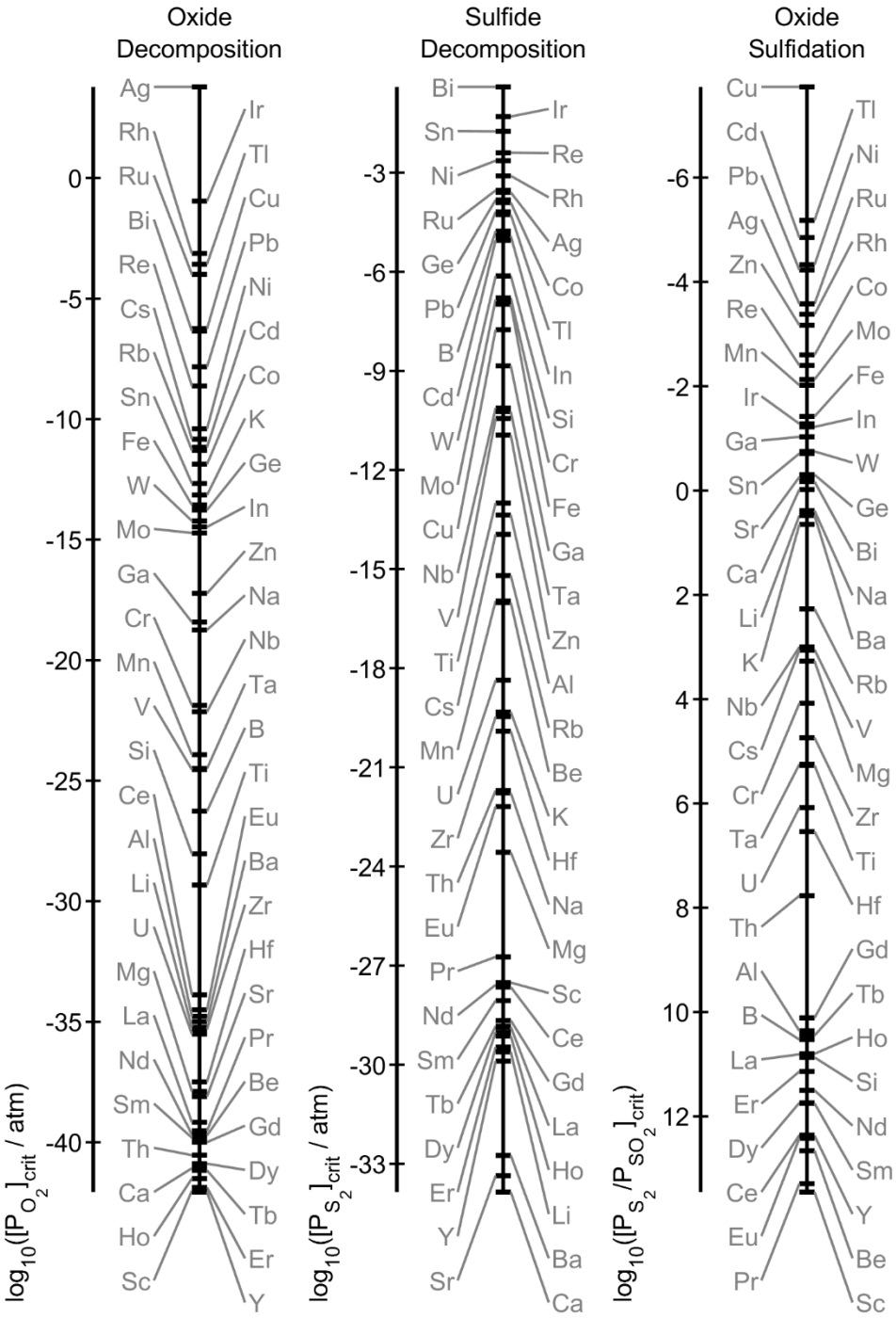

Figure 3.5: Comparison of the Ellingham oxide decomposition, Ellingham sulfide decomposition, and oxide sulfidation series at 1000 °C. $\left[P_{S_2}/P_{SO_2}\right]_{crit}$ is calculated graphically. The relative order and spacing between elements are different in each series, suggesting that oxide-sulfide anion exchange chemistry is a versatile pathway to enable improved selectivity in metallic element separation.

Ellingham oxide, and Ellingham sulfide series. When compound stoichiometry and the stability of sulfidation intermediates are considered, trends in ψ (Sections 3.4.1 and 3.4.2) are reproduced in $\left[P_{S_2}/P_{SO_2}\right]_{crit}$. Some element groups that are very difficult to selectively reduce as oxides, such as neodymium (Nd), praseodymium (Pr), and dysprosium (Dy) in rare earth magnets, are predicted to be easier to selectively process as sulfides. Likewise, oxides that are difficult or impossible to selectively reduce to metal can in principle be selectively sulfidized, allowing separation to take place based on the readily-exploitable physical and chemical property differences between oxides and sulfides (Chapter 2, Section 2.1). This facilitates oxide-sulfide anion exchange chemistry to be leveraged as a "wedge" to maximize the thermodynamic and chemical differences between difficult to separate metallic elements.

3.1.4 Solution Effects in Selective Oxide-Sulfide Anion Exchange

The Pourbaix-Kellogg formalism employed in Section 3.1.3 for development of the sulfidation series provides a method to predict the thermodynamics of selectivity in oxide-sulfide anion exchange for pure reactant and product compounds in the absence of solution effects. $\psi_{rxn_{\Delta G}}$ as employed describes the sulfidation and desulfidation behavior of pure oxides, sulfates, oxysulfides, and sulfides, and is independent of the specific system chemistry. Meanwhile, ψ_{sol} captures the contributions to sulfidation and desulfidation thermodynamics arising from differences in the behavior of a compound in different feeds, as reflected by reactant and product activities.

When $\psi_{rxn_{\Delta G}} \gg \psi_{sol}$, the sulfidation / desulfidation thermodynamics are reaction dominated, solution effects are minimal, and $\left[P_{S_2}/P_{SO_2}\right]_{crit}$ is well-described by that of the pure compound[6]. Meanwhile, when $\psi_{rxn_{\Delta G}} \ll \psi_{sol}$, the sulfidation / desulfidation thermodynamics are solution dominated and reaction effects are minimal, the thermodynamics are not well described by those of the pure compound, and knowledge of the solution behavior is essential to predict $\left[P_{S_2}/P_{SO_2}\right]_{crit}$[6]. For selective sulfidation / desulfidation between two metallic elements, the smaller the difference between $\psi_{rxn_{\Delta G}}$, the more likely selectivity will be governed by ψ_{sol} instead of $\psi_{rxn_{\Delta G}}$. When contributions to ψ from ψ_{sol} are considered, $\left[P_{S_2}/P_{SO_2}\right]_{crit}$ may be

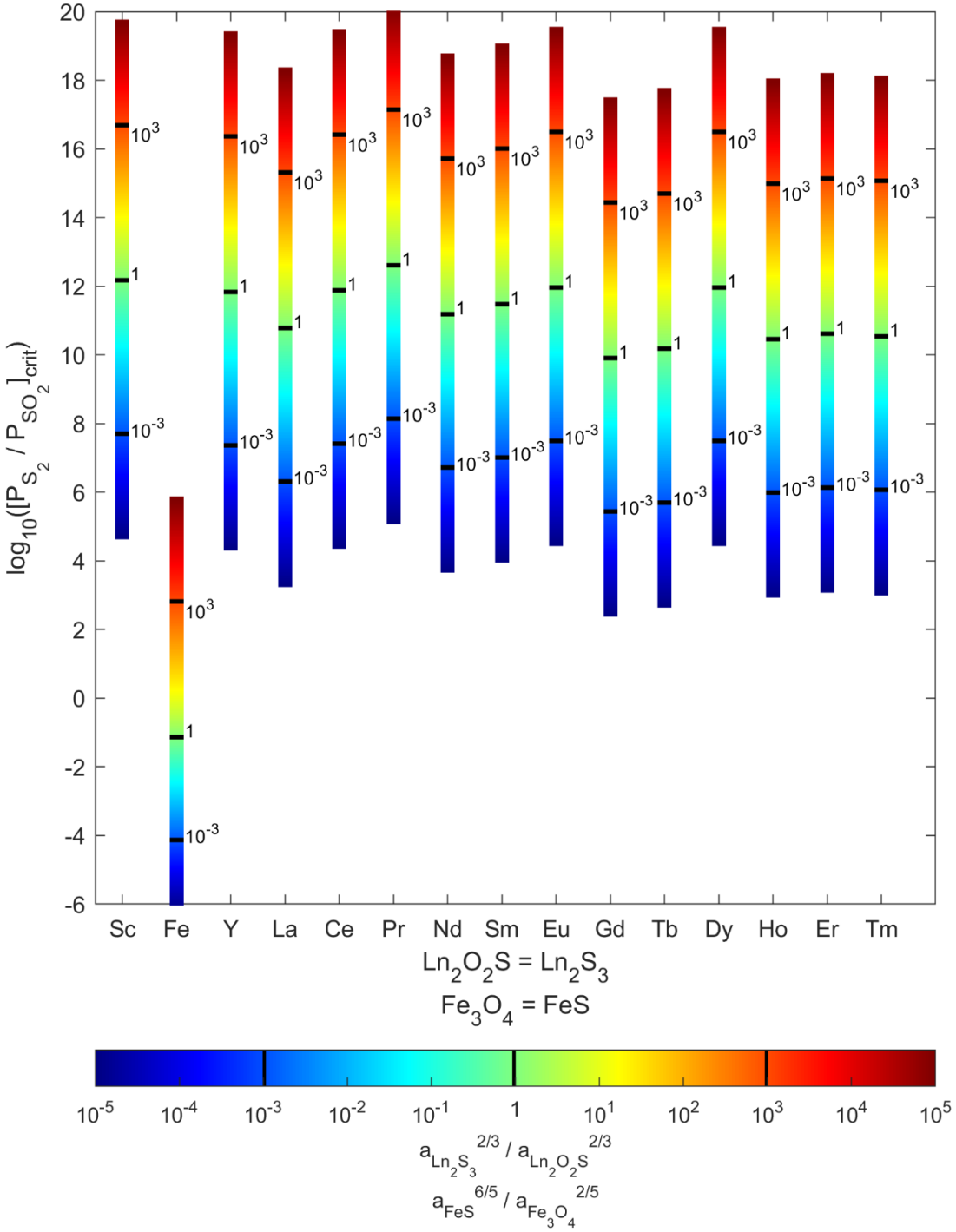

Figure 3.6: Critical sulfur to sulfur dioxide ratio ($\left[P_{S_2}/P_{SO_2}\right]_{crit}$) as a function of reactant and product activities ($a_{M_\beta O_\gamma S_\delta}$ and $a_{M_\epsilon O_\zeta S_\eta}$) for formation of rare earth and iron sulfides at 1400 °C. Selectivity in oxide-sulfide anion exchange between individual rare earth elements is governed by solution effects (ψ_{sol}). In the absence of strong solution effects ($\psi_{rxn_{\Delta G}} \gg \psi_{sol}$), selectivity in oxide-sulfide anion exchange between iron and rare earth elements is predicted to be governed by the behavior of the pure compounds.

determined from ψ as a function of $\Delta_r G°$, T, $a_{M_\gamma O_\delta S_\epsilon}$, and $a_{M_\iota O_\kappa S_\lambda}$ via the Gibb's phase rule and gas phase equilibrium data[6].

For example, values[34] of $\left[P_{S_2}/P_{SO_2}\right]_{crit}$ as a function $a_{M_\epsilon O_\zeta S_\eta}$ and $a_{M_\beta O_\gamma S_\delta}$ for formation of lanthanide sulfides (Ln_2S_3) from oxysulfides (Ln_2O_2S) and iron sulfide (FeS) from iron oxide (Fe_3O_4) are depicted in Figure 3.6. Sulfidation selectivity between individual Ln_2O_2S at a given S_2 to SO_2 ratio is governed by solution effects, shown in the large overlap of sulfidation behavior across different activity ratios. Meanwhile due to large differences in $\psi_{rxn_{\Delta G}}$ between the sulfidation of Fe_3O_4 and Ln_2O_2S (Figure 3.1), in the absence of strong solution effects nearly complete sulfidation of Fe_3O_4 to FeS is predicted with limited co-sulfidation of Ln_2O_2S to Ln_2S_3.

While $\left[P_{S_2}/P_{SO_2}\right]_{crit}$ is readily attainable from $\psi_{rxn_{\Delta G}}$ and ratios of $a_{M_\epsilon O_\zeta S_\eta}$ and $a_{M_\beta O_\gamma S_\delta}$, solution models describing $M-O-S$ interactions between all elements in the system are required to quantitatively predict sulfidation selectivity as a function of the P_{S_2}/P_{SO_2} ratio in the system. Presently, minimal solution data exists for solid state $M-O-S$ systems, especially for terrestrially lithophilic elements rarely processed as sulfides. However, some data exist for liquid oxide-sulfide interactions in the context of pyrometallurgical matte and slag elements[35–37]. As a case study, the role of solution effects is quantified below in the context of the selective sulfidation of chromite ($FeCr_2O_4$) from a mineral concentrate using the FactSage 8.0 FactPS and FT oxid databases.

The composition of a simulated $FeCr_2O_4$concentrate is presented in Table 3.1. Three scenarios for $FeCr_2O_4$ sulfidation are considered:

- Sulfidation of pure and immiscible iron monoxide (FeO) and chromium oxide (Cr_2O_3) to pure and immiscible liquid iron sulfide (FeS) and chromium sulfide (CrS) with inert alumina (Al_2O_3), silica (SiO_2), and magnesia (MgO) gangue minerals.

- Sulfidation of $FeCr_2O_4$ to mixed liquid iron-chromium sulfide ($(Fe,Cr)S$) with inert Al_2O_3, SiO_2, and MgO gangue minerals.

- Sulfidation of $FeCr_2O_4$ to mixed liquid metal sulfide while in thermodynamic equilibrium with Al_2O_3, SiO_2, and MgO gangue minerals.

Component	wt%
$\boldsymbol{MgO}$	11.7
$\boldsymbol{SiO_2}$	2.7
$\boldsymbol{Al_2O_3}$	13.9
$\boldsymbol{Cr_2O_3}$	47.2
$\boldsymbol{FeO}$	24.6

Table 3.1: Composition of simulated chromite ($\boldsymbol{FeCr_2O_4}$) concentrate.

At 1400 °C, the $\left[P_{S_2}/P_{SO_2}\right]_{crit}$ required for sulfidation of pure FeO to FeS and pure Cr_2O_3 to CrS as determined using the Pourbaix-Kellogg formalism in the absence of solution effects (Section 3.1.3) are 0.12 and 2600 respectively. The distributions of iron (Fe) and chromium (Cr) between solid oxide and liquid sulfide phases for sulfidation of $FeCr_2O_4$ in the presence of solution effects are presented in Figure 3.7 as a function of the P_{S_2}/P_{SO_2} ratio in the system. When solution effects are considered between $Fe-Cr-S-O$ in the absence of interactions with gangue minerals, FeO is stabilized more by $Fe-Cr-O$ spinel interactions than FeS is by $Fe-Cr-S$ liquid solution interactions. Meanwhile, Cr_2O_3 is less stabilized by $Fe-Cr-O$ spinel interactions than CrS is by $Fe-Cr-S$ liquid solution interactions. Therefore, the $\left[P_{S_2}/P_{SO_2}\right]_{crit}$ required to achieve 90% distribution in the sulfide phase rises to 4.5 for FeS and falls to 94 for CrS. When interactions of Fe and Cr species with gangue minerals are considered, $\left[P_{S_2}/P_{SO_2}\right]_{crit}$ increases to 79 and 700 for Fe and Cr respectively. This change is attributed to increased stabilization of Cr_2O_3 and FeO through strengthened spinel interactions with gangue materials. Sulfidation of $FeCr_2O_4$ is conducted later in Chapter 7, Section 7.3.3.

The extent to which condensed components within the system remain in equilibrium with one another can shift required operating conditions for sulfidation or desulfidation by orders of magnitude. The changes calculated in $\left[P_{S_2}/P_{SO_2}\right]_{crit}$ for $FeCr_2O_4$ sulfidation highlight the role solution effects can have in modulating the oxide-sulfide anion exchange behavior within a

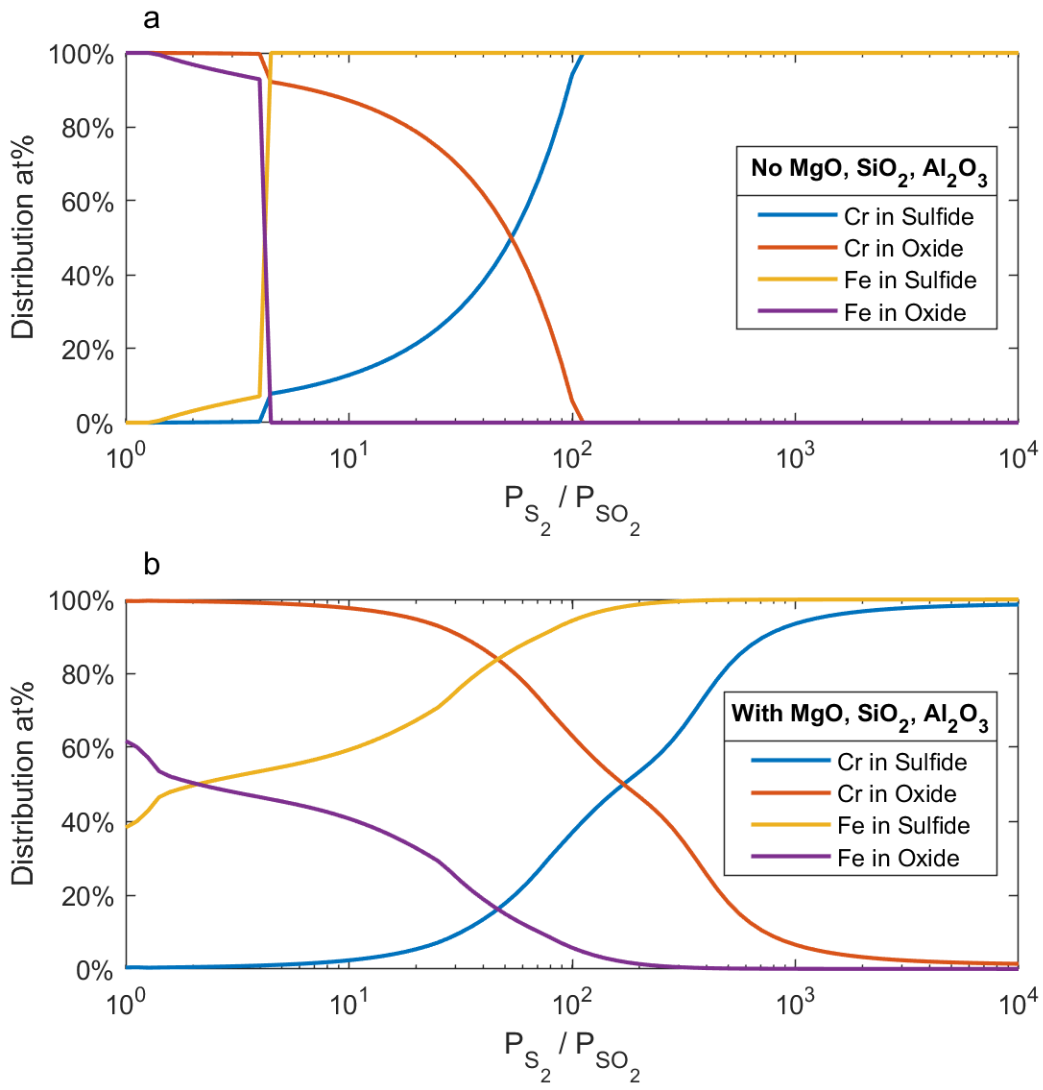

Figure 3.7: Calculated distribution of iron and chromium between oxide and sulfide phases with increasing sulfur to sulfur dioxide (P_{S_2}/P_{SO_2}) ratio for sulfidation of simulated chromite ($FeCr_2O_4$) concentrate at 1400 °C. a: In the absence of solution effects from alumina-silica-magnesia gangue minerals, FeO is preferentially stabilized by $Fe-Cr-O$, while CrS is preferentially stabilized by $Fe-Cr-S$ interactions, increasing $\left[P_{S_2}/P_{SO_2}\right]_{crit}$ for FeO and decreasing $\left[P_{S_2}/P_{SO_2}\right]_{crit}$ for Cr_2O_3 versus the pure oxides. b: Spinel interactions from gangue minerals increase $\left[P_{S_2}/P_{SO_2}\right]_{crit}$ for FeO and Cr_2O_3 versus 3.7a.

materials separation process. Likewise, the fact that industrial materials separations are often conducted far from equilibrium motivates an understanding of kinetic and mass transport effects during oxide-sulfide anion exchange, discussed in the following section.

3.2 Kinetic and Transport Framework for Oxide-Sulfide Anion Exchange

In Section 3.1, $\left[P_{S_2}/P_{SO_2}\right]_{crit}$ was defined as the critical stoichiometric-independent ratio of P_{S_2} to P_{SO_2} required for sulfidation or desulfidation of a compound during an oxide-sulfide anion exchange. As shown in Figures 3.4 and 3.5, at 1000 °C the $\left[P_{S_2}/P_{SO_2}\right]_{crit}$ required for sulfidation of an oxide, oxysulfide, or sulfate to sulfide varies between 10^{-8} and 10^{14} across the periodic table. Since sulfidation of $M_\gamma O_\delta S_\epsilon$ results in the formation of SO_2 within the system (Eqn. 3.1), as $\left[P_{S_2}/P_{SO_2}\right]_{crit}$ increases, maintaining a ratio of P_{S_2} to P_{SO_2} within the reactor ($\left[P_{S_2}/P_{SO_2}\right]_{rx}$) that is sufficiently high for thermodynamic spontaneity becomes increasingly challenging in a closed system. Therefore, sulfidation and desulfidation for materials processing via oxide-sulfide anion exchange is considered in the context of a system open to S_2 and SO_2. Meanwhile, oxide-sulfide anion exchange may be batch or continuous with respect to $M_\gamma O_\delta S_\epsilon$ and $M_\iota O_\kappa S_\lambda$.

3.2.1 Gas-Solid Kinetic and Transport Phenomena for Selectivity in Oxide-Sulfide Anion Exchange

$\left[P_{S_2}/P_{SO_2}\right]_{crit}$, while defining the thermodynamic landscape of sulfidation, also delineates the permissible S_2 inlet and SO_2 accumulation for sulfidation/desulfidation to occur within a reactor[6]. This enables transport and kinetic effects to be considered for an oxide-sulfide anion exchange process. Several avenues to control $\left[P_{S_2}/P_{SO_2}\right]_{rx}$ can be distinguished[6]:

- The intrinsic chemical rate of the sulfidation/desulfidation reaction (Eqn. 3.1)
- Transport limitations to the intrinsic reaction rate
- The gas space time and velocity through the reactor

- The chemical reaction of S_2 and SO_2 with other species within the reactor

The intrinsic chemical rate of pyrometallurgical sulfidation and desulfidation reactions with S_2 are generally unknown, with a few exceptions[38,39]. Trends in sulfidation kinetics may be estimated based on the principles of thermal activation[40] for solid-state processes. For materials of similar crystal structure and coordination number, the rate of solid-state kinetic processes scales with the homologous (fraction of the melting point) temperature of the material. Therefore, at a given operating temperature the rate of oxide-sulfide anion exchange is predicted to be faster in lower melting materials[6]. In general, increasing oxide melting temperature follows similar enthalpic trends for increasing $\psi_{rxn_{\Delta H}}$ (Figure 3.1). Therefore, oxide feedstocks with higher sulfidation affinities are generally predicted to form sulfides both more rapidly and at lower $\left[P_{S_2}/P_{SO_2}\right]_{crit}$ than oxides with lower sulfidation affinities.

Observed kinetics of the gas-solid sulfidation/desulfidation reaction may deviate from the intrinsic, chemically-limited kinetics due to external transport limitations between the bulk gas and solid phases (external limitations), constriction of gas flow within the porous structure of the solid (intergrain limitations), and diffusion of reacting species through the solid to the reaction front (intragrain limitations)[41–43]. Established methodologies exist to quantify transport limitations to the intrinsic reaction rate using experimentally accessible properties of the solid feedstock such as diffusivities, particle size, surface area, and porosity[44,45]. Reaction kinetics are therefore a powerful, yet uncharacterized, lever to selectively apply oxide-sulfide anion exchange to both mineral and recycling systems. Likewise, the morphology of solid feedstocks may be optimized to design external, intergrain, or intragrain limitations to the kinetics of sulfidation/desulfidation in order to achieve a target $\left[P_{S_2}/P_{SO_2}\right]_{rx}$ at a given gas flowrate[32].

Oxygen (O_2) addition provides a lever to chemically decrease $\left[P_{S_2}/P_{SO_2}\right]_{rx}$ during a sulfidation or desulfidation process via the following reaction[6]:

$$S_2 + 2O_2 = 2SO_2 \tag{3.9}$$

Meanwhile, carbon (C) addition provides a lever to chemically increase $\left[P_{S_2}/P_{SO_2}\right]_{rx}$ via the following reactions between SO_2, S_2, C, carbon monoxide (CO) and carbon dioxide (CO_2)[6]:

$$SO_2 + C = CO_2 + \frac{1}{2}S_2 \tag{3.10}$$

$$SO_2 + 2C = 2CO + \frac{1}{2}S_2 \tag{3.11}$$

These reactions establish a carbothermically driven sulfur reflux (CDSR) within the system. The competition between Eqns. 3-10 and 3-11 may be viewed in the context of the Boudouard equilibrium[34]:

$$2CO = CO_2 + C \tag{3.12}$$

Gaseous sources of C, such as hydrocarbons or direct introduction of CO may also be considered for CDSR[32]. During an oxide-sulfide anion exchange process, the reducing power of a C source towards SO_2 must be balanced with its reducing power towards $M_\gamma O_\delta S_\epsilon$. As described in by the author elsewhere[6], excessive C addition leads to a loss of selectivity for different $M_\gamma O_\delta S_\epsilon$ species during oxide-sulfide anion exchange. Loss of selectivity arises due to excessively high $\left[P_{S_2}/P_{SO_2}\right]_{rx}$ with respect to the sulfidation series, co-reduction and subsequent co-sulfidation of different $M_\gamma O_\delta S_\epsilon$ compounds, or formation of carbon disulfide (CS_2) – a non-selective sulfidizing reagent[6].

In a selective oxide-sulfide anion exchange process for materials separation, $\left[P_{S_2}/P_{SO_2}\right]_{rx}$ must meet the criteria for spontaneity governed by $\left[P_{S_2}/P_{SO_2}\right]_{crit}$. The critical space time (τ_{space}^{max}) and space velocity (v_{space}^{min}) of gasses through the reactor for $\left[P_{S_2}/P_{SO_2}\right]_{rx}$ to equal $\left[P_{S_2}/P_{SO_2}\right]_{crit}$ may be determined from a mass balance over the inlet rate of S_2 and other species along with their rates of generation / consumption as governed by reaction kinetics[6]. In Figure 3.8, τ_{space}^{max} and v_{space}^{min} for sulfidation of a metal sesquioxide (M_2O_3) are plotted as a function of $\left[P_{S_2}/P_{SO_2}\right]_{crit}$ and carbon addition for gas phase reactions at 1000 °C and sulfidation kinetics corresponding to those of lanthanum oxide (La_2O_3) at a homologous temperature of 60% without transport limitations[6]. CS_2 formation is assumed to be kinetically sluggish compared to other reactions in the system. An increase in the C/M_2O_3 feed ratio leads to a loss of selectivity

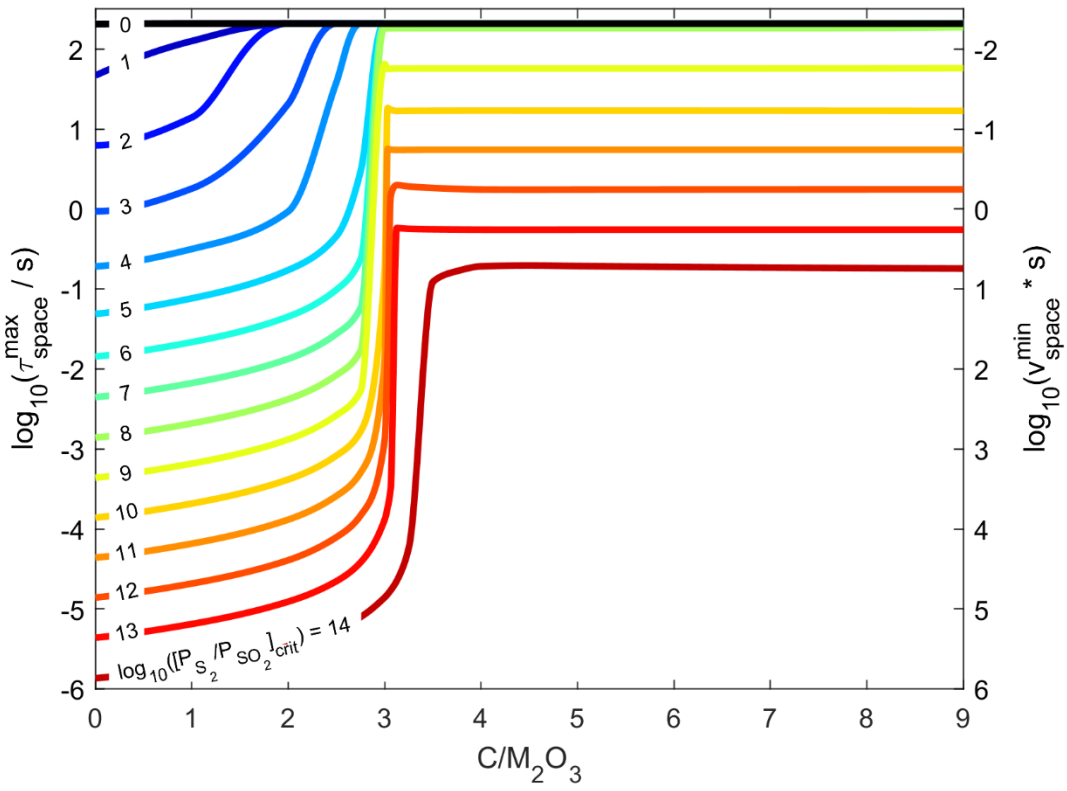

Figure 3.8: Critical space time (τ_{space}^{max}) and space velocity (v_{space}^{min}) versus carbon to oxide ratio (C/M_2O_3) to achieve a critical sulfur to sulfur dioxide ratio ($[P_{S_2}/P_{SO_2}]_{crit}$). $[P_{S_2}/P_{SO_2}]_{crit}$ is achieved in a sulfidation reactor for τ_{space}^{max} or v_{space}^{min} through control of C/M_2O_3 via CDSR, tabulated here for a well-mixed gas phase at 1000 °C and M_2O_3 at a homologous (fraction of melting point) temperature of 60% using La_2O_3 sulfidation kinetics (Chapter 4, Section 4.2) observed for the same homologous temperature. Excess C addition results in selectivity challenges for the $[P_{S_2}/P_{SO_2}]_{crit}$ characteristic of many transition metals (~10^{-5} to ~10^{-1}) due to cosulfidation at a given τ_{space}^{max} or v_{space}^{min}.

due to co-sulfidation in the range of $[P_{S_2}/P_{SO_2}]_{crit}$ characteristic of many transition metals[6]. This corroborates the well-known lack of selectivity observed during carbosulfidation of transition metal oxides[46–48]. The gas-solid kinetic framework presented herein provides a path forward for designing sulfidation and desulfidation processes for selective oxide-sulfide anion exchange. The role of solid-state kinetic phenomenon on anion exchange product morphology are briefly discussed in the following section.

3.2.2 Solid-State Kinetic Phenomena and Oxide-Sulfide Anion Exchange Product Morphology

Under the pyrometallurgical conditions (>800 °C) proposed herein for oxide-sulfide anion exchange via sulfidation and desulfidation, solid-state kinetic phenomenon such as nucleation, growth, coarsening, and sintering will occur in parallel with the gas-solid reaction. These phenomena work together to increase the size of individual grains of product phases, but also contribute to intergrain and intragrain mass transport limitations as discussed below. Grain size of product phases is one of the key factors in determining the economic and energetic competitiveness of different chemical and physical separation methods[49]. As product grain size decreases, the energy burden associated with liberation of individual phases for physical separation increases and the mineralogical energy barrier between chemical and physical separation processes decreases[50] (Chapter 1, Figure 1.3). At a critically-small product grain size, chemical separation may overtake physical separation as the energetically-preferred method of product recovery[51]. While the science and engineering of product grain size is essential for optimizing downstream separation technologies, the main focus of this work is on elucidating the nature of the oxide-sulfide anion exchange process and its role in decarbonizing metal production. Therefore, experimental demonstration of oxide-sulfide anion exchange will focus on gas-solid sulfidation and desulfidation reactions and new methods of compound reduction facilitated by the reactions. Future works on the evaluation of relevant nucleation, growth, and coarsening phenomenon to maximize product liberation effectiveness are discussed in Chapter 8, Section 8.2.2.

As oxide-sulfide anion exchange progresses, a product layer may form on the surface of the unreacted feedstock. The morphology of this product layer can lead to intragrain diffusion limitations to the rate of reaction via passivation of the reaction front. This effect may be quantified using a modified Pilling–Bedworth ratio[52] ($R_{PD}{}'$), defined herein as the ratio of the molar volume of an elementary cell of the product to that of the reactant per unit of metal cation. For an oxide-sulfide anion exchange reaction described by Eqn. 3.1, $R_{PD}{}'$ is calculated as follows, where m^* and ρ correspond to molar mass and density respectively.

$$R'_{PD} = \frac{\beta\gamma}{\theta\iota}\frac{m^*_{M_\iota O_\kappa S_\lambda}\rho_{M_\gamma O_\delta S_\epsilon}}{m^*_{M_\gamma O_\delta S_\epsilon}\rho_{M_\iota O_\kappa S_\lambda}} \quad 3.13$$

When $R'_{PD} < 1$, the product is not expected to sterically passivate the reactant due to gaps in the product coating and limited intragrain mass transport limitations through the product layer are expected. When $R'_{PD} > 2$, the product is expected to flake off the reactant and limited intragrain mass transport limitations through the product layer are expected. When $1 < R'_{PD} < 2$, the product is expected to form a shell that passivates the reactant at the reaction front. This event can lead to intragrain mass transport diffusion limitations during oxide-sulfide anion exchange if the product coating is sufficiently thick or the intrinsic oxide-sulfide anion exchange reaction kinetics are sufficiently fast. When the product forms as a liquid or vapor, these passivation effects are mitigated. Even if R'_{PD} is sufficiently small or large to suggest that the product will not fully passivate the reaction front, depending on the reaction mechanism intragrain diffusion limitations may still exist inside the reaction front within the reactant.

R'_{PD} is defined for some oxide-sulfide anion exchange reactions at both 20 °C and 727 °C in Table 3.2, where a pure sulfide is produced from a pure oxide with unchanging cation valency. Oxide densities at 727 °C were determined using published relations between coefficient of thermal expansion and temperature[53]. Sulfide densities at 727 °C were approximated using their melting point values[v] compiled from various sources by the author elsewhere[32]. However, significant uncertainties in sulfide melting points often exist, accompanied by wide ranges of reported values for liquidus temperature[54]. Experimental values for sulfide density at elevated temperatures are preferable when available.

For most oxide sulfidation reaction tabulated in Table 3.2, R'_{PD} is found to fall between 1 and 2, suggesting that sulfide products are inclined to passivate oxide reactants. When the sulfide layer is sufficiently thick to slow diffusion versus the intrinsic chemical rate of oxide sulfidation, intragrain mass transport may limit the reaction rate. Oxide-sulfide anion exchange may still progress if thermodynamically spontaneous, albeit at a slower rate than in the absence

[v] While coefficients of thermal expansion have been extensively measured, tabulated, and reviewed for oxides[53], measured values for sulfide thermal expansion are less publicly available. Herein, at the sulfide melting point a 3% total linear expansion in the material from 20 °C is assumed[53]. The extent of linear expansion is assumed to scale linearly as a function of temperature from 20 °C to melting. The volumetric expansion of the sulfide is taken to be a factor of 3 larger than the linear expansion.

of mass transport limitations. This finding highlights the importance of managing mass transport during oxide-sulfide anion exchange to develop integrated thermodynamic, kinetic, and transport models for oxide-sulfide anion exchange processes. An experimental framework is discussed in the next section. Sulfidation reaction kinetics and mass transport limitations are quantified experimentally in Chapter 4.

Metal Cation	ρ_{oxide} (g/cm^3)		Sulfide melting point (°C)	$\rho_{sulfide}$ (g/cm^3)		R'_{PD} for oxide sulfidation	
	20 °C	727 °C		20 °C	727 °C	20 °C	727 °C
$Al(III)$	3.95	3.88	1100	2.32	2.22	2.51	2.58
$Ba(II)$	5.72	5.50	2235	5.22	5.09	1.21	1.19
$Ca(II)$	3.34	3.25	2357	2.59	2.53	1.66	1.66
$Co(II)$	6.44	6.26	1182	5.45	5.22	1.43	1.46
$Cr(III)$	5.22	5.13	1535	3.77	3.64	1.82	1.86
$Dy(III)$	7.80	7.67	1810	6.08	5.90	1.45	1.47
$Er(III)$	8.64	8.50	1738	6.07	5.88	1.60	1.63
$Fe(II)$	5.74	5.58	1180	4.84	4.64	1.45	1.47
$Gd(III)$	7.41	7.29	1830	6.11	5.93	1.37	1.39
$Ho(III)$	8.41	8.27	1735	5.92	5.74	1.60	1.62
$La(III)$	6.51	6.35	2110	4.91	4.78	1.52	1.52
$Lu(III)$	9.42	9.27	1727	6.25	6.06	1.69	1.72
$Mg(II)$	3.58	3.48	1906	2.68	2.60	1.87	1.87
$Mn(II)$	5.37	5.21	1655	3.99	3.86	1.65	1.65
$Nd(III)$	7.24	7.06	1920	5.18	5.03	1.60	1.60
$Ni(II)$	6.67	6.48	1000	5.87	5.59	1.38	1.41
$Pr(III)$	6.90	6.79	2037	5.04	4.90	1.57	1.59
$Sc(III)$	3.86	3.79	2018	2.91	2.83	1.79	1.81
$Si(IV)$	2.65	2.57	1092	1.85	1.77	2.20	2.23
$Sm(III)$	8.35	8.18	1720	5.87	5.69	1.62	1.64
$Sn\ (IV)$	6.95	6.89	865	4.50	4.26	1.87	1.96
$Sr(II)$	4.70	4.58	2300	3.70	3.61	1.47	1.47
$Ti(IV)$	4.23	4.15	1780	3.22	3.12	1.84	1.86
$Ur(IV)$	10.97	10.74	1850	7.54	7.32	1.63	1.64
$W(IV)$	10.80	10.71	1900	7.50	7.29	1.65	1.69
$Y(III)$	5.01	4.93	1717	3.87	3.75	1.57	1.59
$Yb(III)$	9.17	9.02	1820	7.06	6.85	1.46	1.48
$Zn(II)$	5.61	5.53	1658	4.09	3.96	1.64	1.67
$Zr(IV)$	5.68	5.60	1450	3.82	3.68	1.87	1.92

Table 3.2: Modified Pilling-Bedworth ratio (R'_{PD}) for some oxide sulfidations.

3.3 Experimental Framework for Oxide-Sulfide Anion Exchange

The thermodynamic and kinetic frameworks established in Sections 3.1 and 3.2 inform the experimental demonstration of oxide-sulfide anion exchange via selective sulfidation and desulfidation processes. To achieve thermodynamically-predicted selectivity across various materials systems, design of the sulfidation / desulfidation reactor must be kinetically informed. In the following subsections, material feedstock selection, reactor design, and kinetic measurements are discussed in the context of pyrometallurgical sulfidation and desulfidation reactions for oxide-sulfide anion exchange.

3.3.1 Material Systems

As outlined in Sections 3.1 and 3.2, sulfidation and desulfidation reactions occur across a wide range of $\left[P_{S_2}/P_{SO_2}\right]_{crit}$ values. To determine the general efficacy of sulfidation and desulfidation oxide-sulfidation anion exchange reactions, material systems that are representative of a range of operating conditions and chemistries are considered. For demonstration of selective oxide-sulfide anion exchange, material systems are chosen that exhibit high environmental impacts and costs with existing technologies, or lack an industrially scalable processing route. Sulfidation / desulfidation experiments for oxide-sulfide anion exchange are conducted in three stages:

- Sulfidation of pure compounds
- Selective sulfidation / desulfidation of physically-mixed compounds
- Selective sulfidation of natural and industrial materials

Pure compound sulfidation of oxides is conducted first to demonstrate that $\left[P_{S_2}/P_{SO_2}\right]_{rx}$ can meet the $\left[P_{S_2}/P_{SO_2}\right]_{crit}$ required for oxide-sulfide anion exchange. From Figures 3.4 and 3.5, rare earth oxides exhibit among the highest $\left[P_{S_2}/P_{SO_2}\right]_{crit}$, on the order of 10^{10}-10^{14}. Figure 3.8 shows that such levels of $\left[P_{S_2}/P_{SO_2}\right]_{rx}$ are achievable through control of gas residence time and CDSR. Therefore, sulfidation of La_2O_3 and Sc_2O_3 are chosen as case studies to confirm the level of $\left[P_{S_2}/P_{SO_2}\right]_{rx}$ that is practically attainable using S_2 as a sulfidizing agent. The oxides of pure zirconium (Zr) and tungsten (W) as chosen as secondary case studies since they exhibit high $\left[P_{S_2}/P_{SO_2}\right]_{crit}$ compared to many other transition metal oxides. Lanthanum (La)[55], Sc[56], Zr[57], and W[58] are all currently extracted using tedious and unsustainable hydrometallurgical routes that may be improved using selective oxide-sulfide anion exchange. Sulfidation of magnesium carbonate ($MgCO_3$), calcium carbonate ($CaCO_3$), strontium carbonate ($SrCO_3$), and barium sulfate ($BaSO_4$) are also considered under equivalent conditions to serve as a point of comparison for kinetic and mass transport phenomenon.

After establishing the sulfidation conditions and behavior for pure compounds, the selectivity of oxide-sulfide anion exchange is explored for multicomponent systems. Simple physical binary and tertiary mixtures of compounds are first considered in a preliminary attempt to understand the selectivity achievable in oxide-sulfide anion exchange via sulfidation and desulfidation processes, without complications arising from convoluted, natural feed chemistries. While not strictly representative of mineralogical or industrial abundances in many material separations, equimolar or equimass ratios of feed compounds are utilized so that trends in product purity and impurity solubility are readily apparent for different sulfidation conditions. Three chemistries for mixed compound selective sulfidation / desulfidation are considered:

- Iron sesquioxide (Fe_2O_3) and Sc_2O_3
- FeS and lanthanum sulfide (La_2S_3)
- Neodymium oxide (Nd_2O_3), praseodymium oxide (Pr_6O_{11}), and dysprosium oxide (Dy_2O_3)

Sulfidation of mixed Fe_2O_3 and Sc_2O_3 is chosen as a first trial for selectivity due to their wide gap in $\left[P_{S_2}/P_{SO_2}\right]_{crit}$ ($10^{-1.4}$ and 10^{13} for formation of sulfides respectively at 1000 °C as shown in Figure 3.5) and their predicted differences in sulfidation reaction kinetics[vi]. $Sc-Fe$ separation also remains a critical challenge in materials recovery from red mud tailings produced in the Bayer process for alumina production[56].

Oxide-sulfide anion exchange of mixed FeS and La_2S_3 is selected as a trial of selectivity in desulfidation, with similar differences in $\left[P_{S_2}/P_{SO_2}\right]_{crit}$ for the desulfidation reaction as for Fe_2O_3 and Sc_2O_3 sulfidation (Figure 3.5). Understanding desulfidation in FeS and La_2S_3 systems is of interest for characterizing the behavior of oxygen impurities in molten sulfide electrolytic processes for chalcopyrite ($CuFeS_2$) processing[59].

To characterize the ability of CDSR to control $\left[P_{S_2}/P_{SO_2}\right]_{rx}$, mixed Nd_2O_3, Pr_6O_{11}, and Dy_2O_3 are sulfidized in the presence of varying levels of solid C addition. These rare earth elements are of interest in magnet recycling[60], as well as in the context of technologies under development to support presorting of light and heavy rare earth elements prior to separation[61].

Following experimental verification of selectivity in oxide-sulfide anion exchange for physical mixtures of oxides and sulfides, the sulfidation behaviors of the following natural and industrial materials are considered:

- Rare earth magnets
- Complex nickeliferous laterite ore
- Copper smelter slags
- Lithium-ion battery cathode materials

[vi] Fe_2O_3 and Sc_2O_3 exhibit melting points of 1597 °C and 2470 °C respectively[71,72]. From the observed correlation between the rate of thermally-activated solid-state kinetic processes with homologous temperature, at a given operating temperature the sulfidation rate of Fe_2O_3 is predicted to be faster than that of Sc_2O_3. In general, increasing oxide melting temperature follows enthalpic trends for increasing $\psi_{rxn_{\Delta H}}$ (Figure 3.2). Therefore, Fe_2O_3 is predicted sulfidize more rapidly and at a lower P_{S_2}/P_{SO_2} ratio than Sc_2O_3, as discussed in Section 3.2.1.

These systems are chosen with a range of modern materials processing and sustainability challenges in mind. The use of a "collector" phase is coupled with kinetic control of sulfidation selectivity in the recycling of rare earth magnets[6]. The role of oxide basicity in modulating sulfidation conversion and solution effects is explored in nickeliferous laterite and copper slag sulfidation. Finally, selective sulfidation is applied to recycling of lithium-ion battery cathode materials to demonstrate avenues for process intensification by increasing the selectivity of pyrometallurgical processes[6]. Together, experiments across this range of materials inform the applicability of oxide-sulfide anion exchange as a materials agnostic processing technology.

In practice, materials plagued by difficult separations often exhibit anion chemistries or impurities outside of the oxide-sulfide framework established in Sections 3.1 and 3.2. Therefore, to understand the behavior of fluorine (F) and phosphorous (P) anion impurities during oxide-sulfide anion exchange, sulfidation of lanthanum phosphate ($LaPO_4$) and lanthanum oxyfluoride ($LaOF$) are chosen as case studies due to their relevance to rare earth element processing[62]. To understand the behavior of other pnictogens and other chalcogenides during oxide-sulfide anion exchange, sulfidation of tennantite ($Cu_{12}Sb_{0.6}As_{3.4}S_{13}$) and enargite ($Cu_3AsS_4$) minerals are conducted. These results confirm that pyrometallurgical oxide-sulfide anion exchange remains relevant for reactor operation in the presence of impurities. In the following subsection, design of a sulfidation / desulfidation reactor and methodology for kinetics measurements are elucidated.

3.3.2 Reactor Design and Kinetics

To experimentally demonstrate selective oxide-sulfide anion exchange for the chemistries outlined in Section 3.3.1, a packed bed reactor geometry is proposed for sulfidation and desulfidation experiments on the scale of 1-3 grams of material[6]. The use of a packed bed reactor allows well-established mass transport and kinetic models[42–45] to be applied for characterization of reactor performance and scalability. A schematic of the packed bed reactor[6] employed for oxide-sulfide anion exchange via sulfidation and desulfidation is included in Figure 3.9 and detailed by the author elsewhere[6]. Sulfidation experiments conducted at larger scales are described by the author elsewhere[59]. For determination of the extent of conversion

1. Furnace
2. Alumina furnace tube
3. Stainless steel fitting
4. O-ring
5. O-ring compression ring
6. O-ring compression screw
7. Ar carrier gas inlet
8. Alumina support tube
9. Alumina support rod / O_2 inlet
10. Stainless steel crucible
11. Liquid sulfur
12. Packed bed reactor
13. Oxide to sulfidize
14. Gas outlet to gravity separator and IR sensor

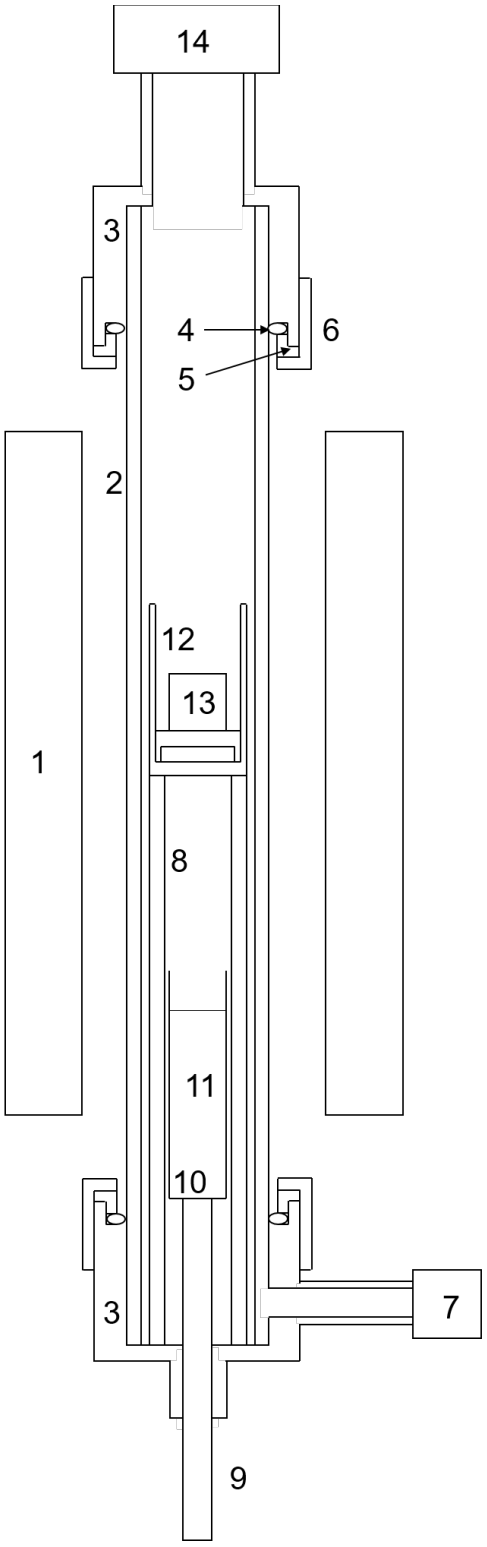

Figure 3.9: Packed bed reactor employed for oxide-sulfide anion exchange.

during an oxide-sulfide anion exchange reaction, the CO, CO_2, and SO_2 composition of product gasses are measured as a function of ${P_{S_2}}^6$.

Frameworks have been developed by Sohn et. al to isolate the intrinsic chemical rate of a gas-solid reaction from transport effects[42–45], allowing for the measurement of sulfidation kinetics in a packed bed reactor geometry. In general, the initial rate of reaction and reactant partial pressures or concentrations are typically utilized to determine reaction kinetics through relation via a suitable rate law, with activation energy subsequently determined by fitting the rate constant and reactant temperature to an Arrhenius expression. However, for a fluid-solid reaction, the observed initial rate of reaction does not inherently reflect the intrinsic chemical rate due to the presence of internal (within the porous solid) and external (to the surface of the porous solid) mass transfer limitations[45]. In order the measure intrinsic chemical kinetics, experiments must be performed in regimes where both internal and external mass transfer limitations are shown to be negligible[43]. The intrinsic chemical kinetics[6] of the oxide-sulfide anion exchange reaction are distinguished from external, intergrain, and intragrain mass transfer limitations for the sulfidation of La_2O_3 as described later in Chapter 4 Section 4.2.

Experimental conditions and results for the sulfidation and desulfidation of pure compounds, mixed compounds, and industrial feedstocks in the packed bed reactor are presented in Chapters 4 and 5. Together, these experimental results illuminate a path forward to decarbonizing materials separation and metal production through oxide-sulfide anion exchange. Frameworks to evaluate the sustainability and economic competitiveness of new materials separation technologies based on sulfidation and desulfidation are presented in the following section.

3.4 Technoeconomic and Sustainability Framework for Oxide-Sulfide Anion Exchange

In Sections 3.1-3.3, an integrated thermodynamic, kinetic, and experimental framework is proposed to evaluate the technical feasibility of improving material separations via selective oxide-sulfide anion exchange chemistry. However, in order to overcome inertia held by legacy technologies in mining, extractive metallurgy, and recycling, technical process innovations are

best coupled with sustainability improvements and cost reductions. In Section 3.4.1, the capital costs (CAPEX) and operating costs (OPEX) are estimated for new materials separation pathways employing selective sulfidation and physical separation. Calculated CAPEX and OPEX are contextualized through comparison to technoeconomic trends in chemical separation via liquid-liquid hydrometallurgy. In Section 3.4.2, the environmental impacts of materials separation via selective sulfidation and physical separation are quantified via life cycle assessment across the impact categories of global warming potential (GWP), terrestrial acidification (TA), and water resource depletion (WRD). Together, technoeconomic and sustainability results can inform the deployment of experimentally-verified selective oxide-sulfide anion exchange processes in an industrially-competitive manner.

3.4.1 Capital and Operating Cost Estimation

Thermodynamic models in Section 3.1 illustrate that material separations enabled by selective oxide-sulfide anion exchange have a wide range of applicability across different process conditions and chemistries. Detailed technoeconomic analysis of a process optimized for one specific material chemistry can misrepresent nuances of a different materials chemistry. Therefore, economic comparison is conducted across a generic materials processing pathway between physical separation enabled via selective oxide-sulfide anion exchange and chemical separation enabled via conventional hydrometallurgical processes.

Oxide-sulfide anion exchange via selective sulfidation as proposed herein can be conducted at scale in pyrometallurgical reactors conventionally used for feed drying, roasting, and calcination[6]. The product of sulfidation can be processed with orthodox beneficiation technologies for comminution and physical separation of product phases. The capital structures of these processes are well-established[63], allowing for economic comparison of the CAPEX for selective sulfidation to presently-deployed hydrometallurgical technologies using scaling factor estimates as detailed by the author elsewhere[6]. The OPEX for a generic hydrometallurgical process is not estimated, as it is known to vary strongly with location, feed solubility, liquid-liquid extractor chemistry, and liquid-liquid contactor design[61]. These variation in contributions to OPEX are not well-quantified in academic literature. Therefore, comparison of OPEX

between generic processes centered on sulfidation and liquid-liquid hydrometallurgy is presently not attempted.

The CAPEX of a generic, binary metal separation from equimolar mixed oxides is estimated for hydrometallurgical processing. Its flowsheet consists of acid roasting for impurity removal and formation of soluble metal compounds, gas treatment, leaching of the target elements, solvent extraction (SX) for metal element separation, and precipitation of product metal compounds[6] with operating conditions reported by the author elsewhere[6]. Meanwhile, the CAPEX and OPEX for separation via selective sulfidation from the same mix is estimated by considering air separation for nitrogen carrier gas production, sulfidation in a multihearth fluidized bed reactor, comminution, physical separation via froth flotation, and downstream gas handling and treatment, with conditions reported by the author elsewhere[6]. Flowsheets for the generic selective sulfidation and physical separation process with and without CDSR[6] are included in Figures 3.10 and 3.11. The costs of some possible sulfidation feed preparation and impurity management techniques, such as feed drying, dehalogenation or dephosphorization via roasting/calcination, and sulfidation/calcination for sintering of material feeds are also considered, as well as costs surrounding CDSR[6]. Flowsheets for selective sulfidation and physical separation with pretreatment steps are included in Figures 3.12 and 3.13[6]. For all CAPEX estimates, American Association of Cost Engineers (AACE) International Class 4 methodology[64] is employed.

OPEX for the generic selective sulfidation processes described above are estimated from reagent, utility, and waste treatment usage and prices, correlations for labor costs with relevant chemical process unit operations, correlations for management and overheads with labor cost, and correlations for maintenance costs with CAPEX, as detailed by the author elsewhere[6]. Revenue credits from byproduct sulfuric acid production are presently excluded in OPEX analysis for the generalized anion exchange separation process. However, economic value derived from valuable byproducts such as sulfuric acid is important to consider in determining the economic viability of a materials separation technology for a specific feedstock and geography[65]. OPEX as estimated herein also does not include processing steps upstream of selective sulfidation and its supporting pretreatments, such as mining and preliminary comminution / mineral dressing in primary production from ores, or material collection and crushing / disassembly in secondary materials production from recycled materials[6]. These

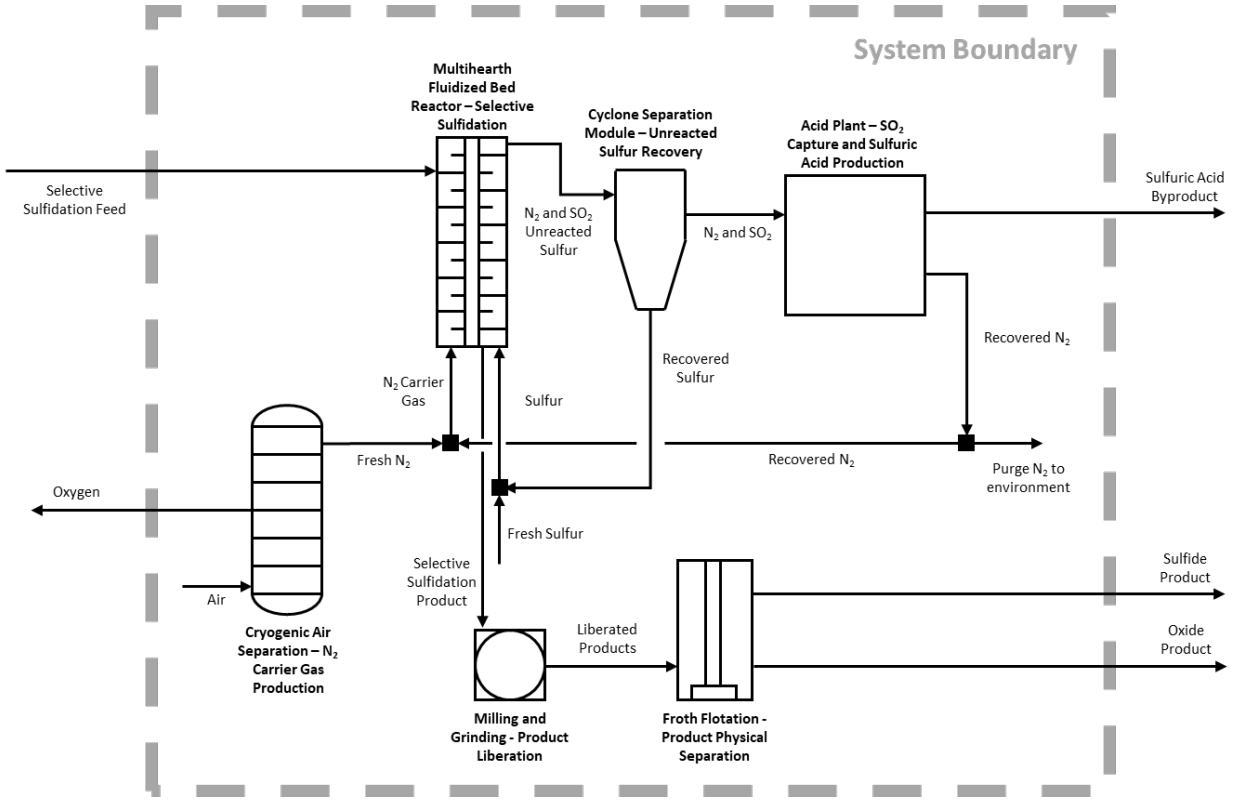

Figure 3.10: Flowsheet of a generic selective sulfidation process without carbothermically driven sulfur reflux (CDSR) for separation of an equimolar, mixed, binary oxide feed. Processing steps include of selective sulfidation in a multihearth fluidized bed reactor, product comminution and physical separation via froth flotation, and downstream gas handling and treatment via a cyclone separator for solid particle removal and an acid plant for sulfur dioxide (SO_2) recovery.

upstream steps are not considered since they are necessary regardless of the downstream materials separation technique employed (leaching, SX, pyrometallurgical smelting, selective sulfidation, etc.), and may or may not be conducted at the same facility as downstream materials processing[6]. Likewise, differences in costs between established and greenfield facilities are not considered herein[6].

Sensitivity analyses for CAPEX and OPEX estimations are conducted via Monte Carlo simulation with 360,000 iterations over relevant process variables as detailed by the author elsewhere[6]. While analysis of a generic processing pathway provides high level insight into the relative economic scaling of oxide-sulfide anion exchange versus conventional hydrometallurgy, conclusions drawn from the generic processing trends are not a replacement for chemistry-

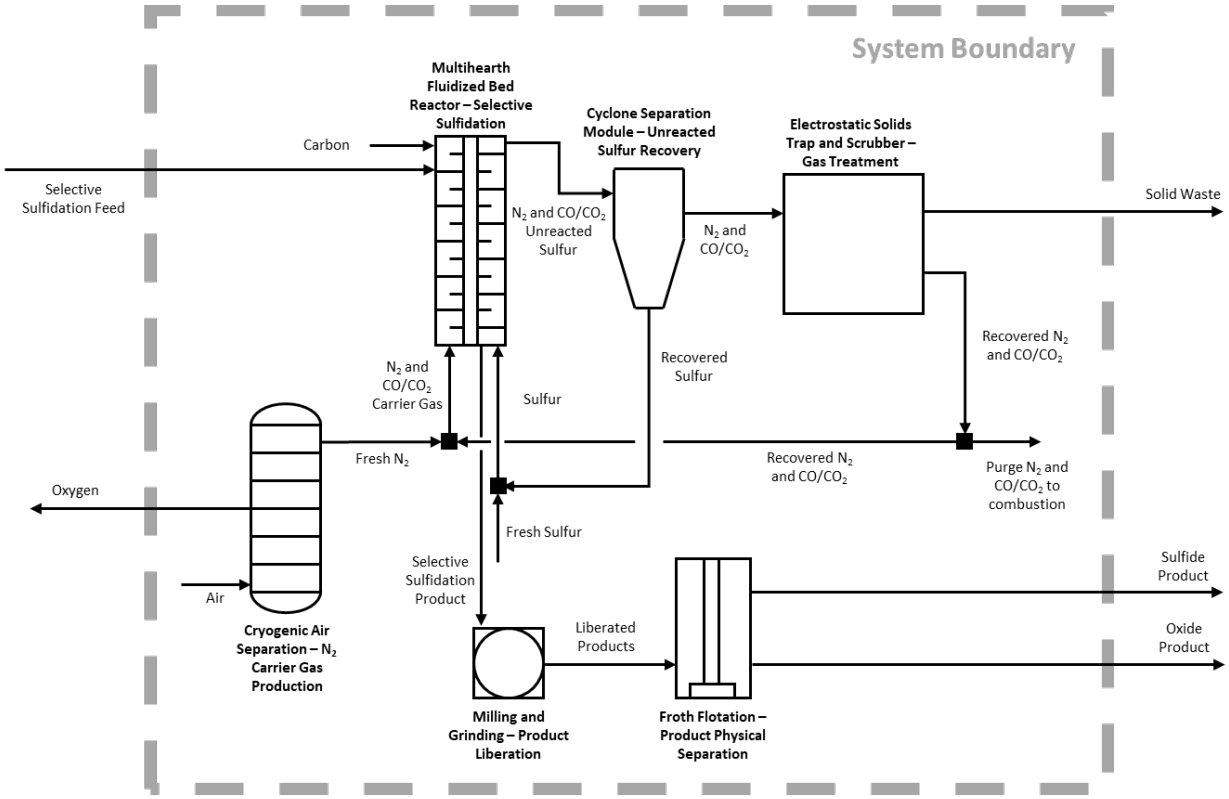

Figure 3.11: Flowsheet of a generic selective sulfidation process utilizing carbothermically driven sulfur reflux (CDSR) for separation of an equimolar, mixed, binary oxide feed. Processing steps include air separation for nitrogen carrier gas production, selective sulfidation in a multihearth fluidized bed reactor, product comminution and physical separation via froth flotation, and downstream gas handling and treatment via a cyclone separator for solid particle removal and an electrostatics solid trap and dual alkali scrubber for sulfur dioxide (SO_2) treatment.

specific design work. To understand the profitability of a given materials separation process utilizing selective sulfidation, detailed design considering geographic-specific factors (ore grade and impurities, labor costs and utilization, level of automation, greenfield versus established facility, CAPEX versus OPEX tradeoffs, value of byproducts, etc.) and refinement of sulfidation operating conditions and chemistries will be necessary[6]. Regional and organizationally-specific factors pertaining to cost of capital, depreciation, and amortization are also critical for understanding the economic competitiveness of oxide-sulfide anion exchange[6]. Other factors to consider in the technoeconomic optimization of sulfidation are costs arising from emissions and environmental impact. Environmental assessment for determining the sustainability of oxide-

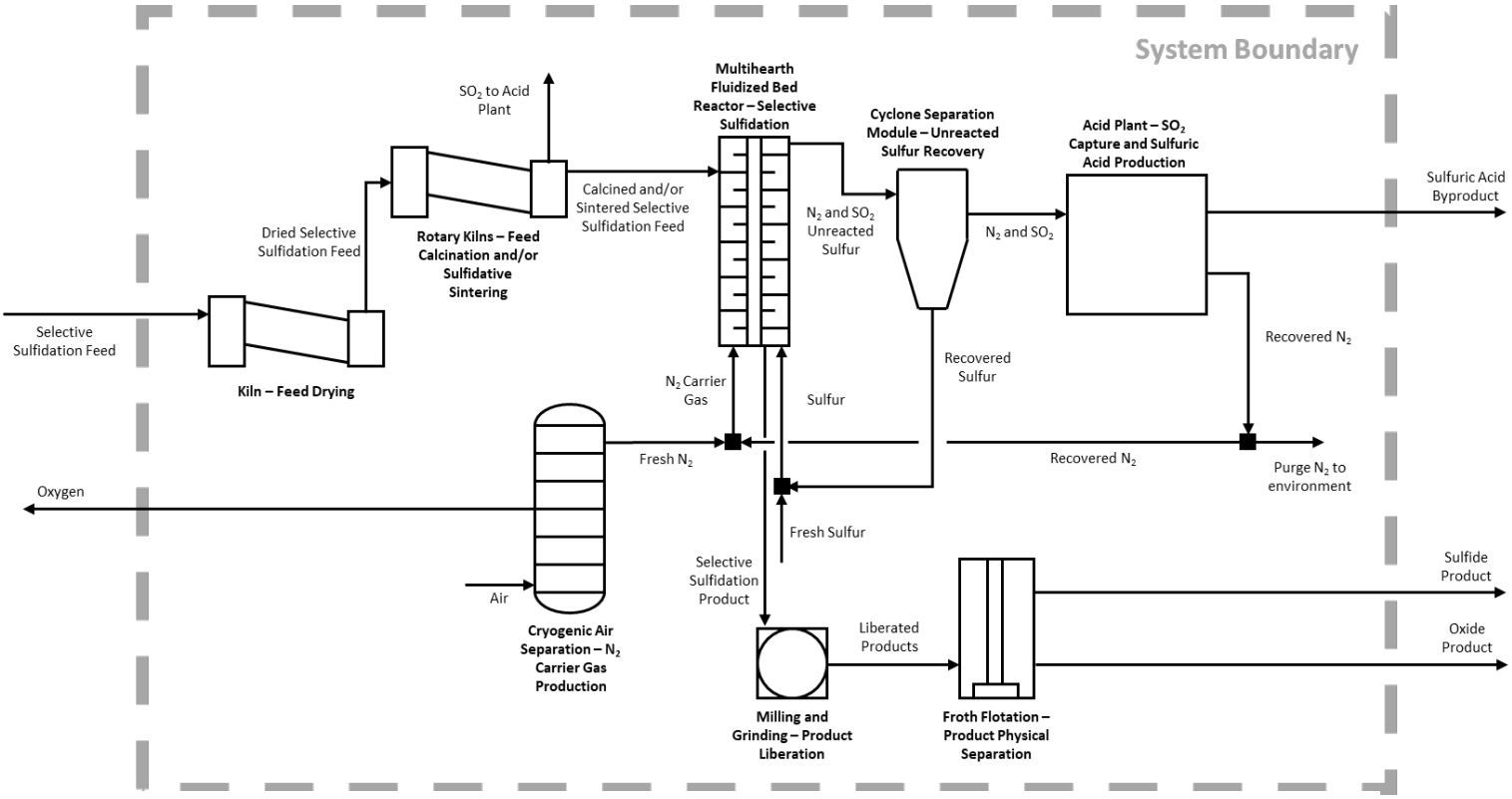

Figure 3.12: Flowsheet of a generic selective sulfidation process without carbothermically driven sulfur reflux (CDSR) for separation of an equimolar, mixed, binary oxide feed with pretreatments. Processing steps include air separation for nitrogen carrier gas production, drying and sulfidation/calcination pretreatments, selective sulfidation in a multihearth fluidized bed reactor, product comminution and physical separation via froth flotation, and downstream gas handling and treatment via a cyclone separator for solid particle removal and an electrostatics solid trap and dual alkali scrubber for sulfur dioxide (SO_2) treatment.

.

sulfide anion exchange with downstream physical separation is discussed in the following section.

3.4.2 Life Cycle Assessment

In Section 3.4.1, a framework is presented for quantifying the CAPEX and OPEX of generic physical material separation processes facilitated with selective oxide-sulfide anion via sulfidation chemistry. The environmental impact of selective sulfidation is estimated via life cycle assessment (LCA) for the same generic materials separation processes presented in Figures

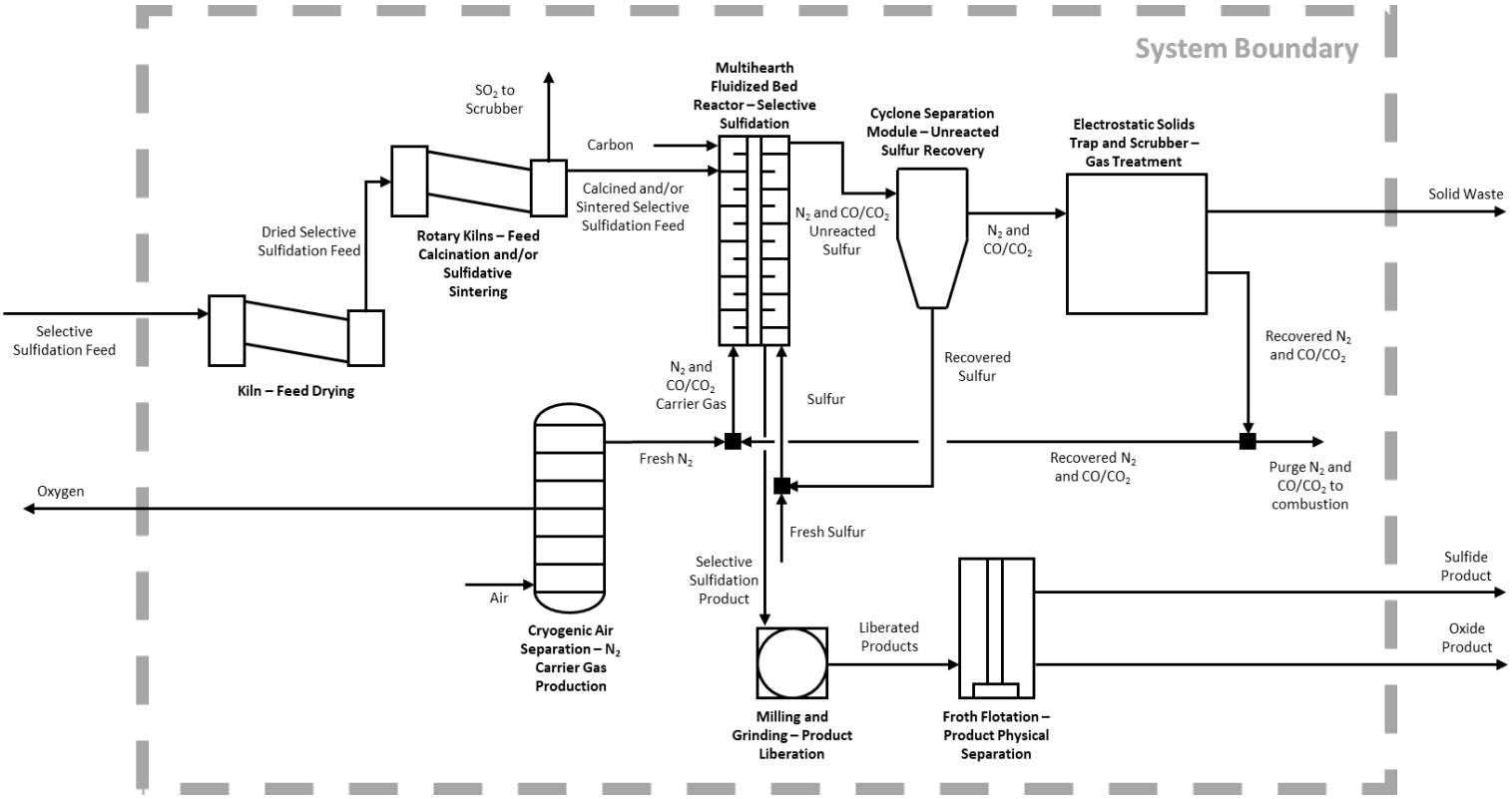

Figure 3.13: Flowsheet of a generic selective sulfidation process with feed pretreatments utilizing carbothermically driven sulfur reflux (CDSR) for separation of an equimolar, mixed, binary oxide feed with pretreatments. Processing steps include air separation for nitrogen carrier gas production, drying and sulfidation/calcination pretreatments, selective sulfidation in a multihearth fluidized bed reactor, product comminution and physical separation via froth flotation, and downstream gas handling and treatment via a cyclone separator for solid particle removal and an electrostatics solid trap and dual alkali scrubber for sulfur dioxide (SO_2) treatment.

3.10-3.13 across the impact categories of GWP, TA, and WRD[6]. The system boundary is defined to be an input of mixed-metal oxide and an output of physically-separated oxide and sulfide[6]. A functional unit of 1 kg of feed oxide is utilized to avoid making assumptions about feed grade or product yield[6]. Processing pathways with and without feed pretreatments (Section 3.4.1) and with and without CDSR are considered, and are shown with system boundaries[6] in Figures 3.10-3.13. To avoid the need for allocation of environmental impacts between coproducts as outlined by ISO 14044[66], system boundaries are established so that the impacts associated with any by- or coproducts are fully attributed to processing the feed oxide. Life

cycle intensity data for inputs into the generic sulfidation process are derived from ecoinvent 3.6 global averages[67] and representative literature data, with impacts quantified using TRACI 2.1 and other United States Environmental Protection Agency and United States Energy Information Agency data[68,69]. Sensitivity analyses is conducted using Monte Carlo simulation as outlined in Section 3.4.1 and discussed by the author elsewhere[6].

Environmental impact data tabulated for the generic sulfidation processes shown in Figures 3.10-3.13 provide a useful framework for predicting the sustainability of oxide-sulfide anion exchange and physical separation per unit of feed material. However, these generic models are not a replacement for detailed design work using chemistry-specific process flowsheets. Due to the strong dependence observed in the Monte Carlo simulation of environmental impact on system chemistry[6], the environmental impacts of utilizing selective-sulfidation-based pathways are calculated for three case studies via LCA:

- Zr-silicon (Si) separation from zircon ($(Zr, Hf)SiO_4$)
- Fe-titanium (Ti) separation from ilmenite ($FeTiO_3$)
- Rare earth element separation from bastnaesite ($LnCO_3F$)

These case studies are selected for two reasons: 1 – the existing processes – alkali fusion, the sulfate process, and acid roasting/leaching/solvent extraction respectively – each involve a combination of non-selective pyrometallurgical and selective hydrometallurgical processes, serving to elucidate the possible environmental impact reduction by increasing the selectivity of pyrometallurgical treatments using oxide-sulfide anion exchange chemistry. 2 – each of these processes has well-documented feed chemistry, LCA data, system boundaries, and allocation strategies for the standard processing route[55,70], supporting fair comparison of impacts between selective sulfidation with physical separation and hydrometallurgical chemical separation[6]. These case studies are detailed in Chapter 6.

3.5 Summary

In Chapters 1 and 2, material separations are framed in the context of anion exchange processes, with oxide-sulfide anion exchange proposed as a promising path forward to economically decarbonize metals separation and production. Control of selectivity in oxide sulfidation processes is identified as the major technical barrier to development of sustainable and economical oxide-sulfide anion exchange, while unknown trends in sulfidation thermodynamics and unexplored reaction kinetics are identified as key scientific gaps.

In Chapter 3, a thermodynamic framework is proposed to predict the order in which different elements in a compound sulfidize with an increasing ratio of sulfur to sulfur dioxide partial pressures in the system. This sulfidation series, which may be reversed for desulfidation processes, allows for thermodynamic quantification of selectivity in oxide-sulfide anion exchange processes. A foundation is laid to meet thermodynamic criteria for selective separation of materials through characterization of kinetics and mass transport phenomena during sulfidation and desulfidation processes.

With criteria established for selective sulfidation via oxide-sulfide anion exchange processes, an experimental methodology is presented to confirm predicted trends in sulfidation/desulfidation behavior. Informed by thermodynamics, economic and environmental evaluation of oxide-sulfide anion exchange for industrial scale materials processing is discussed. Generic oxide-sulfide anion exchange and physical separation process flowsheets are outlined for evaluation of capital cost, operating cost, global warming potential, terrestrial acidification, and water resource depletion. Chemistry-specific case studies are also proposed.

Together, this integrated thermodynamic, kinetic, technoeconomic, life cycle assessment, and experimental framework provides a path forward to analyze the efficacy and competitiveness of oxide-sulfide anion exchange for decarbonizing materials separations. In Chapters 4 and 5, experimental results for selective sulfidation and desulfidation are presented. In Chapter 6, technoeconomic and life cycle assessment results for sulfidation processes are calculated. Experimental findings and process modelling inform the development of new metal reduction technologies, introduced later in Chapter 7.

3.6 References

1. Meyer, B. Elemental Sulfur. *Chem. Rev.* **76**, 367–388 (1976).
2. Le Chatelier, H. La science pure orientée vers les applications et la science industrielle. *Rev. Métallurgie* **9**, 509–512 (1912).
3. Gibbs, J. W. On the Equilibrium of Heterogeneous Substances. *Trans. Connect. Acad. Arts Sci.* **3**, 108–248 (1875).
4. Gibbs, J. W. On the Equilibrium of Heterogeneous Substances. *Trans. Connect. Acad. Arts Sci.* **3**, 343–524 (1877).
5. Guldberg, C. M. & Waage, P. Ueber die chemische Affinität. § 1. Einleitung. *J. für Prakt. Chemie* **19**, 69–114 (1879).
6. Stinn, C. & Allanore, A. Selective sulfidation of metal compounds. *Nature* **602**, 78–83 (2022).
7. Goldschmidt, V. M. The principles of distribution of chemical elements in minerals and rocks. The seventh Hugo Müller Lecture, delivered before the Chemical Society on March 17th, 1937. *J. Chem. Soc.* 655–673 (1937) doi:10.1039/JR9370000655.
8. Ringwood, A. E. The principles governing trace element distribution during magmatic crystallization Part I: The influence of electronegativity. *Geochim. Cosmochim. Acta* **7**, 189–202 (1955).
9. Pauling, L. The Nature of the Chemical Bond. IV. The Energy of Single Bonds and the Relative Electronegativity of Atoms. *J. Am. Chem. Soc.* **54**, 3570–3582 (1932).
10. Shannon, R. D. & Prewitt, C. T. Effective ionic radii in oxides and fluorides. *Acta Crystallogr. Sect. B Struct. Crystallogr. Cryst. Chem.* **25**, 925–946 (1969).
11. Shannon, R. D. Bond Distances in Sulfides and a Preliminary Table of Sulfide Crystal Radii. in *Industrial Chemistry Library* 53–70 (1981). doi:10.1016/B978-0-12-525102-0.50009-8.
12. Allen, L. C. Electronegativity Is the Average One-Electron Energy of the Valence-Shell Electrons in Ground-State Free Atoms. *J. Am. Chem. Soc.* **111**, 9003–9014 (1989).
13. Allred, A. L. Electronegativity values from thermochemical data. *J. Inorg. Nucl. Chem.* **17**, 215–221 (1961).
14. Rockwood, A. L. Relationship of thermoelectricity to electronic entropy. *Phys. Rev. A* **30**,

2843–2844 (1984).

15. Rinzler, C. C. & Allanore, A. Connecting electronic entropy to empirically accessible electronic properties in high temperature systems. *Philos. Mag.* **96**, 3041–3053 (2016).
16. Stinn, C. & Allanore, A. Thermodynamic and Structural Study of the Copper-Aluminum System by the Electrochemical Method Using a Copper-Selective Beta″ Alumina Membrane. *Metall. Mater. Trans. B* **48**, 2922–2929 (2018).
17. Paras, J. & Allanore, A. Contribution of electronic entropy to the order-disorder transition of Cu3Au. *Phys. Rev. Res.* **3**, (2021).
18. Paras, J. & Allanore, A. Electronic entropy contribution to the metal insulator transition in VO2. *Phys. Rev. B* **102**, 1–5 (2020).
19. Pourbaix, M. J. N. & Rorive-Bouté, M. C. M. Graphical study of metallurgical equilibria. *Discuss. Faraday Soc.* **4**, 139–154 (1948).
20. Kellogg, H. H. A Critical Review of Sulfation Equilibria. *Trans. Metall. Soc. AIME* **230**, 1622–1634 (1964).
21. Jacob, K. T. & Iyengar, G. N. K. Thermodynamic study of Fe2O3-Fe2(SO4)3 equilibrium using an oxyanionic electrolyte (Na2SO4-I). *Metall. Trans. B* **17**, 323–329 (1986).
22. Hsieh, K. C. & Chang, Y. A. A solid-state emf study of ternary Ni-S-O, Fe-S-O, and quaternary Fe-Ni-S-O. *Metall. Trans. B* **17**, 133–146 (1986).
23. Dwivedi, R. K. & Kay, D. A. R. Thermodynamics of the oxidation of rare earth oxysulfides at high temperatures. *Metall. Trans. B* **15**, 523–528 (1984).
24. Akila, R., Jacob, K. T. & Shukla, A. K. Gibbs Energies of Formation of Rare Earth Oxysulfides. *Metall. Trans. B* **18B**, 163–168 (1987).
25. Dwivedi, R. K. Determination of the Thermodynamic Properties of Rare Earth-Oxygen-Sulfur Systems at High Temperatures. *PhD Thesis* (McMaster University, 1982).
26. Suponitskii, Y. L., Kuz'micheva, G. M. & Eliseev, A. A. Lanthanide Oxide Sulphides. *Russ. Chem. Rev.* **57**, 209–220 (1988).
27. Wang, M. Enthalpy of formation of LiNiO2, LiCoO2 and their solid solution, LiNi1−xCoxO2. *Solid State Ionics* **166**, 167–173 (2004).
28. Chang, K., Hallstedt, B. & Music, D. Thermodynamic and Electrochemical Properties of the Li−Co−O and Li−Ni−O Systems. *Chem. Mater.* **24**, 97–105 (2011).
29. Konings, R. J. M. *et al.* The Thermodynamic Properties of the f-Elements and their

Compounds . Part 2 . The Lanthanide and Actinide Oxides The Thermodynamic Properties of the f -Elements and their Compounds . Part 2 . The Lanthanide and Actinide Oxides. *J. Phys. Chem. Ref. Data* **43**, 013101 (2014).

30. Kriklya, A. I., Bolgar, A. S. & Pribyl'skii, N. Y. Heat Capacity and Enthalpy of y-Dy2S3 Over a Wide Range of Temperature. *Sov. Powder Metall. Met. Ceram.* **31**, 697–700 (1992).
31. Stinn, C. & Allanore, A. Selective Sulfidation and Electrowinning of Nickel and Cobalt for Lithium Ion Battery Recycling. in *Ni-Co 2021: The 5th International Symposium on Nickel and Cobalt* (eds. Anderson, C. et al.) 99–110 (Springer Nature Switzerland AG, 2021). doi:10.1007/978-3-030-65647-8_7.
32. Allanore, A. & Stinn, C. Selective Sulfidation and Desulfidation (Patent US20210277531A1). (2021).
33. Ellingham, H. J. T. Roasting and Reduction Processes - A General Survey. *Discuss. Faraday Soc.* (1948).
34. Stinn, C. & Allanore, A. Selective Sulfidation for Rare Earth Element Separation. in *Rare Metal Technology 2022* (ed. Ouchi, T.) 259–278 (The Minerals, Metals & Materials Society, 2022). doi:10.1007/978-3-030-92662-5_25.
35. Kang, Y.-B. & Pelton, A. D. Thermodynamic Model and Database for Sulfides Dissolved in Molten Oxide Slags. *Met. Mater. Trans. B* **40B**, 979–994 (2009).
36. Moosavi-Khoonsari, E. & Jung, I. H. Thermodynamic Modeling of Sulfide Capacity of Na2O-Containing Oxide Melts. *Metall. Mater. Trans. B Process Metall. Mater. Process. Sci.* **47**, 2875–2888 (2016).
37. Jung, I. H. & Moosavi-Khoonsari, E. Limitation of Sulfide Capacity Concept for Molten Slags. *Metall. Mater. Trans. B Process Metall. Mater. Process. Sci.* **47**, 819–823 (2016).
38. Sohn, H. Y. & Kim, B.-S. A Novel Cyclic Process using CaSO 4 /CaS Pellets for Converting Sulfur Dioxide to Elemental Sulfur without Generating Secondary Pollutants: Part I. Feasibility and Kinetics of the Reduction of Sulfur Dioxide with Calcium-Sulfide Pellets. *Metall. Mater. Trans. B* **33B**, 711–716 (2002).
39. Zhang, W. *et al.* Reaction mechanism study of new scheme using elemental sulfur for conversion of barite to barium sulfide. *Powder Technol.* **360**, 1348–1354 (2020).
40. Brown, A. M. & Ashby, M. F. Correlations for diffusion constants. *Acta Metall.* **28**, 1085–

1101 (1980).

41. Ishida, M. & Wen, C. Y. Comparison of kinetic and diffusional models for solid-gas reactions. *AIChE J.* **14**, 311–317 (1968).
42. Sohn, H. Y. & Szekely, J. The effect of intragrain diffusion on the reaction between a porous solid and a gas. *Chem. Eng. Sci.* **29**, 630–634 (1974).
43. Sohn, H. Y. & Szekely, J. A structural model for gas-solid reactions with a moving boundary. *Chem. Eng. Sci.* **27**, 763–778 (1972).
44. Sohn, H. Y. Review of fluid-solid reaction analysis—Part 2: Single porous reactant solid. *Can. J. Chem. Eng.* **97**, 2068–2076 (2019).
45. Sohn, H. Y. & Fan, D.-Q. On the Initial Rate of Fluid-Solid Reactions. *Met. Mater. Trans. B* **48B**, 1827–1832 (2017).
46. Liu, W., Zhu, L., Han, J., Jiao, F. & Qin, W. Sulfidation mechanism of ZnO roasted with pyrite. *Sci. Rep.* **8**, 1–12 (2018).
47. Harris, C. T., Peacey, J. G. & Pickles, C. A. Selective sulphidation and flotation of nickel from a nickeliferous laterite ore. *Miner. Eng.* **54**, 21–31 (2013).
48. Ahmad, S., Rhamdhani, M. A., Pownceby, M. I. & Bruckard, W. J. Thermodynamic assessment and experimental study of sulphidation of ilmenite and chromite. *Trans. Institutions Min. Metall. Sect. C Miner. Process. Extr. Metall.* **123**, 165–177 (2014).
49. Norgate, T. & Jahanshahi, S. Low grade ores – Smelt, leach or concentrate? *Miner. Eng.* **23**, 65–73 (2010).
50. Skinner, B. J. A Second Iron Age Ahead? The distribution of chemical elements in the earth's crust sets natural limits to man's supply of metals that are much more important to the future of society than limits on energy. *Sci. Am.* **64**, 258–269 (1976).
51. Skinner, B. J. Earth resources (minerals/metals/ores/geochemistry/mining). *Proc. Natl. Acad. Sci. USA* **76**, 4212–4217 (1979).
52. Pilling, N. B. & Bedworth, R. E. The Oxidation of Metals at High Temperatures. *J. Inst. Met.* **29**, 529–591 (1923).
53. Touloukian, Y. S., Kirby, R. K., Taylor, E. R. & Lee, T. Y. R. *Thermophysical Properties of Matter - the TPRC Data Series. Volume 13. Thermal Expansion - Nonmetallic Solids*. *IFI/Plenum, New York* (1977).
54. Stinn, C., Nose, K., Okabe, T. & Allanore, A. Experimentally Determined Phase Diagram

for the Barium Sulfide-Copper(I) Sulfide System Above 873 K (600 °C). *Metall. Mater. Trans. B* (2017) doi:10.1007/s11663-017-1107-5.

55. Bailey, G. *et al.* Review and new life cycle assessment for rare earth production from bastnäsite, ion adsorption clays and lateritic monazite. *Resour. Conserv. Recycl.* **155**, 104675 (2020).
56. Wang, W., Pranolo, Y. & Cheng, C. Y. Metallurgical processes for scandium recovery from various resources: A review. *Hydrometallurgy* **108**, 100–108 (2011).
57. Manhique, A., Kwela, Z. & Focke, W. W. De wet process for the beneficiation of zircon: Optimization of the alkali fusion step. *Ind. Eng. Chem. Res.* **42**, 777–783 (2003).
58. Shen, L., Li, X., Lindberg, D. & Taskinen, P. Tungsten extractive metallurgy: A review of processes and their challenges for sustainability. *Miner. Eng.* **142**, 105934 (2019).
59. Daehn, K. E. *et al.* Liquid Copper and Iron Production from Chalcopyrite, in the Absence of Oxygen. *Metals (Basel).* **12**, 1440 (2022).
60. Wagner, M.-E. & Allanore, A. Chemical Thermodynamic Insights on Rare-Earth Magnet Sludge Recycling. *ISIJ Int.* **60**, 2339–2349 (2020).
61. Zhao, B., Zhang, J. & Schreiner, B. *Separation Hydrometallurgy of Rare Earth Elements*. (Springer International Publishing AG Switzerland, 2016).
62. Jordens, A., Cheng, Y. P. & Waters, K. E. A review of the beneficiation of rare earth element bearing minerals. *Miner. Eng.* **41**, 97–114 (2013).
63. Woods, D. R. Appendix D: Capital Cost Guidelines. in *Rules of Thumb in Engineering Practice* 376–436 (Wiley-VCH Verlag GmbH & Co. KGaA, 2007). doi:10.1002/9783527611119.app4.
64. Christensen, P. & Dysert, L. *Cost Estimate Classification System as Applied in Engineering, Procurement, and Construction for the Process Industries*. *AACE International Recommended Practice No. 18R-97 COST, TCM Framework: 7.3 - Cost Estimating and Budgeting* (2005).
65. Rush, L. T. Integrative Approach to Metal Extraction and Electrification. (Massachusetts Institute of Technology, 2021).
66. ISO. *ISO 14044*. https://www.iso.org/standard/38498.html (2006).
67. Ecoinvent-Association. ecoinvent 3.6. *Ecoinvent Center* www.ecoinvent.org (2019).
68. USEIA. *Carbon Dioxide Emissions Coefficients*.

https://www.eia.gov/environment/emissions/co2_vol_mass.php (2021).

69. USEPA. TRACI 2.1. *Tool for Reduction and Assessment of Chemicals and Other Environmental Impacts* https://www.epa.gov/chemical-research/tool-reduction-and-assessment-chemicals-and-other-environmental-impacts-traci (2014).
70. Nuss, P. & Eckelman, M. J. Life cycle assessment of metals: a scientific synthesis. *PLoS One* **9**, e101298 (2014).
71. Wriedt, H. A. The Fe-O (Iron-Oxygen) System. *J. Phase Equilibria* **12**, 170–200 (1991).
72. Subramanian, P. R. O-Sc (Oxygen-Scandium). in *Binary Alloy Phase Diagrams* (ed. Massalski, T. B.) 2912–2915 (ASM International, 1990).

Chapter 4

Selective Sulfidation and Desulfidation of Materials

In Chapter 2, it was hypothesized that selective oxide-sulfide anion exchange decreases the solubility of target cation elements in feedstock materials to support their selective extraction and physical separation. Subsequently in Chapter 3, thermodynamic, kinetic, technoeconomic, and sustainability frameworks were put forth to evaluate the efficacy of oxide-sulfide anion exchange for materials separations. Thermodynamically, a metal oxide's enthalpic affinity for sulfidation was correlated with the metallic element's valency, Pauling electronegativity, and ionic (Shannon) radius. Trends in sulfidation behavior between oxides, oxysulfides, and sulfates were rationalized through entropic effects, namely changes in configurational entropy in solid compounds and the generation of gaseous species upon sulfidation. The thermodynamic role of carbon addition in achieving thermodynamic spontaneity in sulfidation was explored via a carbothermically-driven sulfur reflux system. Solution effects were highlighted as contributing to calculated deviations in oxide-sulfide anion exchange behavior between different material feedstocks. These insights provide thermodynamic justification for the ability to conduct oxide-sulfide anion exchange selectively.

Kinetically, oxide-sulfide anion exchange via selective sulfidation or desulfidation is understood to be a thermally activated process, with the rate of reaction increasing with temperature as a fraction of the compound's melting point (homologous temperature). When

periodic trends in compound melting points are unified with observed trends in sulfidation affinity, compounds with a higher affinity for sulfidation are predicted to exhibit faster oxide-sulfide anion exchange kinetics at a given temperature. An integrated thermodynamic and kinetic framework for sulfidation is therefore necessary to evaluate the technical, economic, and environmental competitiveness of pyrometallurgical oxide-sulfide anion exchange for metal separations.

To test the hypothesis that selective oxide-sulfide anion exchange decreases the solubility of target cation elements in feedstock materials to support their selective extraction and physical separation, the following criteria need to be evaluated experimentally:

- The efficacy of oxide-sulfide anion exchange using gaseous elemental sulfur for compounds exhibiting a range of sulfidation affinities
- The thermodynamic and kinetic process levers that enable selective oxide-sulfide anion exchange
- The selective precipitation of distinct product phases that are enriched in target elements
- The ability to physically separate product phases from selective oxide-sulfide anion exchange

In this chapter, the sulfidation and desulfidation behaviors of a range of oxide, oxysulfide, sulfate, and sulfide species are experimentally evaluated, illustrating that oxide-sulfide anion exchange results in the selective precipitation of largely insoluble products from mixed metal compound feedstocks. The intrinsic chemical kinetics of rare earth oxide sulfidation are measured, corroborating the notion of thermal activation in oxide-sulfide anion exchange kinetics and their role in selectivity. The impact of the carbothermically driven sulfur reflux in control of sulfidation affinity is established. The results of sulfidation as applied to natural and industrial feedstocks are then presented, informing the role of solution effects in sulfidation selectivity and conversion. Finally, physical separation of a sulfidized feedstock is

conducted via froth flotation and magnetic separation. Together, these results confirm the hypothesis that selective oxide-sulfide anion exchange decreases the solubility of target cation elements in feedstock materials to support their selective extraction and physical separation. The behavior of pnictogen, chalcogenide, and halide impurities in oxide-sulfide anion exchange processes are subsequently considered in Chapter 5.

4.1 Oxide-Sulfide Anion Exchange Thermodynamics: Sulfidation of Pure Compounds

Prior to performing selective sulfidation, a range of pure alkaline earth, transition, and rare earth metal oxides, sulfates, and carbonates were tested to confirm that calculated reactor conditions in Chapter 3, Sections 3.1-3.2 for sulfidation were accurate and could be practically achieved. Calculated critical sulfur (S_2) to sulfur dioxide (SO_2) partial pressure ratios ($\left[P_{S_2}/P_{SO_2}\right]_{crit}$) at the employed reaction temperatures are reported in Table 4.1 for pure compounds explored herein: lanthanum oxide (La_2O_3), scandium oxide (Sc_2O_3), zirconium oxide (ZrO_2), tungsten oxide (WO_3), magnesium carbonate ($MgCO_3$), calcium carbonate ($CaCO_3$), strontium carbonate ($SrCO_3$), and barium sulfate ($BaSO_4$). Sulfidation was conducted in graphite reactor trays following the methods detailed in Chapter 3, Section 3.3. Sulfur (S) was evaporated and transported through the reactor bed using an inert argon (Ar) carrier gas[1]. For these experiments, no oxygen (O) containing species were introduced with the gas phase feed; the source of SO_2 was oxygen (O_2) liberated via oxide-sulfide anion exchange. In the presence of the graphite reactor trays, SO_2 reacted with carbon (C) to form S_2 and carbon monoxide (CO) via the carbothermically driven sulfur reflux (CDSR, Chapter 3, Section 3.2.1).

Sulfidation products[1] for La_2O_3 and Sc_2O_3 are reported in Table 4.2. Both rare earth oxides (REOs) formed sesquisulfides (La_2S_3 and Sc_2S_3) through oxysulfide intermediates (La_2O_2S and Sc_2O_2S), consistent with trends reported in Chapter 3, Figures 3.1 and 3.3. Lanthanum (La) also exhibited an intermediate sulfide of stoichiometry of La_3S_4. Sulfidation at higher P_{S_2} resulted in the formation of lanthanum disulfide (LaS_2) in an outer shell on the surface of powder bed with complete conversion to La_2S_3 in the core of the powder bed[2]. Greater than 99.9% conversion of La_2O_3 to sulfide was achievable as measured via quantitative x-ray

diffraction (QXRD) analysis. Nevertheless, gas fusion and light element combustion (LECO) analysis revealed some O solubility in La_2S_3 and La_3S_4 products. Work by Ahmadi and Suzuki suggests that oxide-sulfide anion exchange and the subsequent removal of residual solubilized O by sulfidation proceed at different rates, with the later occurring over longer reaction time scales[3]. For sulfidation of La_2O_3, experiments conducted at different temperatures provide insight into the thermal activation of sulfidation kinetics, discussed later in Section 4.2. Unlike the sulfidation of La_2O_3, sulfidation of Sc_2O_3 to Sc_2S_3 was not observed to progress through a Sc_3S_4 intermediate. Complete conversion of Sc_2O_3 to Sc_2S_3 was achievable via mitigation of mass transport limitations, as observed via qualitative x-ray diffraction (XRD)[4].

Reaction	Sulfidation Temperature	$\log_{10}\left(\left[P_{S_2}/P_{SO_2}\right]_{crit}\right)$
$La_2O_3 = La_2O_2S$	1200 °C[a]	-14.6
	1250 °C[a]	-14.4
	1300 °C	-14.1
	1400 °C	-13.6
	1475 °C	-13.3
$La_2O_2S = La_2S_3$	1200 °C[a]	10.8
	1250 °C[a]	10.8
	1300 °C	10.8
	1400 °C	10.8
	1475 °C	10.8
$Sc_2O_3 = Sc_2O_2S$	1400 °C	-9.2
$Sc_2O_2S = Sc_2S_3$	1400 °C	12.2
$ZrO_2 = ZrS_2$	1475 °C	4.4
$WO_3 = WS_2$	1000 °C	-0.8
$MgO = MgS$	1000 °C	3.3
$CaSO_4 = CaS$	1000 °C	-1.2
$SrSO_4 = SrS$	1000 °C	-0.2
$BaSO_4 = BaS$	1000 °C	0.5

Table 4.1: Calculated critical sulfur to sulfur dioxide ratio ($\left[P_{S_2}/P_{SO_2}\right]_{crit}$) and reaction temperatures for pure compound feedstocks. Sulfidation was experimentally conducted using CDSR. [a] Samples from 1200 °C and 1250 °C were only utilized for analysis of sulfidation conversion or sulfidation kinetics (Section 4.2) respectively.

Sulfidation products[1] for ZrO_2 and WO_3 are reported in Table 4.3. In both cases, crystalline oxide phases were sulfidized at conversions greater than 99.9%. For ZrO_2, the sulfidation product was a mix of zirconium disulfide (ZrS_2) and zirconium-deficient sulfide compounds ($Zr_{1-x}S_2$). No zirconium oxysulfide ($ZrOS$) intermediates were observed herein,

but $ZrOS$ has been synthesized by others via reaction of ZrO_2 and hydrogen sulfide (H_2S) or carbon disulfide (CS_2)[5,6]. The use of CDSR likely resulted in a P_{S_2}/P_{SO_2} ratio that was high enough to achieve full conversion of any intermediate $ZrOS$ to ZrS_2 or $Zr_{1-x}S_2$.

Feedstock	Sulfidation Temperature	P_{S_2}	Conversion to sulfide	M_2O_3	M_2O_2S	M_3S_4	M_2S_3	MS_2
La_2O_3	1200 °C	0.1 atm	97.2 wt% [a] >99.9 wt% [b]	<0.1 wt%	<0.1 wt%	13.4 wt%	86.6 wt%	<0.1 wt%
La_2O_3	1300 °C	0.1 atm	96.8 wt% [a] >99.9 wt% [b]	<0.1 wt%	<0.1 wt%	3.9 wt%	96.1 wt%	<0.1 wt%
La_2O_3	1400 °C	0.1 atm	98.3 wt% [a] 95.7 wt% [b]	<0.1 wt%	4.3 wt%	11.2 wt%	84.5 wt%	<0.1 wt%
La_2O_3	1475 °C	0.1 atm	97.4 wt% [a] >99.9 wt% [b]	<0.1 wt%	<0.1 wt%	24.8 wt%	75.2 wt%	<0.1 wt%
La_2O_3 Surface Core	1400 °C	0.9 atm	>99.9 wt% [b]	<0.1 wt% <0.1 wt%	<0.1 wt% <0.1 wt%	28.1 wt% <0.1 wt%	<0.1 wt% >99.9 wt%	71.9 wt% <0.1 wt%
Sc_2O_3	1400 °C	0.1 atm	50 wt% [b]	32.3 wt%	45.1 wt%	<0.1 wt%	23.6 wt%	<0.1 wt%
Sc_2O_3	1400 °C	0.1 atm	95 wt% [b]	<0.1 wt%	4.7 wt%	<0.1 wt%	95.3 wt%	<0.1 wt%
Sc_2O_3	1400 °C	0.1 atm	Complete [c]	ND	ND	ND	~ 100%	ND

Table 4.2: Products from the sulfidation of lanthanum oxide (La_2O_3) and scandium oxide (Sc_2O_3) using carbothermically driven sulfur reflux (CDSR). Data was analyzed via QXRD, XRD, and LECO. M corresponds to a metallic element, here either La or scandium (Sc), and ND corresponds to phases that were not detected during qualitative XRD. Conversions from oxide to sulfide were determined via LECO for O and S contents ([a]), QXRD ([b]), or qualitative XRD ([c]).

Feedstock	Sulfidation Temperature	P_{S_2}	Conversion to sulfide	MO_X	MS_2	$M_{1-x}S_2$
ZrO_2	1475 °C	0.1 atm	>99.9 wt%	<0.1 wt%	11.4 wt%	88.6 wt%
WO_3	1000 °C	0.1 atm	>99.9 wt%	<0.1 wt%	>99.9 wt%	<0.1 wt%

Table 4.3: Products from the sulfidation of zirconium oxide (ZrO_2) and tungsten oxide (WO_3) using carbothermically driven sulfur reflux (CDSR). Data was analyzed using QXRD. M corresponds to a metallic element, here either zirconium (Zr) or tungsten (W), and x corresponds to a stoichiometric value.

Sulfidation products[1] of alkaline earth carbonates and sulfates are included in Table 4.4. While complete conversion of all of these feedstocks to sulfides is presumably achievable under optimal reaction conditions, these four chemistries were sulfidized under identical conditions as

a point of comparison. In the presence of CDSR at a temperature of 1000 °C, P_{S_2} of 0.1 atm, an Ar carrier gas flowrate of 400 sccm, and reaction time of 1 hour, $CaCO_3$ and $SrCO_3$ were sulfidized to calcium sulfide (CaS) and strontium sulfide (SrS) at conversions greater than 99.9%. Whether the presence of C during the reaction stabilized $CaCO_3$ and $SrCO_3$, or they decomposed to oxides or sulfates prior to sulfidation, remains unclear. Limited sulfidation of $MgCO_3$ was observed under these conditions, presumably due to sluggish reaction kinetics and insufficient thermal activation for appreciable magnesium sulfide (MgS) formation. This may be correlated with the higher melting point of magnesium oxide (MgO) versus calcium and strontium oxides (CaO and SrO respectively, Chapter 3, Section 3.2.1). Higher operating temperature or longer reaction time would likely be necessary to achieve complete sulfidation of $MgCO_3$ to MgS for the same gas flowrates and gas compositions. Thermal activation of sulfidation kinetics is further explored experimentally in Sections 4.2 and 4.3.1.

Feedstock	Sulfidation Temperature	P_{S_2}	Conversion to sulfide	MCO_3	MO	MSO_4	MS
$MgCO_3$	1000 °C	0.1 atm	<0.1 wt%	>99.9 wt%	<0.1 wt%	<0.1 wt%	<0.1 wt%
$CaCO_3$	1000 °C	0.1 atm	>99.9 wt%	<0.1 wt%	<0.1 wt%	<0.1 wt%	>99.9 wt%
$SrCO_3$	1000 °C	0.1 atm	>99.9 wt%	<0.1 wt%	<0.1 wt%	<0.1 wt%	>99.9 wt%
$BaSO_4$	1000 °C	0.1 atm	44.8 wt%	<0.1 wt%	<0.1 wt%	55.2 wt%	44.8 wt%

Table 4.4: Products from the sulfidation of magnesium, calcium, and strontium carbonates ($MgCO_3$, $CaCO_3$, and $SrCO_3$) and barium sulfate ($BaSO_4$) using carbothermically driven sulfur reflux (CDSR). Data was analyzed via QXRD. M corresponds to a metallic element, here either magnesium (Mg), calcium (Ca), strontium (Sr), or barium (Ba).

Nevertheless, a balance must be struck with regards to operating temperature; excessive temperatures lead to feedstock sintering and intragrain diffusion limitations to conversion. This was observed for $BaSO_4$ sulfidation, where conversion was limited at 1200 °C. Following sulfidation, sintered clumps of $BaSO_4$ on the order of 0.5mm to 1 mm in size were dispersed within the barium sulfide (BaS) product. Complete sulfidation of $BaSO_4$ can in principle be achieved by employing sulfate precursors with lower packing densities, operating at lower temperatures, or thoroughly mixing with a higher melting compound that inhibits sintering. When BaS was thoroughly mixed with La_2O_3 and sulfidized, conversion of the oxide/sulfate

was not limited by sintering. As illustrated in Table 4.5, conversion of mixed $BaSO_4$ and La_2O_3 to mixed sulfides exceeded 90% when sulfidized using CDSR at a temperature of 1100 °C for 2 hours at the kilogram scale[7].

The demonstrated ability to sulfidize a disparate collection of elements and compounds using S_2, which exhibit a wide range of $\left[P_{S_2}/P_{SO_2}\right]_{crit}$, confirms that sulfidation is a platform treatment applicable to elements across the periodic table. In the following section, a closer look is afforded to the reaction kinetics of REO sulfidation.

Element	$\boldsymbol{Ba}$	$\boldsymbol{La}$	$\boldsymbol{S}$	$\boldsymbol{O}$
Composition	48.1%	29.0%	19.0%	1.80%

Table 4.5: Composition of mixed barium sulfate ($\boldsymbol{BaSO_4}$) and lanthanum oxide ($\boldsymbol{La_2O_3}$) following sulfidation. Analysis was conducted via inductively-coupled plasma mass spectroscopy (ICP-MS) and LECO.

4.2 Oxide-Sulfide Anion Exchange Kinetics: Sulfidation of Lanthanum Oxide

To understand the effect of thermal activation on the rate of the oxide-sulfide anion exchange, the sulfidation kinetics of La_2O_3 were measured[1]. The following equations were proposed to describe the sulfidation reaction:

$$La_2O_3 + \frac{25}{12}S_2 = \frac{2}{3}La_3S_4 + \frac{3}{2}SO_2 \tag{4.1}$$

$$\frac{2}{3}La_3S_4 + \frac{1}{6}S_2 = La_2S_3 \tag{4.2}$$

In Section 4.1, La_3S_4 was observed as an intermediate sulfide product that occurred prior to the formation of La_2S_3. La_2O_2S was also observed as an intermediate. With this proposed mechanism, the reaction of La_3S_4 to La_2S_3 is indiscernible from the rates gas phase product generation due to the reality that no additional gasses containing O species would be liberated.

The reaction rates of La_2O_3 to La_2O_2S and La_2O_2S to La_3S_4 are likewise indistinguishable as the occur simultaneously within the packed bed reactor.

When CDSR is employed, interactions between SO_2 and C are described in Chapter 3, Section 3.2.1 by Equations 3.10 – 3.12 and are taken to be fast compared to sulfidation. The sulfidation reaction is taken to be zero order with regards to concentration of the solid, and the gasses are assumed to form an ideal gas mixture. Considering the density (ρ) of La_2O_3, the reaction rate (r') for La_3S_4 production is described on a La_2O_3 mass basis, where k is the intrinsic chemical reaction rate constant, η_k is a kinetic effectiveness factor between 0 and 1 that scales k as a function of intergrain, intragrain, and external mass transport limitations in the system, n_k is the reaction order in S_2, ϵ_p is the porosity of the pellet, R is the gas constant, and T is the absolute temperature:

$$r'_{La_3S_4} = \frac{4}{9}r'_{SO_2} + \frac{8}{9}r'_{CO} = \frac{18}{25}\frac{\eta_k k}{\rho_{La_2O_3}(1-\epsilon_p)}\left(\frac{P_{S_2}}{RT}\right)^{n_k}[=]\left(\frac{mol_{La_3S_4}}{kg_{La_2O_3}}\right)s^{-1} \quad (4.3)$$

In practice, $r'_{La_3S_4}$ is measured using the rate of oxygen liberation during sulfidation (r'_O), determined from the rates of SO_2 (r'_{SO_2}) and CO (r'_{CO}) generation:

$$r'_O = \frac{9}{2}r'_{La_3S_4} = \frac{81}{25}\frac{\eta_k k}{\rho_{La_2O_3}(1-\epsilon_p)}\left(\frac{P_{S_2}}{RT}\right)^{n_k}[=]\left(\frac{mol_O}{kg_{La_2O_3}}\right)s^{-1} \quad (4.4)$$

η_k may be determined by a variety of methods, such as using the Thiele modulus of heterogeneous catalysis[8] or Sohn's law of additive reaction times[9,10]. Mass transport limitations may also modulate the observed reaction order[11]. When external[vii], intergrain[viii], and intragrain[ix] mass transport limitations are negligible, η_k is equal to 1 and the observed reaction rate is equal

[vii] Ishida et al[66] and Sohn et al[10,67] showed that external mass transport limitations are negligible when a modified Sherwood number comparing the ratio of convective mass transport to effective diffusive mass transport in the bed is greater than 30.

[viii] Sohn and Szekely[67] illustrated that when a generalized fluid-solid reaction modulus relating the ratio of chemical reaction rate to pore diffusion rate is less than 0.1, the surface reaction is not limited by intergrain diffusion.

[ix] Sohn and Szekely[68] showed that intragrain mass transport limitations are negligible when a modified mass transport Biot number comparing ratio of the mass transfer resistance inside a grain within a porous solid versus on the surface of the grain is greater than 1.

to the intrinsic chemical rate. These conditions were met during experiments for the sulfidation of pure La_2O_3 (Section 4.1) and are reported by the author elsewhere[1]. Therefore, product gas flowrate data for SO_2 and CO were used to determine the rate constants of the sulfidation reaction and the reaction order with of S_2 at 1250 °C, 1300 °C, 1400 °C, and 1475 °C:

$$\ln r_O' = n_k \ln\left(\frac{P_{S_2}}{RT}\right) + \ln\left(\frac{81}{25}\frac{km_{La_2O_3}}{\rho_{La_2O_3}(1-\epsilon_p)}\right) \tag{4.5}$$

$m_{La_2O_3}$ is the initial mass of oxide. Experimental data[1] for La_2O_3 sulfidation are fitted to Equation 4.5 in Figure 4.1. The sulfidation reaction is observed to be approximately 1st order ($n_k \approx 1$) with respect to P_{S_2}[1]. Following, the Arrhenius equation was used to determine activation energy (E_A) from the rate constant, with the fit of the natural log of k versus inverse absolute temperature ($1/T$) shown in Figure 4.1. E_A was found to be 114 kJ/mole for the sulfidation of lanthanum oxide[1]. As discussed in Chapter 3, Section 3.2, differences in thermal activation likely contribute to differences in sulfidation rate for compounds at a given temperature. For compounds exhibiting large differences in melting points, this is an opportunity for selectivity in oxide-sulfide anion exchange.

As illustrated in Chapter 3, Figure 3.8, kinetic data may in turn be used to inform sulfidation behavior in a continuous process where the rate of sulfidation contributes to the ratio of P_{S_2} to P_{SO_2} present in the reactor ($\left[P_{S_2}/P_{SO_2}\right]_{rx}$). Controlling $\left[P_{S_2}/P_{SO_2}\right]_{rx}$ and leveraging differences in reaction rates offer an integrated thermodynamic and kinetic framework for selective oxide-sulfide anion exchange in mixed metal components. In the following sections, selective sulfidation and desulfidation are demonstrated for physically mixed compounds, industrial materials, and natural mineral concentrates.

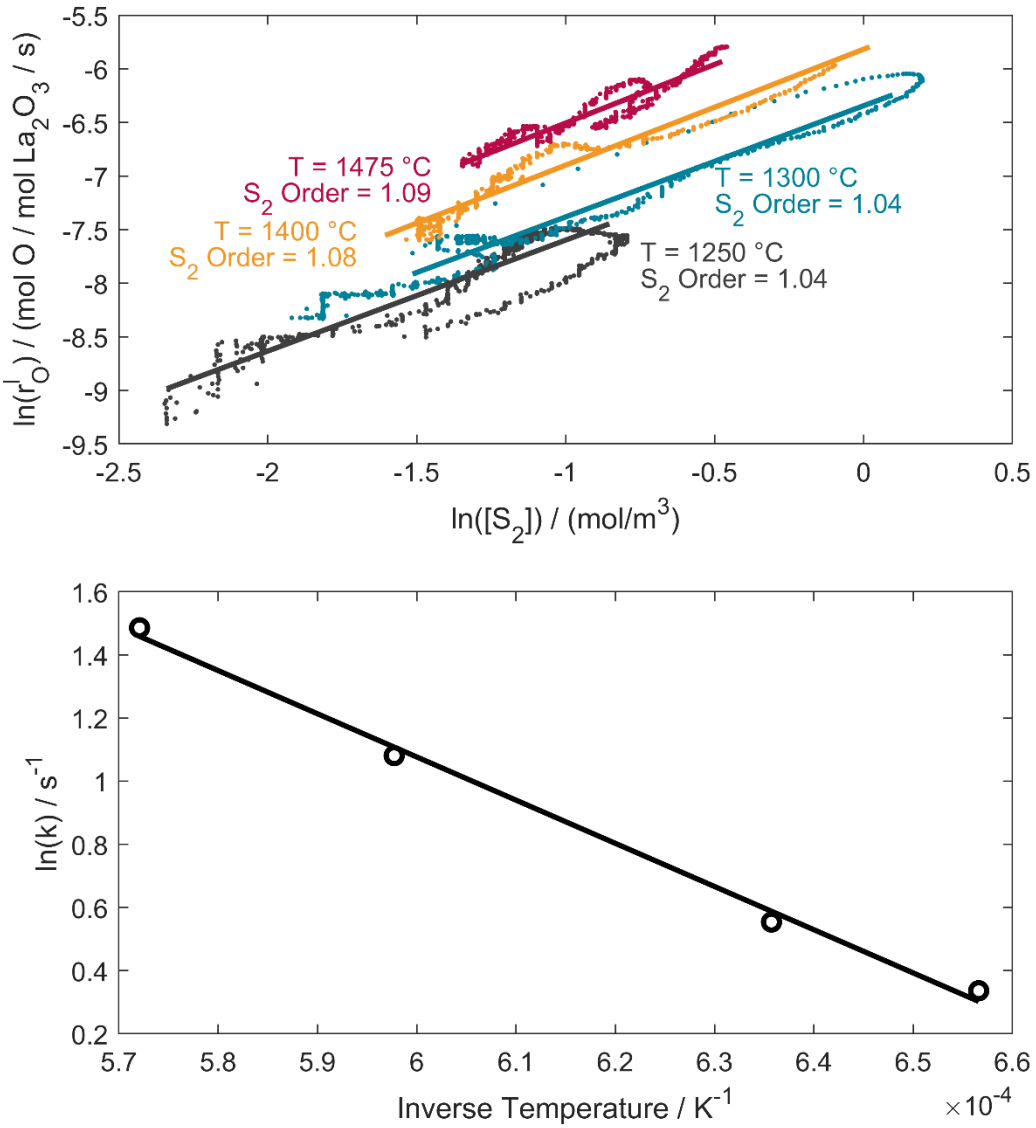

Figure 4.1: Measured sulfidation kinetics of lanthanum oxide (La_2O_3). The upper panel depicts measured sulfidation kinetics relating the rate of oxygen liberation (r_O') to S_2 concentration ($[S_2]$). The lower panel depicts an Arrhenius plot relating the rate constant (k) to the inverse of the reaction temperature ($1/T$).

4.3 Thermodynamic and Kinetic Control of Selectivity: Sulfidation and Desulfidation of Physically-mixed Compounds

In order to explore methods to control the selectivity of oxide-sulfide anion exchange, physically mixed compounds of rare earth and transition metals were sulfidized or desulfidized. In this section, three case studies are presented: selective sulfidation of iron sesquioxide (Fe_2O_3) and Sc_2O_3[12], selective desulfidation of iron sulfide (FeS) and La_2S_3[12], and selective sulfidation of neodymium oxide (Nd_2O_3), praseodymium oxide (Pr_6O_{11}), and dysprosium oxide (Dy_2O_3)[12]. The motivation for choosing these chemistries is multifold; together these systems exhibit a wide range of sulfidation behaviors and morphologies while also being relevant to a span of modern materials processing challenges. Results herein demonstrate that selective sulfidation and desulfidation enable the precipitation of insoluble product phases from mixed metal compound precursors.

4.3.1 Selective Sulfidation of Iron-Scandium Oxides

Sc-iron (Fe) separation remains a critical challenge in materials recovery from red mud tailings produced in the Bayer process for alumina production[13]. As discussed in Chapter 3, Section 3.3.1 and illustrated in Figure 3.5, Fe_2O_3 and Sc_2O_3 exhibit a wide gap in $\left[P_{S_2}/P_{SO_2}\right]_{crit}$ and are predicted to exhibit large differences in thermal activation of sulfidation reaction kinetics. This makes their mixed oxide a promising feedstock for selective oxide-sulfide anion exchange.

Sulfidation of equimolar, physically mixed Fe_2O_3 and Sc_2O_3 was conducted at 800 °C and 1000 °C for one hour under a P_{S_2}/P_{SO_2} ratio of 10 using methods reported in Chapter 3, Section 3.3 and detailed by the author elsewhere[12]. Upon sulfidation, largely insoluble oxide and sulfide phases were formed, illustrated via scanning electron microscope energy dispersive x-ray spectroscopy (SEM-EDS) element maps in Figure 4.2. Fe preferentially partitioned into the sulfide phase over Sc, confirming that oxide-sulfide anion exchange may be conducted

selectively. From Figures 3.3-3.6 in Chapter 3, formation of Sc_2O_2S was thermodynamically predicted to occur alongside FeS production, yet was not observed via QXRD as reported in Table 4.6 or via microscopy. The absence of oxysulfide phases is predominantly attributed to kinetic effects. Assuming Sc_2O_3 and La_2O_3 exhibit similar thermal activation for oxide-sulfide anion exchange (Section 4.2), at reaction temperatures below 1200 °C the sulfidation of Sc_2O_3 to Sc_2O_2S would be kinetically sluggish. At higher reaction temperatures, Sc_2O_2S was observed to form as a sulfidation intermediate (Section 4.1).

Sulfidation Temperature	FeO_x	Sc_2O_3	FeS	Sc_2O_2S	Amorphous
800 °C	<0.1 wt%	38 wt%	28 wt%	<0.1 wt%	33 wt%
1000 °C	<0.1 wt%	30 wt%	29 wt%	<0.1 wt%	42 wt%

Table 4.6: Sulfidation products from an equimass mixture of iron sesquioxide (Fe_2O_3) and scandium oxide (Sc_2O_3). Sulfidation was conducted at 800 °C and 1000 °C for 1 hour at a P_{S_2}/P_{SO_2} ratio of 10. Analysis was conducted via QXRD.

$Fe-Sc-O-S$ solution effects may also lead to deviations in the thermodynamically preferred scandium sulfidation pathway. Sc_2S_3 and FeS exhibit thermodynamically favorable mixing to form stable, high melting iron-scandium sulfide compounds[14]. Likewise, multiple iron-scandium oxide compounds have been observed[15,16], with iron-scandium oxide ($FeScO_3$) known to be show greater thermal stability than Fe-lanthanide (Ln) oxides of the same stoichiometry[15]. Oxide and sulfide mixing thermodynamics may in turn decrease the thermodynamic affinity of Sc for oxysulfide formation in the presence of Fe. In the Sc predominance diagram illustrated in Chapter 3, Figure 3.3, these solution effects could effectively lead to a compression of the oxysulfide phase domain, increasing $\left[P_{S_2}/P_{SO_2}\right]_{crit}$ for oxysulfide formation and decreasing $\left[P_{S_2}/P_{SO_2}\right]_{crit}$ for sulfide formation. The extent of this deviation from standard state thermodynamics remains qualitative in the absence of a solution model that accurately describes $Fe-Sc-O-S$ behaviors (Chapter 8, Section 8.2.1). Interactions between Fe and rare earth elements during oxide-sulfide anion exchange are further discussed in the following sections.

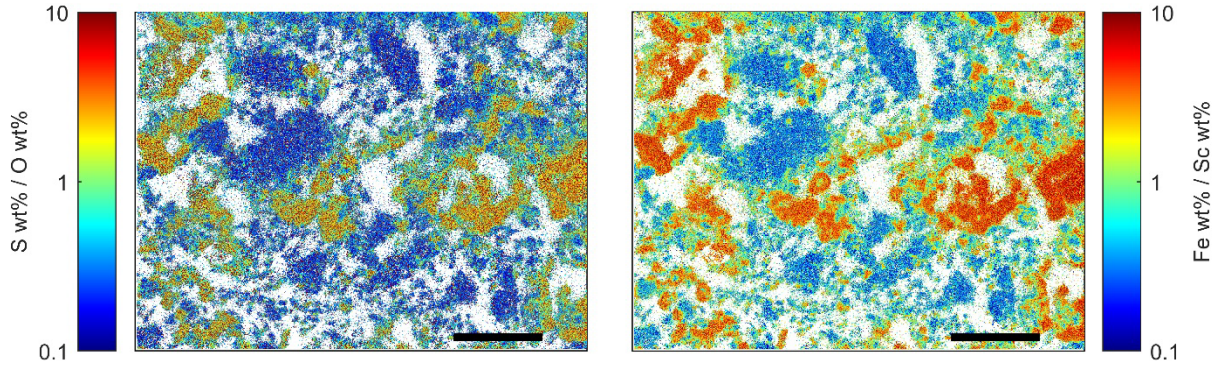

Figure 4.2: Spatial distribution of sulfur (S), oxygen (O), iron (Fe), and scandium (Sc) following selective sulfidation of mixed iron and scandium sesquioxides (Fe_2O_3 and Sc_2O_3) at 1000 °C. Element maps were quantified via SEM-EDS. Distinct oxide and sulfide phases are formed, with Fe preferentially partitioning to sulfide phases versus Sc. Sc_2O_2S formation, while thermodynamically predicted from pure state endmember data to occur under these conditions, was suppressed due to kinetic or solution effects. Scale bars correspond to 50 μm.

4.3.2 Selective Desulfidation of Iron-Lanthanum Sulfides

In Section 4.3.1, selective oxide-sulfide anion exchange was successfully demonstrated in the sulfidation of iron from mixed iron-scandium oxides. Interactions between the sulfides of Fe and rare earth elements are also of metallurgical relevance in both the desulfurization of steels[17] and the electrolytic production of copper (Cu) from mineral sources[7]. For direct electrowinning of Cu and Fe from molten chalcopyrite ($CuFeS_2$) and nickel (Ni), cobalt (Co), molybdenum (Mo), rhenium (Re), and silver (Ag) from other sulfide precursors, BaS and La_2S_3 have been successfully employed as supporting electrolytes[7,18–20]. However, $CuFeS_2$ mineral concentrates often contain O in the form of copper oxide (Cu_xO), copper sulfate (Cu_xSO_4), and residual gangue minerals[7]. From the sulfidation series illustrated in Chapter 3, Figures 3.4-3.5, BaS and La_2S_3 are prone to desulfidation when O or SO_2 are introduced to the electrolysis cell, potentially leading to degradation of the supporting electrolyte. Herein, oxide-sulfide anion exchange in Fe-Ln systems is further explored via selective desulfidation of La_2S_3 and FeS[12]. Sulfidation processes for removal of impurities from Cu ore and concentrate are discussed later in Chapter 5.

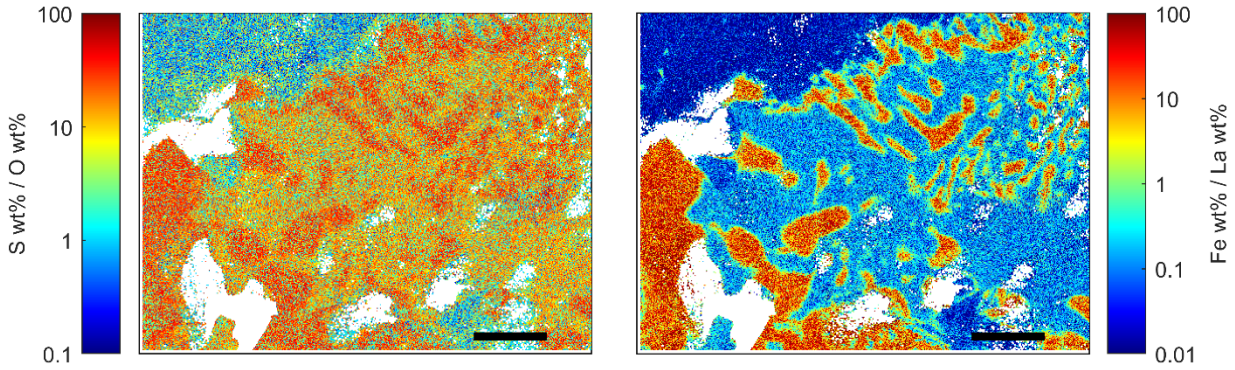

Figure 4.3: Spatial distribution of sulfur (S), oxygen (O), iron (Fe), and lanthanum (La) following selective desulfidation of mixed iron and lanthanum sulfides (FeS and La_2S_3) at 1000 °C. Element maps were quantified via SEM-EDS**.** Distinct oxysulfide and sulfide phases were formed, with lanthanum preferentially partitioning to the oxysulfide phases. Scale bars correspond to 20 μm.

Equal masses of La_2S_3 and FeS were mixed and then desulfidized at 1000 °C for 1 hour at a P_{S_2}/P_{SO_2} ratio between 0.1 to 10 following methods detailed in Chapter 3, Section 3.3 and by the author elsewhere[12]. During desulfidation under these conditions, a liquid sulfide phase was formed from which largely insoluble oxysulfides were selectively precipitated, illustrated in Figure 4.3. Two distinct S/O ratios in the oxysulfides were observed, most likely corresponding to La_2O_2S and a "higher" oxysulfide, $La_{10}OS_{14}$[12]. Fe remained as a sulfide; this is consistent with the calculated sulfidation series presented in Chapter 3, Figures 3.4-3.6 and confirms that oxide-sulfide anion exchange may be conducted selectively from mixed sulfide feedstocks.

Under similar reactor conditions, rare earth oxysulfide formation from Sc_2O_3 was kinetically limited (Section 4.3.1), yet rapidly proceeded from La_2S_3 here. Several explanations are proposed. Desulfidation of La_2S_3 was conducted at a higher homologous temperature than sulfidation of Sc_2O_3, potentially leading to faster reactions in accordance with the thermal activation of kinetic processes. Meanwhile, desulfidation of a sulfide with SO_2 may follow a more rapid reaction mechanism than sulfidation of an oxide with S_2. Oxide-sulfide anion exchange chemistries may also accentuate chemical differences between rare earth elements, contributing to variations in reaction rates. Distinctions in the oxide-sulfide anion exchange

behaviors of rare earth elements are explored in the following section, where selective sulfidation is applied to mixtures of REOs.

4.3.3 Selective Sulfidation of Neodymium-Praseodymium-Dysprosium Oxides

In the previous two sections, oxide-sulfide anion exchange was conducted selectively between iron and rare earth compounds. In both cases, $\left[P_{S_2}/P_{SO_2}\right]_{crit}$ were achieved by controlling the rate of S_2 and SO_2 introduction into the gas phase of the reactor. As illustrated in Chapter 3, Figure 3.8, as $\left[P_{S_2}/P_{SO_2}\right]_{crit}$ increases for target elements, faster gas flowrates or CDSR are required to achieve oxide-sulfide anion exchange. Increasing C content is predicted to increase the minimum gas flowrate in the reactor required to enable thermodynamic spontaneity in oxide sulfidation. A sharp inflection in flowrate occurs at C/O ratio of unity, corresponding to stoichiometric CO formation via CDSR. Herein, the role of CDSR in controlling sulfidation selectivity for REOs is explored by sulfidizing mixtures of Nd_2O_3, Pr_6O_{11}, and Dy_2O_3 with varying levels of C addition[12]. REOs are chosen due to their high $\left[P_{S_2}/P_{SO_2}\right]_{crit}$ for sulfide formation and the tedious nature of their hydrometallurgical separation[1].

To test the sulfidation behavior of mixed rare earth oxides, equal moles of Nd_2O_3, Pr_6O_{11}, and Dy_2O_3 were mixed with varying amounts of graphite powder which served as a C source[12]. C/REO mole ratios of 0, 1.25, 2.5, 3.75, and 6 were utilized. The mixtures were then separately sulfidized at 1400 °C for 50 minutes using methods described in Chapter 3, Section 3.3 and herein[12]. The extents of oxide-sulfide anion exchange and carbon conversion to CO as a function of reaction time, carbon content, and P_{S_2} are illustrated in Figure 4.4.

With increasing C/REO ratios, the extent of oxide-sulfide anion exchange generally increased, confirming the role of CDSR in increasing the ratio of $\left[P_{S_2}/P_{SO_2}\right]_{rx}$[12]. However, the conversion of oxide to sulfide at C/REO ratio of 1.25 was consistently lower than for carbon-free sulfidation. Further research into the thermodynamic and kinetic interactions of $Ln-O-S-C$ species is likely necessary to explain this trend (Chapter 8, Section 8.2.1). Meanwhile, the conversion of C to CO was observed to fall in the range of 30% to 35% for all C/REO ratios[12]. The consistent rates for conversion of C to CO during CDSR is likely due to buffering of the C activity in the system, yet improved understanding of $Ln-O-S-C$ interactions is necessary

to elucidate this trend. Carbon dioxide (CO_2) was not detected at appreciable amounts in the system due to the Boudouard equilibrium (Chapter 3, Eq. 3.12) favoring CO versus CO_2 at these temperatures.

Sulfidized crystalline products are reported as a function of C addition in Table 4.7 as identified via QXRD[12]. With increasing C content, oxysulfide products gave way to sulfide products. The first species to form a sulfide was Nd, consistent with the sulfidation series in Chapter 3, Figures 3.4 and 3.5. However, atomic substitutions between rare earth elements in the crystalline sulfide are likely to occur due to the similar electronic structure and size of Ln elements. Microscopy may provide further insight into the spatial distribution of elements and purity of rare earth product phases, conducted later in Section 4.4.1 for calcined rare earth magnets.

Phase	$C/\mathbf{REO} = 0$	$C/\mathbf{REO} = 1.25$	$C/\mathbf{REO} = 2.5$	$C/\mathbf{REO} = 3.75$	$C/\mathbf{REO} = 6$
Pr_2O_3	<1 wt%	1 wt%	<1 wt%	<1 wt%	<1 wt%
Nd_2O_2S	17 wt%	12 wt%	<1 wt%	<1 wt%	<1 wt%
Dy_2O_2S	27 wt%	28 wt%	12 wt%	<1 wt%	<1 wt%
Pr_2O_2S	3 wt%	1 wt%	<1 wt%	<1 wt%	<1 wt%
$Nd_{10}OS_{14}$	<1 wt%	<1 wt%	25 wt%	<1 wt%	<1 wt%
Nd_3S_4	<1 wt%	<1 wt%	<1 wt%	9 wt%	<1 wt%
Nd_2S_3	<1 wt%	<1 wt%	<1 wt%	16 wt%	16 wt%
NdS_2	<1 wt%	<1 wt%	<1 wt%	<1 wt%	1 wt%
Amorphous	53 wt%	58 wt%	63 wt%	75 wt%	83 wt%

Table 4.7: Product phases from mixed rare earth oxides (REOs) following sulfidation with different levels of carbon (C) addition. Sulfidation was conducted at 1400 °C with product phases analyzed via QXRD.

Higher lanthanide oxysulfide ($Ln_{10}OS_{14}$), intermediate sulfide (Ln_3S_4), and disulfide (LnS_2) phases that were identified via QXRD for rare earth elements were excluded from the predominance diagram in Chapter 3, Figure 3.3 and the sulfidation series in Chapter 3, Figures 3.4-3.6 due to the absence of relevant thermodynamic data. Inclusion of these phases would likely shift the enthalpic and entropic affinities for oxide-sulfide anion exchange following trends for oxysulfide behavior as discussed in Chapter 3, Section 3.1.3. Therefore, the $\left[P_{S_2}/P_{SO_2}\right]_{crit}$ for $Ln_{10}OS_{14}$ formation from Ln_2O_2S is presumably lower than $\left[P_{S_2}/P_{SO_2}\right]_{crit}$ for direct

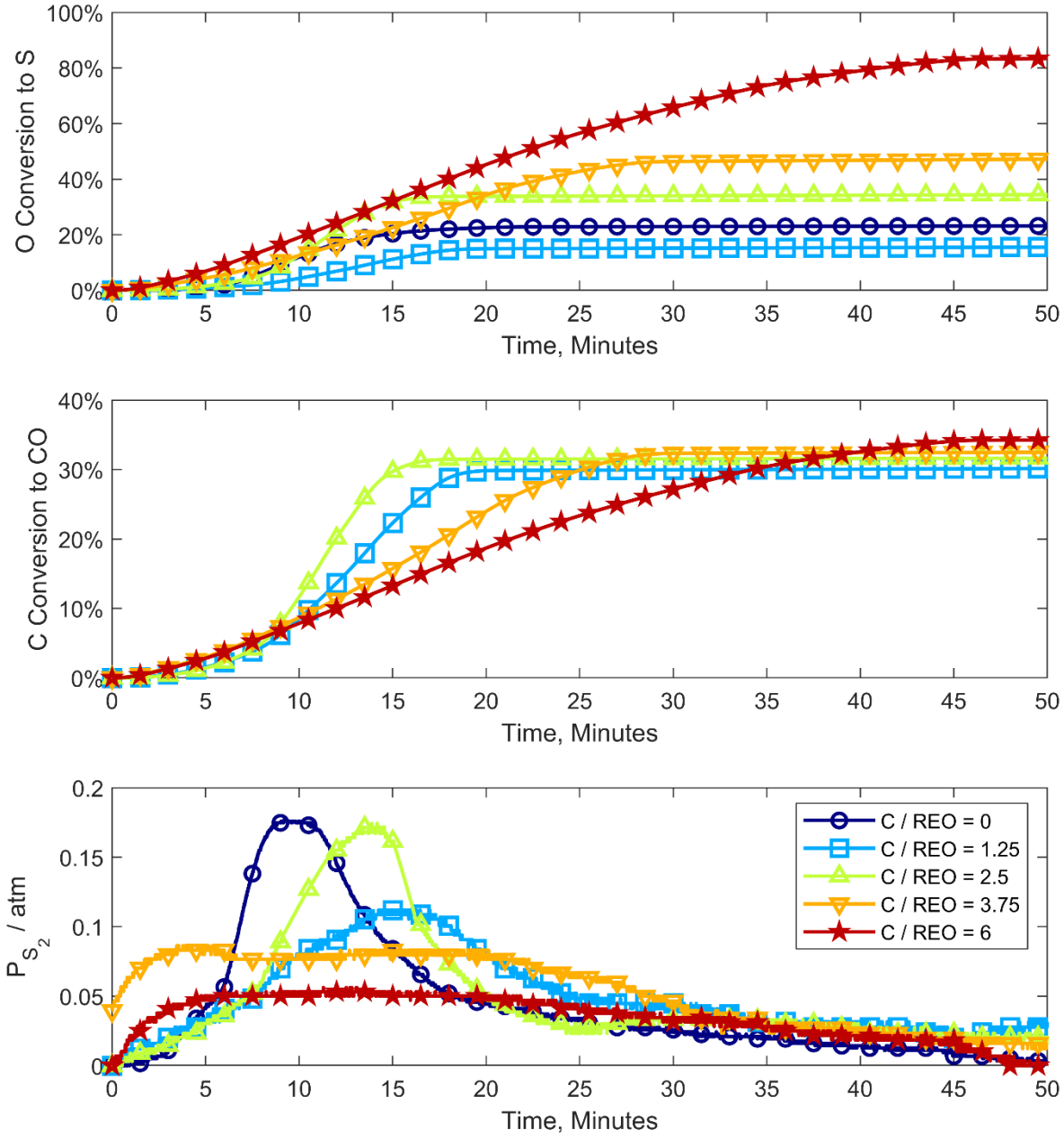

Figure 4.4: Conversion of oxide to sulfide and carbon (C) to carbon monoxide (CO) during sulfidation of mixed rare earth oxides (REOs). Increasing the C/REO ratio in the feed leads to higher conversion of oxides to sulfide, demonstrating the role of CDSR in increasing the $\left[P_{S_2}/P_{SO_2}\right]_{rx}$ ratio.

formation of the Ln_2S_3 from Ln_2O_2S. Likewise, $\left[P_{S_2}/P_{SO_2}\right]_{crit}$ for formation of Ln_2S_3 from $Ln_{10}OS_{14}$ would be higher than for formation from Ln_2O_2S.

In general, the lack of solution models for many mixed oxides and sulfides hinders the direct extrapolation of mechanically-mixed oxide sulfidation behavior to real mineral and industrial feedstocks that contain chemically-mixed metal compounds and solid solutions. In the following section, the oxide-sulfide anion exchange behaviors of some real industrial precursors and products are explored. Sulfidations of these chemically-mixed feedstocks provide insight into deviations in sulfidation affinity and selectivity arising from thermodynamic solution effects. Siderophilic interactions and the acid-base chemistry of oxides provide insight into the partitioning of trace elements during oxide-sulfide anion exchange.

4.4 Solution Interactions for Control of Selectivity: Sulfidation and Desulfidation of Chemically-mixed Compounds

In the previous sections, the oxide-sulfide anion exchange behaviors of pure and mechanically mixed compounds were explored. Sulfidation and desulfidation trials were conducted on a range of feedstocks of varying sulfidation affinity, confirming thermodynamic and kinetic controls of selectivity reported in Chapter 3. However, mixed oxide feedstocks provided limited insight into how the solution effects present in real industrial feedstocks and products influence oxide-sulfide anion exchange. Herein, selective sulfidation is conducted on calcined rare earth magnets[1,21], complex nickeliferous laterite ore[22], and Cu smelter slag. These case studies provide insight into the role of solution effects in modulating sulfidation affinity and selectivity. The roles of siderophilicity and acid-base interactions are afforded particular attention.

4.4.1 Selective Sulfidation of Iron-Neodymium-Boron Magnets

Neodymium (Nd), praseodymium (Pr), and dysprosium (Dy) are the three main rare earth constituents employed in iron-neodymium-boron (FeNdB) magnets[23]. Substitution of up to 10 wt% of the Nd with Dy increases the coercivity and high temperature performance of the magnets[24,25]; terbium (Tb) may also be utilized in a similar role[24]. The main metal feedstocks for magnet production are didymium (Di, an alloy of Nd and Pr), ferrodysprosium (FeDy), ferroboron (FeB), and ultralow C, low alloy steel (AISI 1001 alloy or electrolytic Fe)[23]. In recycling end of life magnets, other impurities such as Cu, Ni, and chromium (Cr) must be separated from rare earth elements. Some Fe separation may also be conducted, as the Di, FeDy, and FeB utilized in magnet manufacture generally contain less Fe than the final magnet composition due to the addition of low alloy steel during manufacturing. The relative amounts of light versus heavy rare earth elements varies in different grades of magnet; therefore grade-agnostic recycling processes should target separation of Nd and Pr from heavy rare earth elements such as Dy.

Recycling of FeNdB magnets is a promising pathway to confront critical material supply uncertainty by redistributing the geography of Ln production, while a selective recovery facilitated by sulfidation could address the unbalanced supply and demand of different Ln, often termed the rare earth balance problem[26]. Many pyrometallurgical[27], hydrometallurgical[28,29], hydrogen decrepitation[30,31], and liquid metal[32] processes have been explored for Ln recovery from FeNdB magnets. Subsequent Ln separations typically follow the conventional hydrometallurgical separation pathway used in primary extraction[33].

Ni-plated FeNdB magnets were heated under air at 500 °C to demagnetize, crushed to a particle size of 90-212 μm, then calcined under air at 1000 °C for 5 hours in a boron nitride (BN) crucible[1,21]. The brittle FeNdB magnet was separated from the ductile Ni coating during comminution. The calcined magnet material was reground to a particle size of 90-212 μm, then sulfidized without CDSR at 1200 °C under a P_{S_2} of 0.1 atm and a P_{S_2}/P_{SO_2} ratio of 10 for one hour using methods described in Chapter 3, Section 3.3 and detailed by the author elsewhere[1,21].

As shown in Figure 4.5, two main product phases with grain sizes of 20-100 microns in size were observed following sulfidation: a Nd-rich oxide and an Fe-rich sulfide, corresponding to light and dark phases respectively[1,21]. The average bulk compositions of the oxide and sulfide

phase were observed to be $Nd_{18.70}Pr_{4.26}Dy_{<0.01}Fe_{0.16}B_{10.35}O_{66.47}S_{0.06}$ and $Nd_{0.13}Pr_{0.02}Dy_{0.04}Fe_{45.55}B_{<0.01}O_{1.29}S_{52.96}$ via electron probe micro analysis wavelength-dispersion x-ray spectroscopy (EMPA-WDS)[1]. The spatial distributions of major elements between phases were determined via SEM-EDS mapping calibrated with EPMA-WDS composition data. Under these conditions, Pr and B were observed to partition mainly to the oxide phase with Nd, consistent with the pure state sulfidation series shown in Chapter 3, Figure 3.4. However, Dy was shown to preferentially partition to the sulfide phase. This is a notable deviation from the pure state sulfidation series, in which Dy is expected to remain an oxide with Nd and Pr. Furthermore, the pure state sulfidation series and experimental results on mixed Nd_2O_3, Pr_6O_{11}, and Dy_2O_3 (Section 4.3.3) indicate that Nd_2O_3 is predicted to have a higher affinity toward sulfidation than Dy_2O_3. Little to no rare earth oxysulfide formation was observed, illustrating that despite presumably sluggish REO sulfidation kinetics (Sections 4.3, 4.3.1), solution effects were strong enough to thermodynamically drive the selective sulfidation of rare earth elements. The corresponding separation factor (β_{sep}, Chapter 2, Eqn. 2.1) for Nd and Dy between the oxide and sulfide phases was observed to be 711, a 100x improvement to Ln-Ln separation over emerging[34] or state of the art[35] hydrometallurgical processing. These results indicate that the combination of $Ln - Fe - B - O - S$ interactions in the system selectively modulate the solution behavior of individual rare earth elements. In turn, a chemical pathway for highly selective sulfidation of Dy from Nd and Pr is unlocked[1].

Insight into $Ln - Fe - B - O - S$ interactions may be discerned from other material systems. Chondrite meteor data suggest that solution effects may shift the chalcophilic, lithophilic, or siderophilic affinities of different rare earth elements (Chapter 2, Section 2.1). Concurrently, the chalcophilic nature of Fe could provide a driving force for both Fe and Dy to sulfidize selectively from Nd, Pr, and B. At the same time, borate compounds have been shown to exhibit varying affinities for different rare earth elements, in particular between Nd and Dy[36]. Together, these solution interactions modulate the relative affinities of the rare earth elements for oxide-sulfide anion exchange.

Dedicated "collector phases" may be present within or introduced into a feedstock that leverage solution effects to increase the selectivity of pyrometallurgical oxide-sulfide anion exchange beyond that predicted from pure state reaction thermodynamics. Like Fe for Dy, these collector phases may also serve as chemical receptacles for oxide-sulfide reaction products[2].

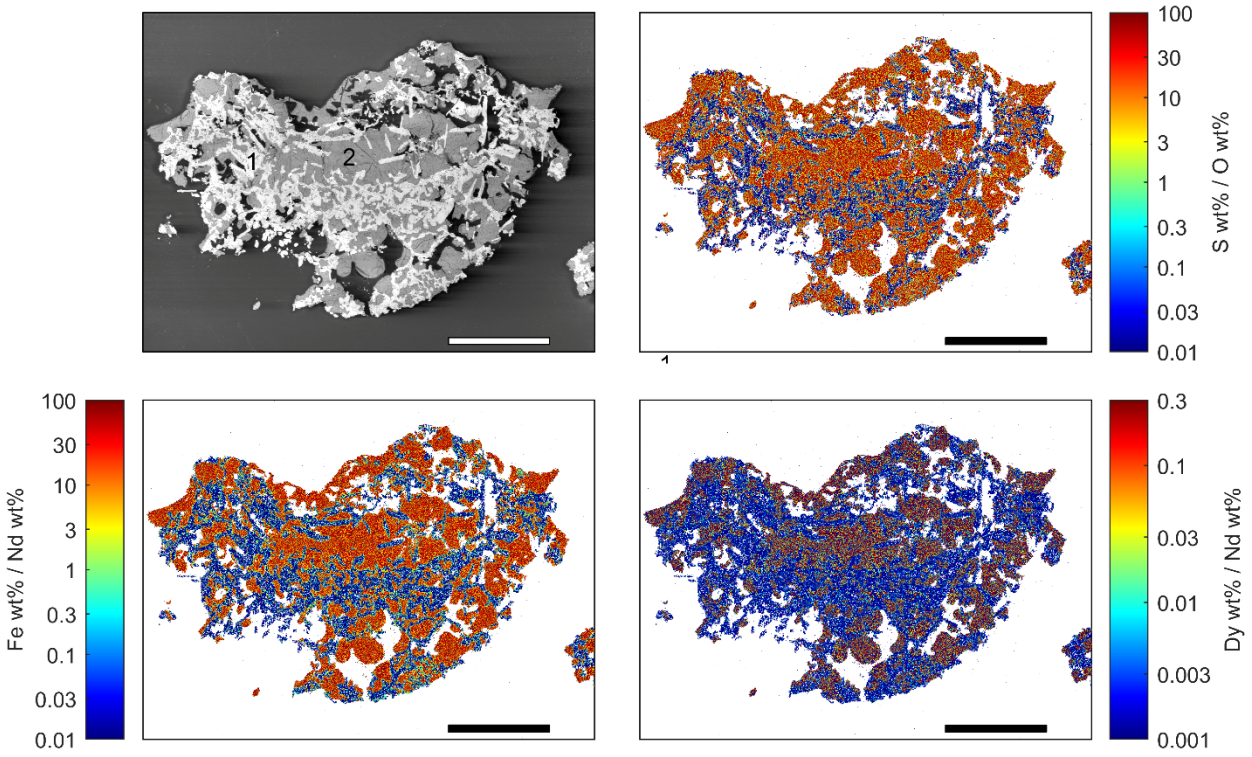

Figure 4.5: Spatial distribution of elements in a sulfidized, calcined iron-neodymium-boron (FeNdB) magnet. Maps were constructed using SEM-EDS spatial distribution of elements calibrated with EPMA-WDS data. FeNdB magnet was demagnetized at 500°C, ground to 90-212 μm, calcined at 1000°C, and sulfidized for one hour at 1200°C. Major sulfidation products are neodymium-rich oxide (1, $Nd_{18.70}Pr_{4.26}Dy_{<0.01}Fe_{0.16}B_{10.35}O_{66.47}S_{0.06}$) and iron-rich sulfide (2, $Nd_{0.13}Pr_{0.02}Dy_{0.04}Fe_{45.55}B_{<0.01}O_{1.29}S_{52.96}$) phases approximately 20-100 μm in size. Scale bars correspond to 300 μm.

Furthermore, solution effects may be utilized to reorder pure state oxide-sulfide anion exchange affinities to target a particular element for selective sulfidation or desulfidation. Fe provides a first point of comparison due to known trends in siderophilicity, however in principle any additive that modulates sulfidation affinity could be utilized. In the following sections, the role of acid-base chemistry in controlling oxide-sulfide anion exchange affinity is explored.

4.4.2 Selective Sulfidation of Complex Nickeliferous Laterite Ore

Ni is crucial for a wide range of applications spanning from super alloys to lithium-ion battery (LIB) cathodes[37]. Ni is predominantly mined from sulfide and laterite deposits, with the latter accounting for approximately 72% of global production[38]. While secondary sources of Ni such as LIB cathode recycling remain important[39], the majority of demand growth is expected to be met by further development of laterite resources[38].

Ni laterite may be divided into three main fractions within a given deposit[40]. Each deposit and fraction exhibit unique chemistry and processing challenges[41]. Heavily weathered Fe-rich limonite generally constitutes the uppermost layer, where Ni and Fe are usually present at grades of 0.8 wt% to 1.5 wt% and 40 wt% to 50 wt% respectively[37]. Deeper in the deposit where less weathering has occurred, Ni and Fe are present in hydrated and magnesium silicate deposits at grades of 1.5 wt% to 4 wt% and 10 wt% to 25 wt% respectively[37]. These regions are termed saprolite. Limonite and saprolite layers are often separated by a layer of smectite clay which exhibits intermediate Fe and Ni levels[40,41]. Some blending of phases between the layers is common[40]. Due to differences in Fe and gangue contents, Ni is conventionally extracted from limonite and saprolite via separate pathways[37].

Sulfidation chemistry is a promising avenue for sustainable and economical extraction of Ni from complex laterite feedstocks. Industrially, sulfidation of reduction roasted saprolite has been practiced at the PT Inco facility since the late 1970's[42], albeit with limited sulfidation selectivity. More recently, Harris et al demonstrated the selective sulfidation of limonite to produce a Ni-rich sulfide concentrate with promising results, yet processing challenges remained[43,44]. Sulfidation was conducted by heating a mixed briquette of S and laterite, potentially hindering control of sulfidation kinetics and mass transport. Operating temperatures below 950 °C produced sub-micron sulfide phases that were not amenable to liberation and separation. At temperatures above 950 °C sulfide particles on the order of 1-10 microns were able to be liberated, but proved challenging to separate via flotation.

An integrated thermodynamic and kinetic framework may be leveraged to improve sulfidation performance[1]. The use of gaseous elemental S enables better control of sulfidation kinetics, mass transport, and nucleation/growth versus condensed or briquetted sources (Chapter 3, Sections 3.1-3.2). Meanwhile, conducting sulfidation at higher temperatures may enable the

formation of immiscible liquid matte and slag products, improving separation and recovery and eliminating the burden of subsequent fine grinding[22].

A nickeliferous lateritic ore from Indonesia was employed as a precursor for sulfidation. Sampling was conducted using the cone and quarter method. Prior to sulfidation, the ore was ground using a mortar and pestle to pass through a 212 micron sieve. The average composition of the nickeliferous laterite[22] is reported in Table 4.8, with the SEM-EDS spatial distributions of some metallic elements illustrated in Figure 4.6. Oxides and hydroxides of Fe were observed to be the most prevalent species, corresponding to a significant limonite fraction in the laterite. Mixed oxides of silicon (Si), aluminum (Al), and Mg were also present, signifying the presence of smectite and saprolite fractions. In Fe-rich phases, Ni is contained at a grade of about 1 wt%. In silica (SiO_2)-rich, magnesia (MgO)-poor phases, Ni content was observed to be lower at approximately 0.3 wt%. In mixed SiO_2 and MgO phases, Ni content was higher at about 3 wt%. Occasional manganese (Mn)-rich phases were found, which exhibited elevated levels of Ni at around 10 wt%.

Component	Laterite Feedstock	Sulfidized Laterite Major Product Phases			
		Fe-rich sulfide	Al-rich oxide (Phase 1)	Fe-rich oxide (Phase 2)	Si-rich oxide (Phase 3)
Ni	1.1 wt% (+/- <0.1)	1.8 wt% (+/- 0.2)	0.4 wt% (+/- 0.1)	0.2 wt% (+/- 0.1)	0.1 wt% (+/- <0.1)
Fe	37.0 wt% (+/- 2.0)	54.3 wt% (+/- 1.4)	15.1 wt% (+/- 1.5)	21.7 wt% (+/- 0.7)	8.0 wt% (+/- 0.7)
Si	12.4 wt% (+/- 1.7)	1.9 wt% (+/- 0.3)	4.2 wt% (+/- 1.2)	4.4 wt% (+/- 0.2)	44.9 wt% (+/- 1.2)
Al	6.5 wt% (+/- 0.9)	1.0 wt% (+/- 0.1)	23.9 wt% (+/- 2.4)	7.3 wt% (+/- 0.5)	1.9 wt% (+/- 0.3)
Mg	2.5 wt% (+-/ 0.4)	0.5 wt% (+/- <0.1)	9.5 wt% (+/- 0.8)	4.1 wt% (+/- 0.6)	0.6 wt% (+/- 0.1)
Cr	1.6 wt% (+/- 0.4)	1.2 wt% (+/- 0.1)	10.0 wt% (+/- 2.9)	29.3 wt% (+/- 0.9)	0.9 wt% (+/- 0.3)
O	35.0 wt% (+/-1.7)	2.4 wt% (+/- 0.7)	33.6 wt% (+/- 1.3)	29.9 wt% (+/- 0.9)	40.7 wt% (+/- 0.9)
S	2.5 wt% (+/- 0.2)	36.8 wt% (+/- 0.2)	3.2 wt% (+/- 0.6)	2.8 wt% (+/- 0.2)	2.7 wt% (+/- 0.3)
Other	0.13 wt% (+/- 0.5)	0.2 wt% (+/- 0.1)	0.2 wt% (+/- 0.1)	0.3 wt% (+/- 0.2)	0.1 wt% (+/- <0.1)

Table 4.8: Average bulk composition of laterite ore before and after sulfidation. Compositions were determined via SEM-EDS. Standard deviations are reported in parenthesis. Phases 1, 2, and 3 correspond to the phases plotted in Figure 4.9.

The nickeliferous laterite was sulfidized in the absence of CDSR at a temperature of 1300 °C and pressure of 1 atm for 1 hour using procedures and equipment described in Chapter 3, Section 3.3 and reported by the author elsehwere[22]. Elemental S was employed as the sulfidizing agent at a P_{S_2} of 0.5 to 0.7 atm in an Ar carrier gas with a flowrate of 500 sccm. Sulfidation resulted in the formation of immiscible liquid sulfide matte and oxide slag phases that coalesced to 100 μm to 5 mm in size[22]. S/O ratios, metallic element weight fractions, and calculated optical basicities of oxide phases[x] are mapped in Figure 4.7. Four major phases were observed: an Fe-rich sulfide matte phase, and SiO_2-rich, Al_2O_3-rich, and Fe-rich oxide phases in the slag. Some matte droplets were entrained in the slag phase and vice versa[22], illustrated in Figure 4.8. This indicates that the time required for coalescence of the liquid phases exceeded that of sulfidation. Operating parameters such as temperature may be optimized to favorably modify viscosity for matte and slag coalescence.

Compositions and phase fractions of products following sulfidation[22] are reported in Table 4.8. Overall, Ni partitioned to the sulfide matte phase at a conversion of 89% for a grade of 1.8 wt%. Fe partitioned to the sulfide phase at a conversion of 83% for a grade of 54 wt%. Limonite phases fully reacted, with Ni and some Fe entering the sulfide matte phase. The remaining Fe from limonite entered the slag oxide phases. Within the slag oxide product, SiO_2-rich phases retained lower concentrations of Ni than MgO-rich and Fe-rich phases. In geochemistry, the Ni levels in mafic minerals are similarly correlated with the presence of Mg and divalent Fe; however, the shared or competing roles of divalent Fe and Mg in driving Ni partitioning have been debated[45–48]. Herein, the level of residual Ni in oxide product phases may be considered using the acid-base chemistry of oxide species, represented using calculated theoretical optical basicities (Λ).

From Figure 4.7, higher Mg/Si ratios are observed to correspond to regions of higher calculated Λ. Mean Ni compositions and S/O ratios in oxide product phases in Table 4.8 are plotted versus calculated Λ at those compositions in Figure 4.9. For sulfidized Ni laterite, the S

[x] The Λ of mixed metal oxide phases were calculated from endmember data using the methodology demonstrated by Sosinsky and Sommerville[49]. Where available, endmember calculated Λ reported by Nakamura et al[69] were employed. These values were supplemented with Λ calculated from the Pauling electronegativity (χ)[49], derived from the heat of formation of the endmember compound[70,71]. The respective contributions from Fe^{2+}/Fe^{3+} and Cr^{3+}/Cr^{6+} species were considered using redox equilibria reported by Duffy[72].

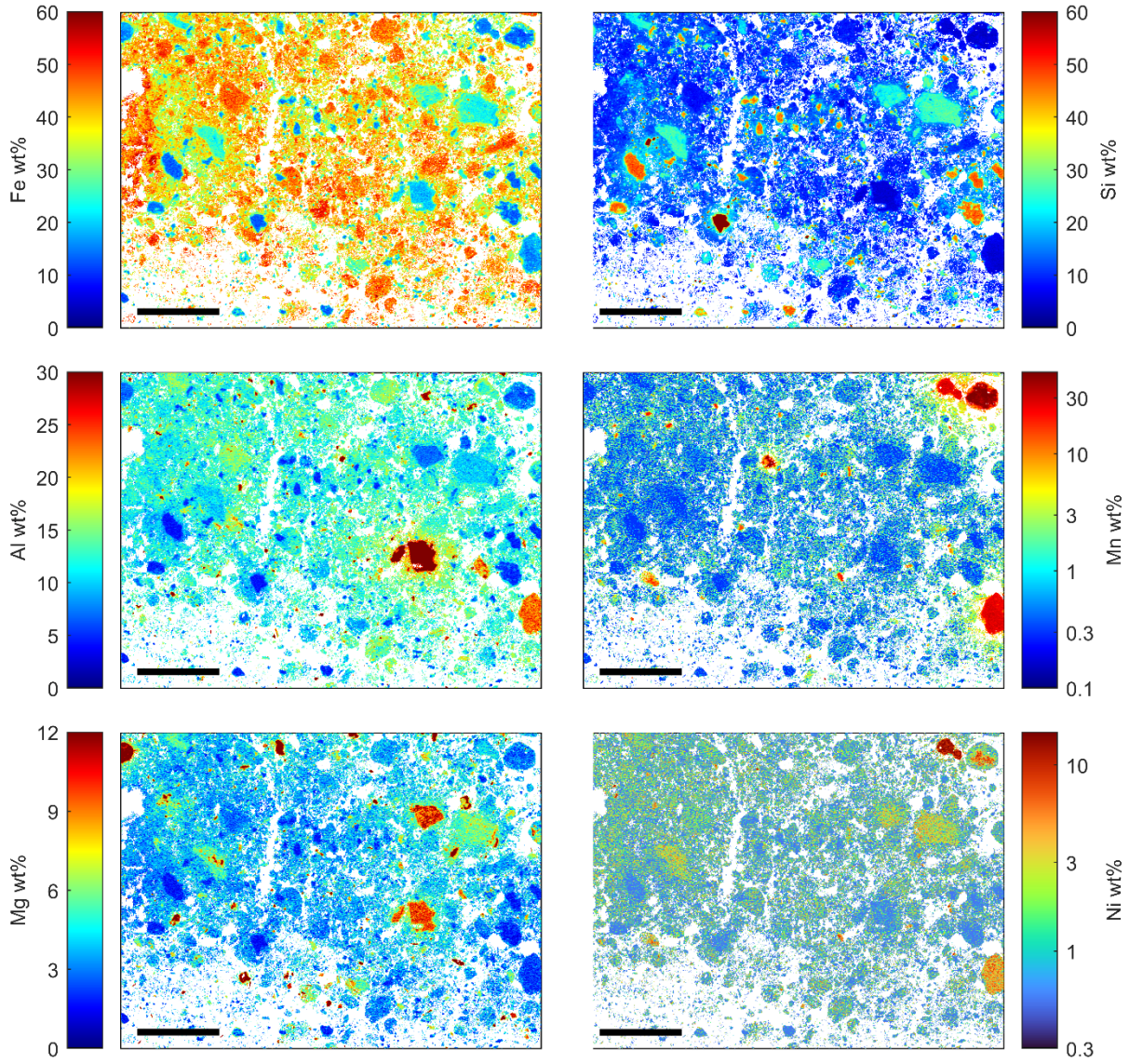

Figure 4.6: Spatial distributions of some elements in laterite ore. Element maps were quantified via SEM-EDS. Scale bars correspond to 500 μm.

contents of oxide product phases were observed to increase with increasing Λ, consistent with known trends in the sulfide capacities of slags[49]. Residual Ni concurrently solubilized at greater levels in the phases that exhibited larger affinities toward S. Therefore, the solubilized Ni contents of oxide phases were found to be directly correlated with increasing Λ and solubility of

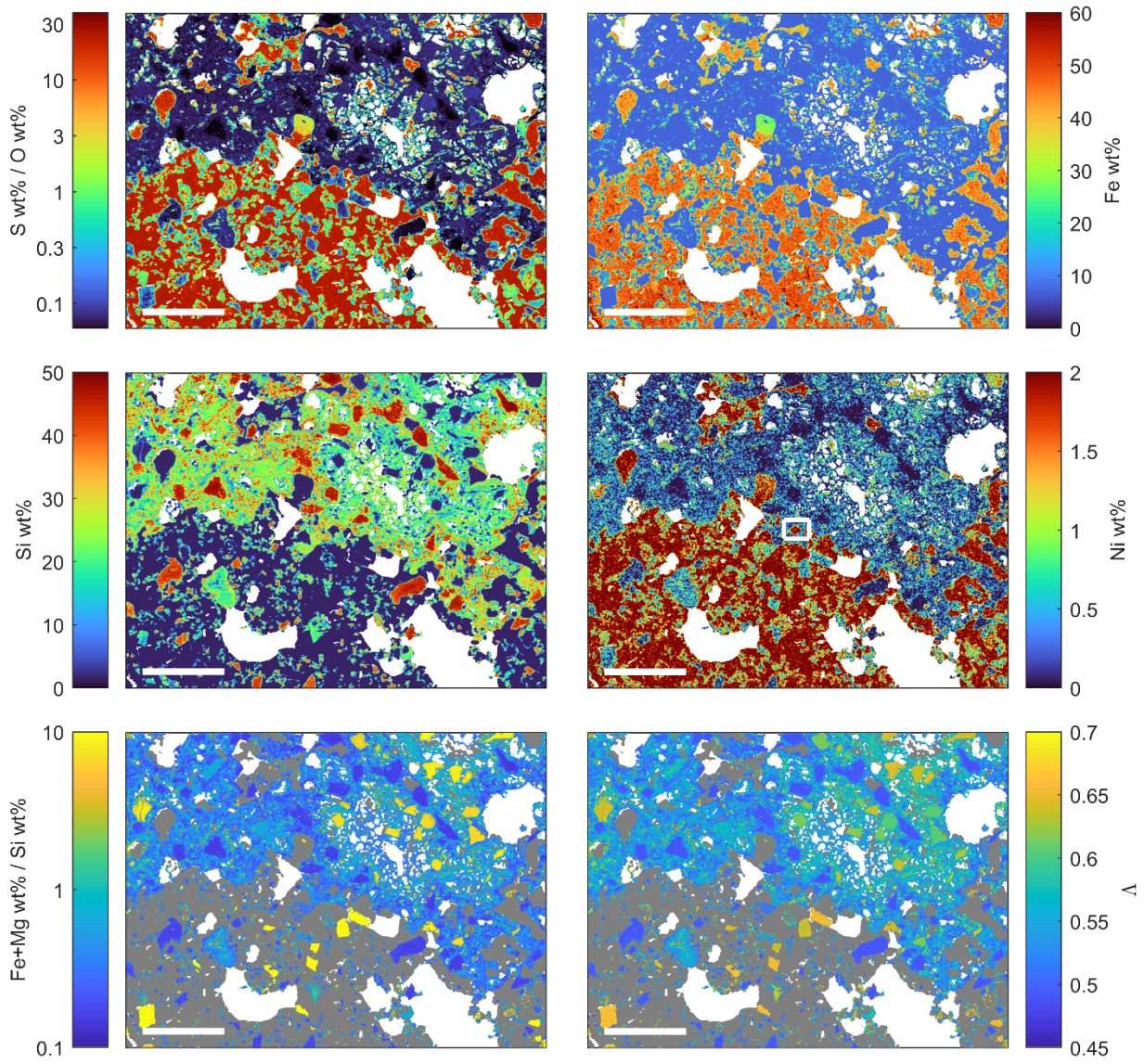

Figure 4.7: Spatial distribution of key elements and calculated optical basicities (Λ) for slag phases following selective sulfidation of laterite ore. Sulfidation was conducted at 1300 °C. Element distributions were quantified via SEM-EDS. For panels detailing mass ratios of slag forming elements and optical basicity, matte phases are denoted in gray. Nickel (Ni) and iron (Fe) are shown to preferentially partition to matte phases versus silicon, magnesium (Mg), and aluminum (Al). Within slag phases, basic oxide phases with higher Fe and Mg contents and lower silicon (Si) contents generally exhibit higher sulfur (S) contents and retain higher fractions of Ni. The boxed region in the Ni panel is shown in Figure 4-8, illustrating matte entrainment in the slag. Scale bars correspond to 500 µm.

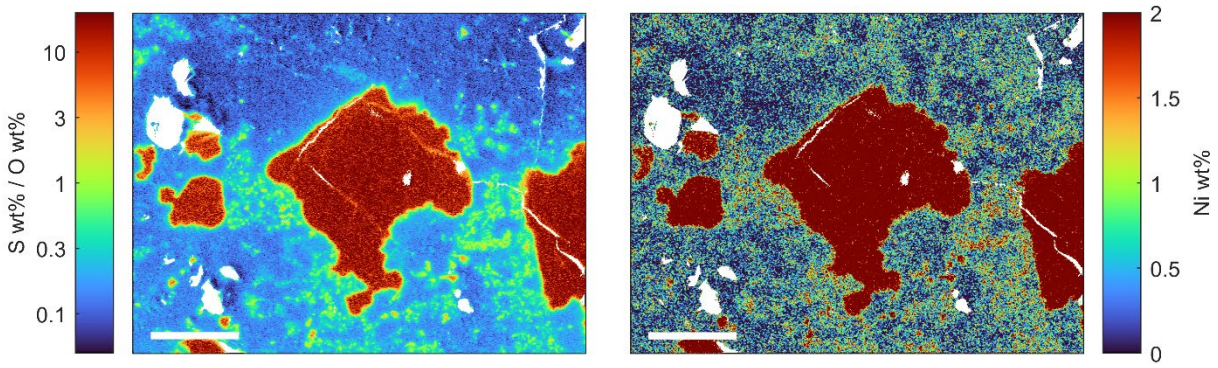

Figure 4.8: Spatial distribution of elements showing entrainment of matte droplets in the slag phase following selective sulfidation of laterite ore. Element distributions were quantified via SEM. Scale bars correspond to 30 µm.

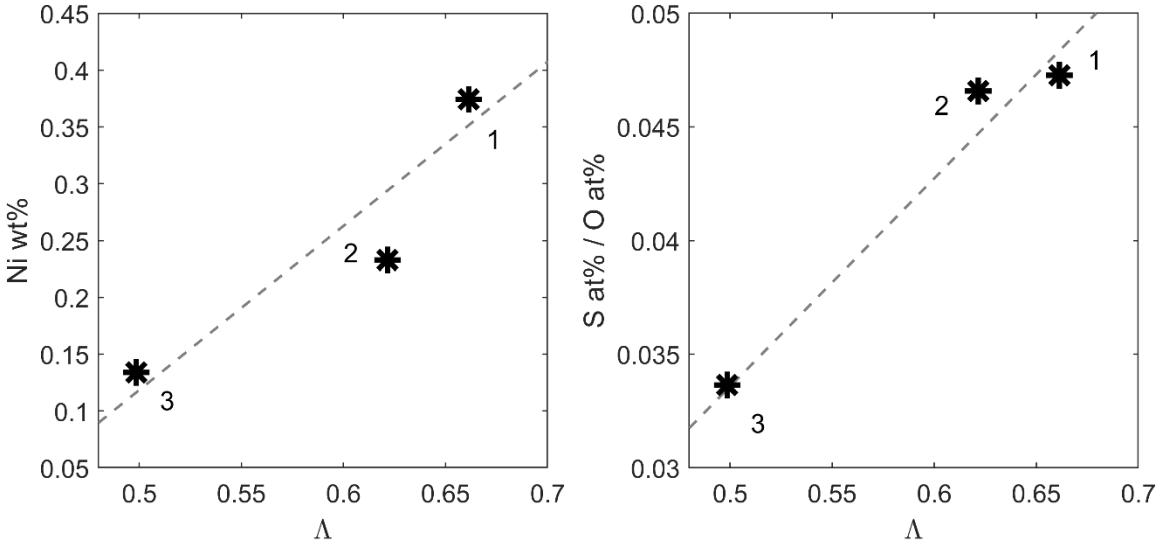

Figure 4.9: Positive correlation between nickel (Ni) and sulfur to oxygen (S/O) ratio versus optical basicity (Λ) in major slag phases following selective sulfidation of laterite. Phases 1, 2, and 3 correspond to phases listed in Table 4.8.

S in the system. This observation has important implications for feedstock upgrading and dressing prior to oxide-sulfide anion exchange. The presence of some residual SiO_2 or other acidic oxides may improve recovery of dilute elements with high sulfidation affinities during

pyrometallurgical oxide-sulfide anion exchange. Sulfidation for mineral processing may therefore tolerate or even benefit from less intensive feedstock comminution and beneficiation. These results highlight the role of sulfidation in modulating the solution effects and solubilities of target cation elements in oxide feedstocks. Sulfidation resulted in the formation of distinct sulfide phases rich in Fe and Ni, thereby reducing the solubility of Fe and Ni in the oxide. Meanwhile, basic oxide phases with higher affinities towards solubilized S likewise exhibited higher affinities towards solubilized Ni. Modulating the acid-base chemistry of oxide sulfidation feedstocks may enable improved selectivity and recovery during sulfidation. In the following section, similar trends between sulfidation affinity, solubility, and Λ are observed in the selective sulfidation of Cu smelting slags.

4.4.3 Selective Sulfidation of Copper Smelter Slags

During conventional pyrometallurgical production of Cu from $CuFeS_2$, Cu is separated from Fe during matte smelting in the presence of a SiO_2-rich slag. Oxygen (O_2) is introduced into the liquid matte which selectively oxidizes Fe. The Fe then partitions to the slag, enabling separation of Cu from Fe. Following, Cu-rich matte is converted to metal, again using O_2 gas in the presence of a slag. Around 1-2 wt% and 4-8 wt% of the Cu in smelting and converting steps respectively enters the slag due to entrainment of matte particles and Cu solubility in oxide phases[50]. Considering that 96.5-96.75% of the Cu value in the concentrate is generally considered "payable" from the smelter to the concentrator[51–53] (subject to deductions in payable Cu content for lower concentrate grades), minimizing the Cu lost to the slag is critical in achieving profitable smelter operation.

A variety of processing steps are currently employed for recovery of residual Cu in slags. Slag cleaning and settling furnaces may be employed for pyrometallurgical recovery of Cu dissolved in the oxide phase and from entrained matte[44]. Slag may also be solidified then sent through comminution and beneficiation circuits to physically recover entrained matte particles for reintroduction into the smelting process[44]. Pyrometallurgical and physical separation methods may reduce the Cu content of the slag down to between 0.5 wt% to 2 wt%[54]. Roasting slags with pyrite[55,56] (FeS_2) or ferric sulfate[57] ($Fe_2(SO_4)_3$) to improve physical separation or

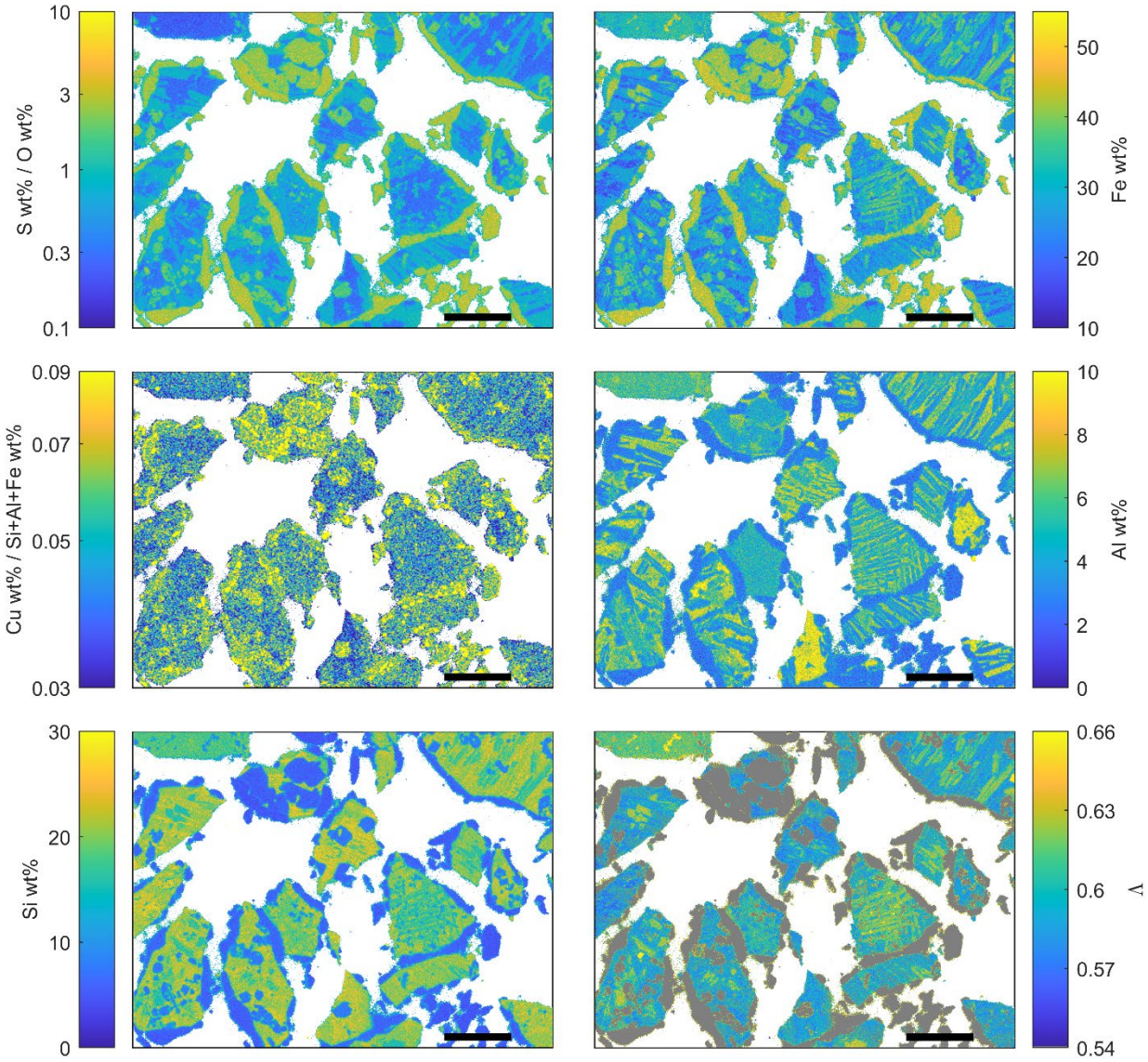

Figure 4.10: Spatial distribution of key elements and calculated optical basicities (Λ) for slag phases following selective sulfidation of copper (Cu) slag. Sulfidation was conducted at 800 °C. Element distributions were quantified via SEM-EDS. For panels detailing mass ratios of slag forming elements and Λ, matte phases are denoted in gray. Cu and a fraction of the iron (Fe) are shown to preferentially partition to matte phases versus silicon (Si) and aluminum (Al). Within slag phases, basic oxide phases generally retain higher fractions of Cu. Scale bars correspond to 100 μm.

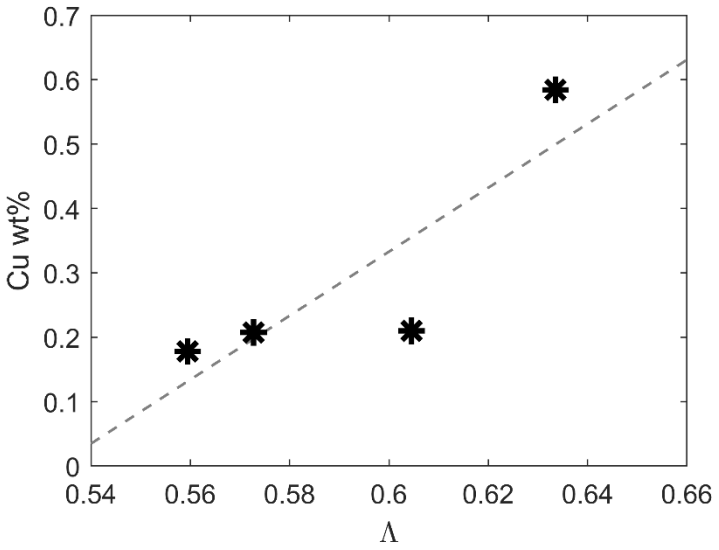

Figure 4.11: Positive correlation between copper (Cu) content and optical basicity (Λ) in major oxide phases following selective sulfidation of Cu smelter slag.

leaching of Cu from slags has been explored with varying levels of success. Selective sulfidation via pyrometallurgical oxide-sulfide anion exchange is a promising avenue to enable further physical recovery of solubilized Cu from oxide phases[21]. Furthermore, through the use of sulfidized Fe collector phases, the liberation size of Cu containing phases may be increased to lower energy usage in grinding and physical separation.

Prior to sulfidation, Cu smelter slags were ground to a particle size of 90-212 micron. The slag was then sulfidized at a temperature of 800 °C in an Al_2O_3 crucible at a P_{S_2} of 0.6 atm with an Ar carrier gas at a flowrate of 500 sccm for 2 hours, following methodologies reported in Chapter 3, Section 3.3 and by the author elsewhere[58]. The SEM-EDS distribution of elements in the slag following sulfidation are illustrated in Figure 4.10. Distinct sulfide phases on the order of 50-200 μm in size are shown to precipitate from the oxide feedstock. Cu is observed to preferentially partition to sulfide phases versus Si and Al. Fe is observed to be present in both oxide and sulfide phases. The optimal extent of collector phase formation via Fe sulfidation depends on balancing the lower costs and energy usage of larger liberations sizes for Cu-containing sulfide phases versus the added treatment volume of sulfidized Fe during subsequent processing of recovered sulfide phases.

The calculated[xi] Λ of oxide phases in the sulfidized slag are shown in Figure 4.10. Average Λ versus the average residual Cu contents of major slag phases are illustrated in Figure 4.11. Basic oxide phases are generally observed to retain higher amounts of Cu following sulfidation. This behavior mirrors the behavior of Ni in slag phases following sulfidation of Ni laterite (Section 4.4.2). In general, recoveries of dilute metals with higher sulfidation affinities are observed to be larger from acidic oxides during sulfidation. These results indicate that solution effects are a powerful method to control oxide-sulfide anion exchange selectivity, in particular for trace elements with high sulfidation affinities.

4.5 Physical Separation of Sulfidation Products

In section 4.4, selective sulfidation of multimetal oxide compounds resulted in the precipitation of distinct sulfide phases ranging from 20 μm to 5 mm in size. These phases are in principle large enough to be liberated from one another via grinding[1]. Oxide and sulfide phases may then be readily separated from one another due to their differences in physical properties (Chapter 2, Section 2.1). In this section, physical separation of sulfidation products via froth flotation and magnetic separation are demonstrated in the context of LIB recycling.

4.5.1 Selective Sulfidation and Physical Separation of Lithium ion Battery Cathode Materials

With increasing adoption of electric vehicles, Co and lithium (Li) for LIB have faced periods of supply uncertainty characteristic of byproduct metals[59,60], motivating efforts to geographically diversify supply and lower emissions associated with their primary production[61]. Industrial pyrometallurgical processes for battery recycling lack selectivity for individual battery metals, requiring economically and environmentally burdensome downstream leaching and subsequent hydrometallurgy to selectively recovery battery elements[39,62]. Meanwhile, direct hydrometallurgical and physical processes for LIB recycling face hurdles associate with

[xi] See methodology in [x].

convoluted chemistry streams and high costs[39,62,63]. However, cathode elements from end of life LIB can be selectively sulfidized to facilitate separation via benign physical processes[1,19,21].

NMC LIB cathode oxide with equal parts Ni, Mn, and Co ($NMC111$) was selectively sulfidized at a temperature of 1000 °C and a P_{S_2}/P_{SO_2} ratio of 30 using methodologies described in Chapter 3, Section 3.3 and by the author elsewhere[1,19,21]. As shown in Figure 4.12, upon sulfidation, the cathode material was observed to melt and form three distinct phases[1,19,21]: a Ni-rich sulfide, a Co-rich sulfide, and a Mn-rich oxysulfide. Mn oxysulfide chemistry is notoriously complex[64]; whether the phase was an oxysulfide, oxysulfate, sulfatosulfide, or mixed oxide/sulfate/sulfide is indiscernible from SEM-EDS element mapping. Product phases[1] as identified via QXRD are reported in Table 4.9. Li was not directly observable via SEM-EDS, yet was found by QXRD to form lithium sulfate (Li_2SO_4). Ni and Co were observed to be largely contained in sulfide phases (Ni_3S_2, Co_9S_8, and $Co_3Ni_6S_8$). Ni and Co sulfides exhibited some solubility within one another. A manganese sulfide (MnS) phase was identified, yet oxysulfides[64] of Mn may show poor crystallinity[65] that convolutes analysis of the Mn oxysulfide product phase; a significant fraction of the product phases was observed to be amorphous. Together, QXRD and microscopy results confirm that Ni, Co, Mn, and Li can be selectively partitioned into distinct phases via oxide-sulfide anion exchange.

In practice, some entrainment of impurities from the battery casing, anode, and electrolyte are expected following physical isolation of cathode material from end of life batteries or shredded battery black mass. Therefore, selective sulfidation was also performed on equimass mixture of $NMC111$ and Al_2O_3, simulating cathode waste calcined with Al impurities. Sulfidation was again conducted at temperature of 1000 °C under P_{S_2}/P_{SO_2} ratios of 30, 15, and 3 using methods reported in Chapter 3, Section 3.3 and herein[1]. Following sulfidation, the products were crushed to a particle size of 149-210 micron for product liberation. Product phases[1] identified via QXRD are reported in Table 4.9. Minimal change in crystalline product phases were observed via QXRD at different P_{S_2}/P_{SO_2} ratios. Similar Ni_3S_2, Co_9S_8, $Co_3Ni_6S_8$, and MnS products were observed following sulfidation with and without Al_2O_3. Li was observed via QXRD to partition to mixed oxide phases with Al ($(Li,Mn)Al_2O_4$, $LiAlO_2$, and $LiAl_5O_8$).

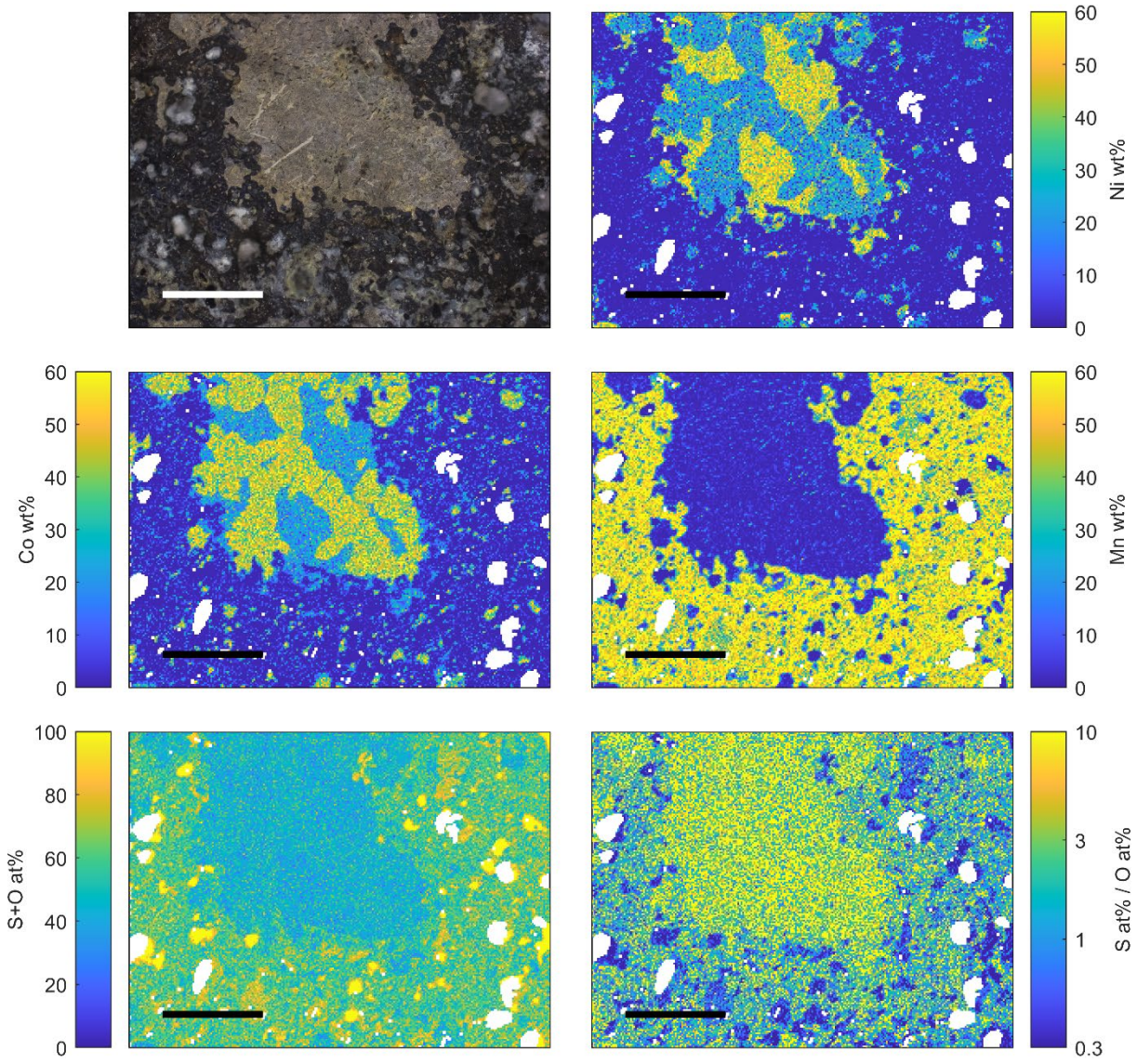

Figure 4.12: Optical image and spatial distribution of key elements following selective sulfidation of nickel-manganese-cobalt cathode oxide ($NMC111$). Sulfidation was conducted at 1000 °C. Element distributions were quantified via SEM-EDS. For panels detailing mass ratios of slag forming elements and optical basicity, matte phases are denoted in gray. While lithium (Li) is not directly observable, regions devoid of nickel (Ni), cobalt (Co), and manganese (Mn) with total sulfur (S) and oxygen (O) atomic fraction exceeding 80% are likely to be Li-rich phases, confirmed with QXRD to be lithium sulfate (Li_2SO_4). Scale bars correspond to 300 μm.

	$NMC111$		$NMC111 + Al_2O_3$		
Compound	**Untreated**	$P_{S_2}/P_{SO_2} = 30$	$P_{S_2}/P_{SO_2} = 30$	$P_{S_2}/P_{SO_2} = 15$	$P_{S_2}/P_{SO_2} = 3$
$Li(Mn,Ni)O_2$	35 wt%	<1 wt%	<1 wt%	<1 wt%	<1 wt%
$Li(Mn,Ni,Co)O_2$	2 wt%	<1 wt%	<1 wt%	<1 wt%	<1 wt%
$(Ni,Mn)O$	<1 wt%	3 wt%	<1 wt%	<1 wt%	<1 wt%
Al_2O_3	<1 wt%	-	4 wt%	2 wt%	2 wt%
$(Li,Mn)Al_2O_4$	<1 wt%	-	<1 wt%	<1 wt%	10 wt%
$LiAlO_2$	<1 wt%	-	11 wt%	9 wt%	11 wt%
$LiAl_5O_8$	<1 wt%	-	28 wt%	36 wt%	21 wt%
MnS	<1 wt%	9 wt%	11 wt%	10 wt%	10 wt%
Co_9S_8	<1 wt%	<1 wt%	11 wt%	10 wt%	9 wt%
Ni_3S_2	<1 wt%	2 wt%	2 wt%	3 wt%	4 wt%
$Co_3Ni_6S_8$	<1 wt%	7 wt%	<1 wt%	<1 wt%	<1 wt%
Li_2SO_4	<1 wt%	5 wt%	<1 wt%	<1 wt%	<1 wt%
Amorphous	63 wt%	74 wt%	33 wt%	30 wt%	33 wt%

Table 4.9: Nickel-manganese-cobalt cathode oxide ($NMC111$) phases before and after sulfidation with and without Al_2O_3 addition. Sulfidation was conducted at 1000 °C and analysis was accomplished via QXRD.

While QXRD showed minimal difference in the crystalline products obtained at P_{S_2}/P_{SO_2} ratios of 3 and 15, only the products obtained from a P_{S_2}/P_{SO_2} ratio of 3 were observed to respond to a magnet and were therefore separated magnetically. Separation conditions[1] are reported in Table 4.10. Magnetic separation enabled isolation of Ni and Co sulfides from the Al, Mn, and Li species at a combined recovery of 84.8% and a combined purity of 82.1 wt%[1].

Sulfidation products obtained from a P_{S_2}/P_{SO_2} ratio of 15 did not respond to the magnet, and were therefore washed and then separated via froth flotation. Washing of the sulfidation product prior to flotation enabled recovery of water-soluble lithium products. Despite the formation of mixed oxide phases containing Li, Li was leached with water for a recovery of 83% and a purity of 70 at% on a dissolved metals basis[1]. This suggests that despite the formation of $(Li,Mn)Al_2O_4$, $LiAlO_2$, and $LiAl_5O_8$, Li in sulfidation products were predominantly water soluble. Subsequent flotation enabled separation of Ni and Co sulfides from Al and Mn oxide and oxysulfide species at a combined recovery of 52.8% and a combined purity of 82.8 wt%[1].

These results indicate that selective sulfidation via oxide-sulfide anion exchange can be used as a pretreatment to enable physical separation of chemically mixed oxides. While oxide, sulfate, oxysulfide, and sulfide species are in principle easy to isolate due to their physical property differences, separation effectiveness is also dependent on the morphology and liberation

behavior of sulfide product phases. As discussed in Chapter 1, Section 1.2, finer grinding of products increases liberation effectiveness at the expense of higher energy usage in both grinding and separation. For a given sulfidized product, optimization of physical separation pathways will be necessary. Due to differences in the thermodynamic stability of oxides and sulfides, post-sulfidation separation via direct reduction of sulfide phases in the presence of oxides is also tenable. New metal reduction pathways enabled by sulfidation are discussed later in Chapter 7.

Sulfidation Conditions	Separation Method	Separation Conditions	Target Metals	Purity (metals basis)	Recovery
$P_{S_2}/P_{SO_2} = 15$	Leaching	Particle Size: 149-210 µm Solvent: Deionized H_2O Concentration: 1g / 100 mL pH: 7 Temperature: 25°C Time: 15 minutes	Li	22.5 wt% 70.0 at%	83.0%
	Flotation	Particle Size: 149-210 µm Collector: KAX, $5x10^{-3}$ M Temperature: 25°C pH: 7 Condition time: 2 minutes Flotation time: 5 minutes	$Ni - Co$	82.8 wt% 75.8 at%	52.8%
$P_{S_2}/P_{SO_2} = 3$	Magnetic	Particle Size: 149-210 µm	$Ni - Co$	82.1 wt% 74.0 at%	84.8%

Table 4.10: Physical separation methods, conditions, and results. Compositions were quantified via ICP-MS.

4.6 Summary

It was hypothesized in Chapter 2 that selective oxide-sulfide anion exchange decreases the solubility of target cation elements in feedstock materials to support their selective extraction and physical separation. Following the methodology proposed in Chapter 3, an integrated thermodynamic and kinetic framework was utilized to confirm this hypothesis. Herein, oxide, oxysulfide, sulfate, sulfide, and carbonate compounds exhibiting a wide range of sulfidation affinities were sulfidized and desulfidized via oxide-sulfide anion exchange. Sulfidized products were observed to precipitate as new, distinct phases that were largely insoluble with their oxide feedstocks. The selectivity of sulfidation or desulfidation for individual elements from

multielement feedstocks was shown to be controllable using thermodynamic and kinetic process levers. Physical separation was illustrated to be viable for recovery of new sulfide phases formed via selective sulfidation.

Measured sulfidation reaction rates for lanthanum oxide illustrate that sulfidation is a thermally activated process that follows Arrhenius kinetics. These findings show that sulfidation may be conducted selectivity for compounds of similar sulfidation affinity that exhibit large differences in melting point. With knowledge of reaction kinetics, gas flowrate and residence time during oxide-sulfide anion exchange may be used to modulate the concentration and accumulation of sulfidation product gasses within the reactor, enabling control of the sulfur, sulfur dioxide, and oxygen partial pressures. Carbon addition to the reactor reduces sulfur dioxide to elemental sulfur, achieving higher partial pressures of sulfur and lower partial pressures of sulfur dioxide within the reactor via carbothermically driven sulfur reflux. By controlling the ratio of sulfur to sulfur dioxide, individual elements may be targeted for oxide-sulfide anion exchange.

For dilute elements, solution effects are found to be critical in modulating their oxide-sulfide anion exchange behavior and their residual solubility in oxide phases. In the presence of iron sulfide collector phases, siderophilic dilute elements are observed to sulfidize at higher rates than less siderophilic dilute elements of similar sulfidation affinity. This approach is especially powerful for rare earth element separation, where light and heavy lanthanides exhibit drastically different affinities for iron sulfide. Meanwhile, oxide acid-base chemistry is shown to moderate the solubility of chalcophilic elements following sulfidation, with acidic oxide phases exhibiting higher conversions of target trace elements to sulfides versus basic phases.

Following selective oxide-sulfide anion exchange for the precipitation of sulfide products from oxide feedstocks, physical separation of oxide and sulfide phases was demonstrated. Selectively sulfidized lithium ion battery cathode oxide with aluminum oxide impurities were washed to recover water soluble lithium species. Nickel and cobalt sulfides were separated from manganese and aluminum phases via both froth flotation and magnetic separation. The optimum choice of physical separation pathway for a given chemistry is dependent on the size, morphology, and physical properties of the precipitated product phases from oxide-sulfide anion exchange.

Together, thermodynamic and kinetic factors contribute to the ability of selective oxide-sulfide anion exchange to precipitate physically separable product phases from mixed metal compound feedstocks. Experiments conducted herein confirm that selective oxide-sulfide anion exchange decreases the solubility of target cation elements in feedstock materials, supporting their selective extraction and physical separation. In the next chapter, the behaviors of some pnictogen, halide, and other chalcogenide impurities are explored. Later in Chapter 6, technoeconomic and environmental factors for oxide-sulfide anion exchange are considered. New metal reduction pathways enabled by selective sulfidation are explored in Chapter 7.

4.7 References

1. Stinn, C. & Allanore, A. Selective sulfidation of metal compounds. *Nature* **602**, 78–83 (2022).
2. Allanore, A. & Stinn, C. Selective Sulfidation and Desulfidation (Patent US20210277531A1). (2021).
3. Ahmadi, E. & Suzuki, R. O. Tantalum Metal Production Through High-Efficiency Electrochemical Reduction of TaS2 in Molten CaCl2. *J. Sustain. Metall.* **7**, 437–447 (2021).
4. Stinn, C., Benderly-Kremen, E. & Allanore, A. Scandium Master Alloy Production Via Sulfidation and Vacuum Aluminothermic Reduction. in *Light Metals 2023* 1195–1203 (Springer, 2023). doi:10.1007/978-3-031-22532-1_160.
5. Kaminskii, B. T., Prokof'eva, G. N., Plygunov, A. S. & Galitskii, P. A. Manufacture of zirconium and hafnium sulfide powders. *Sov. Powder Metall. Met. Ceram.* **12**, 521–524 (1973).
6. McCullough, J. D., Brewer, L. & Bromley, L. A. The crystal structure of zirconium oxysulfide, ZrOS. *Acta Crystallogr.* **1**, 287–289 (1948).
7. Daehn, K. E. *et al.* Liquid Copper and Iron Production from Chalcopyrite, in the Absence of Oxygen. *Metals (Basel).* **12**, 1440 (2022).
8. Thiele, E. W. Relation between Catalytic Activity and Size of Particle. *Ind. Eng. Chem.* **31**, 916–920 (1939).
9. Sohn, H. Y. & Fan, D. Q. On the Initial Rate of Fluid-Solid Reactions. *Met. Mater. Trans.*

B **48B**, 1827–1832 (2017).

10. Sohn, H. Y. & Perez-Fontes, S. E. Application of the Law of Additive Reaction Times to Fluid-Solid Reactions in Porous Pellets with Changing Effective Diffusivity. *Met. Mater. Trans. B* **41B**, 1261–1267 (2010).
11. Fogler, H. S. *Elements of Chemical Reaction Engineering*. (Prentice Hall, 2016).
12. Stinn, C. & Allanore, A. Selective Sulfidation for Rare Earth Element Separation. in *Rare Metal Technology 2022* (ed. Ouchi, T.) 259–278 (The Minerals, Metals & Materials Society, 2022). doi:10.1007/978-3-030-92662-5_25.
13. Wang, W., Pranolo, Y. & Cheng, C. Y. Metallurgical processes for scandium recovery from various resources: A review. *Hydrometallurgy* **108**, 100–108 (2011).
14. Raghavan, V. Fe-S-Sc (Iron-Sulfur-Scandium). *J. Phase Equilibria* **19**, 280–281 (1998).
15. Takasaki, J., Kuribayashi, K. & Ozawa, S. Constitution of stable and metastable phase diagrams for TmFeO3-ScFeO3 system by undercooling solidification using the containerless technique. *Mater. Trans.* **59**, 469–474 (2018).
16. Yanchevskii, O. Z., Kovalenko, L. L. & Belous, A. G. Codoping of scandium-containing zirconia-based solid electrolytes with iron, cerium, and copper oxides. *Inorg. Mater.* **52**, 301–308 (2016).
17. Waudby, P. E. Rare earth additions to steel. *Int. Met. Rev.* **23**, 74–98 (1978).
18. Sahu, S. K., Chmielowiec, B. & Allanore, A. Electrolytic Extraction of Copper, Molybdenum and Rhenium from Molten Sulfide Electrolyte. *Electrochim. Acta* **243**, 382–389 (2017).
19. Stinn, C. & Allanore, A. Selective Sulfidation and Electrowinning of Nickel and Cobalt for Lithium Ion Battery Recycling. in *Ni-Co 2021: The 5th International Symposium on Nickel and Cobalt* (eds. Anderson, C. et al.) 99–110 (Springer Nature Switzerland AG, 2021). doi:10.1007/978-3-030-65647-8_7.
20. Wagner, M.-E. & Allanore, A. Electrochemical Separation of Ag 2 S and Cu 2 S from Molten Sulfide Electrolyte . *J. Electrochem. Soc.* **169**, 063511 (2022).
21. Stinn, C. & Allanore, A. Shifting the Burden of Selectivity from Chemical to Physical Separation Processes via Selective Sulfidation. in *REWAS 2022: Developing Tomorrow's Technical Cycles* (ed. Lazou, A.) 119–136 (The Minerals, Metals & Materials Society, 2022).

22. Stinn, C. & Allanore, A. Ferronickel Production from Nickel Laterite via Sulfide Chemistry. in *Advances in Pyrometallurgy* (ed. Fleuriault, C.) 1–17 (The Minerals, Metals & Materials Society, 2023).
23. Smith, B. J., Riddle, M. E., Earlam, M. R., Iloeje, C. & Diamod, D. *Rare earth permanent magnets - Supply chain deep dive assessment*. *U.S. Department of Energy Response to Executive Order 14017, 'America's Supply Chains'* (2022).
24. Sagawa, M., Fujimura, S., Yamamoto, H., Matsuura, Y. & Hiraga, K. Permanent magnet materials based on the rare earth-iron-boron tetragonal compounds. *IEEE Trans. Magn.* **20**, 1584–1589 (1984).
25. Gauder, D. R., Froning, M. H., White, R. J. & Ray, A. E. Elevated temperature study of Nd-Fe-B–based magnets with cobalt and dysprosium additions. *J. Appl. Phys.* **63**, 3522–3524 (1988).
26. Binnemans, K., Jones, P. T., Müller, T. & Yurramendi, L. Rare Earths and the Balance Problem: How to Deal with Changing Markets? *Journal of Sustainable Metallurgy* vol. 4 126–146 (2018).
27. Firdaus, M., Rhamdhani, M. A., Durandet, Y., Rankin, W. J. & McGregor, K. Review of High-Temperature Recovery of Rare Earth (Nd/Dy) from Magnet Waste. *J. Sustain. Metall. 2016 24* **2**, 276–295 (2016).
28. Kaim, V., Rintala, J. & He, C. Selective recovery of rare earth elements from e-waste via ionic liquid extraction: A review. *Sep. Purif. Technol.* **306**, 122699 (2023).
29. Jha, M. K. *et al.* Review on hydrometallurgical recovery of rare earth metals. *Hydrometallurgy* **165**, 2–26 (2016).
30. Jönsson, C. *et al.* The extraction of NdFeB magnets from automotive scrap rotors using hydrogen. *J. Clean. Prod.* **277**, 124058 (2020).
31. Walton, A. *et al.* The use of hydrogen to separate and recycle neodymium-iron-boron-type magnets from electronic waste. *J. Clean. Prod.* **104**, 236–241 (2015).
32. Rasheed, M. Z. *et al.* Review of the Liquid Metal Extraction Process for the Recovery of Nd and Dy from Permanent Magnets. *Metall. Mater. Trans. B 2021 523* **52**, 1213–1227 (2021).
33. Jowitt, Si. M., Werner, T. T., Weng, Z. & Mudd, G. M. Recycling of the Rare Earth Elements. *Curr. Opin. Green Sustain. Chem.* **13**, 1–7 (2018).

34. Li, X. Z. *et al.* A supramolecular lanthanide separation approach based on multivalent cooperative enhancement of metal ion selectivity. *Nat. Commun.* **9**, 547 (2018).
35. Zhao, B., Zhang, J. & Schreiner, B. *Separation Hydrometallurgy of Rare Earth Elements*. (Springer International Publishing AG Switzerland, 2016).
36. Yin, X. *et al.* Rare earth separations by selective borate crystallization. *Nat. Commun.* **8**, (2017).
37. Crundwell, F. K., Moats, M. S., Ramachandran, V., Robinson, T. G. & Davenport, W. G. *Extractive Metallurgy of Nickel, Cobalt, and Platinum-Group Metals*. (Elsevier, 2011).
38. Stanković, S. *et al.* Options for Hydrometallurgical Treatment of Ni-Co Lateritic Ores for Sustainable Supply of Nickel and Cobalt for European Battery Industry from South-Eastern Europe and Turkey. *Metals (Basel).* **12**, (2022).
39. Harper, G. *et al.* Recycling lithium-ion batteries from electric vehicles. *Nature* vol. 575 75–86 (2019).
40. König, U. Nickel laterites—mineralogical monitoring for grade definition and process optimization. *Minerals* **11**, (2021).
41. Gleeson, S. A., Butt, C. R. M. & Elias, M. Nickel Laterites: A Review. *Soc. Econ. Geol. Newsl.* 11–18 (2003) doi:10.5382/SEGnews.2003-54.fea/5400602/segnl-54-1.pdf.
42. Diaz, C. M., Landolt, C. A., Vahed, A., Warner, A. E. M. & Taylor, J. C. A Review of Nickel Pyrometallurgical Operations. *JOM* **40**, 28–33 (1988).
43. Harris, C. T., Peacey, J. G. & Pickles, C. A. Selective sulphidation of a nickeliferous lateritic ore. *Miner. Eng.* **24**, 651–660 (2011).
44. Harris, C. T., Peacey, J. G. & Pickles, C. A. Selective sulphidation and flotation of nickel from a nickeliferous laterite ore. *Miner. Eng.* **54**, 21–31 (2013).
45. Burns, R. G. & Fyfe, W. S. Behaviour of nickel during magmatic crystallization [6]. *Nature* **210**, 1147–1148 (1966).
46. Burns, R. G. The partitioning of trace transition elements in crystal structures: a provocative review with applications to mantle geochemistry. *Geochim. Cosmochim. Acta* **37**, 2395–2403 (1973).
47. Goldschmidt, V. M. The principles of distribution of chemical elements in minerals and rocks. The seventh Hugo Müller Lecture, delivered before the Chemical Society on March 17th, 1937. *J. Chem. Soc.* 655–673 (1937) doi:10.1039/JR9370000655.

48. Ringwood, A. E. The principles governing trace element distribution during magmatic crystallization Part I: The influence of electronegativity. *Geochim. Cosmochim. Acta* **7**, 189–202 (1955).
49. Sosinsky, D. J. & Sommerville, I. D. The composition and temperature dependence of the sulfide capacity of metallurgical slags. *Metall. Trans. B* **17**, 331–337 (1986).
50. Schlesinger, M. E., King, M. J., Sole, K. C. & Davenport, W. G. *Extractive Metallurgy of Copper*. (Elsevier, 2011). doi:10.1017/CBO9781107415324.004.
51. Edmunds, C., Thomas, M. & Major, K. *Preliminary Economic Assessment of the Kemess Underground Project, British Columbia, Canada*. (2011).
52. *Atalaya Mining Plc Annual Report*. (2018).
53. Kill, R., Kulla, G., Wortman, G., Melnyk, J. & Rogers, D. *Galore Creek Project, British Columbia, Ni 43-1-1 Technical Report on Pre-Feasibility Study*. https://www.sec.gov/Archives/edgar/data/1173420/000120445911002494/exhibit99-1.htm (2011).
54. Gorai, B., Jana, R. K. & Premchand. Characteristics and utilisation of copper slag—a review. *Resour. Conserv. Recycl.* **39**, 299–313 (2003).
55. Bulut, G., Perek, K. T., Gül, A., Arslan, F. & Önal, G. Recovery of metal values from copper slags by flotation and roasting with pyrite. *Miner. Metall. Process.* **24**, 13–18 (2007).
56. Guo, Z., Zhu, D., Pan, J. & Zhang, F. Mechanism of Mineral Phase Reconstruction for Improving the Beneficiation of Copper and Iron from Copper Slag. *Jom* **68**, 2341–2348 (2016).
57. Altundoğan, H. S. & Tümen, F. Metal recovery from copper converter slag by roasting with ferric sulphate. *Hydrometallurgy* **44**, 261–267 (1997).
58. Stinn, C., Gutierrez, C., Daehn, K. & Allanore, A. Sulfidation for Copper Mineral Processing and Impurity Management. in *The Igo Wilkomirsky Symposium on Pyrometallurgy* (ed. IIMCh) 785–796 (Copper 2022, 2022).
59. Olivetti, E. A., Ceder, G., Gaustad, G. G. & Fu, X. Lithium-Ion Battery Supply Chain Considerations: Analysis of Potential Bottlenecks in Critical Metals. *Joule* vol. 1 229–243 (2017).
60. Nassar, N. T., Graedel, T. E. & Harper, E. M. By-product metals are technologically

essential but have problematic supply. *Sci. Adv.* **1**, e1400180 (2015).

61. Dunn, J. B., Gaines, L., Sullivan, J. & Wang, M. Q. Impact of Recycling on Cradle-to-Gate Energy Consumption and Greenhouse Gas Emissions of Automotive Lithium-Ion Batteries. *Environ. Sci. Technol.* **46**, 12704–12710 (2012).
62. Ciez, R. E. & Whitacre, J. F. Examining different recycling processes for lithium-ion batteries. *Nat. Sustain.* **2**, 148–156 (2019).
63. Shi, J. *et al.* Sulfation Roasting Mechanism for Spent Lithium-Ion Battery Metal Oxides Under SO2-O2-Ar Atmosphere. *JOM* **71**, 4473–4481 (2019).
64. Bastanov, S. S., Ryabinina, O. I., Obzherina, K. F. & Derbeneva, S. S. On the Chemical Structure of Manganese Oxysulfides. *Bull. Acad. Sci. USSR, Div. Chem. Sci.* **17**, 6–11 (1968).
65. Liu, M. *et al.* Flower-like manganese-cobalt oxysulfide supported on Ni foam as a novel faradaic electrode with commendable performance. *Electrochim. Acta* **191**, 916–922 (2016).
66. Ishida, M. & Wen, C. Y. Comparison of kinetic and diffusional models for solid-gas reactions. *AIChE J.* **14**, 311–317 (1968).
67. Sohn, H. Y. & Szekely, J. A structural model for gas-solid reactions with a moving boundary—III. *Chem. Eng. Sci.* **27**, 763–778 (1972).
68. Sohn, H. Y. & Szekely, J. The effect of intragrain diffusion on the reaction between a porous solid and a gas. *Chem. Eng. Sci.* **29**, 630–634 (1974).
69. Nakamura, T., Ueda, Y. & Toguri, J. M. A New Development of the Optical Basicity. *Journal of the Japan Institute of Metals* vol. 50 456–461 (1986).
70. Allred, A. L. Electronegativity values from thermochemical data. *J. Inorg. Nucl. Chem.* **17**, 215–221 (1961).
71. Pauling, L. The Nature of the Chemical Bond. IV. The Energy of Single Bonds and the Relative Electronegativity of Atoms. *J. Am. Chem. Soc.* **54**, 3570–3582 (1932).
72. Duffy, J. A. A Review of Optical Basicity and its Applications to oxidic systems. *Geochemica Cosmochim. Acta* **57**, 3961–3970 (1993).

Chapter 5

Sulfidation in the Presence of Other Anions

In Chapter 4, selective sulfidation and desulfidation were demonstrated for oxide and sulfide material separations. Oxide-sulfide anion exchange was confirmed to decrease the solubility of target cation elements in feedstock materials to support their selective extraction and physical separation. The efficacy of this process was established over a wide range of chemistries and sulfidation affinities spanning transition, alkaline earth, and rare earth metal systems. Testing was confined to mechanically and chemically mixed feedstocks containing oxide, sulfate, oxysulfide, sulfide, and carbonate anions. This scope covers a substantial span of industrially-relevant material feedstocks and products.

Other anion impurities may be present during oxide-sulfide anion exchange however, especially in mineral feedstocks. For copper production from sulfide minerals, anion impurities are becoming more and more relevant as ore grades decline and ore complexities increase. Sulfosalt minerals such as enargite and tennantite contain mixed arsenic, antimony, and sulfur anion chemistries. Selenium and tellurium may also substitute for sulfur in sulfide and sulfosalt phases. Meanwhile for lanthanides, fluorocarbonate and phosphate mineral phases are the most commercially relevant primary sources of critical rare earth elements.

In this chapter, the behaviors of arsenic, antimony, selenium, tellurium, phosphorous, and fluorine impurities during oxide-sulfide anion exchange are briefly explored in some copper and rare earth mineral systems. Complete characterizations of the sulfidation and desulfidation thermodynamics, kinetics, and chemistries of these impurities remain outside the scope of this

work. Case studies considered herein are intended to confirm that oxide-sulfide anion exchange remains a powerful tool for enabling material separation even in the presence of other anion chemistries and impurities.

5.1 Sulfidation of Copper Minerals and Concentrates Containing Arsenic, Antimony, Selenium, and Tellurium

The majority of exploitable global copper (Cu) reserves take the form of sulfide minerals, which are conventionally processed using pyrometallurgy[1]. However, this method of smelting is plagued by high capital and operating costs, and new smelters cannot be established profitably in many markets[2]. These challenges have been further compounded by falling ore grades and increasing mineralogical complexity[3]. Management and utilization of nonmetal impurities in Cu have remained areas of importance since antiquity[4,5]. Today, treatments of high-arsenic (As) and antimony (Sb) concentrates are particularly unrewarding burdens, with smelters leveling financial penalties for feeds containing As and Sb contents above 0.5% and 0.2% respectively[6]. In contrast selenium (Se) and tellurium (Te) impurities are valuable byproducts with growing demand, yet exhibit recoveries below 10% due to losses during beneficiation and smelting[7,8].

Previously, sulfidation of As-rich electrostatic precipitator dusts using elemental sulfur (S) at temperatures of 600°C – 700 °C enabled the removal of As and Sb as volatile sulfides[9]. Partial roasting of As-containing sulfide minerals with pyrite (FeS_2) enables vaporization of arsenic (As) in elemental, oxide, or sulfide forms[10], yet reliance on FeS_2 decomposition for sulfur gas (S_2) generation limits the mass transport and kinetics of such processes[11]. As motivated in Chapter 3 and confirmed experimentally in Chapter 4, introduction of gaseous elemental S_2 during metallurgical sulfidation improves process control and product selectivity. Herein, the effectiveness of pyrometallurgical sulfidation is evaluated for the removal of As, Sb, Se, and Te directly from Cu concentrates or minerals.

5.1.1 Thermodynamics of Copper Mineral Sulfidation

Through controlling the sulfur gas (S_2) partial pressure (P_{S_2}) in a pyrometallurgical sulfidation reactor, anion impurities may be extracted and recovered as gaseous or volatile sulfides prior to smelting. The sulfidation of a condensed metal oxide, selenide, telluride, arsenide, or antimonide compound ($M_\gamma X_\delta(s,l)$) with S_2 to form a condensed metal sulfide ($M_\eta S_\theta(s,l)$) and a gaseous impurity sulfide ($X_\kappa S_\lambda(g)$) is described by the following reaction, where β, γ, δ, ϵ, ζ, η, θ, ι, κ, and λ are stoichiometric factors[12]:

$$\beta M_\gamma X_\delta(s,l) + \epsilon S_2(g) = \zeta M_\eta S_\theta(s,l) + \iota X_\kappa S_\lambda(g) \tag{5.1}$$

$X_\kappa S_\lambda$ may correspond to sulfur dioxide (SO_2), selenium sulfide (SeS), tellurium sulfide (TeS), arsenic sulfide (As_4S_4), or antimony sulfide (Sb_2S_3). From Le Chatelier's principle, there exists a critical ratio of the S_2 to $X_\kappa S_\lambda$ partial pressures ($\left[P_{S_2}/P_{X_\kappa S_\lambda}\right]_{crit}$) at which $M_\gamma X_\delta$ is sulfidized to $M_\eta S_\theta$. For a given reaction shown in Eq. 5.1, this relationship may be established using the methodology described in Chapter 3, Section 3.1. Compounds with lower $\left[P_{S_2}/P_{P_{X_\kappa S_\lambda}}\right]_{crit}$ exhibit higher affinities for S and are more inclined to form $M_\eta S_\theta$ while expelling volatile $X_\kappa S_\lambda$.

$\left[P_{S_2}/P_{SO_2}\right]_{crit}$, $\left[P_{S_2}/P_{SeS}\right]_{crit}$, and $\left[P_{S_2}/P_{TeS}\right]_{crit}$ at a temperature of 800 °C and a pressure of 1 atm are reported in Figure 5.1 for some pure, immiscible compounds relevant to Cu mineral processing[12]. Thermodynamically, different oxides sulfidize over many orders of magnitude of $\left[P_{S_2}/P_{SO_2}\right]_{crit}$, while most pure selenides and tellurides sulfidize with $\left[P_{S_2}/P_{SeS}\right]_{crit}$ and $\left[P_{S_2}/P_{TeS}\right]_{crit}$ of less than 10. More chalcophilic elements have a stronger tendency toward covalent bonding. This leads to a general reversal in sulfidation affinity trends for selenides and tellurides versus oxides. Further deviations from these trends likely arise due to variations in metallic element's oxidation state and ionic (Shannon) radius ($\overline{r_S}$), discussed in Chapter 3, Section 3.1.1 for oxide-sulfide anion exchange. The presence of mixed anion sulfosalts between pure end member single anion compounds, such as enargite (Cu_3AsS_4)

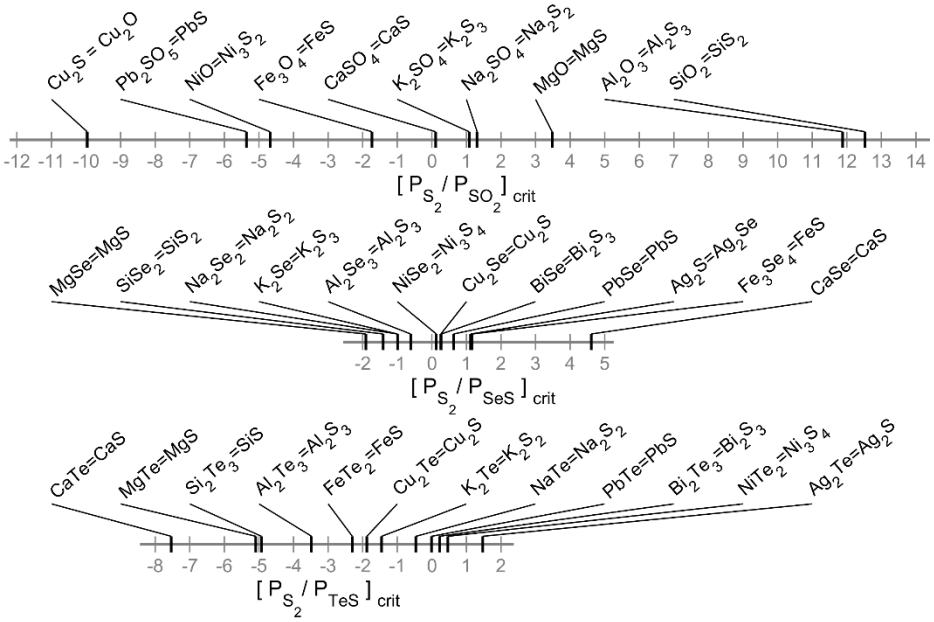

Figure 5.1: Sulfidation series for some oxides, selenides, and tellurides at 800 °C and 1 atm.

between copper sulfide (Cu_2S) and copper arsenide (Cu_3As), shifts phase domains and $\left[P_{S_2}/P_{P_{X_\kappa S_\lambda}}\right]_{crit}$ as described in the context of oxysulfides in Chapter 3, Section 3.1.3.

During sulfidation, a collection of anion exchange reactions may occur simultaneously between oxide, sulfide, selenide, telluride, arsenide, and antimonide compounds via interactions with $S - As - Sb - O - Se - Te$ species in the gas phase of the reactor. Both the extent of $As - Sb - Se - Te$ impurity volatilization and undesirable sulfidation of gangue oxides increase with increasing P_{S_2}. Therefore, an optimal P_{S_2} must be realized in order to minimize both anion and cation impurities in the sulfide product[12]. Methods for controlling P_{S_2} and P_{S_2}/P_{SO_2} are discussed in Chapter 3, Section 3.2 and may be extended for $P_{As_4S_4}$, $P_{Sb_2S_3}$, P_{SeS}, and P_{TeS}. In the following section, sulfidation is experimentally demonstrated for the removal of Sb, As, and Se from Cu-containing minerals and concentrates.

5.1.2 Sulfidation of Enargite and Tennantite

To study As, Sb, selenium, and Te removal upstream of Cu smelting, sulfidation was conducted on two natural Cu sources: blended Cu_3AsS_4-rich mineral concentrate and unconcentrated tennantite ($Cu_{12}Sb_{0.6}As_{3.4}S_{13}$) ore[12]. The blended Cu_3AsS_4-rich concentrate was produced by thoroughly mixing chalcopyrite ($CuFeS_2$) concentrate from the Sierrita Mine in Arizona with a crushed (< 106 μm) Cu_3AsS_4-rich mineral sample collected from the Leonard Mine in Butte, Montana. The $Cu_{12}Sb_{0.6}As_{3.4}S_{13}$ ore sample was collected near Alta, Utah and crushed to a particle size of < 106 μm.

Cu_3AsS_4-rich Cu concentrate and $Cu_{12}Sb_{0.6}As_{3.4}S_{13}$ were sulfidized at 800 °C and a pressure of 1 atm for 2 hours under P_{S_2} of 0.6 atm following the methods described in Chapter 3, Section 3.3 and by the author elsewhere[12]. The crystalline phases present before and after sulfidation are reported in Table 5.1 as measured with quantitative X-ray diffraction (QXRD). Bulk Cu, As, Sb, and Se contents are reported in Table 5.2 as measured with inductively-coupled plasma atomic emission spectroscopy (ICP-AES).

Upon sulfidation of the enargite-rich concentrate, crystalline Cu_3AsS_4 and famatinite (Cu_3SbS_4) phases decomposed and reacted with FeS_2 in the system to form $CuFeS_2$, illustrated in the scanning electron microscope energy dispersive X-ray spectroscopy (SEM-EDS) map[12] in Figure 5.2. The As and Sb contents were reduced by 99% and 72% from 5.1 wt% to 0.06 wt% and 0.34 wt% to 0.08 wt% respectively[12]. No speiss product phases were observed via SEM-EDS or QXRD, indicating that both As and Sb were presumably expelled from the system as volatile sulfides. Further analysis is necessary to confirm the form As and Sb took upon vaporization. A range of sequestration methods for As, Sb, and Se vapors are available, such as reaction of the As or Sb sulfide vapors with a dedicated collector phase to produce stable cement compounds for disposal[13]. From the sulfidation series in Figure 2, calcium (Ca) compounds may serve as thermodynamically favorable collectors for Se. Distillation processes could also be employed for separation of As, Sb, S, Se, and Te products[14].

Sulfidation herein is an improvement over alternative pyrometallurgical methods, which has been inconsistent in reducing As contents below 0.3 wt%[11]. Electron probe micro analysis wavelength-dispersive X-ray spectroscopy (EPMA-WDS) showed that residual As and Sb were

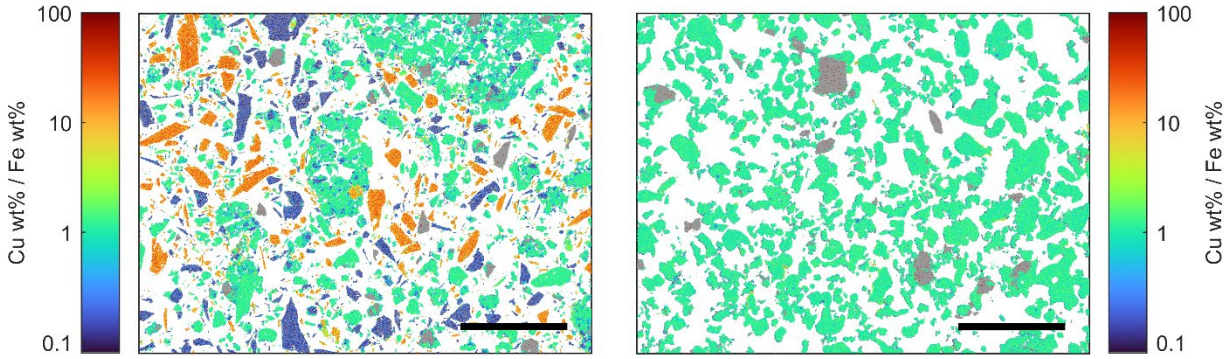

Figure 5.2: Copper to iron (Cu/Fe) ratio in enargite (Cu_3AsS_4)-rich concentrate before (left) and after (right) sulfidation. Spatial distributions of elements were mapped via SEM/EDS. Orange phases correspond to Cu_3AsS_4 and famatinite (Cu_3SbS_4), blue phases correspond to pyrite (FeS_2), green phases correspond to chalcopyrite ($CuFeS_2$), and grey phases correspond to oxide / silicate gangue. Scale bar: 300 µm

concentrated in oxide/silicate gangue in the sulfidized concentrate[12]. Due to the anion exchange of heavy As and Sb with lighter S, the Cu grade increased by 19% from 25.6 wt% to 30.1 wt%. Se was not detected at levels above 0.01 wt% before or after sulfidation, while measurement of Te content proved erratic, with values ranging from 0.03 wt% to 0.11 wt%. Higher initial levels of Se and Te in the sulfidation feedstock would aid in understanding their sulfidation behavior. Crystalline quartz (SiO_2) content was observed to increase upon sulfidation, likely due to the decomposition of amorphous gangue phases with increasing P_{S_2}. These results show that Cu phases were preferentially sulfidized versus silica (SiO_2)-containing phases which remained as oxides; this is consistent with the sulfidation series in Chapter 3, Figures 3.4 and 3.5, confirming that oxide-sulfide anion exchange remains selective during As compound sulfidation.

Upon sulfidation of the $Cu_{12}Sb_{0.6}As_{3.4}S_{13}$ ore, the majority of crystalline $Cu_{12}Sb_{0.6}As_{3.4}S_{13}$ decomposed and reacted with FeS_2 in the system to form $CuFeS_2$[12]. No crystalline speiss phases were observed in the sulfidized product via QXRD. The As and Sb contents were reduced by 99% and 80% from 0.76 wt% to <0.01 wt% and 4.4 wt% to 0.79 wt% respectively[12], an improvement over roasting with FeS_2 alone[11]. Additional research is necessary to determine if Sb and As sulfides here exhibit similar vaporization mechanisms as in the Cu_3AsS_4-rich concentrate. Se content decreased by 85% from 0.30 wt% to 0.04 wt%[12].

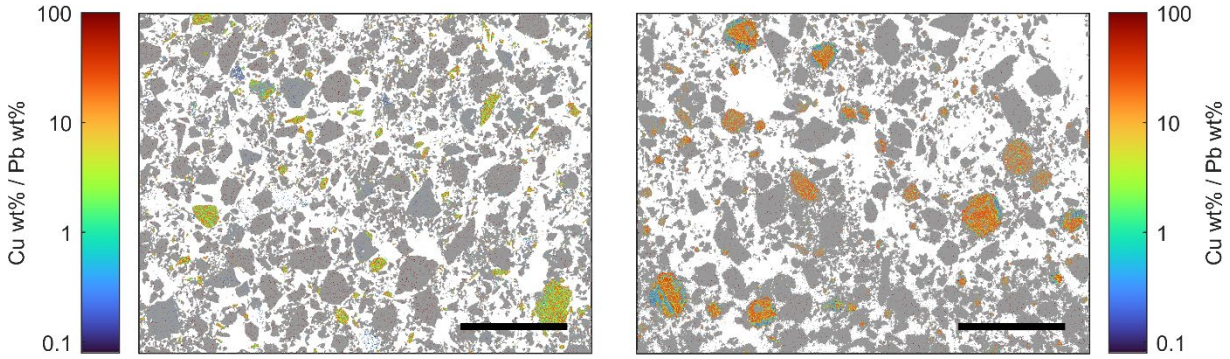

Figure 5.3: Copper to lead (Cu/Pb) ratio in tennantite ($Cu_{12}Sb_{0.6}As_{3.4}S_{13}$) ore before (left) and after (right) sulfidation. Spatial distributions of elements were mapped via SEM-EDS. Greenish-yellow phases correspond to $Cu_{12}Sb_{0.6}As_{3.4}S_{13}$, orange phases correspond to chalcopyrite ($CuFeS_2$), blue phases correspond to lead (Pb)-rich sulfide, and grey phases correspond to pyrite (FeS_2) and oxide / silicate gangue. Scale bar: 300 μm

This confirms that Se may be removed and potentially recovered from Cu mineral feedstocks upstream of smelting via pyrometallurgical sulfidation. Further analysis is required to determine whether Te exhibits analogous behavior during sulfidation. Crystalline SiO_2 content was observed to increase in the $Cu_{12}Sb_{0.6}As_{3.4}S_{13}$ ore during sulfidation due to the decomposition of muscovite ($KAl_2(AlSi_3O_{10})(F,OH)_2$) and kaolinite ($Al_2Si_2O_5(OH)_4$) phases, indicating that sulfidation remained selective for Cu compounds versus SiO_2 compounds in the presence of As, Sb, and Se impurities.

Dissolved lead (Pb) was expelled from Cu-containing phases during sulfidation, precipitating a Pb -rich sulfide as illustrated[12] in Figure 5.3. EPMA-WDS revealed that the Pb-rich phase was also enriched in bismuth (Bi) and silver (Ag), with an average composition of $Cu_{0.11}Ag_{0.09}Pb_{0.15}Bi_{0.15}S_{0.50}$. This finding suggests that in addition to management of As, Sb, and Se impurities, sulfidation may also be used as a pretreatment to improve physical separation of Pb and Bi during copper ore beneficiation and concentrate production[12]. Sulfidation is also demonstrated to crack sulfosalt anion chemistries for the selective precipitation of deleterious or product metal sulfides. In the following section, the behaviors of pnictogen impurities are afforded further attention in the context of phosphate compound sulfidation.

	Cu_3AsS_4-rich Concentrate		$Cu_{12}Sb_{0.6}As_{3.4}S_{13}$ Ore	
	Initial	**Sulfidized**	**Initial**	**Sulfidized**
Cu_3AsS_4 **(Enargite)**	43.9 wt%	< 0.1 wt%	< 0.1 wt%	< 0.1 wt%
$CuFeS_2$ **(Chalcopyrite)**	29.7 wt%	96 wt%	< 0.1 wt%	6.2 wt%
FeS_2 **(Pyrite)**	21.5 wt%	< 0.1 wt%	3.1 wt%	1.2 wt%
Cu_3SbS_4 **(Famatinite)**	4.9 wt%	< 0.1 wt%	< 0.1 wt%	< 0.1 wt%
$Cu_{12}Sb_{0.6}As_{3.4}S_{13}$ **(Tennantite)**	< 0.1 wt%	< 0.1 wt%	7.5 wt%	0.9 wt%
Lead sulfide (Galena or Angelaite)	< 0.1 wt%	< 0.1 wt%	< 0.1 wt%	0.9 wt%
SiO_2 **(Quartz)**	< 0.1 wt%	4.0 wt%	51.0 wt%	67.6 wt%
$KAl_2(AlSi_3O_{10})(F,OH)_2$ **(Muscovite)**	< 0.1 wt%	< 0.1 wt%	30.9 wt%	23.2 wt%
$Al_2Si_2O_5(OH)_4$ **(Kaolinite)**	< 0.1 wt%	< 0.1 wt%	7.5 wt%	< 0.1 wt%

Table 5.1: Crystalline phase contents in copper (Cu) feedstocks before and after sulfidation. Products were analyzed via QXRD[12].

	Cu_3AsS_4-rich Concentrate		$Cu_{12}Sb_{0.6}As_{3.4}S_{13}$ Ore	
	Initial	**Sulfidized**	**Initial**	**Sulfidized**
Cu	25.6 wt%	30.5 wt%	6.5 wt%	7.3 wt%
As	5.1 wt%	0.06 wt%	0.76 wt%	< 0.01 wt%
Sb	0.34 wt%	0.08 wt%	4.4 wt%	0.79 wt%
Se	< 0.01 wt%	< 0.01 wt%	0.30 wt%	0.04 wt%

Table 5.2: Copper (Cu), arsenic (As), antimony (Sb), and selenium (Se) contents in Cu feedstocks before and after sulfidation. Products analyzed via ICP-AES[12].

5.2 Sulfidation of Rare Earth Phosphate, Oxyfluoride, and Monazite

The most commercially relevant sources of lanthanide (Ln) rare earth minerals are bastnaesite ($LnCO_3F$) and monazite/xenotime ($LnPO_4$)[15]. The normally occurring radioactive materials (NORMs) uranium (U) and thorium (Th) are also present. Rare earth elements are currently extracted from primary sources using a series of hydrometallurgical processing steps[16]. Following mining and physical beneficiation, rare earth minerals are digested or "cracked" using alkaline fusion or acid roasting to produce soluble rare earth compounds[15]. These compounds

are then dissolved in acidic solution for aqueous-organic liquid-liquid solvent extraction (SX). Cracking of rare earth minerals is operated as the one of the only "targeted" processes in the beneficiation pathway, aiming to sequester Th and a significant fraction of cerium (Ce) in insoluble compounds prior to leaching and downstream SX[16]. Currently, environmental impacts are concentrated in cracking, dissolution, and solvent extraction steps[17]. Technical improvements have been proposed to reduce the intensity of hydrometallurgical routes[18], yet significant economic and environmental burdens remain. Different primary separation pathways have also been proposed, ranging from halogenation with chemical vapor transport[19] to borate crystallization[20] to selective reduction of rare earth oxides[21] (REOs). Merritt demonstrated sulfidation of rare earth phosphate minerals with hydrogen sulfide (H_2S) in the presence of alkaline and alkaline-earth compounds[22], finding that phosphorous (P) could be sequestered in alkaline and alkaline-earth compounds, NORMs in oxide phases, and rare earth elements in oxysulfide phases. These findings illustrate that sulfide-based separation chemistries are promising alternatives to legacy, environmentally degrading processing pathways.

5.2.1 Sulfidation of Lanthanum Phosphate and Oxyfluoride

Conditions for the selective sulfidation of rare earth elements from mixed oxides were modelling in Chapter 3, Section 3.1 and demonstrated experimentally in Chapter 4, Sections 4.3 and 4.4. To test the efficacy of oxide-sulfide anion exchange directly on $LnCO_3F$ and $LnPO_4$ feedstocks, sulfidations were conducted on pure lanthanum phosphate ($LaPO_4$) and oxyfluoride ($LaOF$)[23]. Anhydrous $LaPO_4$ was produced by dehydrating lanthanum phosphate hydrate ($LaPO_4 * xH_2O$) at a temperature of 1200 °C over the course of 3 hours under an argon (Ar) atmosphere[23]. Rare earth fluorocarbonate is known to decompose to oxyfluoride when heated[24]. $LaOF$ was therefore synthesized directly by heating a stoichiometric mixture of lanthanum sesquioxide (La_2O_3) and lanthanum fluoride (LaF_3) at 1427 °C for 28 hours in a graphite crucible under argon[23].

Sulfidation of $LaPO_4$ was conducted at temperatures of 1200 °C and 1350 °C with and without carbothermically-driven sulfur reflux (CDSR) following the methodologies described in Chapter 3, Section 3.3 and by the author elswhere[23]. $LaPO_4$ sulfidation products[23] quantified via QXRD are reported in Table 5.3. No crystalline La_2O_3, oxysulfide (La_2O_2S), or intermediate

sulfide (La_3S_4) products were observed at 1200 °C with marginal La_2O_2S formation at 1350° C. Some unknown product phases were also observed, likely corresponding to previously uncharacterized thiophosphate compounds (Section 5.2.2). These results indicate that rare earth phosphates show lower tendencies toward sulfidation than their corresponding oxides with or without CDSR. This trend may be due to the formation of gaseous phosphorous pentoxide[xii] (P_4O_{10}) or phosphorous pentasulfide (P_4S_{10}) during sulfidation. These are relatively large gas molecules, which are entropically unfavorable products compared to diatomic reactant S_2 due to their possession of fewer degrees of freedom per atom in the gas phase (Chapter 3, Section 3.1.2 and Figure 3.1). Concurrently, phosphates may exhibit substantially different intrinsic sulfidation kinetics. Further work is necessary however to understand the differences in sulfidation rate and thermodynamic affinity between oxide and phosphate species.

To minimize P-containing gas phase limitations to conversion, sulfidation of $LaPO_4$ was also conducted in the presence of calcium carbonate ($CaCO_3$), which served as a condensed P "collector" phase[xiii]. Following sulfidation at 1200 °C of a mixture of $LaPO_4$ and $CaCO_3$, La_2O_2S, La_3S_4, calcium sulfide (CaS), and calcium phosphate ($Ca_3(PO_4)_2$) products[23] were observed as reported in Table 5.3. These results indicate that the presence of a dedicated phosphate collector phase can aid in selective sulfidation of rare earth phosphates such as $LnPO_4$. Further research is necessary however to differentiate improvements to sulfidation tendencies due to more favorable thermodynamic solution effects versus intrinsically improved reaction kinetics.

Sulfidation of $LaOF$ was also conducted in the presence of $CaCO_3$ collector phase at a temperature of 1200 °C using methods described in Chapter 3, Section 3.3 and by the author elsewhere[23]. As determined via QXRD and reported in Table 5.4, some crystalline CaS, La_2O_2S, La_3S_4, and oxyfluorosulfide phases were identified, with the majority of phases being unidentified[23]. The formation of oxyfluorosulfide and other phases complicates direct sulfidation of fluorocarbonates such as bastnaesite, yet may provide additional opportunities for selective

[xii] Phosphorous pentoxide and pentasulfide have empirical formulas of P_2O_5 and P_2S_5 respectively, yet exhibit molecular formulas of P_4O_{10} and P_4S_{10}.

[xiii] Following the methodology in Chapter 3, Section 3.1.3, a critical ratio of P_4O_{10} and oxygen (O_2) partial pressures ($\left[P_{P_4O_{10}}/P_{O_2}\right]_{crit}$) may be derived to describe an oxide's relative affinity for phosphate formation. Some oxides ordered by increasing phosphate formation affinity at 1200° C are $SiO_2 < Fe_2O_3 < Al_2O_3 < MgO < La_2O_3 < CaO < Li_2O < BaO < Na_2O < K_2O_2$.

rare earth separation of fluorocarbonate feedstocks into multiple distinct phases. Alternatively, defluorination of $LnCO_3F$ is readily accomplished via roasting with sodium carbonate (Na_2CO_3), forming REO, CO_2, and water-soluble sodium fluoride (NaF) that is easily removable via washing[16,25]. Selective sulfidation could then be conducted on the resulting mixed REO. Defluorination prior to sulfidation would also serve to reduce the burden of sulfur hexafluoride (SF_6) management from direct oxyfluoride sulfidation. A variety of conventional and emerging methods exist for SF_6 abatement[26]. Further testing of sulfidation on $LnCO_3F$ is necessary to elucidate trends in fluorine (F) management and sulfidation selectivity. In the following section, sulfidation is conducted on natural $LnPO_4$ mineral in the presence of both rare earth and phosphate collector phases.

Temperature	**As dehydrated**	**1200°C**	**1200°C**	**1350°C**	**1200°C**
Reaction Time	-	1 hour	1 hour	1 hour	1 hour
$C/LaPO_4$ Mass Ratio	-	-	0.05	0.05	-
$CaCO_3/LaPO_4$ Mass Ratio	-	-	-	-	1
$LaPO_4$	>99.9 wt%	96.2 wt%	99.8 wt%	98.9 wt%	21.0 wt%
CaS	-	-	-	-	36.5 wt%
$Ca_3(PO_4)_2$	-	-	-	-	33.2 wt%
La_2O_2S	-	<0.1 wt%	<0.1 wt%	1.1 wt%	3.3 wt%
La_3S_4	-	<0.1 wt%	<0.1 wt%	<0.1 wt%	3.0 wt%
Unknown	<0.1 wt%	3.8 wt%	0.2 wt%	<0.1 wt%	3.0 wt%

Table 5.3: Lanthanum phosphate ($LaPO_4$) sulfidation conditions with feedstock and product compositions. Compositions were determined via QXRD[23].

5.2.2 Sulfidation of Monazite

Crushed natural $LnPO_4$ mineral, iron sesquioxide (Fe_2O_3), and $CaCO_3$ were utilized as sulfidation feedstocks. Fe_2O_3 served as a rare earth element collector upon sulfidation (Chapter 4, Section 4.4) and $CaCO_3$ served as a phosphate collector (Section 5.2.1). Two blends of materials were sulfidized in separate alumina (Al_2O_3) reactors at 1200 °C using methods described in Chapter 3, Section 3.3 and by the author elsewhere[27]: one free of $CaCO_3$ containing

equal parts by mass of $LnPO_4$ and Fe_2O_3 and one containing $LnPO_4$, Fe_2O_3, and $CaCO_3$ in a 3:3:2 mass ratio.

Temperature	As synthesized	1200°C
Sulfidation Reaction Time	na	1 hour
$CaCO_3/LaOF$ Mass Ratio	na	1
La_2O_3	<0.1 wt%	<0.1 wt%
LaF_3	<0.1 wt%	<0.1 wt%
$LaOF$	95.2 wt%	<0.1 wt%
La_3S_4	-	present
CaS	-	present
$La-S-O-F$	-	present
Unknown	4.8 wt%	major

Table 5.4: Lanthanum oxyfluoride ($LaOF$) sulfidation conditions with feedstock and product compositions. Compositions were determined via QXRD[23].

Compositions of major product phases were analyzed using SEM-EDS[27] and EPMA-WDS following sulfidation with and without $CaCO_3$. Composition measured via EPMA-WDS are reported in Table 5.5. Both SEM-EDS[27] and EPMA-WDS analyses showed that sulfidation without $CaCO_3$ resulted in the formation of rare earth phosphate ($LnPO_4$) and iron sulfide (FeS) product phases, confirming that limited rare earth phosphate sulfidation occurs without a phosphorous collector phase. However, SEM/EDS faced challenges in differentiating individual dilute light rare earth elements solubilized in the FeS product[27]. EPMA-WDS provided improved analytical resolution for individual light rare earth elements; samarium (Sm) and lanthanum (La) were found to be enriched in the FeS collector phase versus cerium (Ce), neodymium (Nd), praseodymium (Pr), and gadolinium (Gd). Dilute heavy rare earth elements were also ostensibly present in feedstocks and sulfidation products, but fell below the detection limits of both SEM-EDS and EPMA-WDS.

Separation factors (β_{sep}), defined as the ratio of the distribution coefficients between phases (Chapter 2, Section 2.1), are reported in Table 5.5 between FeS and $LnPO_4$ phases. β_{sep} for Sm and Nd, Pr, and Gd exceed conventional industrial hydrometallurgical β_{sep}[16] by two

orders of magnitude and geologic β_{sep}observed between oxide and sulfide phases in chondrite meteorites by an order of magnitude (Chapter 2, Table 2.3). These results illustrate that even in the presence of bulk phosphate compounds and impurities, sulfidation remains selective.

Sulfidation of the mixed monazite, Fe_2O_3, and $CaCO_3$ resulted in the formation of at least 7 major product phases as identified via EPMA-WDS and reported in Table 5.4: rare earth phosphate ($LnPO_4$), iron-rich sulfide (FeS), calcium-rich oxysulfide ($Ca-O-S$), calcium and rare earth-rich oxysulfide ($Ca-Ln-O-S$), calcium and rare earth-rich phosphate ($Ca-Ln-O-P$), rare earth-rich thiophosphate ($Ln-O-P-S$), and iron-rich thiophosphate ($Fe-O-P-S$). The FeS phase was observed to again be enriched in Sm, albeit less selectively than in the absence of the $CaCO_3$ phosphate collector. Here, the FeS phase was also slightly enriched in Ce as opposed to La as in the trial without $CaCO_3$ addition.

These results suggest that when a phosphate collector is present to enable improved $LnPO_4$ cracking via sulfidation, rare earth sulfidation selectivity into the FeS collector phase actually decreases. In essence, rare earth elements' affinities for phosphate formation inhibit sulfidation, enabling only the rare earth elements with the largest solution driven increases in sulfidation affinity to be sulfidized with the FeS collector phase. The results confirm that sulfidation remains selective in the presence of non-chalcogenide anions and suggest that phosphate, sulfide, and Fe driven solution effects accentuate minute chemical and thermodynamic differences between individual rare earth elements. The addition of P donator or collector phases can be envisioned to tune the selectivity of oxide-sulfide anion exchange or sulfide collector phases in other material systems, similar to the possible role of boron (B) observed in rare earth magnet recycling via selective sulfidation[23] (Chapter 4, Section 4.4.1). Meanwhile, sulfidation may be promising for targeted synthesis of thiophosphate compounds with applications ranging from froth flotation[28,29] to lubrication[30] to battery materials[31] and catalysts[32].

	No $CaCO_3$		With $CaCO_3$						
	$LnPO_4$	FeS	$LnPO_4$	FeS	$Ca-O-S$	$Ca-Ln-O-S$	$Ca-Ln-O-P$	$Ln-O-P-S$	$Fe-O-P-S$
Ca	0.12 wt%	0.03 wt%	0.40 wt%	1.10 wt%	37.99 wt%	11.65 wt%	21.68 wt%	14.33 wt%	20.27 wt%
Fe	0.30 wt%	61.95 wt%	<0.01 wt%	57.27 wt%	4.67 wt%	3.66 wt%	1.75 wt%	4.22 wt%	13.27 wt%
La	11.36 wt%	0.24 wt%	13.94 wt%	0.28 wt%	3.36 wt%	11.37 wt%	6.45 wt%	8.29 wt%	4.57 wt%
Ce	22.56 wt%	0.14 wt%	27.33 wt%	0.81 wt%	7.53 wt%	25.80 wt%	11.96 wt%	16.86 wt%	9.06 wt%
Pr	3.99 wt%	<0.01 wt%	4.39 wt%	<0.01 wt%	1.14 wt%	3.33 wt%	2.45 wt%	2.48 wt%	1.11 wt%
Nd	8.65 wt%	<0.01 wt%	10.59 wt%	<0.01 wt%	3.46 wt%	8.56 wt%	5.87 wt%	6.73 wt%	3.87 wt%
Sm	2.13 wt%	0.29 wt%	1.80 wt%	0.14 wt%	1.04 wt%	1.75 wt%	1.10 wt%	1.40 wt%	1.14 wt%
Gd	2.44 wt%	<0.01 wt%	3.17 wt%	<0.01 wt%	0.38 wt%	2.37 wt%	0.97 wt%	1.72 wt%	1.21 wt%
O	32.59 wt%	<0.01 wt%	25.82 wt%	1.83 wt%	10.31 wt%	5.92 wt%	29.13 wt%	23.12 wt%	23.42 wt%
P	15.80 wt%	0.14 wt%	12.57 wt%	0.69 wt%	4.41 wt%	2.77 wt%	12.67 wt%	7.39 wt%	10.68 wt%
S	0.05 wt%	37.20 wt%	<0.01 wt%	37.88 wt%	25.71 wt%	22.83 wt%	5.97 wt%	13.47 wt%	11.41 wt%

Table 5.5: Compositions of major sulfidation product phases of monazite ($LnPO_4$) and iron sesquioxide (Fe_2O_3) sulfidized with and without calcium carbonate ($CaCO_3$). Compositions were identified via EPMA-WDS.

	Ce	Pr	Nd	Sm	Gd
La	3.40	>8.37	>18.1	6.59	>5.12
Ce		>2.46	>5.34	22.4	>1.50
Pr			na	>55.1	na
Nd				>120	na
Sm					>33.7

Table 5.6: Separation factors (β_{sep}) for lanthanides (Ln) between sulfide and phosphate product phases following sulfidation of monazite ($LnPO_4$) and iron sesquioxide (Fe_2O_3) without calcium carbonate ($CaCO_3$).

5.3 Summary

In Chapter 2, it was hypothesized that oxide-sulfide anion exchange decreases the solubility of target cation elements in feedstock materials to support their selective extraction and physical separation. Following methodologies reported in Chapter 3, this hypothesis was confirmed in Chapter 4 for oxide and sulfide-based system chemistries. However, anion impurities such as pnictogens, other chalcogenides, and halides are sometimes present in mineral or industrial feedstocks. Herein, the efficacy of selective sulfidation in the presence of phosphorous, arsenic, antimony, selenium, tellurium, and fluorine were briefly considered using sulfidation case studies for copper and rare earth mineral feedstocks.

These results illustrate that pyrometallurgical oxide-sulfide anion exchange remains a powerful tool for material processing even in the presence of other anion chemistries. Phosphorous can lower sulfidation affinities while increasing the selectivity of sulfidation in conjunction with collector phases. Meanwhile, arsenic, antimony, and selenium impurities in sulfosalts are experimentally confirmed to readily form volatile sulfides, enabling their separation and abatement. Sulfidation of oxyfluorides and phosphates can enable the formation of oxyfluorosulfides and thiophosphates respectively, which may provide new avenues for materials separation or synthesis. Overall, pyrometallurgical oxide-sulfide anion exchange is confirmed to support the selective extraction of key elements and manage impurities in industrially relevant materials systems. In the following chapter, technoeconomic and environmental impacts are considered in the context of industrial deployment of selective sulfidation for materials separations.

5.4 References

1. Schlesinger, M. E., King, M. J., Sole, K. C. & Davenport, W. G. *Extractive Metallurgy of Copper*. (2011). doi:10.1017/CBO9781107415324.004.
2. Rush, L. T. Integrative approach to metal extraction and electrification. (Massachusetts Institute of Technology, 2021).
3. Flores, G. A., Risopatron, C. & Pease, J. Processing of complex materials in the copper

industry: challenges and ppportunities ahead. *Jom* **72**, 3447–3461 (2020).
4. Oppenheim, A. L. The Seafaring Merchants of Ur. *J. Am. Orient. Soc.* **74**, 6–17 (1954).
5. Lechtman, H. & Klein, S. The production of copper-arsenic alloys (arsenic bronze) by cosmelting: modern experiment, ancient practice. *J. Archaeol. Sci.* **26**, 497–526 (1999).
6. AME. *Copper - dealing with impurities*. (2017).
7. Kavlak, G. & Graedel, T. E. Global anthropogenic selenium cycles for 1940-2010. *Resour. Conserv. Recycl.* **73**, 17–22 (2013).
8. Kavlak, G. & Graedel, T. E. Global anthropogenic tellurium cycles for 1940-2010. *Resour. Conserv. Recycl.* **76**, 21–26 (2013).
9. Henao, H., Paredes, I., Diaz, R. & Ortiz, J. Characterization and pyrometallurgical removal of arsenic from copper concentrate roasting dust. *J. Miner. Mater. Charact. Eng.* **09**, 609–620 (2021).
10. Adham, K. & Lee, C. Fluid Bed Roasting of Metal Ores and Concentrates for Arsenic Removal. in *Towards Clean Metallurgical Processing for Procfit, Social, and Environmental Stewardship* 109–116 (2012).
11. Safarzadeh, M. S. & Miller, J. D. The pyrometallurgy of enargite: A literature update. *Int. J. Miner. Process.* **157**, 103–110 (2016).
12. Stinn, C., Gutierrez, C., Daehn, K. & Allanore, A. Sulfidation for Copper Mineral Processing and Impurity Management. in *The Igo Wilkomirsky Symposium on Pyrometallurgy* (ed. IIMCh) 785–796 (Copper 2022, 2022).
13. Houngaloune et al. Stabilization of arsenic in the mining and metallurgical industries - a review. *23rd World Min. Congr.* 1–14 (2013).
14. Whelan, J. M., Struthers, J. D. & Ditzenberger, J. A. Separation of sulfur, selenium, and tellurium from arsenic. *J. Electrochem. Soc.* **107**, 982 (1960).
15. Jordens, A., Cheng, Y. P. & Waters, K. E. A review of the beneficiation of rare earth element bearing minerals. *Miner. Eng.* **41**, 97–114 (2013).
16. Zhao, B., Zhang, J. & Schreiner, B. *Separation Hydrometallurgy of Rare Earth Elements*. (Springer International Publishing AG Switzerland, 2016).
17. Bailey, G. *et al.* Review and new life cycle assessment for rare earth production from bastnäsite, ion adsorption clays and lateritic monazite. *Resour. Conserv. Recycl.* **155**, 104675 (2020).

18. Li, X. Z. *et al.* A supramolecular lanthanide separation approach based on multivalent cooperative enhancement of metal ion selectivity. *Nat. Commun.* **9**, 547 (2018).
19. Wang, Z. C., Zhang, L. Q., Lei, P. X. & Chi, M. Y. Rare earth extraction and separation from mixed bastnaesite-monazite concentrate by stepwise carbochlorination-chemical vapor transport. *Metall. Mater. Trans. B Process Metall. Mater. Process. Sci.* **33**, 661–668 (2002).
20. Yin, X. *et al.* Rare earth separations by selective borate crystallization. *Nat. Commun.* **8**, (2017).
21. Nakanishi, B. R. & Allanore, A. Electrochemical Investigation of Molten Lanthanum-Yttrium Oxide for Selective Liquid Rare-Earth Metal Extraction. *J. Electrochem. Soc.* **166**, E420–E428 (2019).
22. Merritt, R. R. High Temperature Methods for Processing Monazite: II. Reaction with Sodium Carbonate. *J. Less-Common Met.* **166**, 211–219 (1990).
23. Stinn, C. & Allanore, A. Selective sulfidation of metal compounds. *Nature* **602**, 78–83 (2022).
24. Zhao, L. *et al.* Thermal decomposition and oxidation of bastnaesite concentrate in inert and oxidative atmosphere. *J. Rare Earths* **36**, 758–764 (2018).
25. Chi, R., Li, Z., Peng, C., Gao, H. & Xu, Z. Preparation of enriched cerium oxide from bastnasite with hydrochloric acid by two-step leaching. *Metall. Mater. Trans. B Process Metall. Mater. Process. Sci.* **37**, 155–160 (2006).
26. Parthiban, A., Gopal, A. A. R., Siwayanan, P. & Chew, K. W. Disposal methods, health effects and emission regulations for sulfur hexafluoride and its by-products. *J. Hazard. Mater.* **417**, 126107 (2021).
27. Stinn, C., Kaker, V., Adams, Z. K. & Allanrore, A. Separation of Rare Earth Elements from Monazite Via Sulfidation. in *Rare Metal Technology 2023* (ed. Ouchi, T.) (The Minerals, Metals & Materials Society, 2023). doi:10.2472/jsms.12.559.
28. Burwell, B. T. Process and Reagent for Recovery of Molybdenite from Copper Sulfide-Molybdenite Flotation Concentrates. (1968) doi:10.1145/178951.178972.
29. McCarthy, J. R. Reagent for Froth Flotation of Bituminous Coal. (1983).
30. Delfort, B., Born, M., Daoudal, B. & Chivé, A. Colloidal thiophosphorus calcium salt as antiwear additive. *Lubr. Sci.* **8**, 129–143 (1996).

31. Ghidiu, M., Ruhl, J., Culver, S. P. & Zeier, W. G. Solution-based synthesis of lithium thiophosphate superionic conductors for solid-state batteries: A chemistry perspective. *J. Mater. Chem. A* **7**, 17735–17753 (2019).
32. Song, J. *et al.* Sub-2 nm Thiophosphate Nanosheets with Heteroatom Doping for Enhanced Oxygen Electrocatalysis. *Adv. Funct. Mater.* **31**, 1–9 (2021).

Chapter 6

Technoeconomic and Environmental Assessment of Selective Sulfidation

Oxide-sulfide anion exchange is proposed to be a promising avenue to improve the efficacy and efficiency of metals extraction and processing. In Chapter 2, it was hypothesized that increasing the selectivity of pyrometallurgical processes via oxide-sulfide anion exchange reduces the need for subsequent hydrometallurgy, potentially lowering the cost and environmental impact of materials separations. In Chapters 4 and 5, selective sulfidation was successfully demonstrated for a range of mineral and industrial feedstocks. Those experimental results illustrated that material separations previously requiring a series of tedious, hydrometallurgical processes may now be replaced with a single pyrometallurgical operation followed by physical separation. Oxide-sulfide anion exchange via selective sulfidation may therefore enable process intensification in the domain of metals processing.

Following the framework proposed in Chapter 3, capital cost, operating cost, global warming potential, terrestrial acidification, and water resource demand are estimated herein for selective sulfidation. Cost and sustainability metrics are modelled across generalized process flowsheets for a wide range of chemistries and operating conditions. These results are compared with equivalent hydrometallurgical pathways as appropriate. The results herein contextualize the promising thermodynamic, kinetic, and separation outcomes from Chapters 3, 4 and 5 in the sustainability and technoeconomic landscapes of decarbonizing metals processing.

6.1 Technoeconomic Assessment of Materials Separation via Selective Sulfidation

6.1.1 Capital Costs for Materials Separation via Selective Sulfidation

To understand the economic implications of material processing via selective sulfidation, the capital cost(s) (CAPEX) of four generic material separations are estimated. These are selective sulfidation with and without feed pretreatments, each with and without carbothermically-driven sulfur reflux (CDSR). Process flow diagrams are included in Chapter 3, Figures 3.10-3.13. For selective sulfidation and physical separation without pretreatment, the following process blocks are employed: nitrogen separation from air for sulfidation carrier gas production, sulfidation in a multihearth fluidized bed reactor, comminution, physical separation via froth flotation, and waste gas stream handling via a cyclone separator, followed by either electrostatic solids precipitation and dual alkali scrubbing (when CDSR is utilized in sulfidation) or sulfuric acid production (No CDSR). Feedstocks containing impurities such as normally occurring radioactive materials (NORMs) or anions other than oxygen (O) and sulfur (S) may require additional pretreatments prior to selective sulfidation (Chapter 5). The CAPEX of selective sulfidation with some possible material feed preparation / pretreatment steps are also considered, such as feed drying, calcination for defluorination of fluorocarbonate minerals or lithium ion battery (LIB) electrolytes and oxidation of mixed metal compounds such as rare earth magnets, sulfidation for dephosphorization of phosphate minerals and dethoriation of rare earth concentrates, and sulfidation/calcination for sintering of material feeds too finely ground for effective liberation and physical separation of sulfide precipitants post selective sulfidation. Operating conditions for selective sulfidation are reported in Chapters 4 and 5 and by the author elsewhere[1,2].

The CAPEX of equivalent generic hydrometallurgical processes are estimated for comparison with selective sulfidation. Their flowsheets consist of acid roasting for impurity removal and formation of soluble metal compounds, gas treatment via acid plant, leaching of the target elements, solvent extraction (SX) for metal element separation, and precipitation of product metal compounds[1]. Operating conditions are reported by the author elsewhere[1]. The

liquid-liquid separation effectiveness for two metals (M_1 and M_2) achieved by an aqueous-organic separation system is described by the hydrometallurgical separation factor[3] β_{sep}, defined previously in Chapter 2, Eqn. 2.1. Generally, industrially-realized separation factors range from near one for many binary rare earth separations into the thousands and tens of thousands for some binary transition metal separations[3–5]. Four scenarios for β_{sep} are considered for SX in the hydrometallurgical separation pathway: pulsed-column and mixer-settler liquid-liquid contactors, each at separation factors of 1.5 and 10,000 corresponding to f and d-block hydrometallurgical element separations respectively[1].

For the generic hydrometallurgical and selective sulfidation based pathways, the feedstock is assumed to be an equimolar mixture of two metal oxides, with chemistry represented by copper(I) oxide (Cu_2O), nickel oxide (NiO), or neodymium oxide (Nd_2O_3)[1]. Feed capacities ranging from 10,000 to 1,000,000 tonnes per year are considered. Product purities of 99% are assumed following separation of the binary oxide feed. The economics of upstream beneficiation and comminution processes and downstream metal reduction processes are taken to be largely unchanged for either the solvent extraction or selective sulfidation pathways[1].

For cost analysis, Class 4 (+/- 30% accuracy) estimates are utilized as described by the American Association of Cost Engineers (AACE) International[6–9]. Class 4 CAPEX estimates employ scaling relations based on individual unit operations, making them useful for high-level comparison of technologies. A typical scaling relation for CAPEX is as follows, where a_c is a pre-exponential factor and P_c is the relevant metric by which the operation is scaled (typically size or throughput), and n is an exponent corresponding to the economy of scale[7]:

$$\text{CAPEX} = a_c {P_c}^n \tag{6.1}$$

Class 4 CAPEX estimates do not replace the insight gained from detailed design work however; they only illustrate general trends[9]. Nevertheless, solvent extraction is a well-established technology that affords a good understanding of its capital framework and individual unit operations[3,8]. Meanwhile, selective sulfidation as envisioned herein employs a high temperature fluidized bed multihearth reactor, such as currently employed for calcination, and orthodox physical separations[1], all relying on well-documented unit operations with quantifiable

economics[8]. Therefore, a Class 4 CAPEX analysis for selective sulfidation and solvent extraction is based in a convention that supports reasonable comparison of hypothetical process economics.

Scaling relations for capital cost are determined using the factorial method[7,8], described below. The total fixed capital cost, or total module cost (C_T) of a processing block may be determined through the following relation[1]:

$$C_T = a_{LF} a_{TM} a_{BM} a_{PM} a_{LM} a_{FOB} \left(\frac{I_y}{I_R}\right) {P_c}^n \tag{6.2}$$

a_{LF}, a_{TM}, a_{BM}, a_{PM}, a_{LM}, and a_{FOB} are scaling preexponential factors. I_y is the cost index for the year utilized for the estimate, here the 2020 Chemical Engineering Plant Cost Index[10] (CEPCI), whereas I_R is the reference cost index. a_{FOB} corresponds to the free on board scaling factor to determine the free on board purchase price (C_{FOB}) of a given piece of equipment as a function of the relevant scaling metric and herein includes material factors[1]:

$$C_{FOB} = a_{FOB} \left(\frac{I_y}{I_R}\right) {P_c}^n \tag{6.3}$$

a_{LM} corresponds to the scaling factor to account for instruments and buildings within the battery limit. a_{PM} corresponds to the scaling factor to include taxes, freight, and insurance associated with installation of the process block. The physical module cost (C_{PM}) of the process block is described as follows[1]:

$$C_{PM} = a_{PM} a_{LM} a_{FOB} \left(\frac{I_y}{I_R}\right) {P_c}^n \tag{6.4}$$

The inside battery limits (ISBL) cost (C_{ISBL}) of the process is taken as the sum of C_{PM} for the processing blocks[1]:

$$C_{ISBL} = \sum \left(a_{PM} a_{LM} a_{FOB} \left(\frac{I_y}{I_R}\right) {P_c}^n \right) \tag{6.5}$$

a_{TM} and a_{BM} correspond to scaling factors for offsites/indirect/field expenses and design/engineering/contingency respectively. a_{LF} is a location factor to scale CAPEX between different geographic regions. The total fixed capital cost, or total module cost, (C_{FC}) of the full process may be described as the sum of the total module costs of each process block[1]:

$$C_{FC} = \sum \left(a_{LF} a_{TM} a_{BM} a_{PM} a_{LM} a_{FOB} \left(\frac{I_y}{I_R} \right) {P_c}^n \right) \tag{6.6}$$

a_{LF}, a_{TM}, a_{BM}, a_{PM}, a_{LM}, a_{FOB}, P_c, I_y, I_R and n for relevant processing operations for both the hydrometallurgical and sulfidation processing pathways are included by the author elsewhere[1].

Figure 6.1 compares the total fixed CAPEX for a materials separation facility based on conventional liquid-liquid hydrometallurgy versus oxide-sulfide anion exchange via selective sulfidation[1]. For the generic binary separation of equimolar mixed metal oxides, the selective sulfidation pathway is predicted to exhibit a 65-90% reduction in CAPEX compared to hydrometallurgical separation at β_{sep} of 1.5-10,0000, representative of SX for f-block elements and d-block elements separation respectively[1]. Attribution of CAPEX to individual processing steps in the sulfidation pathway without pretreatments are presented[1] in Figure 6.2. Individual pretreatment steps for feed drying, sintering, and roasting/calcination each marginally increase the CAPEX of selective sulfidation by 10% to 20%[1], as tabulated in Table 6.1. The low CAPEX burdens of drying, sintering, and calcination pretreatments are well established industrially, where all of these processes are already utilized effectively in low-margin commodity-scale processing of metals and minerals[1]. Sensitivity analysis for CAPEX estimation is discussed in Section 6.1.3.

The large reduction in CAPEX between hydrometallurgical separation and selective sulfidation is driven by to two main factors:

- The relative volume of reactors and materials processed
- The relative number of reactors and unit operations required to achieve a given material separation.

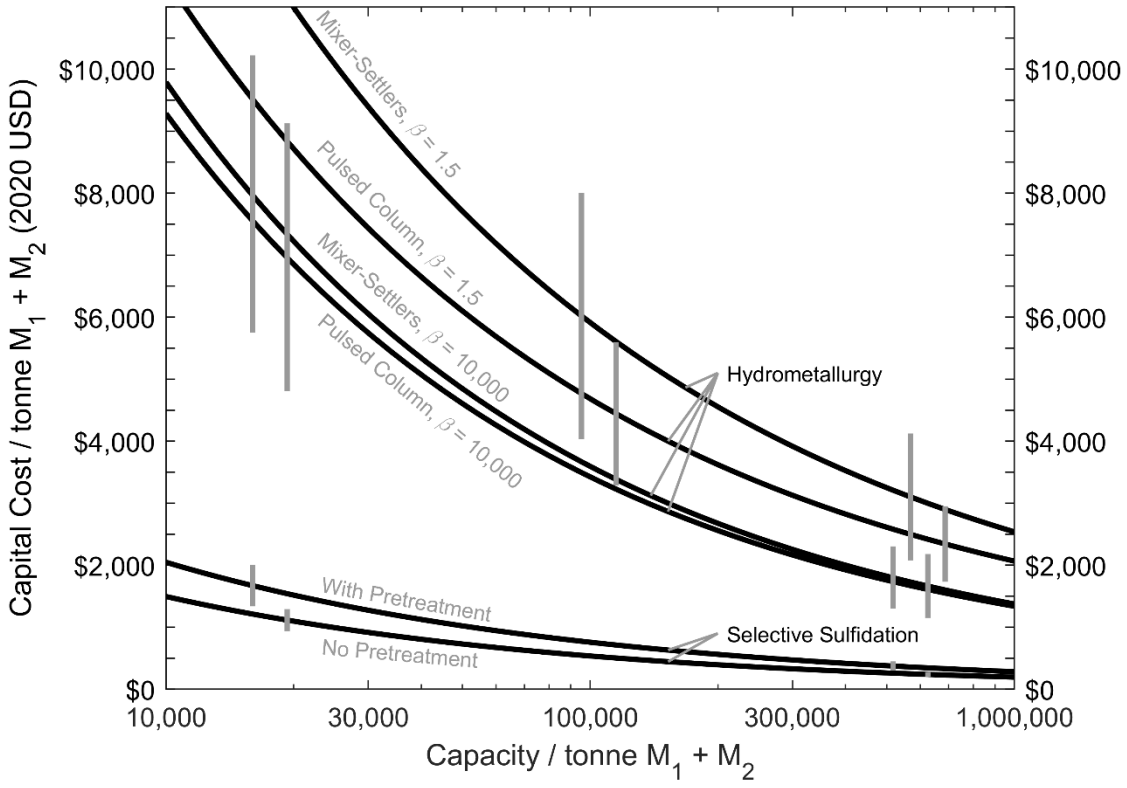

Figure 6.1: Capital cost (CAPEX) estimates for selective sulfidation coupled with physical separation, compared with conventional hydrometallurgical processing. Selective sulfidation with physical separation is predicted to exhibit lower total fixed capital costs for binary metal oxide (M_1, M_2) separations than conventional mixer-settler or pulsed column liquid-liquid hydrometallurgy with acid roasting and leaching pretreatments, for both transition metals (hydrometallurgical separation factor $\beta_{sep} = 10{,}000$) and rare earth metals ($\beta_{sep} = 1.5$). Error bars correspond to +/- one standard deviation, as determined through Monte Carlo simulation (Section 6.1.3).

In hydrometallurgical processing operations that require complete dissolution of feedstocks, such as liquid-liquid solvent extraction, solids are generally diluted during dissolution to concentrations on the order of 1 M industrially[3]. For an f-block oxide with a molar mass (m^*) of 350 g and a density of 7 g/cm^3, dissolution of the material to a concentration of 1 M corresponds to a 20 times dilution by volume of the feedstock. Therefore, hydrometallurgical reactors must process much higher total volumes of material that an equivalent pyrometallurgical sulfidation reactor where feedstock require no dilution.

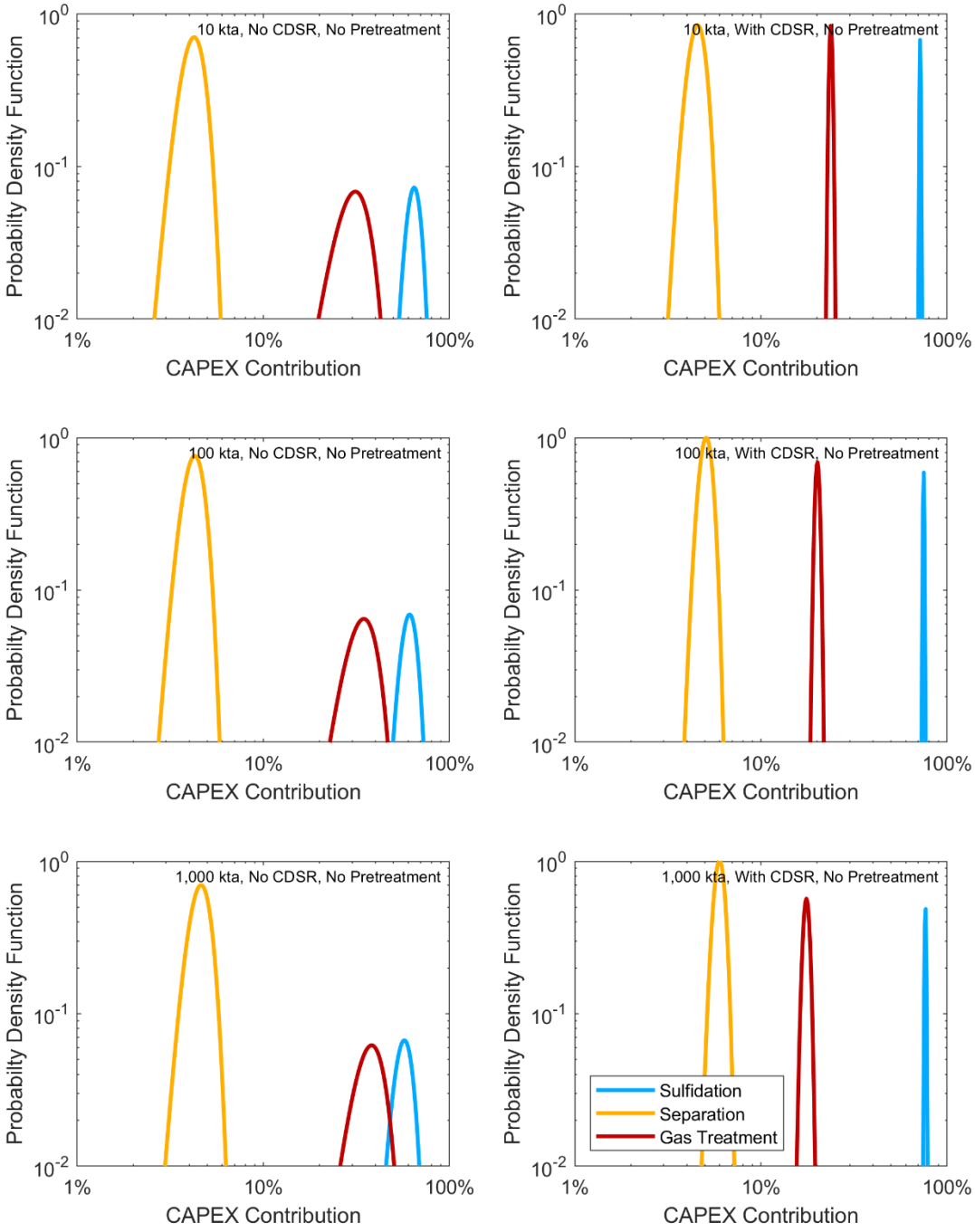

Figure 6.2: Capital cost (CAPEX) contributions for selective sulfidation. CAPEX for individual processing steps with and without CDSR without pretreatment, corresponding to the flowsheets in Chapter 3, Figures 3.10 and 3.11. Probability distributions are determined using Monte Carlo simulation (Section 6.1.3).

Materials fabrication costs for acids handling and pyrometallurgical processing are known to be approximately the same order of magnitude for a given reactor size[8,11]. Hydrometallurgical separation pathways however require many more processing steps than oxide-sulfide anion exchange via selective sulfidation/desulfidation[1]. Solvent extraction typically requires between 5 and 150 stages for transition metal and rare earth metal separation respectively[3–5,12]. In contrast, experimental results shown in Chapter 4, Section 4.4.1, Chapter 5, Section 5.2.2, and later in Chapter 7, Section 7.3.1, β_{sep} for rare earth separations via selective sulfidation may be in the hundreds, thousands, or higher, potentially enabling single stage separation for some rare earth element pairs. Fewer reactor stages, coupled with higher material concentrations, leads to smaller reactors for a given process residence time.

Separation performance and conditions in Chapters 4 and 5 would suggest that residence times on the order of an hour or two can be effective for selective sulfidation. Liquid-liquid separation generally requires a residence time of 5 to 10 minutes for each extraction and stripping stage[3]. When hydrometallurgical stage counts and dilutions are considered, selective sulfidation still benefits from reactor volumes that are one or more orders of magnitude smaller than equivalent liquid-liquid separation pathways, justifying the much lower CAPEX predicted for selective sulfidation over established hydrometallurgical processing.

6.1.2 Operating Costs for Materials Separation via Selective Sulfidation

While direct comparison of CAPEX between generic selective sulfidation and equivalent hydrometallurgical pathways is readily achievable due to well established trends in equipment costs, evaluation of operating cost(s) (OPEX) is less straightforward[1]. It is presently infeasible to define a generalizable OPEX for a generic hydrometallurgical process due to well-known but unquantified fluctuations in costs that vary greatly with the location of the facility[1]. These include the price of reagent feedstocks, labor and overhead requirements for hydrometallurgy at each location, and the proprietary liquid-liquid extractor chemistry and liquid-liquid contactor employed[3]. Therefore, a direct comparison of OPEX between a generic selective sulfidation and hydrometallurgical process is not attempted.

OPEX of selective sulfidation is estimated for the generic processes discussed in Section 6.1.1. Flowsheets are illustrated in Chapter 3, Figures 3.10-3.13. OPEX are estimated from

reagent, utility, and waste treatment prices, correlations for labor costs with relevant chemical process unit operations, correlations for management and overheads with labor cost, and correlations for maintenance costs with CAPEX[1]. Input costs and methodologies for OPEX contributions are reported by the author elsewhere[1]. Revenue credits from byproduct sulfuric acid production are excluded in OPEX analysis of the generic process[1], but may be included in economic evaluation of a real project[13]. OPEX as estimated herein does not include processing steps upstream of selective sulfidation and its supporting pretreatments, such as mining and preliminary comminution / mineral dressing in primary production from ores, or material collection and crushing / disassembly in secondary materials production from recycled materials. These upstream steps are not considered since they are necessary regardless of the downstream materials separation technique employed (leaching, SX, pyrometallurgical smelting, selective sulfidation, etc.), and may or may not be conducted at the same facility as downstream materials processing[1]. Likewise, differences in costs between established and greenfield facilities are not considered herein.

The OPEX of oxide-sulfide anion exchange via selective sulfidation is predicted to be on the order of $50, $100, and $300 (2020 USD) per tonne of feed at feed capacities of 1,000, 100, and 10 kilotonnes per year respectively[1]. Attribution of OPEX to individual processing steps are presented in Figure 6.3. Individual pretreatment steps for feed drying, sintering, and roasting/calcination each marginally increase the OEPX of selective sulfidation by around 10% to 20%[1], as tabulated in Table 6.1. Sensitivity analysis for OPEX estimation is discussed in Section 6.1.3.

6.1.3 Technoeconomic Impact Sensitivity Analysis

Sensitivity analysis for OPEX and CAPEX is conducted via Monte Carlo simulation[7] at selective sulfidation and liquid-liquid hydrometallurgy at feed capacities of 10, 100 and 1,000 kilotonnes per year (kta)[1]. At each feed capacity, 360,000 iterations of the CAPEX and OPEX models were conducted[1]. Operating parameters and conditions, reagent costs, labor requirements and costs, yearly maintenance cost as a fraction of CAPEX, Class 4 CAPEX error (+/-30%), and geographic scaling factors were each randomly varied using continuous triangular distributions centered around known or calculated values, as tabulated by the author elsewhere[1]. When

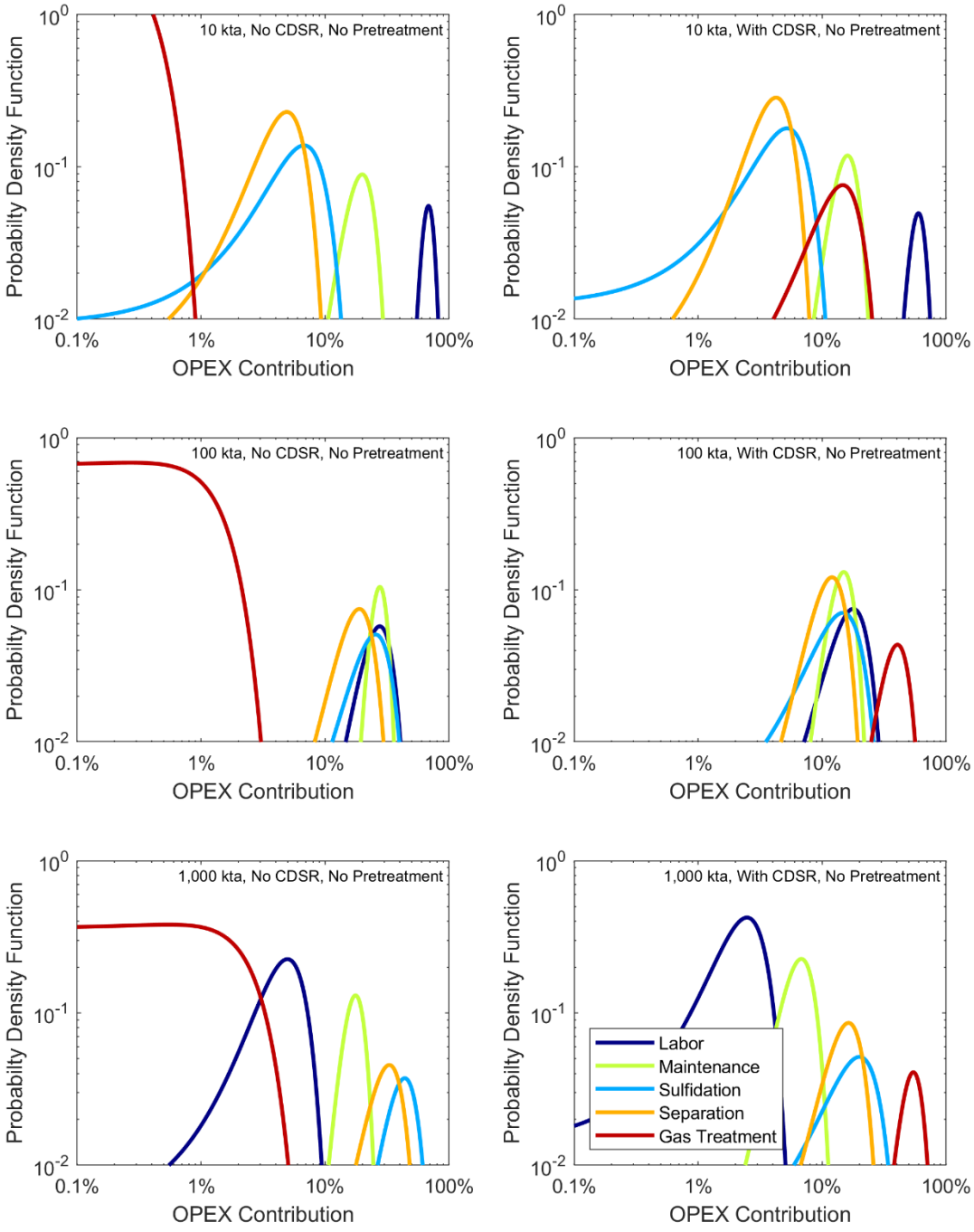

Figure 6.3: Operating cost (OPEX) contributions for selective sulfidation. OPEX for individual processing steps with and without CDSR without pretreatment, corresponding to the flowsheets in Chapter 3, Figures 3.10 and 3.11. Probability distributions are determined using Monte Carlo simulation (Section 6.1.3).

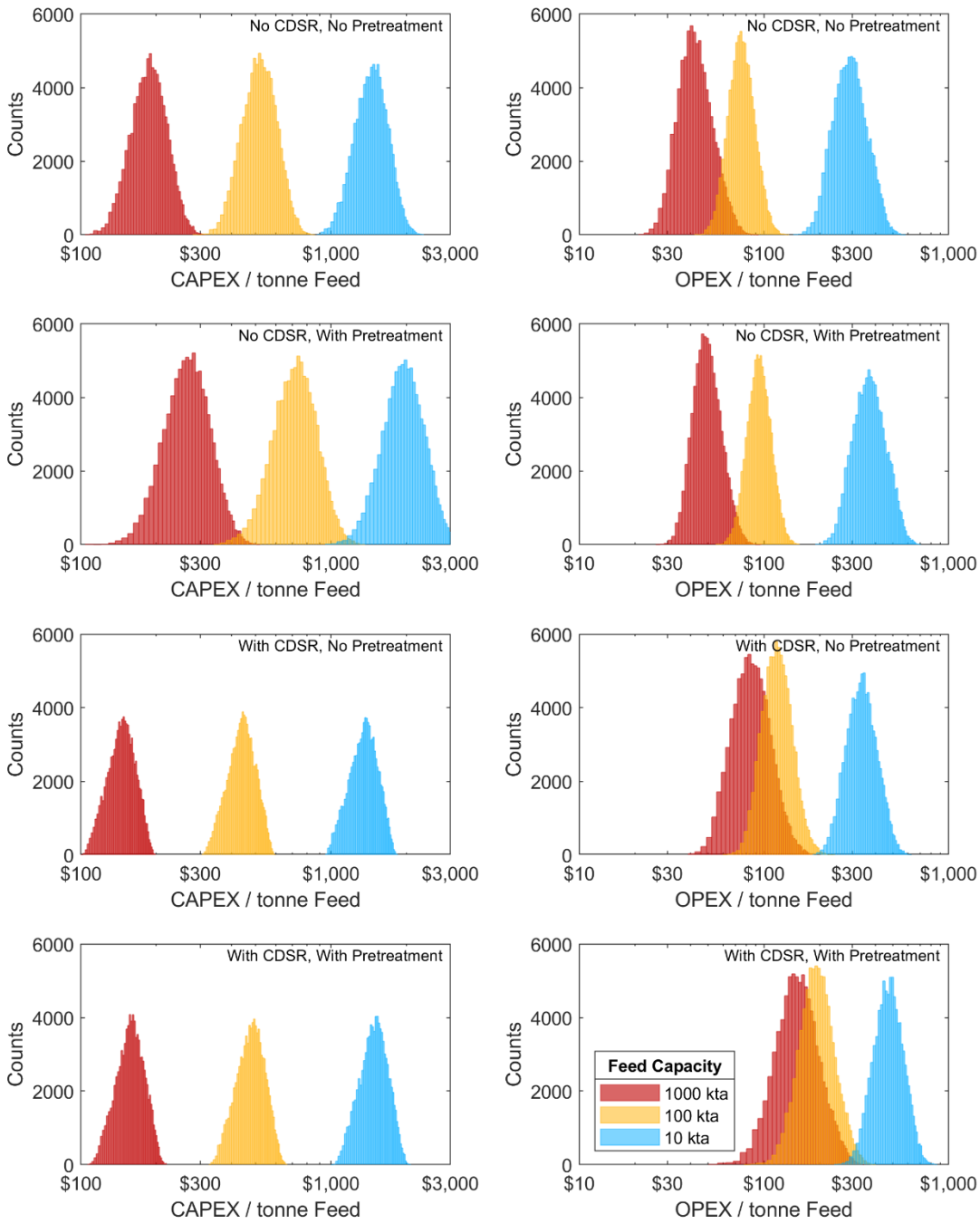

Figure 6.4: Capital cost (CAPEX) and operating cost (OPEX) distributions for selective sulfidation. Distributions for selective sulfidation with and without feed pretreatments and with and without carbothermically-driven sulfur reflux (CDSR) (Chapter 3, Figures 3.10-3.13) are determined via Monte Carlo simulation. Probability distributions employed for CAPEX, OPEX, and operating condition parameters are described by the author elsewhere.

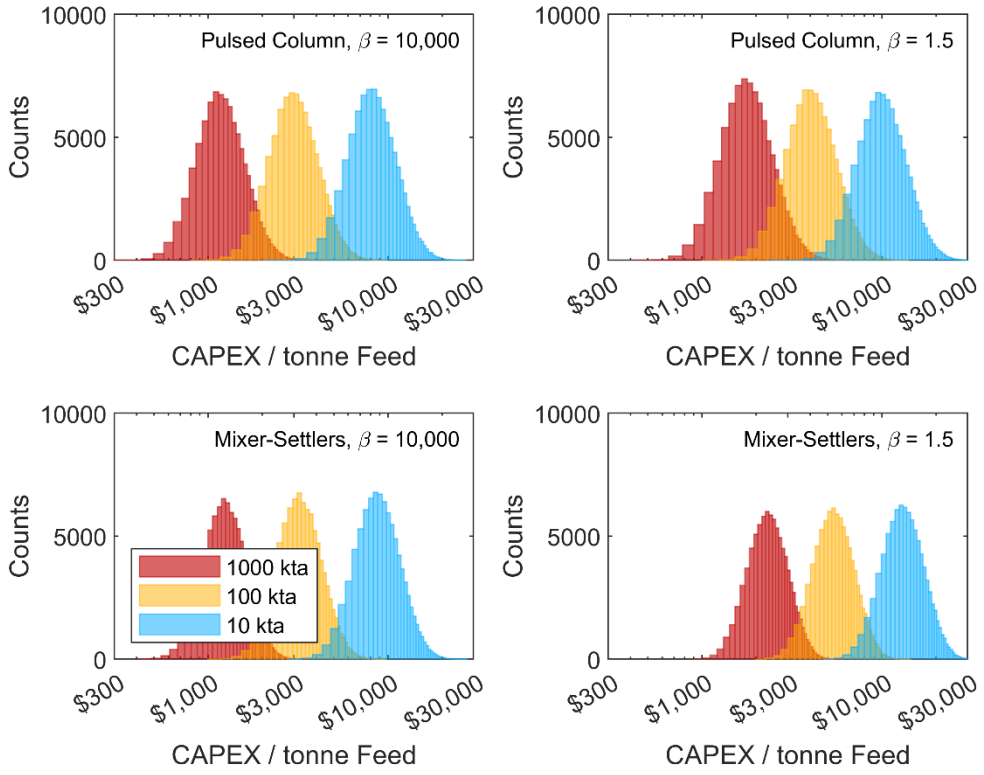

Figure 6.5: Capital cost (CAPEX) distributions for acid roasting and liquid-liquid separation processes. CAPEX distributions for the generic hydrometallurgical separation process utilizing pulsed column or mixer-settler liquid-liquid contactors, at hydrometallurgical separation factors of 1.5 and 10,000 corresponding to f-block and d-block element separation respectively. Distributions are determined via Monte Carlo simulation. Consistent with conventional wisdom, at high separation factors, pulsed columns and mixer settlers are predicted to be capitally competitive, while at low separation factors, pulsed columns are predicted to be capitally favorable.

uninformed by literature, upper and lower bounds for triangular distributions[7] were taken as -50% to +100% of the base value. Thermodynamic inputs for mass and energy balances and chemistry-specific operating conditions were randomly varied using coupled discrete, uniform distributions across Cu_2O, NiO, Nd_2O_3 sulfidation feedstock chemistries, as outlined by the author elsewhere[1]. Calculated distributions of OPEX and CAPEX are depicted in Figure 6.4 for selective sulfidation and physical separation. Calculated distributions of CAPEX for liquid-liquid hydrometallurgy are depicted in Figure 6.5.

From the Monte Carlo simulation, error in CAPEX and OPEX parameters are taken as +/- one standard deviation from the mean of the distribution. For CAPEX, the error was larger

as a percentage of the mean for the generic hydrometallurgical routes than the generic sulfidation routes due to a stronger dependence on chemical factors, namely feed concentration[1]. For selective sulfidation, the feed concentration is unity, since the solid feed is introduced directly to the sulfidation reactor[1]. Meanwhile in the hydrometallurgical pathway, the solid feed is dissolved prior to pretreatment, and the concentration of the feed was varied during Monte Carlo simulation. The resultant larger uncertainty highlights the difficulty of describing the economic framework of a generic hydrometallurgical process[1]. Nevertheless, the predicted reduction in CAPEX by adopting selective sulfidation and physical separation in place of hydrometallurgical chemical separation is resilient to these chemistry uncertainties[1].

	Feed Capacity, No CDSR			**Feed Capacity, With CDSR**		
Impact without Pretreatments	**10 kta**	**100 kta**	**1,000 kta**	**10 kta**	**100 kta**	**1,000 kta**
CAPEX Mean / tonne Feed	1495	536	194	1379	448	148
CAPEX Standard Deviation / tonne Feed	223	83	31	171	55	18
OPEX Mean / tonne Feed	312	79	45	356	124	93
OPEX Standard Deviation / tonne Feed	65	13	10	68	23	23
	Feed Capacity, No CDSR			**Feed Capacity, With CDSR**		
Impact with Pretreatments	**10 kta**	**100 kta**	**1,000 kta**	**10 kta**	**100 kta**	**1,000 kta**
CAPEX Mean / tonne Feed	2047	757	282	1514	488	161
CAPEX Standard Deviation / tonne Feed	384	148	58	189	61	20
OPEX Mean / tonne Feed	396	97	52	495	207	167
OPEX Standard Deviation / tonne Feed	80	14	9	90	45	45
	Feed Capacity, No CDSR			**Feed Capacity, With CDSR**		
% Change With Pretreatments	**10 kta**	**100 kta**	**1,000 kta**	**10 kta**	**100 kta**	**1,000 kta**
CAPEX Mean / tonne Feed	38%	43%	47%	12%	10%	10%
CAPEX Standard Deviation / tonne Feed	26%	27%	28%	20%	20%	20%
OPEX Mean / tonne Feed	27%	24%	15%	40%	68%	83%
OPEX Standard Deviation / tonne Feed	2%	3%	6%	10%	26%	36%

Table 6.1: Comparison of capital cost (CAPEX) and operating cost (OPEX) burdens for sulfidation with and without pretreatments and carbothermically driven sulfur reflux (CDSR).

6.2 Life Cycle Assessment for Materials Separation via Selective Sulfidation

6.2.1 Goal and Scope

Selective sulfidation for f-block and d-block element separation embodies a shift from hydrometallurgy and chemical separations to pyrometallurgy and physical separations. To understand the environmental impacts of material processing via selective sulfidation, the environmental impacts of four generic material separations are analyzed using life cycle assessment (LCA)[1]. These are selective sulfidation with and without feed pretreatments, each with and without CDSR. Flowsheets are included in Chapter 3, Figures 3.10-3.13.

For selective sulfidation and physical separation without pretreatment, the following process blocks are employed: nitrogen separation from air for sulfidation carrier gas production, sulfidation in a multihearth fluidized bed reactor, comminution, physical separation via froth flotation, and waste gas stream handling via a cyclone separator, followed by either electrostatic solids precipitator and dual alkali scrubbing (when the carbothermically-driven sulfur reflux, CDSR, is utilized in sulfidation) or sulfuric acid production (No CDSR)[1]. Materials containing impurities such as NORMs or anions other than oxygen and sulfur may require additional pretreatments prior to selective sulfidation.

The environmental impacts of selective sulfidation with some possible material feed preparation / pretreatment steps are also considered, such as feed drying, calcination for defluorination of fluorocarbonate minerals or LIB electrolytes and oxidation of mixed metal compounds such as rare earth magnets, sulfidation for dephosphorization of phosphate minerals and dethoriation of rare earth concentrates, and sulfidation/calcination for sintering of material feeds too finely ground for effective liberation and physical separation of sulfide precipitants post selective sulfidation[1]. Operating conditions are reported by the author elsewhere[1].

For these scenarios, three representative sulfidation feedstock chemistries are considered: Cu_2O, NiO, Nd_2O_3[1]. System boundaries consisting of an input of feed and an output of processed feed for each of the four generic processes are included in Chapter 3, Figures 3.10-3.13. The impacts of flows originating within the system boundary are evaluated from the cradle

through usage in the process, while the impacts of flows originating outside the system boundary are evaluated from the system gate through usage in the process. Environmental impact categories of global warming potential (GWP), terrestrial acidification (TA), and water resource depletion (WRD) are adopted. A functional unit of 1 kg of selective sulfidation feed is chosen[1], enabling the avoidance of allocation of environmental impacts between coproducts in accordance with ISO series 14040[14]. Impacts may be reallocated per unit of product if the product grade and recovery fraction are known, with allocation conducted via ISO 14040 (ISO 14044) hierarchy[14]:

1. Partition of processes steps into sub-processes to isolate the impacts of individual coproducts.

2. Allocation of impacts between coproducts based on physical relationships, such as mass fraction.

3. Allocation of impacts between coproducts based on non-physical relationships, such as economic value.

To compare environmental impacts of material processing via selective sulfidation versus nonselective pyrometallurgy with selective hydrometallurgy, three materials-specific case studies are chosen: Zirconium (Zr) and silicon (Si) separation from zircon ($(Zr, Hf)SiO_4$), iron (Fe) and titanium (Ti) separation from ilmenite ($FeTiO_3$), and rare earth element separation from bastnaesite ($LnCO_3F$)[1]. These case studies are selected for two reasons:

1. The existing processes – alkali fusion, the sulfate process, and acid roasting/leaching/solvent extraction respectively – each involve a combination of non-selective pyrometallurgical and selective hydrometallurgical treatments, serving to elucidate the possible environmental impact reduction by increasing the selectivity of pyrometallurgical processing steps using sulfidation chemistry[1].

2. Each of these processes has well-established feedstocks, LCA data, system boundaries, and allocation strategies for the standard processing route[15,16],

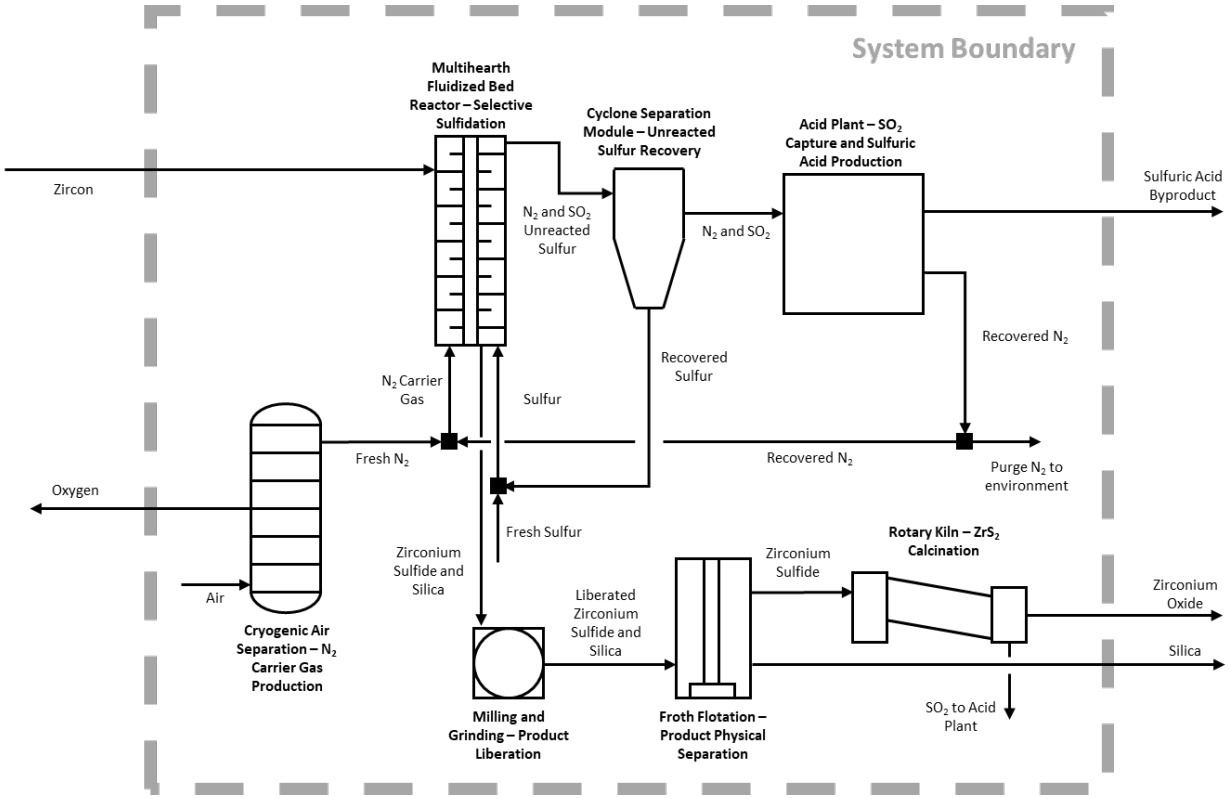

Figure 6.6: Proposed flowsheet for zirconium oxide (ZrO_2) production from zircon ($(Zr,Hf)SiO_4$) via selective sulfidation. The process consists of air separation for nitrogen carrier gas production, selective sulfidation in a multihearth fluidized bed reactor, product comminution and physical separation via froth flotation, product calcination, and downstream gas handling and treatment via a cyclone separator for solid particle removal and an acid plant for sulfur dioxide (SO_2) recovery.

supporting fair comparison of impacts between selective sulfidation with physical separation and hydrometallurgical chemical separation[1].

The environmental impact of zirconium oxide (ZrO_2) and silicon oxide (SiO_2) separation from $(Zr,Hf)SiO_4$is compared between the standard alkali fusion process and selective sulfidation using LCA[1]. Environmental impact data for alkali fusion is available in a published study[16]. System boundaries for selective sulfidation are defined to be an input of $(Zr,Hf)SiO_4$, and an output of $SiO_2$and mixed zirconium-hafnium oxide ($(Zr,Hf)O_2$) as shown in Figure 6.6. A functional unit of 1 kg of ZrO_2 is adopted for the impact categories of GWP, TA, and WRD. Division of environmental impacts between coproducts is conducted via the ISO 14040[14]

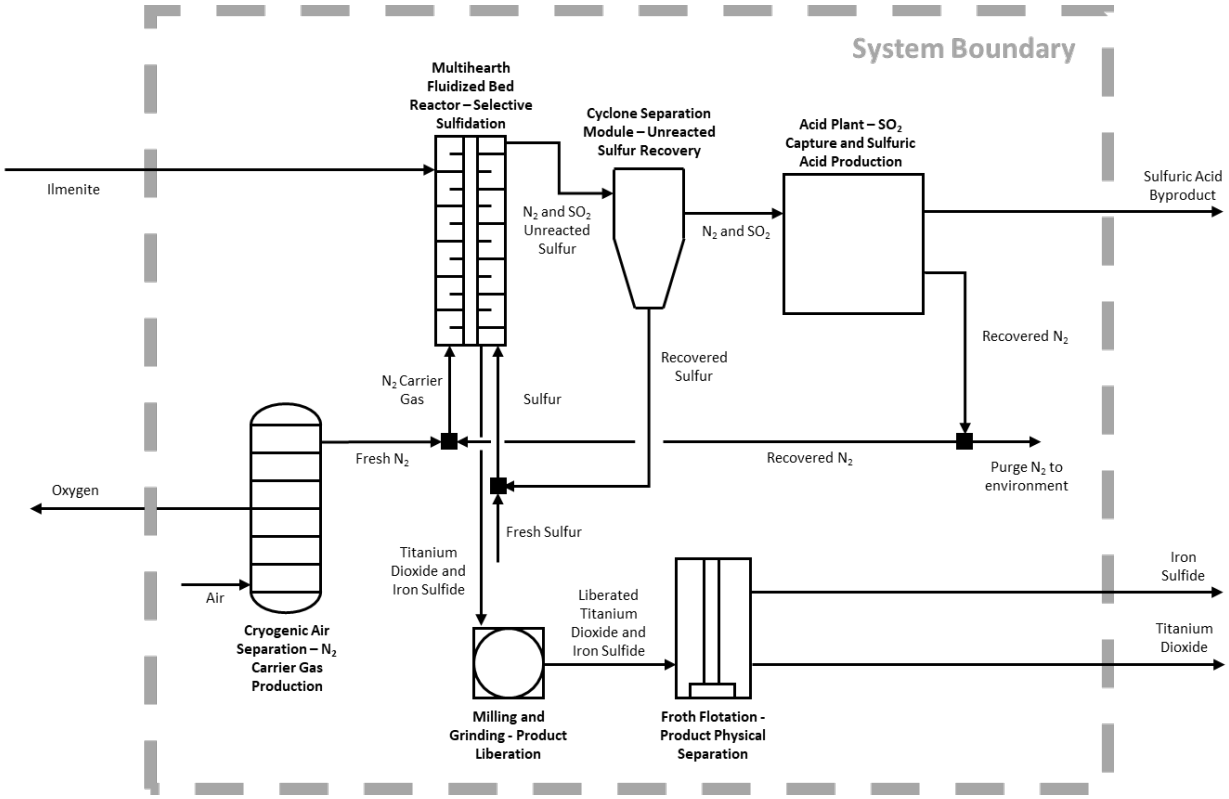

Figure 6.7: Proposed flowsheet for titanium dioxide (TiO_2) production from ilmenite ($FeTiO_3$) via selective sulfidation. The process consists of air separation for nitrogen carrier gas production, selective sulfidation in a multihearth fluidized bed reactor, product comminution and physical separation via froth flotation, and downstream gas handling and treatment via a cyclone separator for solid particle removal and an acid plant for sulfur dioxide (SO_2) recovery.

hierarchy. Allocation of impacts between Zr and hafnium (Hf) product oxides are conducted on a mass basis, as detailed by the author elsewhere[1]. The same allocation fractions[1] are adopted herein as those for the published study[16] on the alkali fusion process, supporting equitable comparison of impacts between the pathways.

The environmental impact of Fe and Ti separation from $FeTiO_3$ is compared between the standard sulfate process and selective sulfidation using life cycle assessment[1]. LCA impact data for the sulfate process is available in a published study[16]. System boundaries for selective sulfidation are defined to be an input of $FeTiO_3$, and an output of titanium dioxide (TiO_2) and iron sulfide (FeS), as shown in Figure 6.7. A functional unit of 1 kg of TiO_2 is adopted for the impact categories of GWP, TA, and WRD[1]. As for the published LCA of the sulfate process[16],

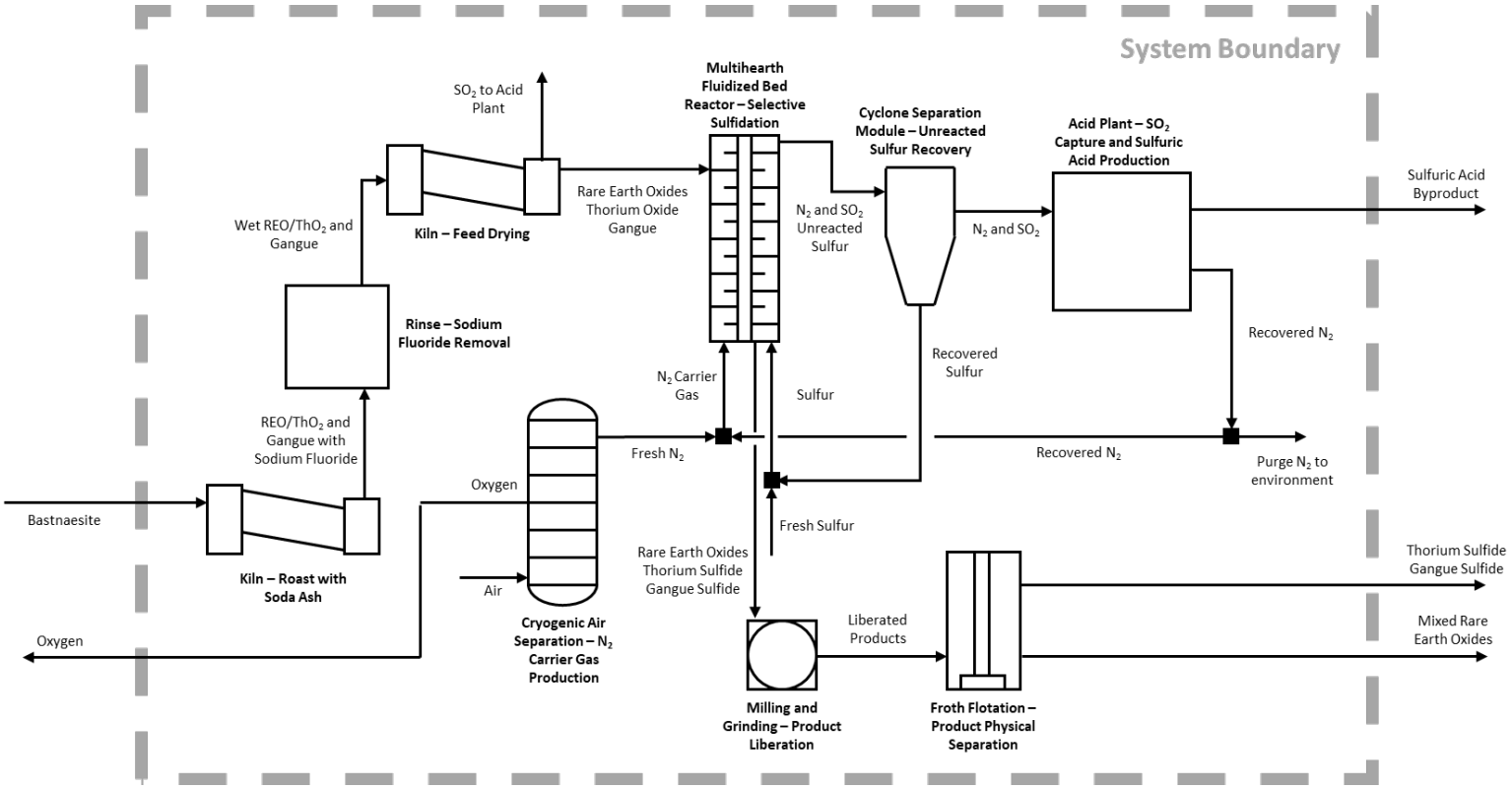

Figure 6.8: Proposed flowsheet for bastnaesite ($LnCO_3F$) defluorination and dethoriation to produce a mixed rare earth oxide (REO) via selective sulfidation. The process consists of feed roasting with soda ash, feed rinsing, feed drying, air separation for nitrogen carrier gas production, selective sulfidation in a multihearth fluidized bed reactor, product comminution and physical separation via froth flotation, and downstream gas handling and treatment via a cyclone separator for solid particle removal and an acid plant for sulfur dioxide (SO_2) recovery.

environmental impacts are fully attributed to TiO_2 production, supporting equitable comparison of impacts between the two pathways and eliminating the need for environmental impact allocation[1].

The environmental impact of rare earth element separation from $LnCO_3F$, the most commercially-relevant source of light rare earth elements, is compared between the standard acid roasting, leaching, and SX pathway and selective sulfidation using LCA[1]. Environmental impact data for the standard hydrometallurgical route is available in a published study[15]. System boundaries for selective sulfidation are defined to be an input of pre-concentrated (non-defluorinated, non-dethoriated) $LnCO_3F$, and an output of separated rare earth element compounds as shown in Figures 6.8 and 6.9, hypothetically processed at the world's largest rare

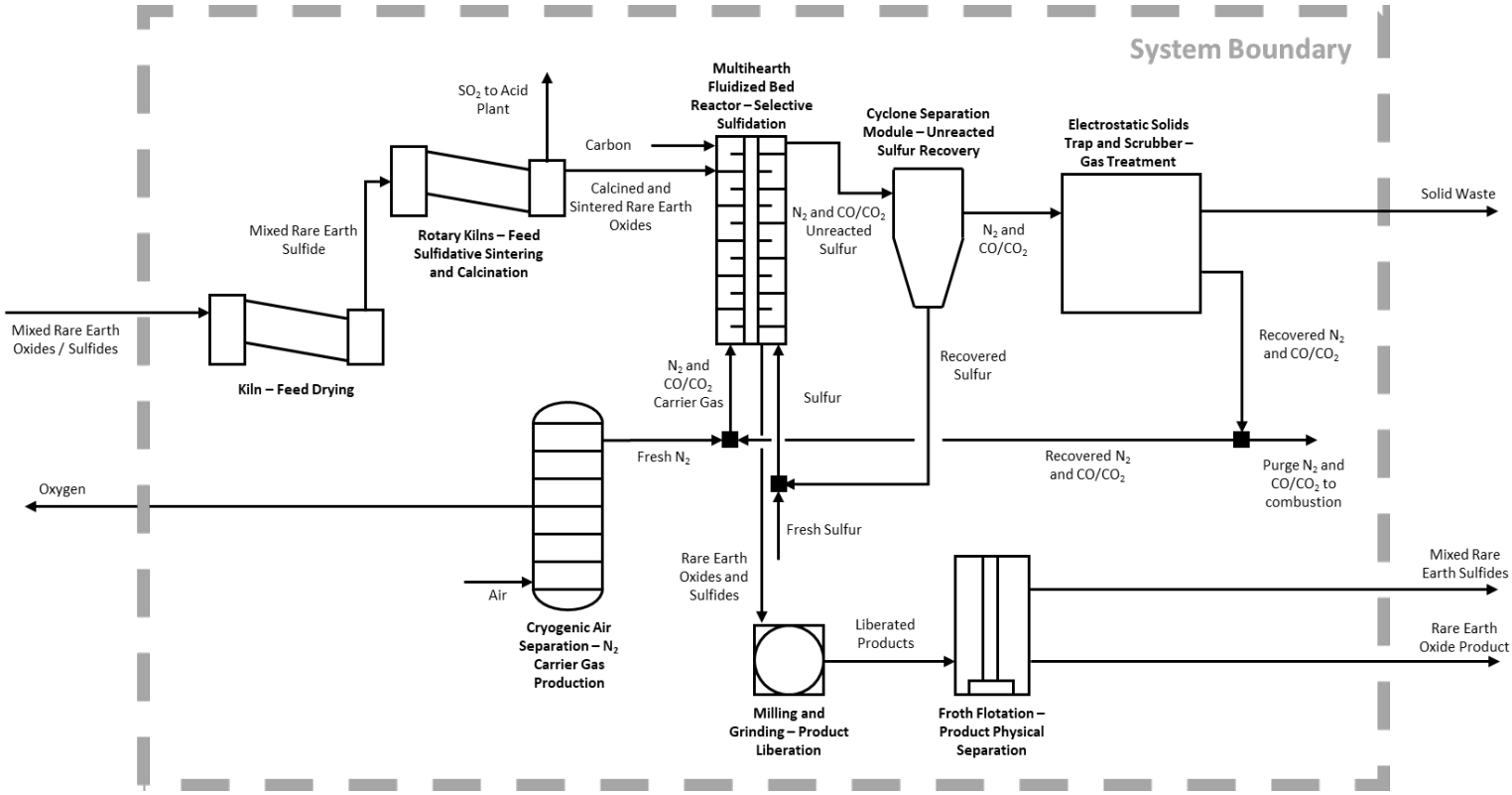

Figure 6.9: Proposed flowsheet for rare earth element separation via selective sulfidation. The process consists of feed drying, sulfidative sintering / calcination, air separation for nitrogen carrier gas production, selective sulfidation in a multihearth fluidized bed reactor utilizing carbothermically-driven sulfur reflux (CDSR), product comminution and physical separation via froth flotation, and downstream gas handling and treatment via a cyclone separator and electrostatics solid trap for solid particle removal, with a dual alkali scrubber and an acid plant for sulfur dioxide (SO_2) treatment and recovery. This flowsheet may be repeated for each individual rare earth separation.

earth element facility at Bayan Obo in China[1]. A functional unit of 1 kg of separated rare earth elements is adopted for the impact categories of GWP, TA, and WRD. To avoid the need for allocation of environmental impacts between rare earth coproducts as recommended by ISO 14040[14], environmental impacts are reported on the basis of total mass of separated rare earth oxide (REO). This eliminates the need for allocation of environmental impact between REO by- and coproducts, and supports fair comparison of environmental impacts to the published study[15] detailing the hydrometallurgical route, which also reports impacts for a functional unit of 1 kg of total separated rare earth oxides. Allocation data is detailed by the author elsewhere[1].

6.2.2 Inventory Analysis

To determine environmental impacts for the four generic sulfidation processes, process flow diagrams with system boundaries are depicted in Chapter 3, Figures 3.10-3.13. For these processes, a functional unit of 1 kg of selective sulfidation feed is adopted. When product feed grade and recovery are known, impacts may be reallocated to the product itself. Baseline, lower bound, and upper bound operating conditions for the generic processes are reported by the author elsewhere[1]. For the case studies of Zr and Si, Fe and Ti, and rare earth element separations via selective sulfidation, process flow diagrams are included in Figures 6.6-6.9, with operating conditions reported by the author elsewhere[1]. For estimation of the predicted environmental impacts of separation via selective sulfidation, the following assumptions are made[1]:

- The substitution of a selective sulfidation process for an existing process does not result in any major upstream (mining and beneficiation), downstream (oxide reduction to metal), or product feedstock chemistry changes.

- For Zr and Si, Fe and Ti, and rare earth element separations, new byproducts produced via selective sulfidation that are not present in the established processes[15,16] (sulfuric acid or metal compounds previously lost to waste) are presently not considered as allocable coproducts for environmental impacts. While they may be marketable byproducts, this is to support fair comparison of environmental impacts for selective sulfidation with the existing process.

- Comminution for product liberation following sulfidation is taken to have similar technosphere inputs as for high intensity stirred milling in conventional sulfide ore beneficiation[17,18].

- Physical separation of products via froth flotation following sulfidation is taken to have similar technosphere inputs as for conventional sulfide ore beneficiation[19].

- For the generic Zr, Si and Fe, Ti selective sulfidation processes the environmental impacts associated with electricity, heat, and reagent production are taken from global average inventory data, as available through the ecoinvent 3.6 database[20]. Natural gas combustion is assumed for heat production, with emissions as reported by the United States Environmental Protection Agency[21,22]. Electricity production (high voltage) is assumed to occur via natural gas combustion at a combined cycle power plant, with global average data from ecoinvent 3.6 employed[20].

- For rare earth element separation, the environmental impacts associated with electricity, heat, reagent production, and transportation are assumed to be that reported for the Inner Mongolia region of China, as available through the ecoinvent 3.6 database[20]. For inputs where data for the Inner Mongolia region is unavailable, China national average data from the ecoinvent 3.6 database[20] is employed. For inputs where data is unavailable for Inner Mongolia or China as a whole, global average data as available through the ecoinvent 3.6 database[20] is utilized. Natural gas combustion is assumed for heat production, with emissions as reported by the United States Environmental Protection Agency[21,22]. Electricity production via heavy fuel oil combustion in Inner Mongolia is assumed as reported in the ecoinvent 3.6 database[20].

- Environmental impacts associated with feedstock transportation are excluded for the generic Zr, Si and Fe, Ti selective sulfidation processes. Transportation is also excluded in the published LCA[16] for Zr and Si separation via alkali fusion, as well as Fe and Ti separation via the sulfate process, supporting fair comparison.

- Reagent transportation requirements are assumed to be equivalent for rare earth element separation via selective sulfidation and the conventional pathway, as reported in the published hydrometallurgical study[15].

- Nitrogen carrier gas, S, and carbon (C) utilization are informed by the experimental results presented in Chapters 4. Carrier gas is recycled at a rate of 90%, corresponding to a purge fraction of 10%. When CDSR is employed, carbon monoxide (CO) in the purge stream is combusted to carbon dioxide (CO_2), with no heat recovered.

- The stepwise order of metal separation is taken to follow the sulfidation series presented in Chapter 3, Figure 3.5. In practice metal removal could be performed for the most prevalent metals first by employing parallel sulfidation reaction pathways, reducing energy consumption from material heating.

- Sulfur dioxide (SO_2) produced in sulfidation and calcination reactions is recovered for sulfuric acid production at a rate of 99%, on par with modern sulfuric acid production efficiencies as reported in ecoinvent 3.6[20].

- In conventional sulfuric acid production, some electricity is generated from steam produced during sulfur combustion to SO_2[23]. Since SO_2 is produced as a biproduct of the sulfidation reaction and not from direct S combustion, this electricity generation is excluded in the present analysis.

- In conventional sulfuric acid production, some electricity is generated from hot acid heat recovery systems[23]. This electricity generation is included in the present analysis to partially offset electricity needs in selective sulfidation and physical separation.

- The environmental impacts associate with offsite solid and liquid waste processing are presently not considered for selective sulfidation. Likewise, the are also not considered in the published studies[15,16] of Zr and Si, Fe and Ti, and rare earth element separations from $LnCO_3F$ via the conventional process.

- Contributions to environmental impact from facility construction and infrastructure are excluded, as in the published study[15] for rare earth elements separation via the conventional process.

- For selective sulfidation, each element separated is taken to require its own selective sulfidation and physical separation circuits.

- Initial removal of fluorine (F) from $LnCO_3F$ is accomplished via sodium carbonate (Na_2CO_3) roasting and subsequent washing with water.

- Na_2CO_3 consumption is assumed to be stoichiometric for defluorination of bastnaesite.

- The sulfidative sintering process in rare earth element processing is predicted to be autothermal, as observed for conventional industrial roasting processes[1].

- The thermodynamics of mixed REO and rare earth mineral gangue are taken to be well represented by those for Nd_2O_3 and iron sesquioxide (Fe_2O_3) respectively.

- Error bars in the environmental impacts for the generic sulfidation processes are taken to be +/- two standard deviations as determined via Monte Carlo simulation. Baseline, lower bound, and upper bound operating conditions are reported by the author elsewhere[1]. Error is discussed in greater detail later in Section 6.2.5.

- Error bars for the environmental impacts of Zr and Si, Fe and Ti, and rare earth element separations via selective sulfidation are taken to be an equivalent percentage above and below the mean as determined through Monte Carlo simulation of the relevant generic case. Error is discussed in greater detail later in Section 6.2.5.

While such assumptions may seem academic, they establish a framework that supports quantifiable determination of a life cycle inventory (LCI) for selective sulfidation as it could possibly be applied at an industrial scale. Energy inputs for pyrometallurgical reactions are calculated using FactSage 8.0, with a summary of relevant thermodynamic data reported by the author elsewhere[1]. The environmental impacts of electricity, process heat, and reagent generation, production, and usage are compiled from ecoinvent 3.6 data[20] for relevant locations as described in the above assumptions. The net material and energy balance for production of ZrO_2 production from $(Zr,Hf)SiO_4$, TiO_2 from $FeTiO_3$, and separated REO from $LnCO_3F$ concentrate as processed via selective sulfidation are presented as the LCIs reported by the author elsewhere[1]. Impact assessment, interpretation, and sensitivity analysis for these LCIs are described in the Sections 6.2.3-6.2.5.

6.2.3 Impact Assessment

In Section 6.2.2, LCIs are discussed for generic materials separation processes, as well as ZrO_2 production from $(Zr,Hf)SiO_4$, TiO_2 from $FeTiO_3$, and separated REO from $LnCO_3F$ concentrate via hypothetical pyrometallurgical selective sulfidation processes[1]. They are used to explore the possible environmental impacts of selective sulfidation and compare those impacts in the categories of GWP, TA, and WRD to conventional processes that employ a series of nonselective pyrometallurgical and selective hydrometallurgical steps. These impact categories are selected due to their straightforward determination from presumed process-scale and thermodynamic data available for and pertinent to a hypothetical selective sulfidation process[1].

However, many other environmental impact categories exist, including but not limited to ozone depletion, eutrophication, particle emissions, ecotoxicity, and mineral resource depletion, which need to be considered to fully understand the environmental sustainability of a hypothetical selective sulfidation process. These impact categories would benefit from further analysis. In general, comparison and scaling of multiple industrial ecology studies can be difficult due to different underlying assumptions and allocations that necessitate the need for data harmonization[24]. Production of ZrO_2 from $(Zr,Hf)SiO_4$, TiO_2 from $FeTiO_3$, and separated REO from $LnCO_3F$ concentrate are selected as case studies due to well-established feedstocks, LCA data, system boundaries, and allocation strategies for the standard processing route[1]. This

supports fair comparison of impacts between selective sulfidation with physical separation and hydrometallurgical chemical separation, as discussed in Section 6.2.1.

Energy, reagent, water and emission data for selective sulfidation are compiled using mass balances, energy balances, and published unit operation data, supplemented as required with data from ecoinvent 3.6[20]. GWP and TA are quantified over the system boundaries (Chapter 3, Figures 3.10-3.13, Figures 6.6-6.9) using the Tool for Reduction and Assessment of Chemicals and Other Environmental Impacts (TRACI 2.1)[25]. WRD is tabulated following the methodology employed in the published LCA for rare earth element separation via the conventional processing pathway[15].

Distributions of GWP, TA, and WRD produced via Monte Carlo simulation of the generic process[1] (Chapter 3, Figures 3.10-3.13) are depicted in Figure 6.10. For a generic sulfidation process without CDSR, the GWP, TA, and WRD are estimated to be on the order of 0.20 (+/- 0.06) kg CO_2-eq, $9x10^{-3}$ (+/- $5x10^{-3}$) kg of SO_2-eq, and 9 (+/- 4) kg H_2O respectively per kg of feed[1]. The inclusion of pretreatments such as feed drying, calcination/roasting, and sintering on average increase GWP by about 50%, WRD by 30% and TA by double over the base case[1], as shown in Table 6.2. The use of CDSR in selective sulfidation meanwhile increases GWP by a factor of 4-5x and WRD by a factor of 3-4x[1]. These trends are discussed in Section 6.2.4. Clearly, the sustainability of every materials separation challenge is influenced differently by feedstock chemistry, grade, and purity, motivating materials-specific case studies.

The GWP, TA, and WRD of ZrO_2 production via separation of Zr and Si $(Zr, Hf)SiO_4$, TiO_2 via separation of Ti and Fe from $FeTiO_3$, and separated REO from $LnCO_3F$ concentrate are shown in Table 6.3. For $LnCO_3F$ processing, these impacts may be broken down into contributions from defluorination, dethoriation, rare earth element separation, and reagent transportation, included in Table 6.4. Comparison of the predicted environmental impacts of selective sulfidation to that of existing processes are discussed in the following section.

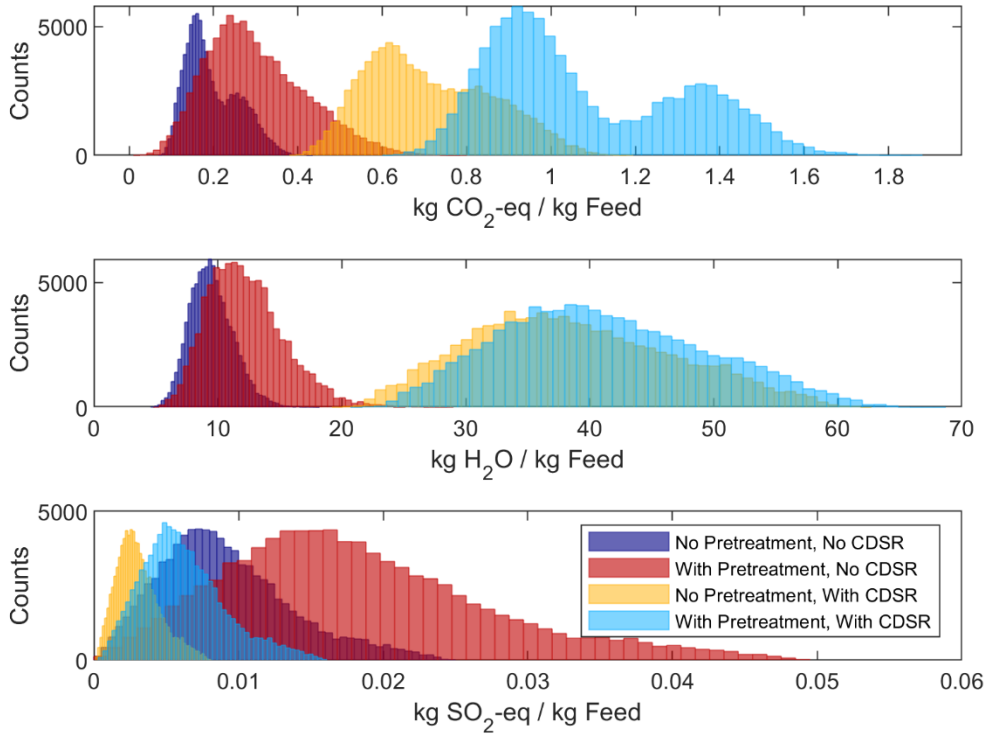

Figure 6.10: Global warming potential (GWP), water resource depletion (WRD), and terrestrial acidification (TA) distributions for generic selective sulfidation processes. Selective sulfidation is conducted with and without feed pretreatments, with and without CDSR, for a functional unit of 1 kg of selective sulfidation feed following the flowsheets depicted in Chapter 3, Figures 3.10-3.11. Distributions are determined via Monte Carlo simulation, with probability distribution for operating condition parameters described by the author elsewhere. The inclusion of feed pretreatments increases GWP by about 50%, WRD by 30% and TA by double, while CDSR increases GWP by a factor of 3-5x and WRD by a factor of 3-4x. The bimodal nature of the GWP distribution is due to differences in oxygen content of the three model chemistries considered in the Monte Carlo simulation, highlighting the role of system chemistry in influencing environmental impact.

6.2.4 Interpretation

Predicted environmental impacts for the generic sulfidation case study serve as a first pass estimate for the environmental impact of a selective sulfidation process. However, the values reported in Figure 6.10 and Table 6.2 are not a substitute for chemistry and process-specific analysis. Of note, the bimodal nature of the GWP distribution is due to differences in oxygen (O) content of the three model chemistries considered in the Monte Carlo simulation,

highlighting the role of system chemistry in determining environmental impact[1]. The generic process also makes no distinction between adding selective sulfidation as a pretreatment at an established facility versus conducting selective sulfidation at a greenfield project[1]. This distinction is particularly important with regards to the use of selective sulfidation during mineral processing and beneficiation. Comminution can dominate the energy usage and GWP of beneficiation steps[26], so care must be taken to avoid over or undercounting the environmental impact of comminution when contextualizing the environmental impacts of the generic selective sulfidation process.

Impact without Pretreatments	**Feed Capacity, No CDSR**			**Feed Capacity, With CDSR**		
	10 kta	**100 kta**	**1,000 kta**	**10 kta**	**100 kta**	**1,000 kta**
GWP Mean (kg CO_2 / kg feed)	2.0E-01	2.0E-01	2.0E-01	7.1E-01	7.1E-01	7.1E-01
GWP Standard Deviation (kg CO_2 / kg feed)	6.3E-02	6.3E-02	6.3E-02	1.5E-01	1.5E-01	1.5E-01
TA Mean (kg SO_2 / kg feed)	9.1E-03	9.1E-03	9.1E-03	3.0E-03	3.0E-03	3.0E-03
TA Standard Deviation (kg SO_2 / kg feed)	4.6E-03	4.6E-03	4.6E-03	1.5E-03	1.5E-03	1.5E-03
WRD Mean (kg H_2O / kg feed)	9	9	9	39	39	39
WRD Standard Deviation (kg H_2O / kg feed)	2	2	2	8	8	8
Impact with Pretreatments	**Feed Capacity, No CDSR**			**Feed Capacity, With CDSR**		
	10 kta	**100 kta**	**1,000 kta**	**10 kta**	**100 kta**	**1,000 kta**
GWP Mean (kg CO_2 / kg feed)	3.0E-01	3.0E-01	3.0E-01	1.1E+00	1.1E+00	1.1E+00
GWP Standard Deviation (kg CO_2 / kg feed)	1.2E-01	1.2E-01	1.2E-01	2.3E-01	2.3E-01	2.3E-01
TA Mean (kg SO_2 / kg feed)	1.8E-02	1.8E-02	1.8E-02	6.2E-03	6.2E-03	6.2E-03
TA Standard Deviation (kg SO_2 / kg feed)	9.1E-03	9.1E-03	9.1E-03	2.9E-03	2.9E-03	2.9E-03
WRD Mean (kg H_2O / kg feed)	12	12	12	41	41	41
WRD Standard Deviation (kg H_2O / kg feed)	3	3	3	8	8	8
% Change with Pretreatments	**Feed Capacity, No CDSR**			**Feed Capacity, With CDSR**		
	10 kta	**100 kta**	**1,000 kta**	**10 kta**	**100 kta**	**1,000 kta**
GWP Mean (kg CO_2 / kg feed)	51%	51%	51%	52%	52%	52%
GWP Standard Deviation (kg CO_2 / kg feed)	28%	28%	28%	10%	10%	10%
TA Mean (kg SO_2 / kg feed)	100%	100%	100%	107%	107%	107%
TA Standard Deviation (kg SO_2 / kg feed)	0%	0%	0%	16%	16%	16%
WRD Mean (kg H_2O / kg feed)	28%	28%	28%	7%	7%	7%
WRD Standard Deviation (kg H_2O / kg feed)	12%	12%	12%	3%	3%	3%

Table 6.2: Comparison of global warming potential (GWP), terrestrial acidification (TA), and water resource demand (WRD) burdens for sulfidation with and without pretreatments and carbothermically driven sulfur reflux (CDSR)[1].

Separation	Zr and Si		Ti and Fe		Rare Earth Element	
Feed	$(Zr, Hf)SiO_4$		$FeTiO_3$		$LnCO_3F$ Concentrate	
Product	ZrO_2		TiO_2		Separated REO	
Functional Unit	1 kg ZrO_2		1 kg TiO_2		1 kg of separated REO	
Process	**Alkali Fusion**	**Selective Sulfidation**	**Sulfate Process**	**Selective Sulfidation**	**Acid Roasting / SX**	**Selective Sulfidation**
$P_{2.5\%}$ GWP	2 kg CO_2-eq	0.07 kg CO_2-eq	4.6 kg CO_2-eq	0.32 kg CO_2-eq	-	6.4 kg CO_2-eq
$P_{50\%}$ GWP	2.7 kg CO_2-eq	0.12 kg CO_2-eq	5.2 kg CO_2-eq	0.53 kg CO_2-eq	32.8 kg CO_2-eq	8.1 kg CO_2-eq
$P_{97.5\%}$ GWP	3.5 kg CO_2-eq	0.17 kg CO_2-eq	5.8 kg CO_2-eq	0.74 kg CO_2-eq	-	9.6 kg CO_2-eq
$P_{2.5\%}$ TA	-	0.01 kg SO_2-eq	-	0.005 kg SO_2-eq	-	0.01 kg SO_2-eq
$P_{50\%}$ TA	-	0.02 kg SO_2-eq	-	0.01 kg SO_2-eq	0.69 kg SO_2-eq	0.09 kg SO_2-eq
$P_{97.5\%}$ TA	-	0.03 kg SO_2-eq	-	0.02 kg SO_2-eq	-	0.19 kg SO_2-eq
$P_{2.5\%}$ WRD	-	6 kg H_2O	-	9 kg H_2O	-	47 kg H_2O
$P_{50\%}$ WRD	-	15 kg H_2O	-	18 kg H_2O	477 kg H_2O	79 kg H_2O
$P_{97.5\%}$ WRD	-	24 kg H_2O	-	26 kg H_2O	-	110 kg H_2O
Source	Nuss[16]	Stinn[1]	Nuss[16]	Stinn[1]	Bailey[15]	Stinn[1]

Table 6.3: Environmental impact of selective sulfidation for zirconium (Zr) and silicon (Si), titanium (Ti) and iron (Fe), and rare earth element separation.

For selective sulfidation processes without CDSR, the largest sources of GWP are electricity usage in comminution and air separation for nitrogen carrier gas production[1]. When CDSR is employed, direct CO_2 emissions increase GWP[1]. The decarbonization of electricity production is one avenue to lower the GWP of selective sulfidation[1]. Likewise, the use of CDSR for process control should be avoided when possible[1]. Acidification is largely the result of imperfect conversion of SO_2 to sulfuric acid. The use of CDSR lowers terrestrial acidification[1]. The other major contributor to acidification is S_2 production, with smaller contributions from power generation and fuel combustion[1]. WRD is mostly driven by cooling water loss to steam during cryogenic air separation[1], with some water resource depletion also occurring during electricity generation, physical separation via froth flotation, reagent production, and acid production.

Selective sulfidation with physical separation is predicted to reduce the GWP of hydrometallurgical Zr, Si and Fe, Ti separations by over 80% each[1]. Meanwhile, selective

sulfidation with CDSR and physical separation is predicted to show reductions to GWP of 60-90%, TA of over 70%, and WRD of 65-85% for rare earth separation versus conventional hydrometallurgical processing of $LnCO_3F$ via acid roasting, leaching, and SX[1] (Tables 6.3, 6.4). These reductions to environmental impacts are not a surprise.

Presently, ZrO_2 production $Si\ (Zr, Hf)SiO_4$ via alkaline fusion, TiO_2 production from $FeTiO_3$ via the sulfate process, and separated REO production from $LnCO_3F$ via acid roasting, leaching, and SX all require a series of nonselective pyrometallurgical pretreatments followed selective hydrometallurgical processes[1]. When the selectivity of these pyrometallurgical steps can be increased through the use of sulfidation chemistry, the complexity and number of hydrometallurgical treatments required downstream may be reduced, thereby lowering the environmental impact of the process[1].

Impact Category	Processing Step				
	Defluorination	**Dethoriation**	**REO Separation**	**Transportation**	**Total**
GWP (kg CO_2-eq / kg separated REO)	0.48	0.034	7.2	0.42	8.1
TA (kg SO_2-eq / kg separated REO)	4.6E-04	1.3E-02	6.7E-02	6.8E-03	8.8E-02
WRD (kg H_2O / kg separated REO)	17	6.8	48	3.2E-05	72

Table 6.4: Environmental impacts for processing steps employed in rare earth separation via selective sulfidation. GWP, TA, and WRD for separation of REO is divided between defluorination, dethoriation, separation, and materials transportation stages. As for the conventional liquid-liquid separation pathway, rare earth elements separation exhibits the largest environmental impacts.

6.2.5 Sensitivity Analysis

Sensitivity analysis for the environmental impacts of the generic sulfidation processes are conducted via Monte Carlo simulation[7]. For each of the four generic processes 360,000 iterations were conducted over process parameters as reported by the author elsewhere[1]. Thermodynamic inputs for mass and energy balances were randomly varied using coupled discrete, uniform distributions across the sulfidation chemistries of Cu_2O, NiO, Nd_2O_3, each with and without employment of CDSR[1]. Operating conditions were varied using continuous triangular distributions. When uninformed by literature, upper and lower bounds for triangular

distributions were taken as -50% to +100% of the base value[7]. Distributions for GWP, TA, and WRD for each generic sulfidation process are included in Figure 6.10.

Sensitivity analysis via Monte Carlo simulation reveals that the largest source of uncertainly in the GWP of selective sulfidation is whether or not CDSR is employed in the process[1]. Meanwhile, for WRD, the largest source of uncertainty is whether or not feed pretreatments are required[1]. Specifically, the need for sulfidative sintering increases the amount of nitrogen carrier gas employed, thereby increasing WRD associated with air separation. For TA, uncertainty is shared between process operating conditions, the use of pretreatments, and the use of CDSR[1].

For a given generic selective sulfidation process, the largest sources of uncertainty for environmental impacts per mass of feed are the feedstock chemistry and sulfidation conversion[1]. Differences in compound m^* and stoichiometry lead to large variations in the amount of anion O that can be exchanged with S. Differences in chemistry affect not only the O content of the feed, but also the amount of external heating required for the reactor to remain at temperature. Variations in conversion likewise are responsible for differences in the amount of anion O that can be exchanged with S, and thereby the exothermicity of the sulfidation reaction. Heating requirements are also affected by the efficiency of waste heat recovery in the thermal recuperator, although uncertainty in this parameter is often outweighed by those in chemistry and conversion, which themselves lead to bimodal distributions in GWP[1]. Variation in WRD is tied almost exclusively to variation in cooling water usage, which largely outweighs water lost in froth flotation and utilized in acid and reagent production[1]. TA is almost directly related to conversion and chemistry, and exhibits wide error distributions with respect to its mean[1].

For error analysis in the material specific case studies for Zr and Si, Ti and Fe, and rare earth separations, error bars are determined from Monte Carlo simulation of the relevant generic process[1] (with or without pretreatment, with or without CDSR). Error bar for GWP, WRD, and TA are determined from the generic case study by employing the percent error that corresponds to +/- two standard deviations as a percentage of the generic case study mean. Since feed chemistry is the largest contributor to the error in the environmental impact of selective sulfidation, and chemistry is a known factor for each of these case studies, this methodology likely overestimates the error of each material specific process[1]. Experimental verification of operating conditions is necessary however to quantitatively reduce error in the environmental

impact assessment. Nevertheless, calculated improvements to environmental impact afforded using selective sulfidation remain resilient to these levels of uncertainty.

6.3 Summary

Calculated and experimental findings from Chapters 3, 4, and 5 indicate that elements previously requiring a series of harsh pyrometallurgical and hydrometallurgical separations can now be isolated through a single, pyrometallurgical oxide-sulfide anion exchange process that supports simple and conventional physical separation technologies. Selective sulfidation is also a promising alternative for nonselective pyrometallurgical processes that rely on subsequent hydrometallurgy for selective product recovery, such as pyrometallurgical lithium-ion battery recycling, rare earth element separation, and many transition metal extraction pathways.

Technoeconomic assessment estimates that pyrometallurgical oxide-sulfide anion exchange may decrease capital costs by 65-90% compared to conventional hydrometallurgical routes, due to the ability to employ smaller reactors with fewer processing steps. Operating costs are also determined to be low, on the order of $100 (2020 USD) or less per tonne of feedstock. While preliminary CAPEX and OPEX estimates are promising, to understand the profitability of a given materials separation process utilizing selective sulfidation, detailed design considering geographic-specific factors (ore grade and impurities, labor costs and utilization, trends in automation, greenfield versus established facility, etc.) and further refinement of sulfidation operating conditions and chemistries will be necessary. Regional and organizationally-specific factors pertaining to cost of capital, depreciation, and amortization are also critical for understanding the economic competitiveness of selective sulfidation.

Life cycle assessment results indicate that when pyrometallurgical oxide-sulfide anion exchange methods are sufficiently selective to minimize the need for subsequent hydrometallurgical treatments, the environmental impact of materials processing may be lowered. Feed chemistry is found to be the largest contributor to the error in the environmental impact of selective sulfidation. Thermodynamic and experimental results (Chapters 3 and 4) provide a framework to determine whether feed pretreatments or CDSR are required for an oxide-sulfide anion exchange process. Experimental verification of operating conditions for selective sulfidation is necessary to decrease error in environmental impact assessments.

When pyrometallurgical oxide-sulfide anion exchange is employed for materials processing, the cost and environmental impact of materials separations may be lowered. However, the use of sulfidation chemistry for separations produces novel metal sulfide products that can be difficult to process downstream using established metal reduction technologies. In the following chapter, technologies that could employ sulfide materials as feedstocks for metal production are considered. Thermodynamic modelling informs the design and experimental demonstration of new metal production pathways from sulfides.

6.4 References

1. Stinn, C. & Allanore, A. Selective sulfidation of metal compounds. *Nature* **602**, 78–83 (2022).
2. Stinn, C., Gutierrez, C., Daehn, K. & Allanore, A. Sulfidation for Copper Mineral Processing and Impurity Management. in *The Igo Wilkomirsky Symposium on Pyrometallurgy* (ed. IIMCh) 785–796 (Copper 2022, 2022).
3. Zhao, B., Zhang, J. & Schreiner, B. *Separation Hydrometallurgy of Rare Earth Elements*. (Springer International Publishing AG Switzerland, 2016).
4. Flett, D. S. Solvent extraction in hydrometallurgy: the role of organophosphorus extractants. *J. Organomet. Chem.* **690**, 2426–2438 (2005).
5. Cheng, C. Y. & Zhu, Z. Solvent extraction technology for the separation and purification of niobium and tantalum: A review. *Hydrometallurgy* **107**, 1–12 (2011).
6. Green, D. W. & Perry, R. H. *Perry's Chemical Engineer's Handbook*. (McGraw-Hill, 2008).
7. Towler, G. & Sinnott, R. *Chemical Engineering Design*. (Elsevier, 2013).
8. Woods, D. R. Appendix D: Capital Cost Guidelines. in *Rules of Thumb in Engineering Practice* 376–436 (Wiley-VCH Verlag GmbH & Co. KGaA, 2007). doi:10.1002/9783527611119.app4.
9. Christensen, P. & Dysert, L. *Cost Estimate Classification System as Applied in Engineering, Procurement, and Construction for the Process Industries*. *AACE International Recommended Practice No. 18R-97 COST, TCM Framework: 7.3 - Cost Estimating and Budgeting* (2005).

10. Jenkins, S. Plant Cost Index Archives - Chemical Engineering. *Plant Cost Index Archives - Chemical Engineering* https://www.chemengonline.com/site/plant-cost-index/ (2020).
11. Stinn, C. & Allanore, A. Estimating the Capital Costs of Electrowinning Processes. *Electrochem. Soc. Interface* **29**, 44–49 (2020).
12. Crundwell, F. K., Moats, M. S., Ramachandran, V., Robinson, T. G. & Davenport, W. G. *Extractive Metallurgy of Nickel, Cobalt, and Platinum-Group Metals*. (Elsevier, 2011).
13. Rush, L. T. Integrative Approach to Metal Extraction and Electrification. (Massachusetts Institute of Technology, 2021).
14. ISO. *ISO 14044*. https://www.iso.org/standard/38498.html (2006).
15. Bailey, G. *et al.* Review and new life cycle assessment for rare earth production from bastnäsite, ion adsorption clays and lateritic monazite. *Resour. Conserv. Recycl.* **155**, 104675 (2020).
16. Nuss, P. & Eckelman, M. J. Life cycle assessment of metals: a scientific synthesis. *PLoS One* **9**, e101298 (2014).
17. Bleiwas, D. I. *Estimates of Electricity Requirements for the Recovery of Mineral Commodities , with Examples Applied to Sub-Saharan Africa*. *USGS Open-File Report 2011-1253* http://pubs.usgs.gov/of/2011/1253/report/OF11-1253.pdf (2011).
18. de Bakker, J. Energy Use of Fine Grinding in Mineral Processing. *Metall. Mater. Trans. E* **1**, 8–19 (2014).
19. Bleiwas, D. I. *Estimated Water Requirements for the Conventional Flotation of Copper Ores*. *USGS Open-File Report 2012-1089* (2012).
20. Ecoinvent-Association. ecoinvent 3.6. *Ecoinvent Center* www.ecoinvent.org (2019).
21. USEIA. *Henry Hub Natural Gas Spot Price*. (2021).
22. USEIA. *Carbon Dioxide Emissions Coefficients*. https://www.eia.gov/environment/emissions/co2_vol_mass.php (2021).
23. King, M. J., Davenport, W. G. & Moats, M. S. *Sulfuric Acid Manufacture - Analysis, Control and Optimization*. (2013).
24. K Lee, J. C. & Wen, Z. Pathways for greening the supply of rare earth elements in China. *Nat. Sustain.* **1**, 598–605 (2018).

25. USEPA. TRACI 2.1. *Tool for Reduction and Assessment of Chemicals and Other Environmental Impacts* https://www.epa.gov/chemical-research/tool-reduction-and-assessment-chemicals-and-other-environmental-impacts-traci (2014).
26. Norgate, T. & Jahanshahi, S. Low grade ores – Smelt, leach or concentrate? *Miner. Eng.* **23**, 65–73 (2010).

Chapter 7

Reduction of Sulfides to Metals

Thus far, the viability of pyrometallurgical oxide-sulfide anion exchange for materials processing has been explored for a range of system chemistries. In Chapter 3, an integrated thermodynamic, kinetic, and mass transport framework was developed to control pyrometallurgical oxide-sulfide anion exchange reactions. This methodology informed subsequent experimental procedures, technoeconomic modelling, and life cycle assessment. In Chapter 4, individual components from mixed metal feedstocks were found amenable to selective sulfidation and desulfidation, enabling physical isolation of product compounds. In Chapter 5, these processing pathways were shown to be resilient to the presence of other anion impurities. Technoeconomic and environmental impact assessments in Chapter 6 illustrated that selective sulfidation is cost competitive versus conventional hydrometallurgy while enabling substantial reductions in greenhouse gas emissions, terrestrial acidification, and water usage. Together, these developments presented a promising pathway for decarbonizing industrial materials separation. In this chapter, approaches for reducing metal sulfides to metal alloy products are considered and demonstrated.

Sulfidation of an oxide was hypothesized in Chapter 2 to decrease the thermodynamic barrier to metal reduction, potentially supporting the use of less reactive reductants or direct thermal decomposition for metal production. This hypothesis is confirmed herein. Conventional oxidative pathways for converting sulfides to metals are compared with emerging molten sulfide and metallothermic alternatives. Aluminum is identified as a promising reductant for sulfides

due to calculated trends in the thermodynamic stabilities and volatilities of sulfides and metals. Vacuum thermal decomposition and aluminothermic reactive vacuum distillation are then experimentally demonstrated for the reduction of sulfides to produce aluminum alloys and ferroalloys.

7.1 Framework for Sulfide Reduction

In Chapters 3-6, pyrometallurgical oxide-sulfide anion exchange for materials separation was demonstrated to be technically feasible, resilient to impurities, and economically and environmentally favorable versus currently deployed alternatives. Metal sulfide compounds were generated as products from these selective sulfidation processes. While sulfide materials are increasingly critical for a range of optical, electronic, magnetic, battery, and catalytic applications[1–6], sulfides must still be reduced to metals for most metallurgical end products. Herein, a thermodynamic and experimental framework for sulfide reduction is presented. Vacuum thermal decomposition and aluminothermic reduction via reactive vacuum distillation are identified as promising techniques for production of a wide range of metals and alloys without employing carbon as a reductant.

7.1.1 Thermodynamic Pathways for Sulfide Reduction Processes

As illustrated in Chapter 2, Figure 2.1, most sulfides are less thermodynamically stable than oxides, thereby exhibiting lower thermodynamic barriers to metal reduction. At a temperature of 1000 °C and sulfur or oxygen partial pressures (P_{S_2} and P_{O_2} respectively) of 1 atm, two classes of exceptions to this trend are discussed here. Alkali metal cations heavier than lithium (Li) exhibit disproportionately large ionic radii for their atomic number; for heavier alkali elements monoxide formation becomes sterically hindered while peroxide or superoxide formation become more favorable[7,8]. This also translates into the increased thermodynamic stabilities of sulfides and polysulfides of sodium (Na), potassium (K), rubidium (Rb), and cesium (Cs) versus their monoxides[7].

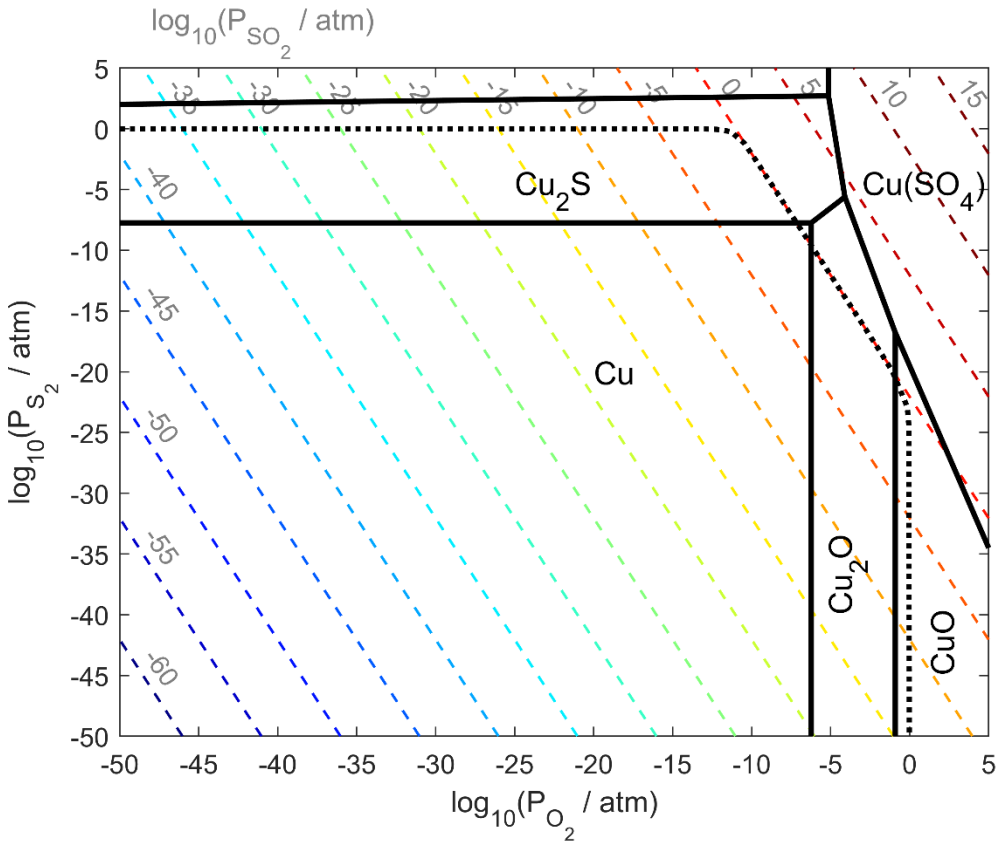

Figure 7.1: Predominance area diagram for copper (Cu), oxygen (O), and sulfur (S) compounds with unit activities at a temperature of 1000 °C and a total pressure of 1 atm. Solid lines correspond to phase domains, dashed lines to sulfur dioxide partial pressure (P_{SO_2}) isobars, and the dotted line to the 1 atm of total pressure isobar. Increasing P_{O_2} along the isobar from the Cu_2S domain results in the formation of metallic Cu, indicating the ability of O_2 to serve as a reductant in this system. Noble metals such as Ag and Pt exhibit similar behavior.

Meanwhile, the sulfides of some noble metals including copper (Cu), silver (Ag), gold (Au), platinum (Pt), and iridium (Ir) are also observed to be more stable than their oxides. This is due to decreased affinity for ionic versus covalent bonding stemming from the s-block relativistic contraction[9,xiv]. A predominance area diagram is depicted for the Cu, oxygen (O), and sulfur (S) system as a function of P_{S_2} and P_{O_2} at a temperature of 1000 °C and a system pressure of 1 atm in Figure 7.1. For noble metals such as Cu, Ag, Au, and Pt, a domain of metal stability intersects the calculated domains of oxide and sulfide stabilities. The decreased stability of the

[xiv] This same phenomenon contributes to mercury's (Hg) stability as a liquid at room temperature[9].

oxide versus the sulfide enables conditions in which oxygen gas (O_2) is able to serve as a reductant to react the sulfide to produce metal and sulfur dioxide (SO_2) (Chapter 4, Section 4.4.3). Referred to industrially as converting, this phenomenon serves as the basis for conventional Cu production today from sulfide ores via established pyrometallurgical pathways[10].

For most other metals where the oxide phase is more stable than the sulfide, roasting of the sulfide with O_2 results in the formation of an oxide, oxysulfide, or sulfate. By considering the gas phase equilibrium between O_2, sulfur gas (S_2), and SO_2 (Chapter 3, Section 3.1.3), the oxidation affinity during roasting process may be understood via the sulfidation/desulfidation series illustrated in Chapter 3, Figures 3.4-3.5. Subsequent oxide reduction is generally conducted carbothermically for oxides with low affinities for carbide formation. When carbide formation hinders carbothermic reduction, such as for rare earth elements (Ln), metallothermic or halide-based electrolytic reduction pathways are usually utilized[11]. Molten oxide electrolytic[12–14] or hydrogen reduction pathways for oxides are also under various stages of development and deployment[15]. Aqueous electrowinning approaches are available, but are most commonly used for metal refining or after hydrometallurgical separation[10,16]. Aqueous reduction is generally hindered for reactive metals such as Ln due to the electrolytic decomposition of water; alloying metal products into amalgam cathodes or employing organic liquid solutions can overcome these challenges[17,18], albeit at substantially increased cost versus molten state electrolysis[19].

Employing sulfides directly as a feedstock for reduction is a pathway to leverage their smaller thermodynamic barrier to metal production. An Ellingham diagram is shown in Figure 7.2 depicting the reduction series of some metal sulfides as a function of their Gibbs energy of formation ($\Delta_f G°$), decomposition potential ($E°$), and temperature (T), calculated using data reported in the FactSage 8.0 FactPS database. Reactions between carbon (C) and S species are not depicted; direct carbothermic reduction of sulfides in practice requires an oxygen source such as calcium oxide (CaO) to maintain practically achievable carbon disulfide (CS_2) or carbon monosulfide (CS) partial pressures (P_{CS_2} and P_{CS} respectively) [20].

A wide range of thermodynamic stabilities are present among sulfides. Some are amenable to direct vacuum thermal reduction. Figure 7.3 depicts an Ellingham-style diagram of the critical sulfur partial pressure ($\left[P_{S_2}\right]_{crit}$) for direct vacuum thermal reduction as a function of

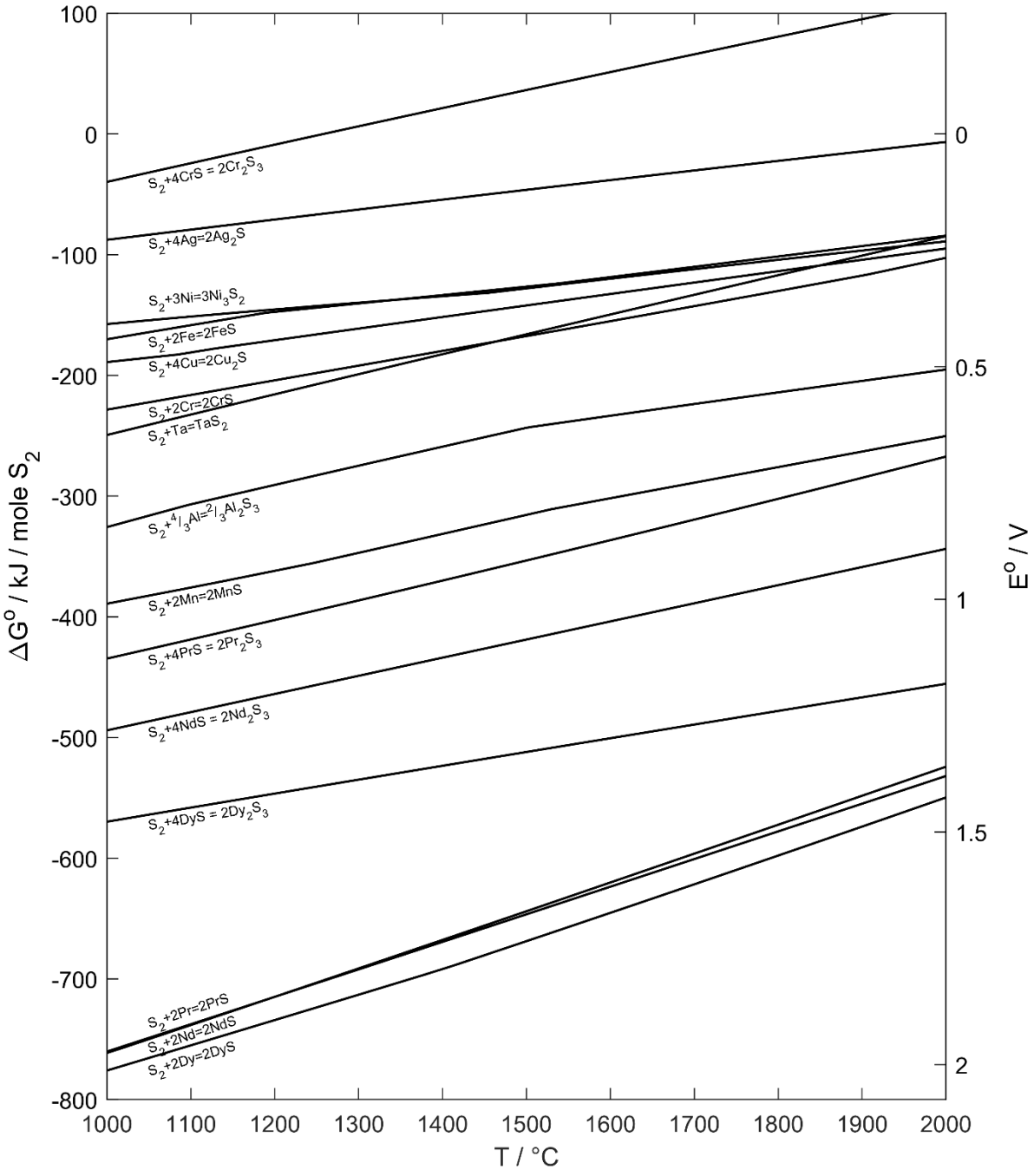

Figure 7.2: Ellingham diagram for sulfides depicting standard Gibbs energy of formation ($\Delta_f G°$) and standard electrochemical decomposition potential ($E°$).

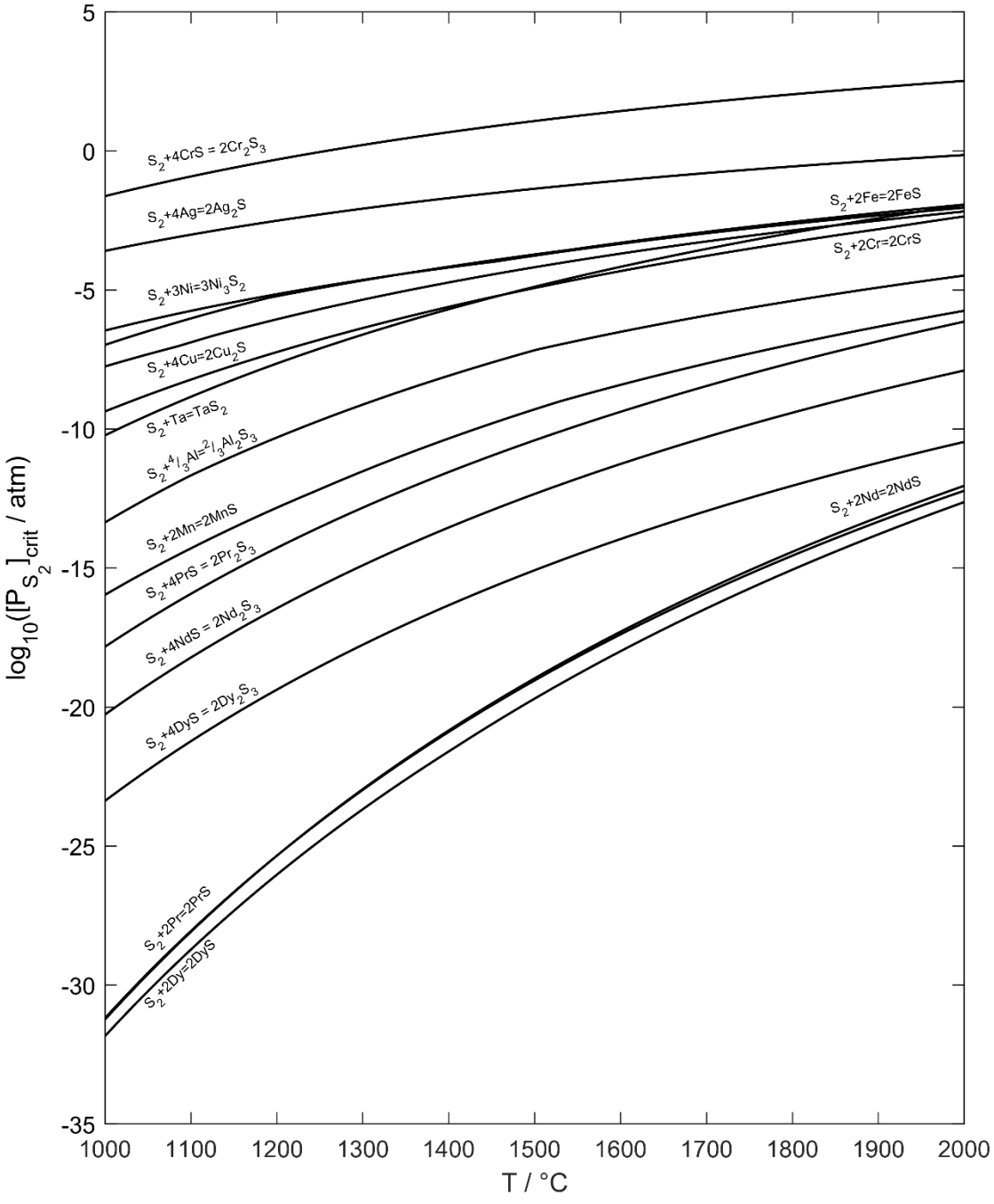

Figure 7.3: Ellingham diagram for sulfides depicting critical sulfur partial pressure $\left[P_{S_2}\right]_{crit}$ for thermal decomposition.

T, calculated following the methodology presented in Chapter 3, Section 3.1.3. Of note, iron sulfide (FeS) is amenable to vacuum thermal reduction below metallic iron's (Fe) melting point. Given the role of Fe as a collector phase during selective sulfidation (Chapter 4, Sections 4.4.1-4.4.3 and Chapter 5, Section 5.2.2), direct thermal decomposition of sulfide rich in Fe is a pathway for production of ferroalloys from sulfidized products. This is demonstrated experimentally later for rare earth ferroalloys in Section 7.4. Meanwhile when a metal sulfide is too stable for direct thermal decomposition, a dedicated reductant must be utilized.

Electrolytic reduction is a carbon-free pathway to produce metals from sulfides; however direct reduction is challenging due to the semiconducting nature of many liquid sulfides. Electrolysis of molten sulfides in an ionic molten halide supporting electrolyte was demonstrated by 1902 and patented in 1906[21]. Since then, molten halide electrolysis pathways for sulfides have been revisited many times at the laboratory scale for a wide range of metals spanning Cu[22] to aluminum (Al)[23] to tantalum (Ta)[24]. In some embodiments, a metal sulfide was dissolved directly in a molten halide for electrolysis. In others, a metal halide was electrolytically reduced to enable in situ metallothermic reduction of the sulfide. These approaches suffer due to the low solubility of metal sulfides in halides and poor mass transport respectively[25]. Halide-based liquid sulfide ion conductors separating the molten sulfide from the metal cathode product have instead been proposed to inhibit current efficiency losses stemming sulfide electronic conductivity, demonstrated for antimony (Sb) production from antimony sulfide (Sb_2S_3)[25]. The addition of a third immiscible liquid layer to the electrochemical cell provides an additional materials compatibility challenge, in particular for the electrochemical production of high melting metals outside the thermal stability range of known liquid sulfide ion conductors.

An alternative approach is the use of a sulfide-based supporting electrolyte to improve the ionic conductivity of the melt. From the Ellingham diagram for sulfides in Figure 7.2, alkaline earth and lanthanide (Ln) sulfides are promising candidates for supporting electrolytes due to their relatively large decomposition potential; they are also characterized by large band gaps suggestive of promoting ionic conduction in melts[26]. For electrowinning of Cu from liquid sulfides, barium sulfide (BaS) was found to serve as a suitable supporting electrolyte due to its high solubility for Cu_2S[27,28]. The addition of lanthanum sulfide (La_2S_3) to the supporting electrolyte increased the thermal stability of the melt[29] and improved electrochemical transport[26]. This $Ba-La$ sulfide supporting electrolyte was successfully demonstrated for the production of

Cu[30], Fe[30], nickel (Ni)[31], cobalt (Co)[31], rhenium (Re)[26], molybdenum (Mo)[26], and Ag[32]. Molten sulfide electrolytes likewise enable higher current densities than molten halide alternatives[33], resulting in lower capital costs per unit of metal produced[19]. The Wagner-Allanore thermodynamic framework provides insight into controlling electrochemical deposition selectivity during molten sulfide electrolysis[34]. However, the general lack of phase stability, solution thermodynamics, viscosity, and conductivity models for mixed sulfides hinders optimization of supporting electrolytes and identification of optimal mass transport conditions.

Metallothermic reduction of sulfides is another promising method for metal production without direct greenhouse gas emissions. While metallothermic reductions of oxides using Al, silicon (Si), magnesium (Mg), calcium (Ca), and other metals have long been common for a range of pure metal, aluminum alloy, and ferroalloy products[11,35], this approach has seen less application to sulfides. Prior to 1910, reduction of zinc sulfide (ZnS) was demonstrated using Fe as a reductant[36]. By 1964, a range of metallothermic reduction processes using base metal reductants were considered for metal sulfide minerals, in particular molybdenite (MoS_2)[37,38]. Application of vacuum during aluminothermic reduction of MoS_2 to produce molybdenum powder was shown to enable vaporization of product aluminum sulfide (Al_2S_3) and unreacted Al from the system, increasing conversion[39]. Mechanochemical methods of sulfide metallothermic reduction have also been explored[40,41]. The management of waste products remains a burden in oxide metallothermic reductions, where slags must be utilized to flux the resultant oxide product in order for the metal product to sink and agglomerate in the liquid bath[35]. However, differences in the chemical nature of oxides and sulfides equip sulfide chemistry to better deal with this challenge. The thermodynamics of metallothermic reduction pathways for sulfides are considered in more detail in the following section.

7.1.2 Thermodynamics of Sulfide Metallothermic Reduction

Most metal sulfides exhibit higher vapor pressures than their oxide counterparts due to the increased covalent nature of their bonding. This provides an opportunity to leverage volatility in order to remove a product sulfide from the system. When the metal product forms as a liquid alloy and if the sulfide product forms a volatile liquid (miscible or immiscible), they may be separated using distillation process[42]. The metallothermic reduction of a metal sulfide

($M_{1_\gamma}S_\delta$) with a second metal (M_2) using reactive vacuum distillation may be described by the following reaction, where M_1 corresponds to the condensed metal product, $M_{2_\theta}S_\iota$ to a volatile metal sulfide product, and β, γ, δ, ϵ, ζ, η, θ, ι, and κ are stoichiometric factors:

$$\beta M_{1_\gamma}S_\delta(s,l) + \epsilon M_2(s,l) = \zeta M_1(l) + \eta M_{2_\theta}S_\iota(g) \tag{7.1}$$

The apparent[xv] vapor pressures of some pure metal sulfides[43] at 1300 °C are reported in Table 7.1. Aluminum and silicon metals (Al and Si respectively) are identified as promising reductants due to the high vapor pressure of their sulfides (Al_2S_3 and SiS respectively). Reviewing the Ellingham diagram in Figure 7.2, Al is found to be a stronger reductant than Si and is also more readily available as scrap. Together, these benefits make Al a promising candidate for a sulfide reductant.

Sulfide	P_{vap} / atm
$Al_2S_3(l)$	$2.7*10^{-1}$
$SiS(s)$	$4.7*10^{-1}$
$MnS(s)$	$2.8*10^{-6}$
$MgS(s)$	$5.4*10^{-6}$
$TiS(s)$	$1.1*10^{-10}$
$FeS(l)$	$2.2*10^{-5}$
$Cu_2S(l)$	$1.8*10^{-5}$
$ZnS(s)$	$2.0*10^{-2}$
$VS(s)$	$1.3*10^{-9}$
$ZrS_2(s)$	$1.5*10^{-12}$
$ScS(s)$	$1.2*10^{-12}$
$Li_2S(l)$	$3.6*10^{-5}$
$Ni_3S_2(l)$	$2.3*10^{-5}$
$CrS(s)$	$1.1*10^{-6}$
$BeS(s)$	$2.3*10^{-7}$
$LaS(s)$	$1.1*10^{-11}$

Table 7.1: Calculated apparent vapor pressures of some metal sulfides at 1300 °C.

[xv] The evaporation behaviors of metal sulfides are notoriously complex[73], arising from their tendency to disassociate and evolve sulfur upon vaporization or thermal decomposition, resulting in the use of an "apparent" vapor pressure that includes both gas evolution from stoichiometric vaporization and disassociation[43].

In a system open to Al_2S_3, by le Chatelier's principle vacuum distillation may be employed to expunge Al_2S_3 product, thereby driving the equilibrium of Eqn. 7.1 toward the products. The aluminothermic reduction of $M_{1_\gamma}S_\delta$ via reactive vacuum distillation may be described by the following equation:

$$\beta M_{1_\gamma}S_\delta + \epsilon Al = \zeta M_1 + \eta Al_2S_3 \tag{7.2}$$

Unlike in aluminothermic reduction of oxides, in which the aluminum oxide (Al_2O_3) product remains a solid or must be fluxed by a slag, Al_2S_3 can be easily distilled from the system at temperatures of 1300 °C or higher. Al_2S_3 may then be condensed and recycled back to Al electrolytically on site or calcined to Al_2O_3 for reintroduction to established Al supply chains[42,43]. Alternatively, Al_2S_3 vapors may be scrubbed through reaction with a matte or slag phase that is immiscible with the metal product[42,44].

Assuming the metal sulfide feedstock is nonvolatile and immiscible with all other species, from the law of mass action the extent of the aluminothermic reduction reaction (Eqn. 7.2) is governed by the partial pressure of Al_2S_3 ($P_{Al_2S_3}$) in the system and the mixing thermodynamics between the Al feedstock and the metal product. For a given product alloy composition with known mixing thermodynamics, a critical $P_{Al_2S_3}$ ($\left[P_{Al_2S_3}\right]_{crit}$) may be determined for the reaction to proceed thermodynamically spontaneously[42,43]. Using pure compound data from the FactSage 8.0 FactPS database, mixing thermodynamics from the FactSage 8.0 FTlite database, and Trouton's rule, $\left[P_{Al_2S_3}\right]_{crit}$ at 1300 °C is calculated for a collection of Al alloy products formed by aluminothermic reduction of the pure metal sulfide via reactive vacuum distillation. Calculated relations between $\left[P_{Al_2S_3}\right]_{crit}$ versus composition for some liquid Al alloy products[43] are reported in Figure 7.4. In principle, any metal sulfide may be aluminothermically reduced by continuously distilling Al_2S_3 from the system while maintaining sufficiently low $P_{Al_2S_3}$ for formation of the metal product. In contrast, the aluminothermic reduction of many oxides is hindered due to accumulation of Al_2O_3 in the system; for the oxide feedstock stronger reductants such as Ca or Mg must be employed[35]. This notion further informs the hypothesis that sulfidation decreases the thermodynamic barrier to metal reduction,

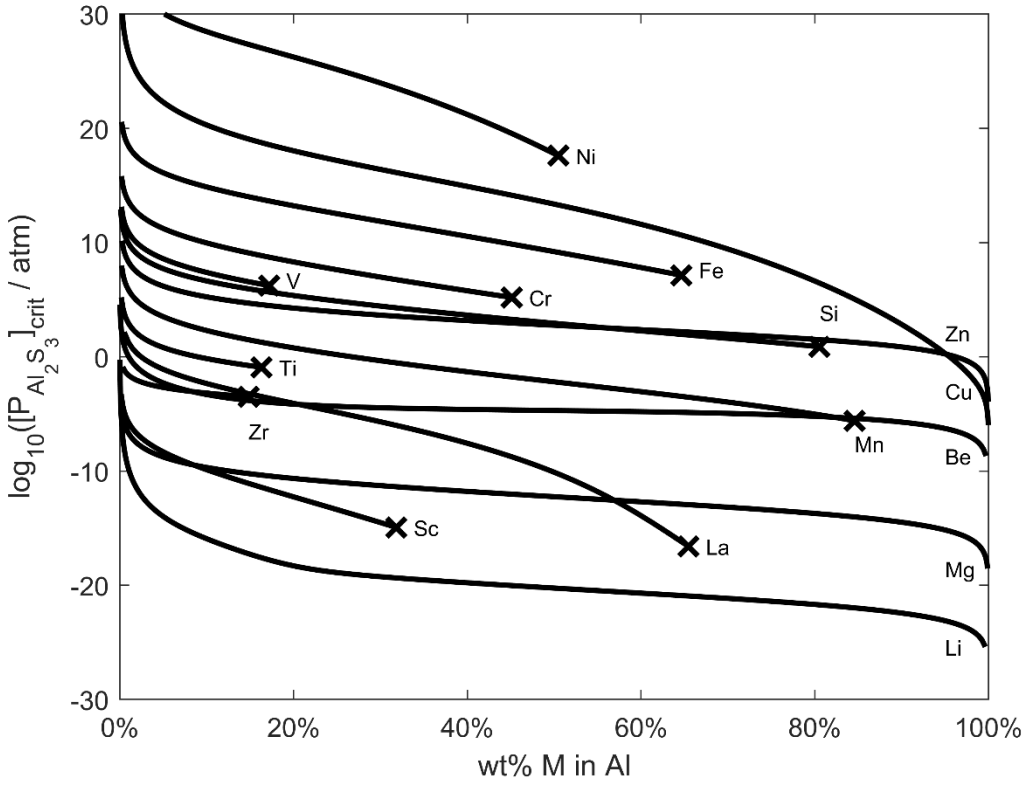

Figure 7.4: Calculated critical aluminum sulfide partial pressure ($[P_{Al_2S_3}]_{crit}$) for aluminothermic reduction of a sulfide to produce an aluminum alloy up to the alloying element's (M) solubility limit (X) at 1300 °C.

supporting the use of less reactive reductants or direct thermal decomposition for metal production.

Metal product volatility should be less than that of Al_2S_3 in order for distillation to be selective toward Al_2S_3. Calculated vapor pressures (P_{vap}) in Al for the alloying elements depicted in Figure 7.4 are shown in Figure 7.5. Elements that are substantially less volatile than Al_2S_3, can be readily produced via reactive vacuum distillation. For elements that are more volatile than Al_2S_3, other pathways must be considered to expunge either Al_2S_3 or the metal product from the system.

In practice, most single stage steam jet ejector vacuum pumps employed at metal smelters reach a pressure of 10^{-3} atm[45]. This sets a practical lower limit industrially for relying on vacuum alone to minimize $P_{Al_2S_3}$ without the use of more complicated multistage pumps. One

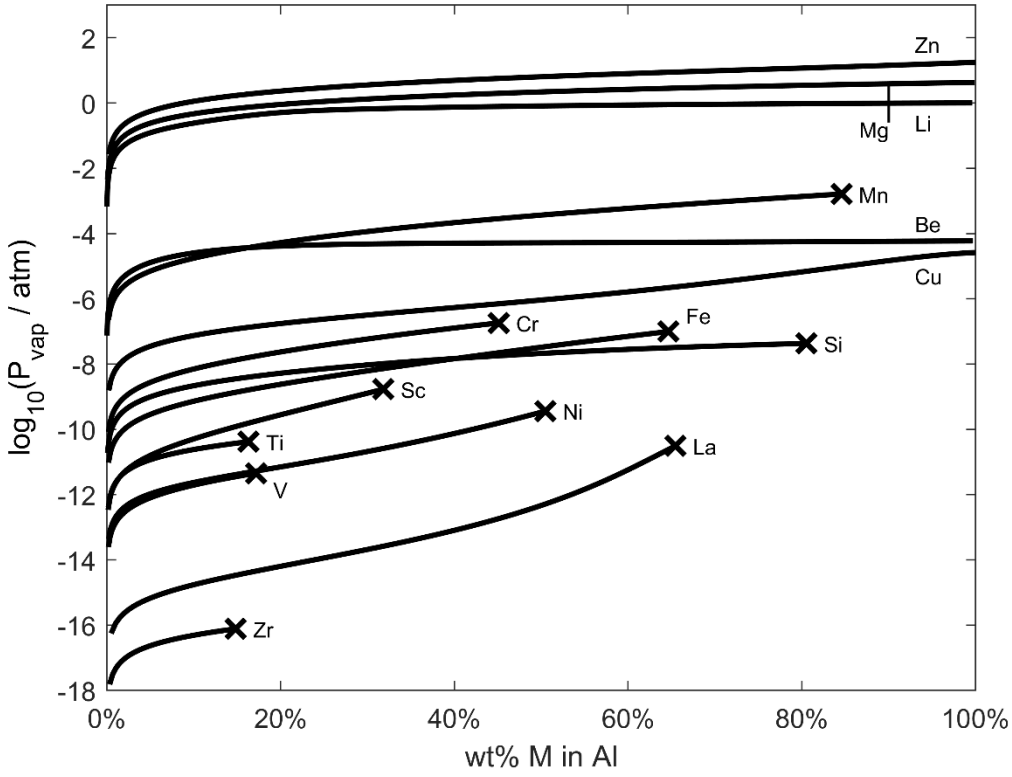

Figure 7.5: Calculated vapor pressure (P_{vap}) of some alloying elements (M) in binary aluminum alloys up to their solubility limit (X) at 1300 °C.

approach to minimize $P_{Al_2S_3}$ is to react it with another component in the system. From the sulfidation series depicted in Chapter 3, Figures 3.4-3.5, Al_2O_3 exhibits a low sulfidation affinity; Al_2S_3 is thermodynamically predicted to sulfidize most other most oxides and itself revert to Al_2O_3. This may be leveraged by introducing a slag phase containing CaO to the reactor. Al introduced as a reductant lacks the reducing power to substantially reduce CaO. However from Chapter 3, Figures 3.4-3.5, Al_2S_3 will sulfidize CaO to produce CaS, effectively lowering $P_{Al_2S_3}$ in the system. This reaction is illustrated below:

$$Al_2S_3(g) + 3CaO(l, slag) = 3CaS(l, matte\ or\ slag) + Al_2O_3\ (l, slag) \qquad (7.3)$$

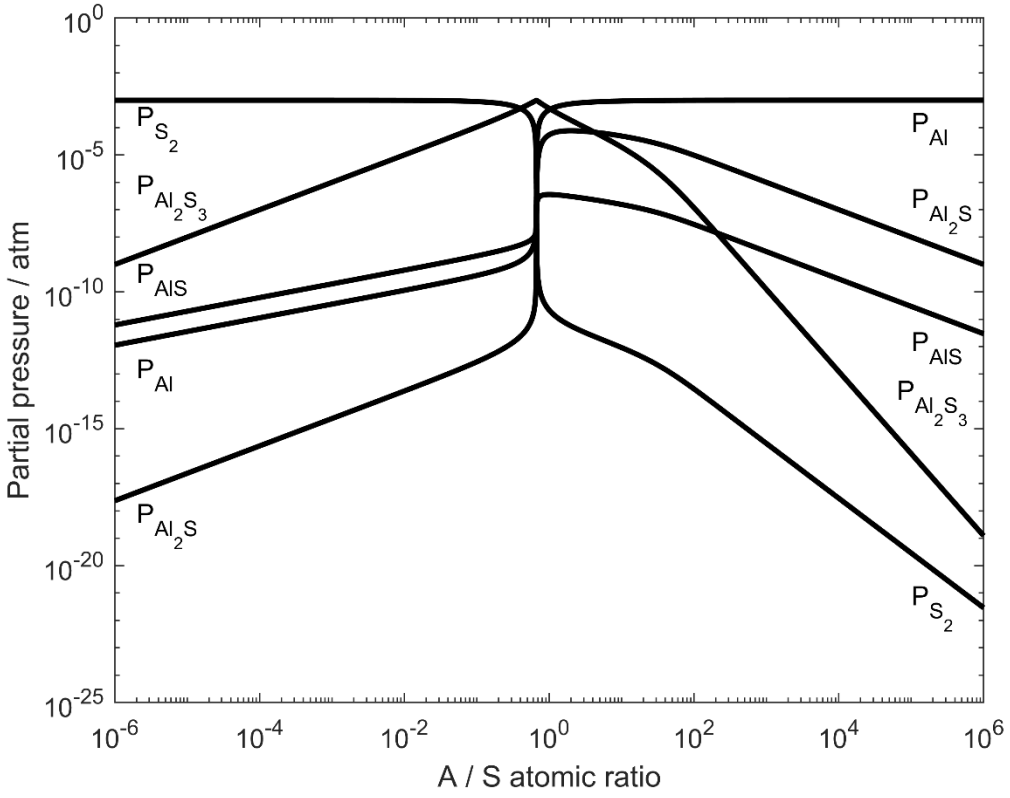

Figure 7.6: Calculated equilibrium composition of an aluminum-sulfur ($Al-S$) gas phase at a total pressure of 10^{-3} atm and a temperature of 1400 °C.

Through comparing oxide sulfidation series, sulfide reduction series, and oxide reduction series (Chapter 3, Figure 3.5), other compounds suitable for scrubbing Al_2S_3 distillate may also be identified. Unlike slagging of Al_2O_3 which often exhibits slower solid-liquid reaction kinetics, the Al_2S_3 distillate vapor bubbles may react with the slag via a more rapid liquid-gas reaction[42].

Alternatively, $P_{Al_2S_3}$ during reactive vacuum distillation may be reduced by modulating the ratio of Al to S in the distillate vapor. Using the FactSage 8.0 FactPS database, Trouton's rule, and the FactSage 8.0 Equilib module, an $Al-S$ containing vapor phase at temperature of 1400 °C and system pressure of 10^{-3} atm was modeled[42]. The relative abundances of different $Al-S$ species as a function of Al to S atomic ratio in the vapor phase are reported in Figure 7.6. $P_{Al_2S_3}$ is maximized at a stoichiometric ratio of Al to S. The presence of additional Al in the distillate product decreases $P_{Al_2S_3}$ and increases the reducing power of Al in the system. During

shifting of the Al to S ratio within the distillate phase, care must be taken to maintain P_{S_2} below the critical threshold for thermodynamic spontaneity during metal sulfide reduction (Figure 7.3). The presence of other reactive metallic species in the distillate vapor may also be employed to modulate $P_{Al_2S_3}$, with contributions from Ca, Mg, and Ba detailed by the author elsewhere[42].

In practice, the distillation of excess Al is likely a more energy intensive pathway to lowering $P_{Al_2S_3}$ than the reaction of Al_2S_3 with a slag containing CaO, the later of which is exothermic and may enable autothermal operation of the reduction reactor[44]. However, when high purity Al_2S_3 is condensed separately outside of a slag phase, it may be reintroduced into the Al supply chain as a marketable byproduct for Al remanufacture. The choice between employing a slag and shifting the Al to S ratio of the gas phase will depend on the specific system chemistry, as well as the sulfide feedstock's and metal product's compatibilities with slags. In the following section, an experimental framework is proposed for testing the efficacy of aluminothermic reduction of sulfides via reactive vacuum distillation. Later, aluminum-manganese (AlMn), ferronickel (FeNi), ferrochromium (FeCr), aluminum-scandium (AlSc), and rare earth ferroalloy production are demonstrated from sulfide feedstocks.

7.1.3 Experimental Methods for Aluminothermic Reduction via Reactive Vacuum Distillation

As discussed in the previous section, aluminothermic reduction via reactive vacuum distillation and direct thermal decomposition of sulfides are thermodynamically promising avenues for reduction of sulfides to metals. In subsequent sections, these approaches will be validated for a range of sulfide feedstocks and metal alloy products using methodologies and reactors described herein.

Aluminothermic reduction via reactive vacuum distillation and direct thermal decomposition of sulfides were conducted in a coreless induction furnace (UltraFlex UPT M35/150, HS-35/150, coil ID: 100 mm, coil height: 100 mm). A quartz (SiO_2) furnace tube was positioning in the center induction coil to contain the sample under vacuum. Furnace tubes with outer diameters of 50 mm or 90 mm and inner diameters of 46 mm or 85 mm respectively with lengths of 610 mm or 762 mm respectively were employed depending on the size of the sample.

Within the SiO_2 furnace tube, a graphite susceptor crucible served as a conductive body for inductive heating. The graphite crucible was supported in the center of the induction coil using a 25 mm OD, 21 mm ID support tube made of either SiO_2 or alumina (Al_2O_3). For tests in the 50 mm tube, samples were held within smaller graphite or alumina crucibles and placed in the susceptor crucible. For tests in the 90 mm tube, the susceptor crucible held the sample directly. Crucible and susceptor dimensions were tuned for each of the system chemistry, discussed in subsequent sections.

For the 50 mm outer diameter quartz tube, commercial KF50 vacuum fittings were employed at the top and bottom of the tube. For the 90 mm outer diameter tube, fittings were machined in house. The 50 mm top fitting contained a viewport window, enabling observation of the sample during reduction as shown in Figure 7.7. The bottom fitting in both sizes contained a centered 25 mm compression fitting which served to hold and center the susceptor crucible support tube. The support tube protruded through the bottom compression fitting and was sealed at the bottom with separate 25 mm diameter furnace fitting machined in house. This bottom fitting contained a port on the side for the vacuum line inlet and a 6 mm compression fitting on the bottom for a thermocouple inlet. The thermocouple ran up through the center support tube with the temperature-sensing tip positioned to touch the bottom of the susceptor crucible.

Prior to heating a sample, the system was evacuated down to a pressure of 10^{-3} atm and refilled with argon (Ar) back to ambient pressure three times. Following, the system was again evacuated to a pressure of 10^{-3} atm. Heating to the reaction temperature was conducted under vacuum for each sample as described in subsequent sections, generally over the course of 15 minutes to a half hour. Upon reaching temperature, the sample was held at temperature for the required reaction time. Afterwards, the furnace power was turned off, allowing the sample to cool. During an experiment, as seen in Figure 7.7 bubbles were observed to form in the melt, corresponding to the distillate vapor. Vapor was observed to condense at the top of the susceptor crucible. Following cooling, the inner crucible with or without the susceptor crucible was mounted in epoxy and cross section for analysis via microscopy. Results for aluminothermic reduction via reactive vacuum distillation and direct vacuum thermal reduction of sulfides are presented in the following sections.

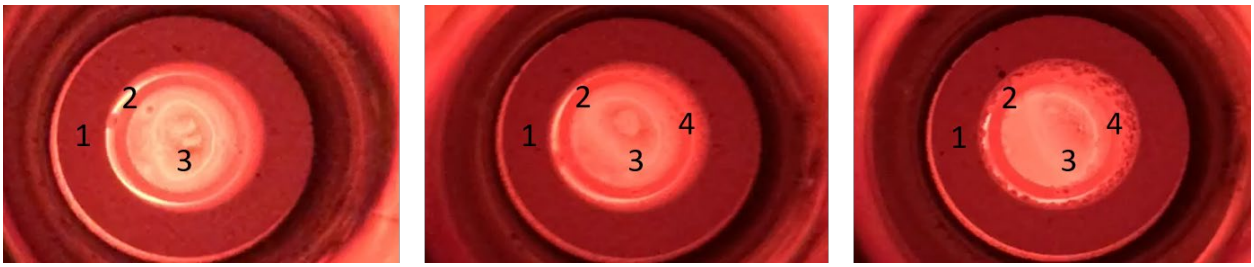

Figure 7.7: View through the top window of an induction furnace fitting during aluminothermic reduction via reactive vacuum distillation. Panels from left to right correspond to the melt upon reaching temperature, after 10 minutes at temperature, and after 20 minutes at temperature. Point 1 corresponds to the graphite susceptor crucible, 40mm in outer diameter. Point 2 corresponds to an inner alumina crucible containing the melt. Point 3 corresponds to the melt with bubble formation due to Al_2S_3 distillation. Point 4 correspond to the buildup of recondensed Al_2S_3 deposit over the course of the experiment higher up on the susceptor outside the furnace hotzone.

7.2 Aluminum Alloy Production from Sulfides

In Section 7.1, aluminothermic reduction of sulfides via reactive vacuum distillation was identified as a promising avenue to produce metals that have previously required more powerful reductants (Mg, Ca, etc.) when reduced from oxides. Herein, AlMn and AlSc alloy production are proposed as case studies to test the efficacy of aluminothermic reduction of sulfides via reactive vacuum distillation. As shown in Figure 7.4, AlMn alloy production at a grade of 10 wt% Mn in Al is thermodynamically spontaneous at $P_{Al_2S_3}$ of 10^{-3} atm, making it a good case study for simple reactive vacuum distillation. Due to the high vapor pressure of Mn even when alloyed with Al, this trial also serves as a test of the selectivity achievable in the distillate phase.

From Figure 7.4, AlSc alloy production is predicted to require substantially lower $P_{Al_2S_3}$ than for AlMn. This case study in turn provides insight into the efficacy of controlling the Al to S ratio in the distillate vapor to minimize $P_{Al_2S_3}$. As illustrated in Figure 7.1-7.2, Chapter 2, Figure 2.1, and Chapter 3, Figure 3.5, both Mn and Sc are more reactive with S than Al, providing scenarios to test the hypothesis that sulfidation decreases the thermodynamic barrier to metal reduction, supporting the use of less reactive reductants or direct thermal decomposition for metal production. The distillation behaviors of common Al alloying components are also explored, informing the use of scrap Al as a reductant. When purified Al_2S_3 distillate is

recovered, it may be reintroduced into the supply chain for Al remanufacture. This provides an avenue to integrate Al recycling with sulfide metal reduction.

7.2.1 Aluminum-Manganese Alloy Production

Manganese (Mn) is the major alloying addition to 3XXX series aluminum (Al) alloys, used for moderate strength applications in consumer and architectural products[46]. Mn for Al alloy production is generally sourced as a master alloy with Mn contents ranging from 10 wt% to over 60 wt%[47]. Alternatively, Mn may be introduced to the Al melt using a briquet of Mn metal or compound mixed with a halide flux[48]. A typical yield in industrial master alloy production by mixing pure Al with electrolytic Mn powder is of the order of 60% or lower[49]. The industrial production of electrolytic Mn prior to alloying exhibits low efficiency and high energy usage, with Mn yields on the order of 50-75%[50]. Therefore, the yield of Mn in the master alloy across both electrolytic reduction and alloying is only of 30-45%, leading to high costs per unit of Mn in the master alloy product. This motivates the search for master alloy production methods with higher yields in both Mn reduction and alloying with Al. Sulfide chemistry provides a pathway to integrate reduction and alloying into a single, high-yield processing step.

AlMn alloy at a Mn grade of 10 wt% (AlMn10) is chosen as a first case study for production of Al master alloys from metal sulfides using aluminothermic reduction via reactive vacuum distillation. As calculated in Figure 7.5, Mn exhibits a high vapor pressure compared to most other Al alloying elements. Therefore, the extent of Al_2S_3 vaporization and the yield of Mn in the alloy product versus the distillate product provides insight into process feasibility.

Aluminothermic reduction of manganese sulfide (MnS) to Mn in the presence of excess Al to produce volatile aluminum sulfide (Al_2S_3) is described by the following reaction[43]:

$$MnS(s) + \frac{2}{3}Al(l) = Mn(l, in\ Al) + \frac{1}{3}Al_2S_3(g) \tag{7.4}$$

MnS and Al were utilized as feedstocks in a mass ratio of 0.171, corresponding stoichiometrically to a predicted alloy product composition of 10 wt% Mn and 90 wt% Al, within the specifications of AlMn10 master alloy (9-11 wt% Mn[47]). Reduction was conducted

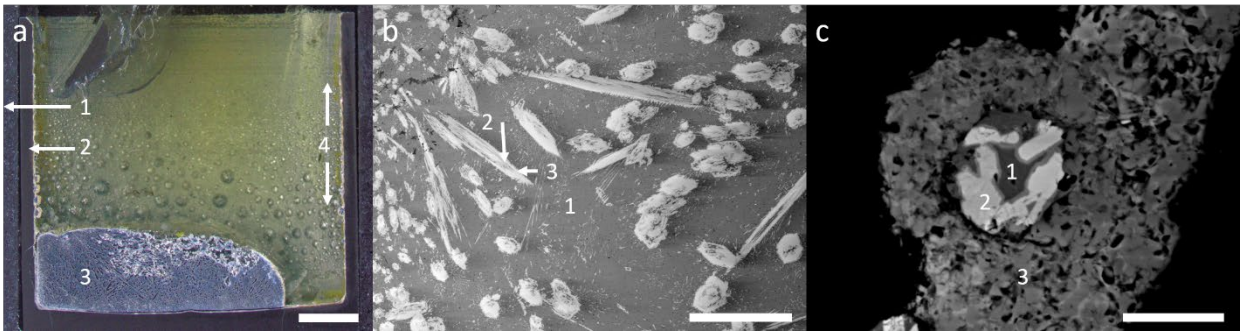

Figure 7.8: Distribution of product phases following aluminothermic reduction of manganese sulfide (MnS) via reactive vacuum distillation. a: Optical image of the cross section of the graphite susceptor (1) and inner graphite crucible (2) containing the $Al-Mn$ metal alloy product (3) in the bottom of the inner crucible, with distillate (4) deposited on the crucible wall above the alloy product. Scale bar corresponds to 5mm. b: SEM/BEC image of the bottom metal alloy product, with the dark gray phase (1) identified as Al, the intermediate gray phase (2) identified as $MnAl_6$, and the light gray phase identified as $MnAl_{4.17}$. Scale bar corresponds to 600 μm. c: SEM/BEC image of the distillate products, with dark gray (1) and light gray phases identified as metal alloys rich in Al and Mn respectively, and the intermediate gray phase (3) identified as a sulfide distillate product. Scale bar corresponds to 30 μm.

via reactive vacuum distillation by heating the mixture at 1300 °C under a pressure of 0.001 atm in an induction furnace for 35 minutes, using methods and procedures described in Section 7.1.2 and detailed by the author elsewhere[43]. Reduction was conducted in both graphite and Al_2O_3 crucibles of equal size held within a graphite susceptor as a point of comparison.

Cross sections of the graphite susceptor, graphite inner crucible, and products following reactive vacuum distillation are depicted[43] in Figure 7.8. Three distinct product regions are visible following reactive vacuum distillation: the metal product that remained within the inner crucible at the bottom, the sulfide distillate that condensed and formed a coating on the upper walls of the inner crucible and graphite susceptor, and a small quantity of dispersed metal distillate that condensed on the upper walls of the inner crucible and graphite susceptor as droplets on the order of 10-500 microns in size alongside the sulfide distillate. Within the metal product found at the bottom, three phases are observed via scanning electron microscope energy-dispersive x-ray spectroscopy (SEM-EDS), corresponding to Al metal and two $Al-Mn$ intermetallic alloys. The same product regions and phases were also observed when reduction

was conducted using an alumina inner crucible. The compositions of the bottom and distillate phases are presented[43] in Table 7.2.

The bottom metal alloy product from the graphite inner crucible was found to exhibit bulk Mn and Al contents of 10.1 wt% and 89.7 wt% respectively, consistent with specifications[47] for AlMn10 master alloys. This shows that aluminothermic reduction of sulfides via reactive vacuum distillation can support the production of Al master alloys in a single processing step that simultaneously encompasses both reduction and alloying, as demonstrated here for AlMn[43]. Al_2S_3 was formed as a distillate byproduct of the aluminothermic reduction reaction, and may be recycled via direct reduction, or calcined to Al_2O_3 and reduced via the conventional Hall-Heroult process. While S impurity content was observed to be on the order of 0-0.4 wt%[43], SEM-EDS analysis was unable to determine if the S content was below the maximum of 0.04-0.05 wt% specified for AlMn10 grade AlMn master alloys[47]. Analytical techniques more sensitive for quantification of sulfur, such as light element combustion analysis (LECO), are necessary to pinpoint the exact sulfur content of the master alloy product.

Crucible Material	Region	Phase	Al	Mn	S
Graphite	Bottom	Bulk Metal	89.7 wt% (+/- 0.9)	10.1 wt% (+/- 0.7)	0.2 wt% (+/- 0.2)
		Al	98.4 wt% (+/- 0.7)	1.5 wt% (+/- 0.3)	0.1 wt% (+/- 0.1)
		$MnAl_6$	78.0 wt% (+/- 0.7)	22.0 wt% (+/- 0.6)	0.1 wt% (+/- 0.1)
		$MnAl_{4.17}$	72.2 wt% (+/- 0.6)	27.6 wt% (+/- 1.3)	0.2 wt% (+/- 0.1)
	Distillate	Bulk Metal	86.1 wt% (+/- 2.2)	13.9 wt% (+/- 1.4)	na
		Sulfide	38.2 wt% (+/- 0.5)	2.2 wt% (+/- 0.3)	59.6 wt% (+/- 0.6)
Alumina	Bottom	Bulk Metal	91.3 wt% (+/- 0.7)	8.5 wt% (+/- 0.4)	0.2 wt% (+/- 0.2)
	Distillate	Bulk Metal	83.2 wt% (+/- 2.4)	14.4 wt% (+/- 2.2)	2.4 wt% (+/- 0.8)

Table 7.2: Average composition of aluminum manganese (AlMn) master alloy products. Compositions were determined via SEM-EDS, where "na" corresponds to species not analyzed. Standard deviations are reported in parenthesis.

The bulk bottom metal product is observed to be made up of two Al alloy phases that were precipitated out of the Al solution upon solidifying (Figure 7.8, panel b), with Mn contents of 22.0 wt%, 27.6 wt%, and 1.5 wt% respectively[43]. The alloy phases rich in Mn are taken to correspond to $MnAl_6$ and $MnAl_{4.17}$ precipitants in Al as charted in the phase diagram by Liu et al[51], with solubility for Al shifting the composition off stoichiometry. The S contents of these three phases in the product are observed to be on the order of 0-0.2 wt%. This S content is less than that observed in the average bulk composition, suggesting minor entrainment of sulfides dispersed in the metal product[43]. When an Al_2O_3 inner crucible was employed instead of a carbon inner crucible, the bulk composition of the bottom product was observed to be less rich in Mn at 8.5 wt% with marginally higher S content at 0-0.5 wt%[43].

Table 3 shows the fraction of Mn, Al, and S that partitioned into each of the bottom metal, distillate metal, and distillate sulfide products, allowing for determination of AlMn master alloy yields[43]. For the system employing the alumina inner crucible, the direct yield of Mn into the bottom AlMn master alloy was 66.2%[43]. In reality, the metal distillate product is readily separated from the sulfide distillate using magnetic separation or flotation, and therefore may be recycled through the aluminothermic reduction system. This provides a practical Mn yield in the AlMn master alloy of about 98.1%[43]. Meanwhile, for the system employing the graphite inner crucible, the direct yield of Mn into the bottom AlMn master alloy was 95.7%, with a practical yield of about 97.9%[43]. These metrics greatly exceed today's industrial yields in AlMn master alloys production, generally on the order of 30-45% in total across Mn reduction and alloying steps[43]. Overall, these results confirm that metal sulfides are viable feedstocks for Al alloy production using aluminothermic reduction via reactive vacuum distillation. In the following sections, this methodology is extended to produce AlSc alloy products while minimizing the presence of metallic impurities introduced during the use of scrap reductants.

7.2.2 Aluminum-Scandium Alloy Production

Scandium (Sc) alloying additions to Al provide numerous benefits, including inhibition of recrystallization during heat treatment, high specific strengthening, grain refinement, reduced hot cracking during welding, and improved fatigue resistance[52]. These attributes have placed Al alloys containing Sc among desired materials for applications requiring good manufacturability

and ultra-high strength to weight ratios[53]. However, examples are currently limited to niche athletic and aerospace uses due to high costs stemming from challenges in Sc extraction, reduction, and alloying[54].

Sc is a highly reactive rare earth metal that forms one of the most stable pure oxides (Chapter 3, Figure 3.4). This presents a thermodynamic challenge for metal reduction. Several processing pathways have been proposed for reduction of scandium oxide (Sc_2O_3) or its halogenated compounds to produce AlSc master alloys, including molten salt electrolysis[55,56] and metallothermic reduction of the oxide or halide[57–59]. While shifting from oxide to halide-based reduction chemistry enables less reactive metallic reductants to be employed, industrial-scale operation using these methods is challenging due to burdens associated with halogenation, high costs, low yields, and undesirable byproduct formation. An alternative sulfide-based pathway for Sc production is attractive; as shown in Chapter 3, Figure 3.4 compared to other metals Sc is relatively less stable as a sulfide than as an oxide. Furthermore, sulfidation exhibits low economic and environmental impacts (Chapter 6). As discussed in Section 7.1, Al is a promising reductant due to both its affinity for S and its volatility as a sulfide. Al is also comparatively less reactive than alternatives such as Ca and magnesium Mg, thereby exhibiting lower environmental impacts in primary production. Al scrap resources are also abundant and may be viable for use as reductants depending on their impurity landscape, explored later in this section.

The aluminothermic reduction of scandium sulfide (Sc_2S_3) may be described by the following reaction[60]:

$$Sc_2S_3 + 2Al(l) = 2Sc(s,l) + Al_2S_3(l,g) \tag{7.5}$$

Sc_2S_3 precursor was synthesized as described in Chapter 4, Section 4.1 and elsewhere by the author[60]. AlSc alloy was produced from Sc_2S_3 through aluminothermic reduction via reactive vacuum distillation in a vacuum induction furnace at the hundred-gram scale using apparatuses and procedures described in Section 7.3.1 and elsewhere by the author[60]. 6061 Al alloy was employed as the reductant with a composition[60] reported in Table 7.3. The Sc_2S_3 and Al in the graphite crucible were reacted at a temperature of 1550 °C and a vacuum pressure of 10^{-3} atm for

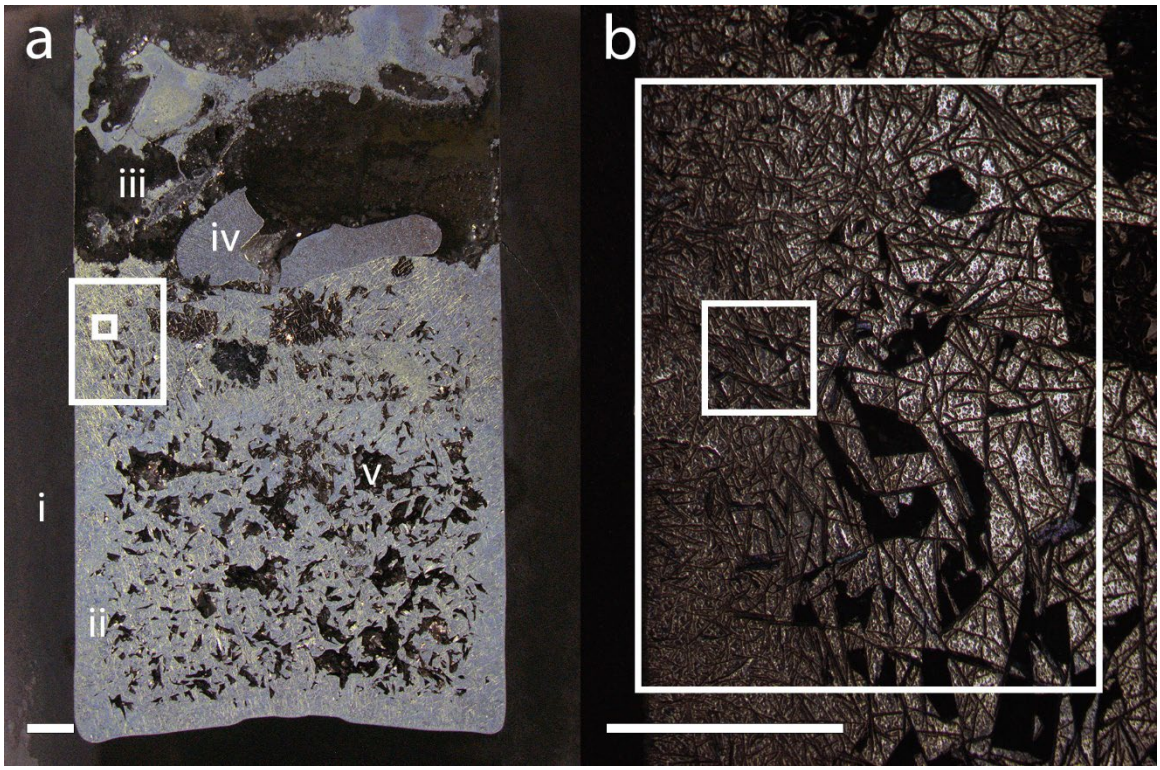

Figure 7.9: Aluminum-scandium (AlSc) alloy produced via reactive vacuum distillation. Panel a corresponds to a cross section of the graphite crucible (i) containing the aluminum-scandium alloy product (ii), sulfide distillate (iii), and aluminum metal distillate (iv). Significant porosity (v) is observed in the aluminum-scandium alloy following cooling. The region marked by the outer box is detailed in panel b, revealing the existence of needle-shaped intermetallic phases throughout the aluminum-scandium alloy product. The chemical composition of the region marked by the inner box is quantified using SEM-EDS element maps in Figure 7.10. Scale bars: 5 mm

25 minutes in an induction furnace. Following the reaction, the furnace power was then shut off and the crucible containing the metal product was allowed to cool under vacuum, dropping from 1550 °C to 600 °C in 10 minutes[60].

Aluminothermic reduction of Sc_2S_3 at 1550 °C produced an $Al - Sc$ metallic product with dispersed needle structures rich in Sc. Metallic and nonmetallic distillates rich in Al were also formed. These regions are depicted in the cross section illustrated[60] in Figure 7.9. The compositions of the metallic products from SEM-EDS, spark optical emission spectroscopy (OES), LECO, and inductively coupled plasma mass spectroscopy (ICP-MS) are reported[60] in Table 7.3. The presence of crystalline product phases was confirmed via x-ray diffraction (XRD), reported elsewhere[60]. Element distributions in the metallic product are shown in the

SEM-EDS maps[60] in Figure 7.10. For quantification of bulk alloy and distillate compositions, representative samplings of 2 mm x 2 mm EDS area spectrums were conducted across the surfaces of the product.

	6061 (OES[a], LECO[b], ICP[c])	**$Al-Sc$, product (OES[a], LECO[b], ICP[c])**	**$Al-Sc$, product (SEM-EDS)**	**$Al-Sc$ product, $ScAl_3$ (SEM-EDS)**	**$Al-Sc$ product, Al (SEM-EDS)**	**$Al-Sc$ product, metallic distillate (SEM-EDS)**
Al	rem	rem	94.4 wt% (+/- 4.0)	76.4 wt% (+/- 0.3)	97.8 wt% (+/- 0.1)	96.1 wt% (+/- 0.9)
Sc	nil[c]	0.38[c]	3.3 wt% (+/- 4.0)	21.4 wt% (+/- 0.3)	0.3 wt% (+/- 0.2)	0.3 wt% (+/- 0.1)
Mg	0.8[a]	0.02[a]	na	na	na	na
Si	0.7[a]	0.57[a]	0.4 wt% (+/- 0.1)	0.2 wt% (+/- 0.1)	0.2 wt% (+/- 0.1)	0.5 wt% (+/- 0.2)
Fe	0.41[a]	0.39[a]	0.4 wt% (+/- 0.1)	0.3 wt% (+/- 0.1)	0.3 wt% (+/- 0.1)	0.5 wt% (+/- 0.1)
Cu	0.33[a]	0.37[a]	0.5 wt% (+/- 0.2)	0.2 wt% (+/- 0.1)	0.6 wt% (+/- 0.1)	0.5 wt% (+/- 0.2)
Cr	0.05[a]	0.05[a]	0.1 wt% (+/- 0.1)	0.4 wt% (+/- 0.1)	0.1 wt% (+/- 0.1)	0.1 wt% (+/- 0.1)
Zn	0.04[a]	0.01[a]	0.1 wt% (+/- 0.1)	0.3 wt% (+/- 0.1)	0.1 wt% (+/- 0.1)	0.2 wt% (+/- 0.1)
Ti	0.02[a]	0.06[a]	0.1 wt% (+/- 0.1)	0.4 wt% (+/- 0.1)	0.1 wt% (+/- 0.1)	0.1 wt% (+/- 0.1)
Mn	0.05[a]	0.04[a]	0.1 wt% (+/- 0.1)	0.1 wt% (+/- 0.1)	0.1 wt% (+/- 0.1)	0.1 wt% (+/- 0.1)
S	nil[b]	0.12[b]	0.5 wt% (+/- 0.1)	0.3 wt% (+/- 0.2)	0.3 wt% (+/- 0.2)	1.6 wt% (+/- 0.7)
O	0.001[b]	3.18[b]	na	na	na	na
C	0.007[b]	0.39[b]	na	na	na	na

Table 7.3: Compositions of 6061 reductant and aluminum-scandium ($Al-Sc$) alloy products. Compositions on a mass fraction basis were determined via spark-OES, LECO, ICP-MS, and SEM-EDS analysis. Error values correspond to +/- one standard deviation, "nil" denotes values below the detection limit, "rem" denotes a component that constitutes the remainder of the composition, and "na" denotes species not analyzed herein via SEM-EDS.

From SEM-EDS area analysis, a total Sc content of approximately 3.3 wt% was achieved in the metal product, with some surveyed 2 mm x 2 mm sections such as in Figure 7.9 exhibiting total Sc contents above 6 wt%[60]. The Sc content of the distillate metal product was significantly lower at 0.3 wt% and less variable. The observed Sc content herein of 3.3 wt% exceeds that of

commercial master alloy, marketed at a grade of 2 wt% Sc[60]. Lower amounts of Sc_2S_3 may be introduced during reduction to produce AlSc alloy at 2 wt% Sc if desired. To test the viability of higher Sc grade master alloys for subsequent alloying, such as those manufactured herein via sulfide chemistry, their melting and mixing behaviors require exploration. The morphology and surface area of the $Al-Sc$ master alloy will require optimization to maximize dissolution rate and yield while minimizing oxidative loss of the phases rich in Sc.

The average Sc content of the needle-shaped intermetallic phases was 21.4 wt%, whereas the Sc content of Al bulk was 0.3 wt%[60]. XRD analysis confirmed the $Al-Sc$ intermetallic to be $ScAl_3$ as reported by the author elsewhere[60]. $Al-S$ precipitants were observed to be present at the interface of the $ScAl_3$ and bulk Al, whereas iron-silicon aluminide ($Fe-Si-Al$) precipitants were dispersed throughout. The $Al-S$ and $Fe-Si-Al$ precipitants were found to be Al_2S_3 and $Fe_3(Al_{0.3}Si_{0.7})$ respectively via XRD as reported by the author elsewhere[60]. Trace amounts of aluminum carbide (Al_4C_4) were also observed via XRD. Carbide, oxide, or oxysulfide byproducts containing Sc were not observed via SEM-EDS or XRD, indicating that complete aluminothermic reduction of Sc_2S_3 to AlSc is possible.

Analysis of the $Al-Sc$ alloy product via ICP-MS yielded a Sc content in the metallic product of 0.38 wt%[60]. This result was inconsistent with those obtained via SEM-EDS and XRD. This discrepancy is likely due to sampling error, and may have explanations rooted in thermodynamics or mass transport[60]. As shown in Figure 7.9, the distillate metal phase is in direct contact with the $Al-Sc$ product, yet they remain unmixed. During reactive vacuum distillation, Al vapors recondensed within the graphite susceptor and flowed back down toward the $Al-Sc$ alloy melt, separating from more volatile Mg and zinc (Zn) species that recondensed elsewhere as discussed later. Due to highly enthalpically-favorable mixing and compound formation between Al and Sc, $Al-Sc$ complexes or associates and short range ordering likely persist hundreds of degrees above the alloy's melting point[61]. The presence of short range ordering may slow diffusion[62] and remixing of $Al-Sc$ product with Al distillate, possibly leading to local macroscopic variations in Sc content that were preserved when the product was quenched. During sampling for ICP-MS, one of these regions deficient in Sc may have been analyzed[60].

Alternatively, oxidation of $ScAl_3$ phases during handling may have hindered analysis. From XRD, oxide phases were not observed in the metal product. However in subsequent

LECO analysis, significant oxidation was observed[60]. Sc is known to exhibit a higher affinity for O than Al in both pure (Chapter 2, Figure 2.1 and Chapter 3, Figure 3.5) and alloyed[63] forms, indicating that preferential oxidation of $ScAl_3$ phases may have occurred during the time between SEM-EDS/XRD and spark-OES/LECO/ICP-MS. $Sc-Al$ oxide coatings on the surface of the intermetallic may have subsequently hindered their aqueous dissolution and analysis via ICP-MS. The ICP-MS results for overall Sc content were comparable to the Sc content observed via SEM-EDS analysis of the bulk Al phases found between intermetallics[60].

Results from SEM-EDS and spark-OES for the partitioning of alloying agents from the 6061 reductant between metal product and distillate phases are in good agreement, suggesting that analytical and sampling challenges were limited to Sc quantification and ICP-MS[60]. Mg, Zn, and some Si impurities introduced as alloying agents in the 6061 feedstock were removed from the system during reactive vacuum distillation. Mg and Zn were also depleted in the condensed Al distillate, suggesting they were condensed in the nonmetallic distillate or outside the graphite susceptor. Fe, Cu, Mn, and chromium (Cr) impurities showed a fairly uniform partitioning between metallic product and metallic distillate phases. Meanwhile, reactive vacuum distillation was shown to enrich the metal product in titanium (Ti). Within the metal product, residual Cu preferentially partitioned to the Al bulk, whereas residual Cr, Zn, and Ti preferentially partitioned to $ScAl_3$ intermetallic phases.

The observed behaviors of trace impurity elements provide a roadmap for how scrap Al may be leveraged for the aluminothermic reduction of sulfides. Mg, Si, and Zn impurities in the reduction feedstock are readily volatilized and have a limited impact on product purity. Fe impurities reacted with Si in the metal product, lowering the extent of Si distillation. Meanwhile, other 6061 alloying agents showed limited selectivity in distillation and may accumulate in the metal product. Depending on the specifications required for the $Al-Sc$ master alloy product, Al scrap with lower levels of deleterious impurities may be employed. The use of unsorted scrap in reduction remains another path of exploration.

Together, these results indicate that sulfidation followed by aluminothermic reduction via reactive vacuum distillation constitutes a promising avenue for AlSc master alloy production with high Sc yields[60]. By processing Sc as a sulfide, Mg and Ca are no longer needed as reductants. This confirms the hypothesis that sulfidation of Sc_2O_3 to Sc_2S_3 decreases its

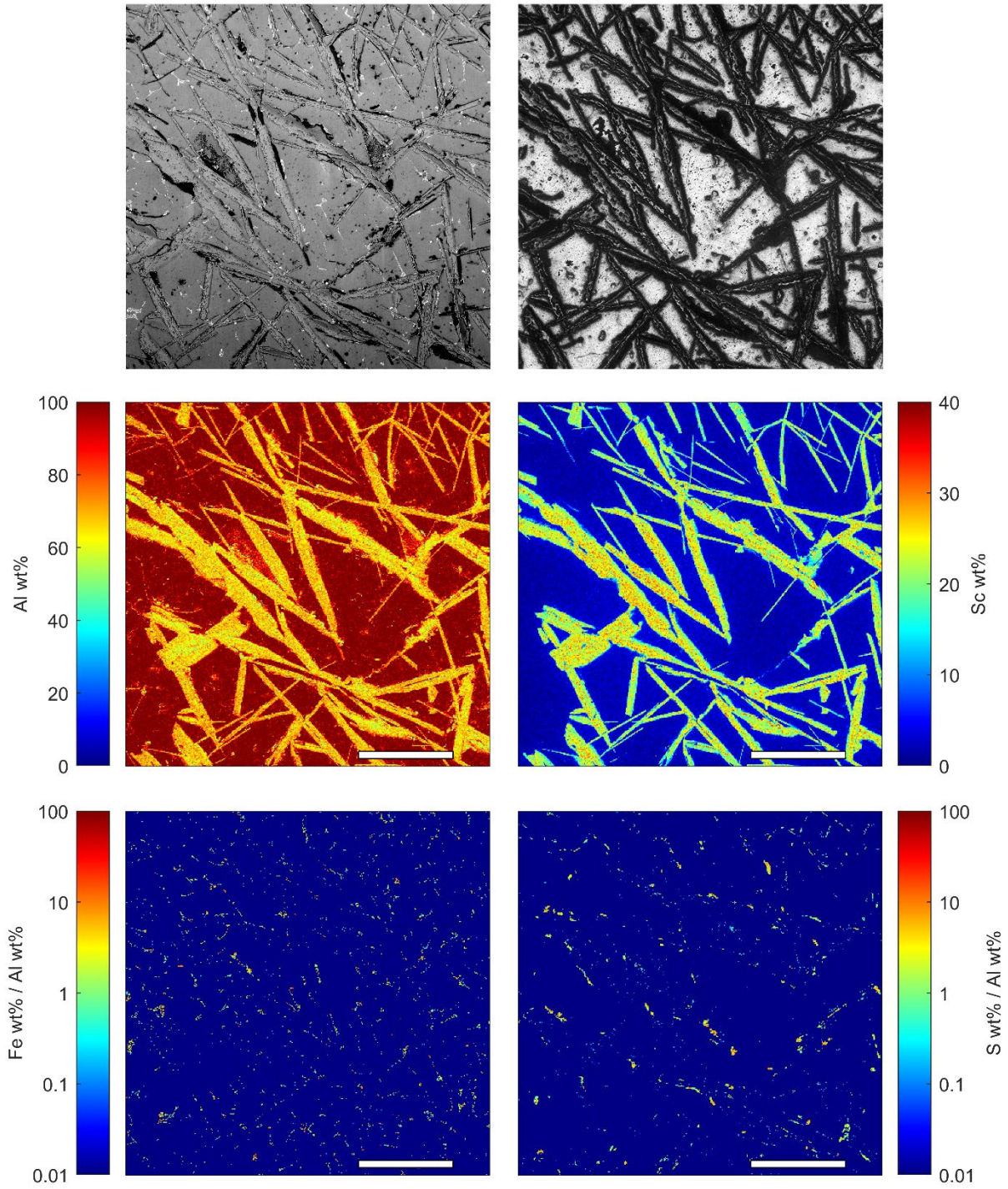

Figure 7.10: Spatial element distribution of aluminum-scandium ($Al-Sc$) alloy components. Mapping was conducted via SEM-EDS. Top left and right panels correspond to SEM backscattered electron composite and optical images respectively of the region analyzed. SEM-EDS maps have been calibrated using SEM-EDS point analysis and XRD data. Scale bars correspond to 500 µm.

thermodynamic barrier to metal reduction, supporting the use of less reactive reductants for metal production. In the following section, reactive vacuum distillation and direct thermal decomposition are demonstrated for the production of ferroalloys.

7.3 Ferroalloy Production from Sulfides

As discussed in Section 7.1.1, some metal sulfides such as iron sulfide (FeS) are amenable to direct vacuum thermal decomposition. Others require the addition of a reductant; the thermodynamic case was made in Section 7.1.2 for aluminothermic reduction via reactive vacuum distillation. In the previous section, aluminothermic reduction was demonstrated for the production of AlMn and AlSc alloys from sulfide feedstocks. Herein, these approaches are extended to the production of ferroalloys.

Fe-lanthanide (Ln) sulfide produced via the sulfidation of rare earth magnets is treated through direct vacuum thermal decomposition to produce a rare earth ferroalloy. Ln partitioning into the metal phase from the sulfide is found to be selective, enabling single-stage separations for groups of critical rare earth elements. Production of rare earth ferroalloy via vacuum thermal treatment supports the hypothesis that sulfidation decreases the thermodynamic barrier to metal reduction, supporting the use of less reactive reductants or direct thermal decomposition for metal production.

Aluminothermic reduction via reactive vacuum distillation is then conducted for FeNi and FeCr production. In these case studies, slag phases are present, illustrating their utility in modulating $P_{Al_2S_3}$ in the system during sulfide reduction and minimizing Al content in the product alloy. These examples further bolster the claim that pyrometallurgical oxide-sulfide anion exchange enables new pathways to carbon-free materials separations and metal production.

7.3.1 Selective Iron-Rare Earth Alloy Production from Rare Earth Magnets

Recycling of rare earth magnets is a promising avenue to confront the mismatch between individual Ln market demand and the relative abundance of different Ln in natural resources, termed the “balance problem”[64]. Additionally, the establishment of local recycling processes for

critical elements helps to decouple domestic consumption from geopolitically sensitive foreign sources. Rare earth magnet remanufacturing poses a particular challenge, as they currently require high purity metal or ferroalloy feedstocks which are currently produced via environmentally degrading molten fluoride or oxyfluoride electrolysis[65]. Different magnet grades require different ratios of light and heavy Ln, meaning that recycling processes for magnet remanufacture should be tuned to separate these earth elements from mixed-grade magnet waste streams. Process bottlenecks exist in both Ln separation and metal reduction.

As demonstrated in Chapter 4, Section 4.4.1, calcined iron-neodymium-boron (FeNdB) magnets may be selectively sulfidized to isolate neodymium (Nd) and praseodymium (Pr) from iron (Fe). Meanwhile, dysprosium (Dy) was observed to preferentially partition to the iron sulfide (FeS) product phase, likely motivated by higher siderophilicity. As illustrated in Figure 7.3, at temperature of 1600 °C the $\left[P_{S_2}\right]_{crit}$ for direct vacuum thermal decomposition of FeS to Fe and S_2 is 10^{-3} atm. Under these same conditions Ln sulfides are predicted to be stable. For highly siderophilic rare earth elements (Ln^{sid}) however, alloying with Fe may serve as a thermodynamic driving force for direct vacuum thermal decomposition of the sulfide. The following reactions are proposed, where β, γ, δ, and ϵ are stoichiometric coefficients:

$$FeS(l) = Fe(l) + \frac{1}{2}S_2(g) \tag{7.6}$$

$$\beta(Ln - Ln^{sid})_2S_3(s,l) = \gamma Ln^{sid}(l, in\ Fe) + \delta Ln_2S_3(s,l) + \epsilon S_2(g) \tag{7.7}$$

Direct vacuum thermal decomposition of mixed rare earth sulfides from sulfidized rare earth magnets was demonstrated[42]. A mixed Fe, Ln, boron (B) sulfide was synthesized via the complete sulfidation of uncoated N38SH magnets held at 1000 °C for 2 hours with a P_{S_2} of 0.2 – 0.8 atm using reactors and equipment described in Chapter 3, Section 3.3.2. Following sulfidation, the mixed sulfide was heated at 1600-1800 °C for 40 minutes under a vacuum of 10^{-3} atm in a graphite crucible. Following the vacuum thermal treatment, two major product phases were identified: a metal rich in Fe and a sulfide rich in Nd and Pr. A minor sulfide phase slightly richer in Fe was occasionally found at the interface between major sulfide and metal phase. The compositions of the three identified product phases are reported in Table 7.4 as

analyzed via electron probe micro analysis wavelength dispersive x-ray spectroscopy (EPMA-WDS)[42]. Separation factors (β_{sep}, Chapter 2, Eqn. 2.1) between the two major phases are reported in Table 7.5.

Under the conditions of the vacuum thermal treatment, standard state thermodynamics (Figure 7.3) predict that FeS would be reduced to Fe metal via the vacuum thermal treatment, which was confirmed experimentally. Surprisingly, cerium (Ce), samarium (Sm), europium (Eu), terbium (Tb), holmium (Ho), and thulium (Tm) were coreduced and partitioned to the metallic phase, despite standard state thermodynamics suggesting that they would remain stable as sulfides (Figure 7.3). Dy and erbium (Er) are observed to be split between the metal and sulfide phases. Trends in rare earth partitioning between metal and sulfide phases may be correlated with trends in chondrite rare earth partitioning (Chapter 2, Figure 2.3). Complete separation is accomplished for many rare earth element pairs down to the detectible limit of EPMA-WDS, indicating that like FeS (Chapter 4, Sections 4.4.1-4.4.3 and Chapter 5, Section 5.2.2), Fe metal may also serve as a selective collector phase for rare earth elements[42]. These results suggest that the sulfide rich in Nd and Pr may be isolated from the metal product rich in Fe and Ln^{sid}, then subsequently reduced to form a $Nd-Pr$ master alloy applicable for most magnet applications. The alloy of Fe and Ln^{sid} could in principle be leveraged for remanufacture of magnets requiring higher fractions of heavy Ln. Further work is needed to determine the extent of product refining required prior to magnet remanufacturing.

The observed differences in thermodynamic stabilities between individual Ln and their sulfides are likely due to solution effects in the metal and sulfide phases. While sulfide affinities for some individual Ln in liquid metallic Fe are known in the dilute limit of S[66,67], the solution thermodynamics of mixed Ln partitioning between sulfide matte and Fe metal phases remain unexplored. Nevertheless, these results indicate that some Ln sulfides may be selectively reduced to metal in an Fe collector phase via vacuum thermal treatment alone. This serves as a promising avenue for rare earth ferroalloy production without the necessity of reactive metal reductants or environmentally degrading fluoride or oxyfluoride electrolysis. This result also confirms the hypothesis that sulfidation decreases the thermodynamic barrier to metal reduction, supporting the use of less reactive reductants or direct thermal decomposition for metal production.

	Sulfide (Major)	Sulfide (Minor)	Metal
Fe	0.2 wt% (+/- 0.2)	5.4 wt% (+/- 1.5)	92.6 wt% (+/- 0.4)
La	0.8 wt% (+/- 0.1)	0.7 wt% (+/- 0.1)	<0.1 wt% (+/- <0.1)
Ce	<0.1 wt% (+/- <0.1)	<0.1 wt% (+/- <0.1)	0.1 wt% (+/- <0.1)
Pr	12.2 wt% (+/- 03)	11.0 wt% (+/- 0.5)	0.1 wt% (+/- 0.1)
Nd	56.0 wt% (+/- 0.6)	48.0 wt% (+/- 1.5)	<0.1 wt% (+/- <0.1)
Sm	<0.1 wt% (+/- <0.1)	<0.1 wt% (+/- <0.1)	0.1 wt% (+/- 0.1)
Eu	<0.1 wt% (+/- <0.1)	<0.1 wt% (+/- <0.1)	2.6 wt% (+/- 0.2)
Gd	3.2 wt% (+/- 0.1)	1.9 wt% (+/- 0.3)	<0.1 wt% (+/- <0.1)
Tb	<0.1 wt% (+/- <0.1)	<0.1 wt% (+/- <0.1)	0.9 wt% (+/- 0.1)
Dy	1.2 wt% (+/- 0.1)	0.9 wt% (+/- 0.1)	0.3 wt% (+/- 0.1)
Ho	<0.1 wt% (+/- <0.1)	0.2 wt% (+/- 0.2)	0.3 wt% (+/- 0.2)
Er	0.3 wt% (+/- 0.2)	0.3 wt% (+/- 0.2)	0.8 wt% (+/- 0.1)
Tm	<0.1 wt% (+/- <0.1)	<0.1 wt% (+/- <0.1)	0.2 wt% (+/- 0.2)
Lu	2.0 wt% (+/- 1.3)	<0.1 wt% (+/- <0.1)	<0.1 wt% (+/- 0.1)
S	24.1 wt% (+/- 0.1)	31.3 wt% (+/- 0.7)	<0.1 wt% (+/- <0.1)
O	0.1 wt% (+/- <0.1)	0.3 wt% (+/- 0.1)	0.3 wt% (+/- <0.1)
B	<0.1 wt% (+/- <0.1)	<0.1 wt% (+/- <0.1)	1.8 wt% (+/- 0.6)

Table 7.4: Composition of major sulfide, minor sulfide, and metal phases following vacuum thermal decomposition of a sulfidized rare earth magnet. Chemical analysis was conducted via EPMA-WDS. Error values in parenthesis correspond to +/- one standard deviation.

	La	Ce	Pr	Nd	Sm	Eu	Gd	Tb	Dy	Ho	Er	Tm	Lu
Fe	>42000	>80	103927	7128278	>50	>2	>200000	>6	2455	>20	205	>30	53357
La		>500	>2	>200	>900	>20000	>4	>7000	>20	>3000	>200	>1000	>1
Ce			>1000	>90000	>2	>40	>2000	>13	>30	>5	>3	>2	>700
Pr				69	>2000	>50000	>2	>20000	42	>6000	507	>3000	2
Nd					>150000	>3000000	>40	>1000000	2904	>400000	34796	>200000	134
Sm						>20	>4000	>8	>50	>3	>4	>1	>1000
Eu							>80000	>3	>1000	>8	>100	>20	>30000
Gd								>30000	>70	>10000	>900	>5000	>3
Tb									>400	>3	>30	>6	>9000
Dy										>200	12	>70	22
Ho											>10	>2	>3000
Er												>6	260
Tm													>2000

Table 7.5: Separation factors (β_{sep}) of metallic elements between the major product sulfide and metal phases following vacuum thermal decomposition of a sulfidized rare earth magnet.

7.3.2 Ferronickel Alloy Production

To test the efficacy of aluminothermic reduction to synthesize a metal product from a sulfide feedstock while minimizing aluminum impurities in that product, FeNi production was chosen as a case study. FeNi is an $Fe-Ni$ master alloy used predominantly in the production of stainless steel via alloying with ferrochromium master alloy, pig iron, and recycled stainless steel scrap. Common FeNi grades are 5-40 wt% Ni in Fe[68]. FeNi is generally produced via the carbothermic smelting of lateritic ores with Fe to Ni ratios close to that of the desired metal product[16]. As discussed in Chapter 4, Section 4.4.2, sulfidation chemistry is a promising pathway to separate Ni and Fe from lateritic mineral feedstocks. Meanwhile, carbon-intensive reduction methods are currently utilized industrially to produce Ni or FeNi products from sulfides containing Fe and Ni. Aluminothermic reduction of $Fe-Ni$ sulfide via reactive vacuum distillation is a potential carbon-free alternative[44].

Aluminothermic reduction of molten $Fe-Ni$ sulfide matte to liquid FeNi via reactive vacuum distillation was proposed to occur via the following reactions of iron sulfide (FeS) and nickel sulfide (NiS) with aluminum (Al):

$$FeS(l,matte)+\frac{2}{3}Al(l)=Fe(l,alloy)+\frac{1}{3}Al_2S_3\ (g) \tag{7.8}$$

$$NiS(l,matte)+\frac{2}{3}Al(l)=Ni(l,alloy)+\frac{1}{3}Al_2S_3\ (g) \tag{7.9}$$

From Figure 7.4, under an industrial vacuum at 10^{-3} atm and $P_{Al_2S_3}$ of 10^{-3} atm, incomplete conversion is possible due to the high solubility of Al in liquid Fe and Ni and $Fe-Al$ or $Ni-Al$ alloys could be formed[44]. Likewise, liquid FeNi is fluxed by both liquid $Fe-Ni$ sulfide matte and Al[69,70], potentially leading to challenges with residual Al and S removal. To achieve higher purity FeNi, $P_{Al_2S_3}$ must be minimized. One avenue to lower the $P_{Al_2S_3}$ is to react the gaseous Al_2S_3 product with a slag containing CaO to form CaS that is immiscible with FeNi. As discussed in Section 7.1.2, Al_2S_3 is expected to sulfidize CaO via Eqn. 7.3.

Depending on the matte and slag chemistry, solution effects may shift the equilibrium of Eqn. 7.3. Whether or not a separate CaS matte phase is precipitated from the slag is dependent

on its sulfide capacity, known to be correlated with optical basicity (Λ)[71] (see also Chapter 4, Section 4.4.2-4.4.3). CaS is a conventional product from FeNi desulfurization processes and is immiscible with FeNi[16]. Therefore, the use of a slag containing CaO during aluminothermic reduction of $Fe-Ni$ matte is a promising pathway to minimize Al and S impurities in the FeNi alloy product.

For aluminothermic reduction of $Fe-Ni$ sulfide, 3 grams of FeS and nickel subsulfide (Ni_3S_2) mixed in a 2:1 mass ratio served as the feedstock. The ratio of Fe to Ni ratio in the feed is expected to be obtainable via selective sulfidation and desulfidation[44]. For the slag phase, 6 grams of Al_2O_3, SiO_2, CaO were mixed in a 3:2:1 mass ratio. For the reductant, 1 g of Al was utilized, corresponding to assumed stoichiometric removal of S as Al_2S_3. The Al, mixed sulfide, and mixed oxide were then sequentially added to an Al_2O_3 crucible. Aluminothermic reduction via reactive vacuum distillation at a temperature of 1500 °C and pressure of 0.001 atm for 40 minutes was conducted using methods reported in Section 7.1.3 and by the author elsewhere[44].

Aluminothermic reduction of $Fe-Ni$ sulfide via reactive vacuum distillation resulted in the formation of a matte, a slag, a metallic pool, and a volatile distillate which collected in the top of the crucible and furnace tube. These products are shown[44] in Figure 7.11. SEM-EDS compositions of metal, matte, and slag phases are included[44] in Table 7.6. The bulk FeNi product contained an Fe to Ni ratio of 1.8, a S content of approximately 1 wt%, an Al content of approximately 0.3 wt%, and a Ca content of <0.1 wt%[44]. Analytical methods that are more sensitive for light and dilute elements, such as LECO or ICP-MS, may be employed to refine these quantifications. Within the FeNi, metallic phases rich in Ni (light) and Fe (dark) were detected. The Si content of the FeNi was 14 wt%[44]. The substantial presence of Si in the metal product suggests that significant excess Al metal reductant was present. This indicates that direct vacuum thermal decomposition of $Fe-Ni$ sulfide was occurring at appreciable rates in the system, leaving unreacted metallic Al to reduce Si from the slag. This also suggests that less Al reductant is required than stoichiometrically expected.

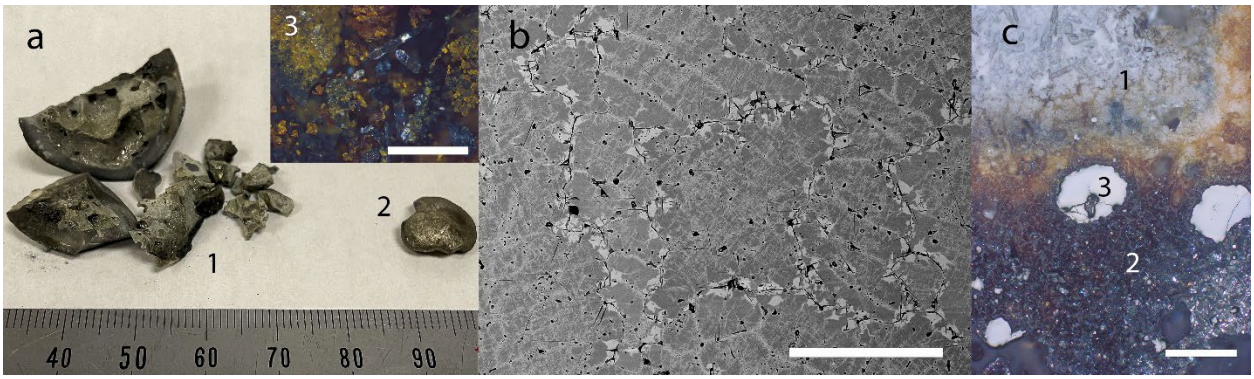

Figure 7.11: Products of aluminothermic reduction of iron-nickel ($Fe-Ni$) sulfide via reactive vacuum distillation. Panel a (optical, inset scale bar: 1mm) corresponds to slag/matte (1), FeNi (2), and condensed distillate (3) products. Panel b (SEM backscatter electron composite, scale bar: 200 μm) shows the microstructure of the solidified ferronickel. Lighter phases were found to be richer in Ni. Panel c (optical, scale bar: 500 μm) shows a cross section of the slag (1) / matte (2) interface, with dispersed droplets of ferronickel (3).

The slag was found to be rich in Al and Si, whereas the product matte was found to rich in Al and depleted in Si. The matte showed unexpectedly high levels of O (Table 7.6, *); it remains unclear whether the matte was actually an oxysulfide liquid or merely oxidized during polishing and analysis[44]. In both the slag and matte phases, only trace levels of Ni were detected. Fe levels were higher in the matte at 4 wt%, indicating that reduction showed some selectivity for Ni[44]. The condensed distillate product was shown to be dominated by $Al-Si-Ca-S-O$ species. Fe and Ni contents of the distillate were below the detectable limit at <0.1 wt%. A mass balance reveals >95% conversion of Ni_3S_2 to FeNi[44].

	O	Al	Si	S	Ca	Fe	Ni
Bulk Metal	1.5 wt% (+/- 0.1)	0.3 wt% (+/- < 0.1)	14.0 wt% (+/- < 0.1)	1.0 wt% (+/- < 0.1)	< 0.1 wt% (+/- < 0.1)	53.7 wt% (+/- 0.2)	29.5 wt% (+/- 0.2)
Bulk Matte	37.9 wt%* (+/- 0.4)	36.5 wt% (+/- 0.8)	1.8 wt% (+/- 0.9)	13.0 wt%* (+/- 0.9)	6.6 wt% (+/- 0.7)	4.0 wt% (+/- 1.7)	0.2 wt% (+/- 0.1)
Bulk Slag	39.0 wt% (+/- 0.3)	31.1 wt% (+/- 0.5)	14.2 wt% (+/- 0.2)	6.5 wt% (+/- 0.5)	8.6 wt% (+/- 0.3)	0.4 wt% (+/- 0.9)	0.1 wt% (+/- < 0.1)

Table 7.6: **Average composition of metal, matte, and slag products following aluminothermic reduction of iron-nickel ($Fe-Ni$) matte via reactive vacuum distillation.** Compositions were measured via SEM-EDS. Standard deviations are reported in parenthesis.

These results suggest that aluminothermic reduction via reactive vacuum distillation is a promising pathway to produce carbon-free FeNi from $Fe-Ni$ matte, with a potentially lower refining burden than conventional methods[44]. Coupled with sulfidation and aluminothermic reduction via reactive vacuum distillation for FeCr production, a sulfide-based pathway may be envisioned for carbon-free production of stainless steel. FeCr production from sulfidized chromite ($FeCr_2O_4$) via reactive vacuum distillation is demonstrated in the following section.

7.3.3 Ferrochromium Alloy Production

To test the efficacy of aluminothermic reduction of sulfides via reactive vacuum distillation in the presence of gangue minerals, FeCr production from sulfidized $FeCr_2O_4$ mineral concentrate was demonstrated. FeCr is an alloy of Fe with 45-95 wt% Cr predominantly utilized as a feedstock for manufacturing stainless steel[72]. Current extraction and processing pathways center on the carbothermic reduction of ores and concentrates containing $FeCr_2O_4$[72]. Sulfidation and subsequent aluminothermic reduction provides a low carbon alternative. The following reactions are proposed, where β, γ, and δ are stoichiometric coefficients:

$$FeCr_2O_4(s) + \frac{5}{2}S_2(g) = FeCr_2S_3(l, matte) + 2SO_2(g) \quad (7.10)$$

$$FeCr_2S_3(l) + \beta Al(l) = FeCr_2(l, alloy) + \gamma Al_2S_3\ (g) + \delta S_2(g) \quad (7.11)$$

Eqn. 7.11 is assumed to require less than the stoichiometric amount of Al due to the anticipated direct vacuum thermal decomposition of FeS and chromium sulfide (CrS) as depicted at temperatures above 1600 °C and pressures on the order of 10^{-3} atm in Figure 7.3.

Natural $FeCr_2O_4$ concentrate was sulfidized at a temperature of 1475 °C and P_{S_2} of 0.1 atm in a graphite reactor using methods described in Chapter 3, Section 3.3.2. As illustrated in

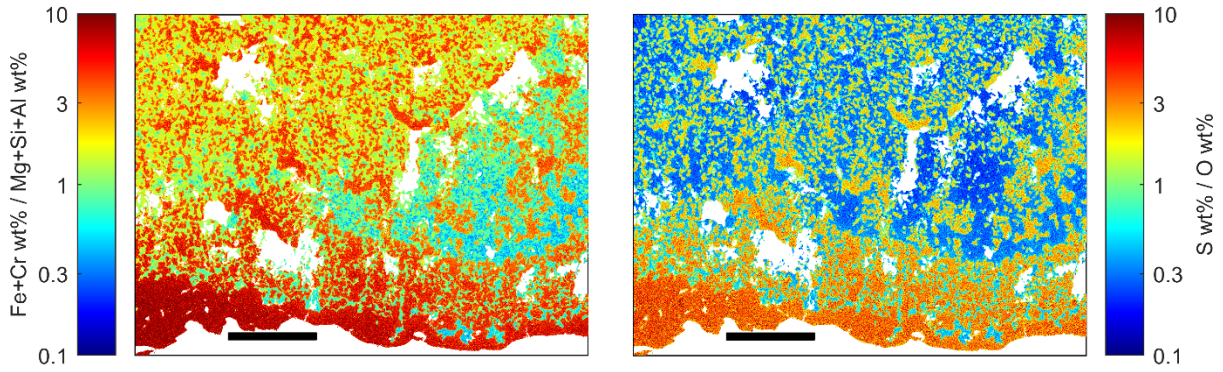

Figure 7.12: Spatial element distributions following selective sulfidation of chromite concentrate. Scale bars correspond to 500 µm.

Figure 7.12, Cr and Fe preferentially partitioned to the sulfide matte phase, while Al, Si, and Mg partitioned to the oxide slag phase[42]. Unseparated matte and slag phases from the sulfidized $FeCr_2O_4$ were then mixed with Al metal in a 27 to 1 mass ratio and heated at 1650 °C for 40 minutes at a pressure of 0.001 atm using methods and apparatuses described in Section 7.1.3. Following aluminothermic reduction via reactive vacuum distillation, a metal product was generated in the form of solidified liquid droplets on the order of 1-2 mm in size, shown in Figure 7.13.

Average product metal composition as determined via SEM-EDS is reported in Table 7.7. The metallic product was observed to have a Cr to Fe ratio of 2, in the range of commercial ferrochromium grades. Preliminary SEM-EDS analysis showed S and Al contents of 0.1 wt% and 1.0 wt% respectively[42]. Further analysis via LECO analysis is needed to better quantify the presence of nonmetallic impurities such as S, O, and C. Optimization of operating conditions in both sulfidation and reduction provide a path toward higher product purity. Some refining of the FeCr product may be required, such as oxidation of residual Al. Overall, these results indicate that aluminothermic reduction of sulfidized mineral feedstocks via reactive vacuum distillation is a promising avenue to integrate low carbon separation and reduction technologies. Coupled with sulfide-based pathways for FeNi reduction (Section 7.3.2), carbon-free production of stainless steel may be realized.

Figure 7.13: Ferrochromium (FeCr) metal droplets produced through aluminothermic reduction of sulfidized chromite ($FeCr_2O_4$) concentrate via reactive vacuum distillation. Droplets shown are 1-2 mm in diameter.

	Fe	Cr	Si	Al	Mg	S	Other
Bulk Metal	30.5 wt% (+/- 4.8)	65.7 wt% (+/- 5.5)	0.3 wt% (+/- <0.1)	1.1 wt% (+/- 0.3)	0.1 wt% (+/- <0.1)	0.1 wt% (+/- <0.1)	2.2 wt% (+/- 0.2)

Table 7.7: Average composition of the metal product following aluminothermic reduction of sulfidized chromite ($FeCr_2O_4$) reduced via reactive vacuum distillation. Analysis was conducted via SEM-EDS and error values in parenthesis correspond to +/- one standard deviation.

7.4 Summary

Pyrometallurgical oxide sulfide anion exchange has been demonstrated to enable the selective sulfidation of metal compounds for materials separations. These processes generate sulfide products, which have been found herein to be suitable for subsequent metal production. In Chapter 2, it was hypothesized that sulfidation decreases the thermodynamic barrier to metal reduction, supporting the use of less reactive reductants or direct thermal decomposition for metal production. In this chapter, the thermodynamics of sulfide reduction to metal were established, motivating the advantages and challenges associated with different metal production pathways. Direct vacuum thermal decomposition was found to be amenable for some sulfide

feedstocks. Aluminum was also shown to be promising metallothermic reductant for sulfides via reactive vacuum distillation of aluminum sulfide.

Sulfide reduction was demonstrated for a range of aluminum alloy and ferroalloy products. Aluminum manganese and aluminum scandium alloys were produced through aluminothermic reduction via reactive vacuum distillation. The aluminum to sulfur ratio in the distillate vapor was found to be a promising lever for controlling the reductive power of aluminum in the system. The distillation behaviors of some common aluminum alloy components were explored, informing the use of aluminum scrap as a reduction feedstock. Operating methods may exist to leverage sulfide reduction for aluminum recycling by allowing purified aluminum sulfide distillate to be reintroduced into aluminum supply chains. For the production of aluminum-free ferroalloy products, the use of a slag phase during aluminothermic reduction via reactive vacuum distillation was observed to effectively scrub aluminum sulfide distillate vapor from the system. Together, these advancements demonstrate that sulfide chemistries are amenable to production of a wide range of metal products. In the following chapter, these findings are contextualized in the broader materials processing landscape, with key avenues for future work identified.

7.5 References

1. Saran, R. & Curry, R. J. Lead sulphide nanocrystal photodetector technologies. *Nat. Photonics* **10**, 81–92 (2016).
2. Tang, H. *et al.* Recent advances in 2D/nanostructured metal sulfide-based gas sensors: Mechanisms, applications, and perspectives. *J. Mater. Chem. A* **8**, 24943–24976 (2020).
3. Afanasiev, P. *et al.* Preparation of the mixed sulfide Nb2Mo3S10 catalyst from the mixed oxide precursor. *Catal. Letters* **64**, 59–63 (2000).
4. Zagorac, D., Doll, K., Zagorac, J., Jordanov, D. & Matovic, B. Barium Sulfide under Pressure: Discovery of Metastable Polymorphs and Investigation of Electronic Properties on ab Initio Level. *Inorg. Chem.* **56**, 10644–10654 (2017).
5. Kolenda, S., Sürgers, C., Fischer, G. & Beckmann, D. Thermoelectric effects in superconductor-ferromagnet tunnel junctions on europium sulfide. *Phys. Rev. B* **95**, 224505 (2017).

6. Liang, Z. *et al.* Understanding the failure process of sulfide-based all-solid-state lithium batteries via operando nuclear magnetic resonance spectroscopy. *Nat. Commun.* **14**, 259 (2023).
7. Hart, W. A., Beumel, O. F. & Whaley, T. P. *The Chemistry of Lithium, Sodium, Potassium, Rubidium, Cesium, and Francium*. (Pergamon Press, 1973).
8. Krawietz, T. R., Murray, D. K. & Haw, J. F. Alkali Metal Oxides, Peroxides, and Superoxides: A Multinuclear MAS NMR Study. *J. Phys. Chem. A* **102**, 8779–8785 (1998).
9. Das, A., Das, U. & Das, A. K. Relativistic effects on the chemical bonding properties of the heavier elements and their compounds. *Coord. Chem. Rev.* **479**, 215000 (2023).
10. Schlesinger, M. E., King, M. J., Sole, K. C. & Davenport, W. G. *Extractive Metallurgy of Copper*. (2011). doi:10.1017/CBO9781107415324.004.
11. Gupta, C. K. & Krishnamurthy, N. Oxide reduction processes in the preparation of rare-earth metals. *Mining, Metall. Explor.* **30**, 38–44 (2013).
12. Allanore, A. Electrochemical engineering of anodic oxygen evolution in molten oxides. *Electrochim. Acta* **110**, 587–592 (2013).
13. Allanore, A., Yin, L. & Sadoway, D. R. A new anode material for oxygen evolution in molten oxide electrolysis. *Nature* **497**, 353–6 (2013).
14. Nakanishi, B. R. & Allanore, A. Electrochemical Investigation of Molten Lanthanum-Yttrium Oxide for Selective Liquid Rare-Earth Metal Extraction. *J. Electrochem. Soc.* **166**, E420–E428 (2019).
15. Rukini, A., Rhamdhani, M. A., Brooks, G. A. & Van den Bulck, A. Metals Production and Metal Oxides Reduction Using Hydrogen: A Review. *J. Sustain. Metall.* **8**, 1–24 (2022).
16. Crundwell, F. K., Moats, M. S., Ramachandran, V., Robinson, T. G. & Davenport, W. G. *Extractive Metallurgy of Nickel, Cobalt, and Platinum-Group Metals*. (Elsevier, 2011).
17. McCoy, H. N. The Electrolysis of Rare Earth Acetates and the Separation of Europium as Amalgam from Other Rare Earths. *J. Am. Chem. Soc.* **63**, 3432–3433 (1941).
18. Kolesov, G. M. & Pankratova, L. N. Separation of Rare-earth Elements by Electrolysis at a Mercury Cathode. *Russ. Chem. Rev.* **37**, 701–710 (1968).
19. Stinn, C. & Allanore, A. Estimating the Capital Costs of Electrowinning Processes. *Electrochem. Soc. Interface* **29**, 44–49 (2020).

20. Morris, A. E. & Flynn, H. Lime-enhanced reduction of sulfide concentrates: A thermodynamic discussion. *Metall. Trans. B* **17**, 914–917 (1986).
21. Townsend, C. P. Process for the Reduction of Ores. (1906).
22. Qu, J. *et al.* Anode electrolysis of sulfides. *Proc. Natl. Acad. Sci.* **119**, 1–7 (2022).
23. Minh, N. Q., Loutfy, R. O. & Yao, N. P. The electrolysis of Al2S3 in AlCl3-MgCl2-NaCl-KCl melts. *J. Appl. Electrochem.* **12**, 653–658 (1982).
24. Ahmadi, E. & Suzuki, R. O. Tantalum Metal Production Through High-Efficiency Electrochemical Reduction of TaS2 in Molten CaCl2. *J. Sustain. Metall.* **7**, 437–447 (2021).
25. Yin, H., Chung, B. & Sadoway, D. R. Electrolysis of a molten semiconductor. *Nat. Commun.* **7**, 12584 (2016).
26. Sahu, S. K., Chmielowiec, B. & Allanore, A. Electrolytic Extraction of Copper, Molybdenum and Rhenium from Molten Sulfide Electrolyte. *Electrochim. Acta* **243**, 382–389 (2017).
27. Stinn, C., Nose, K., Okabe, T. & Allanore, A. Experimentally Determined Phase Diagram for the Barium Sulfide-Copper(I) Sulfide System Above 873 K (600 °C). *Metall. Mater. Trans. B* (2017) doi:10.1007/s11663-017-1107-5.
28. Sokhanvaran, S., Lee, S.-K., Lambotte, G. & Allanore, A. Electrochemistry of Molten Sulfides: Copper Extraction from BaS-Cu2S. *J. Electrochem. Soc.* **163**, D115–D120 (2016).
29. Boury, C. & Allanore, A. Liquid state properties and solidification features of the pseudo binary BaS-La2S3. *Sci. Rep.* **11**, 18189 (2021).
30. Daehn, K. E. *et al.* Liquid Copper and Iron Production from Chalcopyrite, in the Absence of Oxygen. *Metals (Basel).* **12**, 1440 (2022).
31. Stinn, C. & Allanore, A. Selective Sulfidation and Electrowinning of Nickel and Cobalt for Lithium Ion Battery Recycling. in *Ni-Co 2021: The 5th International Symposium on Nickel and Cobalt* (eds. Anderson, C. et al.) 99–110 (Springer Nature Switzerland AG, 2021). doi:10.1007/978-3-030-65647-8_7.
32. Wagner, M.-E. & Allanore, A. Electrochemical Separation of Ag 2 S and Cu 2 S from Molten Sulfide Electrolyte . *J. Electrochem. Soc.* **169**, 063511 (2022).
33. Daehn, K. & Allanore, A. Electrolytic production of copper from chalcopyrite. *Curr.*

Opin. Electrochem. **22**, 110–119 (2020).

34. Wagner, M.-E. & Allanore, A. Non-standard state thermodynamics of metal electrodeposition. *Electrochim. Acta* **389**, 138442 (2021).
35. David Belitskus. Aluminothermic production of metals and alloys. *J. Met.* **24**, 30–34 (1972).
36. Rideal, E. K. *Industrial Electrometallurgy*. (D. Van Nostrand Company, 1919).
37. Nachtman, J. S. & Poole, H. G. Preparation of Metals and Alloys of Molybdenum, Nickel, Cobalt, and Tungsten. (1964).
38. Foos, R. A. & Hobin, M. A. Process for the Preparation of Molybdenum Metal. (1964).
39. Venkataramani, R., Bose, D. K. & Jena, P. K. Alumino-thermic reduction of molybdenite concentrate under vacuum. *Trans. Indian Inst. Met.* **23**, 13–16 (1970).
40. Setoudeh, N. & Welham, N. J. Metallothermic reduction of zinc sulfide induced by ball milling. *J. Mater. Sci.* **52**, 6388–6400 (2017).
41. Akhgar, B. N. & Pourghahramani, P. Mechanochemical reduction of natural pyrite by aluminum and magnesium. *J. Alloys Compd.* **657**, 144–151 (2016).
42. Allanore, A. & Stinn, C. Sulfide Reactive Vacuum Distillation, Absorption, Stripping, and Extraction for Metal Alloy Production. (2023).
43. Stinn, C., Toll, S. & Allanore, A. Aluminothermic Reduction of Sulfides via Reactive Vacuum Distillation. in *Light Metals 2022* 681–688 (2022).
44. Stinn, C. & Allanore, A. Ferronickel Production from Nickel Laterite via Sulfide Chemistry. in *Advances in Pyrometallurgy* (ed. Fleuriault, C.) 1–17 (The Minerals, Metals & Materials Society, 2023).
45. Jorisch, W., S, A. & Hanlon, O. *Vacuum Technology in the Chemical Edited by Related Titles A User ' s Guide to Vacuum Technology , 3rd Edition Handbook of Vacuum Liquid Ring Vacuum Pumps , Freeze-Drying*. (2015).
46. Bray, J. W. Aluminum Mill and Engineered Wrought Products. in *ASM Handbook, Volume 2: Properties and Selection: Nonferrous Alloys and Special-Purpose Materials* 29 (1990). doi:10.31399/asm.hb.v02.a0001059.
47. Cverna, F. *Worldwide Guide to Equivalent Nonferrous Metals and Alloys*. (ASM International, 2001).
48. Kline, J. D., Yeh, Wi. C. T. & Preston, U. A. Articles for Adding Manganese to

Aluminum. (1975).
49. Faunce, J. Method for incorporating metals into molten metal baths. (1972).
50. Jones, T. S. Manganese. in *Minerals Yearbook* (USGS, 1998).
51. Liu, X. J., Ohnuma, I., Kainuma, R. & Ishida, K. Thermodynamic assessment of the Aluminum-Manganese (Al-Mn) binary phase diagram. *J. Phase Equilibria 1999 201* **20**, 45–56 (1999).
52. Ahmad, Z. The Properties and Application of Scandium-Reinforced Aluminum. *J. Miner. Met. Mater. Soc.* **55**, 35–39 (2003).
53. Riva, S., Yusenko, K. V., Lavery, N. P., Jarvis, D. J. & Brown, S. G. R. The scandium effect in multicomponent alloys. *Int. Mater. Rev.* **61**, 203–228 (2016).
54. Botelho Junior, A. B., Espinosa, D. C. R., Vaughan, J. & Tenório, J. A. S. Recovery of scandium from various sources: A critical review of the state of the art and future prospects. *Miner. Eng.* **172**, 107148 (2021).
55. Halmann, M., Frei, A. & Steinfeld, A. Magnesium production by the pidgeon process involving dolomite calcination and MgO silicothermic reduction: Thermodynamic and environmental analyses. *Ind. Eng. Chem. Res.* **47**, 2146–2154 (2008).
56. Nikolaev, A. Y., Suzdaltsev, A. V. & Zaikov, Y. P. Electrowinning of Aluminum and Scandium from KF-AlF3-Sc2O3 Melts for the Synthesis of Al-Sc Master Alloys. *J. Electrochem. Soc.* **166**, D252–D257 (2019).
57. Brinkmann, F., Mazurek, C. & Friedrich, B. Metallothermic Al-Sc co-reduction by vacuum induction melting using Ca. *Metals (Basel).* **9**, (2019).
58. Kulikov, B. P., Baranov, V. N., Bezrukikh, A. I., Deev, V. B. & Motkov, M. M. Preparation of Aluminum-Scandium Master Alloys by Aluminothermal Reduction of Scandium Fluoride Extracted from Sc2O3. *Metallurgist* **61**, 1115–1121 (2018).
59. Xiao, J., Ding, W., Peng, Y., Chen, T. & Zou, K. Preparing Sc-bearing master alloy using aluminum–magnesium thermoreduction method. *Metals (Basel).* **10**, 1–14 (2020).
60. Stinn, C., Benderly-kremen, E. & Allanore, A. Scandium Master Alloy Production Via Sulfidation and Vacuum Aluminothermic Reduction. in *Light Metals 2023* (2023).
61. Shevchenko, M. O., Kudin, V. G. & Berezutskii, V. V. Thermodynamic Poerperties of Al-Sc Alloys. *Powder Metall. Met. Ceram.* **53**, 151–157 (2014).
62. Stinn, C. & Allanore, A. Thermodynamic and Structural Study of the Copper-Aluminum

System by the Electrochemical Method Using a Copper-Selective Beta″ Alumina Membrane. *Metall. Mater. Trans. B* **48**, 2922–2929 (2018).

63. Obidov, Z. R., Amonova, A. V. & Ganiev, I. N. Effect of scandium doping on the oxidation resistance of Zn5Al and Zn55Al alloys. *Russ. J. Phys. Chem. A* **87**, 702–703 (2013).
64. Binnemans, K., Jones, P. T., Müller, T. & Yurramendi, L. Rare Earths and the Balance Problem: How to Deal with Changing Markets? *Journal of Sustainable Metallurgy* vol. 4 126–146 (2018).
65. Wagner, M.-E. & Allanore, A. Chemical Thermodynamic Insights on Rare-Earth Magnet Sludge Recycling. *ISIJ Int.* **60**, 2339–2349 (2020).
66. Suzuki, T. Development of an Electrochemical Method to Investigate the Thermodynamic Behavior of Lanthanum and Sulfur in Liquid Steel. (Massachusetts Institute of Technology, 2021).
67. Han, Q., Xiang, C., Dong, Y., Yang, S. & Chen, D. Equilibria between the rare earth elements, oxygen and sulfur, in molten iron. *Metall. Trans. B* **19**, 409–418 (1988).
68. Polyakov, O. Technology of Ferronickel. in *Handbook of Ferroalloys* (ed. Gaslik, M.) (Elsevier, 2013). doi:10.1016/C2011-0-04204-7.
69. Bradley, A. J. Microscopical studies on the iron-nickel-aluminum system. Part 1 - α + β alloys and isothermal sections of the phase equilibrium diagram. *J. Iron Steel Inst.* **163**, 19–30 (1949).
70. Waldner, P. & Sitte, W. Thermodynamic modeling of Fe–Ni pentlandite. *J. Phys. Chem. Solids* **69**, 923–927 (2008).
71. Sosinsky, D. J. & Sommerville, I. D. The composition and temperature dependence of the sulfide capacity of metallurgical slags. *Metall. Trans. B* **17**, 331–337 (1986).
72. Gasik, M. Technology of Chromium and its Ferroalloys. in *Handbook of Ferroalloys* (ed. Gaslik, M.) (2013).
73. Hsiao, C. M. & Schlechten, A. W. Volatility and Stability of Metallic Sulphides. *J. Mater.* **4**, 65–69 (1952).

Chapter 8

Conclusions and Future Work

Extractive metallurgy and materials production today are faced with a plethora of technical, economic, and societal challenges. Decreasing ore grades, increasing mineralogical complexity, geopolitical uncertainties, and higher demand for trace by- and co-product elements stress supply webs and current processing pathways. These factors manifest in both economic and sustainability pressures to improve manufacturing methods for the metals that humanity needs today. Production burdens exist across applications ranging from bulk structural components to critical feedstocks for electrification. Clearly, technological innovations are needed to unlock new processing paradigms that minimize the environmental impact and cost.

Sustainable materials processing is a multifaceted opportunity with bottlenecks in mining, separation, metal production, and recycling. A distinction may be drawn between physical and chemical methods of material isolation and purification. Physical separations are employed when metallic elements of interest are in distinct phases from their impurities. Chemical separations are needed when target elements are mixed with impurities at an atomic level and generally exhibit higher energy usage and cost. Chemical separation processes generally leverage anion exchange reactions, in which a mixed metal compound is reacted to form distinct metal compounds of different anion chemistries that are immiscible or exhibit marked variations in phase stability. These new physical property differences enable subsequent physical separation. Conventional pyrometallurgical separations, hydrometallurgical separations, and metal reduction in the presence of a matte or slag may all be viewed in this

context. The optimal anion exchange chemistry is that which optimizes process selectivity for target products, maximizes purity and recovery, and minimizes costs.

In Chapters 1 and 2, pyrometallurgical oxide-sulfide anion exchange was established as a promising chemical pretreatment to enable low cost, environmentally benign physical separation and metal reduction. This approach was informed by the natural partitioning of elements within chondrite meteorites. Many elements are observed geologically to exhibit strong affinities toward forming oxide or sulfide phases, termed lithophilic or chalcophilic respectively. Comparing terrestrial geologic trends with those in chondrite meteorites formed in less oxidizing environments than Earth establishes that elements may be chalcophilic or lithophilic based on system conditions. Within this framework, metallic elements may also be classified by how much the presence of certain other metallic elements leads to deviations in lithophilic or chalcophilic behavior. Siderophilic elements are an example, which preferentially substitute into oxide or sulfide phases richer in iron. Together, these interactions have led to geologic partitioning of elements between oxide and sulfide phases that rivals the selectivity observed for some modern industrial separations. This motivates the consideration of oxide-sulfide anion exchange chemistry for improved materials separation.

Oxide-sulfide anion exchange chemistry is also positioned to enable lower energy use in the production of metal or alloy products. Due to the more covalent nature of sulfide bonding versus oxide bonding, the thermodynamic barrier to metal production from a sulfide is often lower than from an oxide. Therefore, when oxide-sulfide anion exchange for materials separation produces a sulfide product, lower burden metal production processes may also be unlocked. Together, oxide-sulfide anion exchange chemistry is a promising pathway to achieve new process synergies that lower the costs and environmental impact of materials.

In Chapter 2, three hypotheses were established:

- Selective oxide-sulfide anion exchange decreases the solubility of target cation elements in feedstock materials, supporting their selective extraction and physical separation.

- Increasing the selectivity of pyrometallurgical processes via oxide-sulfide anion exchange reduces the need for subsequent hydrometallurgical processing, lowering the cost and environmental impact of materials separations.

- Sulfidation of an oxide decreases the thermodynamic barrier to metal reduction, supporting the use of less reactive reductants or direct thermal decomposition for metal production.

These hypotheses were confirmed via experiments and modelling as described in Chapters 3-7. In this chapter, perspectives, future work, and conclusions surrounding oxide-sulfide anion exchange are presented.

8.1 Perspectives

Oxide-sulfide anion exchange chemistry is proposed to be a promising pathway to enable improved materials separation and metal production at reduced costs and environmental impact. The effectiveness of sulfidation chemistry toward meeting these goals is discussed in the following sections.

8.1.1 Efficacy of Oxide-Sulfide Anion Chemistry for Enabling Selective Extraction and Subsequent Physical Separation

In Chapter 2, it was hypothesized that selective oxide-sulfide anion exchange decreases the solubility of target cation elements in feedstock materials to support their selective extraction and physical separation. A thermodynamic framework was established in Chapter 3 to understand the sulfidation affinity of different oxide species. Sulfidation affinity was found to have both entropic and enthalpic components, with higher sulfidation affinities corresponding to lower thermodynamic barriers to sulfide formation. The enthalpic affinity for oxide sulfidation was found to increase with increasing metal ionic (Shannon) radius, increasing electronegativity, and decreasing metal cation charge. Meanwhile, the entropic affinity for compound sulfidation

was observed to be highest for reactions that maximized the configurational entropy or degrees of freedom in the system. For example, oxysulfide formation from oxides exhibits a higher entropic sulfidation affinity than sulfide formation from oxysulfides due to increased configurational entropy in the condensed product versus the reactant. Likewise, sulfide formation from sulfates exhibits a higher entropic sulfidation affinity than from oxides due to an increased higher number of moles of gaseous products. A wide range of sulfidation affinities were calculated, indicating that oxide-sulfide anion exchange can in principle be highly selective. By le Chatelier's principle, the sulfur to sulfur dioxide ratio in the reactor was identified as the main observable for controlling sulfidation selectivity. The use of carbon additions to regenerate sulfur in situ via reduction of sulfur dioxide was considered for control of the sulfur to sulfur dioxide ratio, termed carbothermically driven sulfur reflux. Thermodynamically, carbothermically driven sulfur reflux was found to be unnecessarily for most transition metal sulfidations. The presence of excessive carbon was found the actually decrease the selectivity of sulfidation processes.

In Chapter 4, oxide-sulfide anion exchange was experimentally demonstrated. First, a range of pure compounds of differing sulfidation affinities were successfully sulfidized, confirming that oxide-sulfide anion exchange is a platform approach applicable to feedstocks across the periodic table of elements. The sulfidation kinetics of lanthanum oxide were measured, informing mass and energy balances within sulfidation reactors. Sulfidation kinetics were observed to be thermally activated, indicating that in the absence of mass transport limitations sulfidation occurs more rapidly at temperatures closer to the oxide's melting point. This provided an additional kinetic lever for sulfidation selectivity. Following, selective sulfidation was conducted on a series of physically mixed and chemically mixed oxides.

Selective sulfidation was shown to be amenable to applications ranging from rare earth element separation, lithium ion battery recycling, copper slag recycling, and nickel extraction. In most cases, sulfidation selectivity followed trends in sulfidation affinity calculated for pure compounds. However, thermodynamic solution effects were found to modulate the trends calculated in Chapter 3 for some process chemistries, in particular for systems that contained several components of similar sulfidation affinities. In rare earth magnet recycling, the presence of iron notably increased the sulfidation affinity of siderophilic heavy rare elements. This enabled selective separation of light and heavy rare earth elements that rivals conventional

hydrometallurgical approaches by two orders of magnitude. In nickel and copper extraction, management of solution effects were found to be critical to achieving high recovery of dilute target elements in sulfide product phases. Oxide product phases with higher basicities were correlated with larger residual solubilities for sulfidized metallic elements. This indicated that solution effects in unsulfidized oxides also contribute to the effectiveness of oxide-sulfide anion exchange in precipitating sulfide products.

Within all of these systems, oxide-sulfide anion exchange was able to be conducted selectively for individual species from mixed oxide phases. Product metal sulfides were generally observed to be insoluble with oxide feedstocks and products, enabling their precipitation as distinct phases. These phases were generally on the order of tens to hundreds of microns in size, thereby amenable to liberation via comminution and subsequent physical separation. Washing, magnetic separation, and froth flotation were demonstrated for lithium ion battery cathode sulfidation products, enabling physical separation of lithium, manganese, and nickel-cobalt species.

Together, these sulfidation experiments on oxide feedstocks confirmed the hypothesis that selective oxide-sulfide anion exchange decreases the solubility of target cation elements in feedstock materials to support their selective extraction and physical separation. In Chapter 5, the behavior of pnictogen, chalcogenide, and halide impurities were explored during oxide-sulfide anion exchange for copper and rare earth mineral processing. While each anion chemistry was found to present both new materials processing opportunities and challenges, oxide-sulfide anion exchange remained selective and continued to form distinct sulfidized compounds. These results confirm that pyrometallurgical oxide-sulfide anion exchange is a promising chemical pretreatment to enable physical separation of materials even in the presence of complex feedstock chemistries. In the following section, perspectives on the economic and environmental impact of oxide-sulfide anion exchange are explored.

8.1.2 The Environmental and Economic Impact of Oxide-Sulfide Anion Chemistry

In Chapter 2, it was hypothesized that increasing the selectivity of pyrometallurgical processes via oxide-sulfide anion exchange reduces the need for subsequent hydrometallurgy,

lowering the cost and environmental impact of materials separations. To understand the technoeconomics and sustainability of selective sulfidation for materials processing via pyrometallurgical oxide-sulfide anion exchange, four materials agnostic process flowsheets were considered over a wide range of operating scales and conditions. These were selective sulfidation and physical separation with and without upstream feed pretreatments and with and without carbothermically driven sulfur reflux.

The capital cost of materials separation was compared between the materials agnostic sulfidation flowsheets and an equivalent hydrometallurgical separation flowsheet. The capital cost of selective sulfidation and subsequent physical separation was observed to be 65 – 90% lower compared to the equivalent hydrometallurgical route, aided by the improved separation effectiveness of oxide-sulfide anion exchange chemistry versus conventional aqueous-organic extractant systems. Capital cost was also largely reduced due to the smaller reactor volumes required for processing materials as solid feedstocks versus feedstocks dissolved and diluted in high volumes of aqueous liquids. Operating costs were not compared between pyrometallurgical oxide-sulfide anion exchange and hydrometallurgy due to wide variations in hydrometallurgical operating practices.

To establish the environmental impacts of material processing via selective sulfidation versus nonselective pyrometallurgy with selective hydrometallurgy, environmental impacts were calculated for three real world case studies: zirconium-silicon separation from zircon, iron-titanium separation from ilmenite, and rare earth element separation from bastnaesite. Compared with non-selective pyrometallurgy followed by selective hydrometallurgy, selective sulfidation via pyrometallurgical oxide-sulfide anion exchange and subsequent physical separation was predicted to exhibit 60-90% fewer greenhouse gas emissions. Water resource depletion and terrestrial acidification were also substantially lowered. This improvement to sustainability is largely due to the increased selectivity in the high temperature step that mitigates the need for subsequent selective hydrometallurgy. When hydrometallurgical separation was substituted with physical separation, environmental impacts were predicted to be significantly reduced.

Overall, these findings confirmed the hypothesis that increasing the selectivity of pyrometallurgical processes via oxide-sulfide anion exchange reduces the need for subsequent hydrometallurgy, lowering the cost and environmental impact of materials separations. This indicates that selective sulfidation is a promising technological approach to competitively

decarbonize materials separation. In the following section, perspectives on the use of product sulfides as feedstocks for metal production are explored.

8.1.3 New Reduction Pathways for Metal Production from Sulfides

In Chapter 2, sulfidation of an oxide was hypothesized to decrease the thermodynamic barrier to metal reduction, supporting the use of less reactive reductants or direct thermal decomposition for metal production. Review of sulfide thermodynamics established vacuum thermal methods as promising pathways for metal production. Some sulfides, such as iron sulfide, were found to be amenable to direct vacuum thermal decomposition at industrially relevant temperatures and pressures. For sulfides requiring a reductant, aluminum was identified as a promising candidate due to its volatility as a sulfide.

In conventional oxide aluminothermic reduction, nonvolatile aluminum oxide products accumulate within the system, hindering conversion for more reactive metals via the law of mass action. The high melting aluminum oxide product must also be fluxed to enable sufficient fluidity for metal product agglomeration. Meanwhile for sulfide feedstocks, aluminum sulfide products were found to be amenable to vacuum distillation, minimizing their accumulation in the system. The ability to distill and expunge product aluminum sulfide from the system effectively made aluminum metal a stronger reductant for the vacuum thermal reduction of sulfides versus oxides. The partial pressure of aluminum sulfide in the system was identified as a key lever for process control. Operating under vacuum, shifting the ratio of aluminum to sulfur in the distillate gas phase, and employing slags were identified as pathways to control aluminum sulfide partial pressure and modulate the reducing power of aluminum metal.

Vacuum thermal methods of sulfide reduction were demonstrated for aluminum alloys and ferroalloys. Aluminothermic reduction of sulfides to produce aluminum-manganese alloy and aluminum-scandium alloy confirmed the roll of aluminum sulfide partial pressure in reduction process control. Ferronickel was produced using aluminothermic reduction of mixed iron-nickel sulfide in the presence of a slag; this confirmed that the aluminum sulfide partial pressure may be minimized by reacting it with components of the slag such as calcium oxide. Ferrochromium was produced via aluminothermic reduction of sulfidized chromite concentrate, indicating that selectively sulfidized feedstocks may be directly reduced. A less than

stoichiometric amount of aluminum was employed, indicating that direct vacuum thermal decomposition and aluminothermic reduction via reactive vacuum distillation may occur simultaneously within the system. Coupled with ferronickel production, a carbon free sulfide pathway for stainless steel production was postulated.

Mixed iron rare earth sulfides produced via rare earth magnet sulfidation were vacuum thermally reduced without a metallothermic reductant. As in oxide-sulfide anion exchange, siderophilic heavy rare earth elements partitioned highly selectively with iron in the system, this time to produce a ferroalloy product. Complete separation to analytical detection limits for groups of rare earth elements was accomplished, indicating the efficacy of sulfide chemistry in enabling selective methods of metal reduction.

In summary, these experimental results confirm the hypothesis that sulfidation of an oxide decreases the thermodynamic barrier to metal reduction, supporting the use of less reactive reductants or direct thermal decomposition for metal production. In oxide chemistries, rare earth elements are among the most difficult elements to reduce. In contrast, as sulfides they were readily reduced to metal using vacuum thermal processes in the presence of iron or aluminum. These results indicate that shifting from oxide to sulfide processing chemistries via oxide-sulfide anion exchange is a promising avenue to enable simplified metal reduction without carbon reagents. In the following section, avenues for future work are briefly discussed in order to further develop competitive pyrometallurgical oxide-sulfide anion exchange for decarbonizing metals production and mining.

8.2 Future Work

Sustainable, low cost physical separation and sulfide reduction were facilitated herein via oxide sulfide anion exchange chemistry. This approach was demonstrated successfully for a wide range of separation challenges, including rare earth separation and recycling, lithium ion battery recycling, aluminum alloy production, and ferroalloy production. Many more metal separation and reduction applications could be explored in the future using the framework herein. Through the course of this project however, several fundamental gaps in thermodynamics and kinetics / mass transport where identified. These topics are addressed as avenues for future work in the following sections.

8.2.1 Further Avenues in Thermodynamics

Classical thermodynamics served as the basis for modelling oxide-sulfide anion exchange selectivity herein. For most systems studied herein, the sulfidation affinities of non-dilute components generally followed trends calculated from pure, standard state compound data. As discussed in Chapter 3 however, mixing thermodynamics and solution effects can cause significant deviations from these trends. This was observed experimentally in Chapters 4 and 5, where solution effects with iron lead to large deviations in the sulfidation affinities of heavy versus light rare earth elements. During iron-lanthanide sulfide vacuum thermal reduction in Chapter 7, solution interactions with iron again greatly accentuated differences in the thermodynamic stability between individual rare earth sulfides. More generally, product purity during reduction and the partitioning of trace impurities between metal, sulfide, and gas phases are all governed by often unquantified solution interactions. While such behavior may be rationalized using concepts such as siderophilicity or geological trends, these qualitative insights are difficult to translate directly into quantitative process design insight on their own. Determination of solution models for high temperature mixing thermodynamics remains a critical area of future work.

First principles methods and CALculation of PHAse Diagrams (CALPHAD) computational approaches for thermodynamic prediction have received significant attention in materials science and engineering. Without strong experimental data for training and validation however, such methods remain difficult to refine and calculated behavior remains a hypothesis. Currently, the only way to accurately acquire thermodynamic mixing and solution data is through real, experimental measurements. Methods such as differential thermal analysis, electrochemical potential difference, and equilibrium measurements are robust tools that can be implemented to quantify the mixing nonidealities of relevant metal-oxygen-sulfur systems. Then, experimentally verified solution models can be used to populate classical thermodynamic frameworks. As demonstrated herein, these classical thermodynamic frameworks are highly effective for the design of sustainable materials separation when coupled with informed kinetic and mass transport behavior.

8.2.2 Further Avenues in Kinetics

Thermodynamically predicted sulfidation affinities and conditions were integrated with kinetics and mass transport behavior in Chapter 3 to develop a comprehensive process model for pyrometallurgical oxide-sulfide anion exchange. Sulfidation kinetic measurements obtained in Chapter 4 for lanthanum oxide were used to populate this model, serving as the basis for experimental testing of separation performance across a range of material systems. Kinetics measurements in other systems will help establish how typical lanthanum oxide sulfidation behavior is. Further insight into the mechanisms of sulfidation with element sulfur is also warranted. Kinetic measurements herein were conducted at temperatures where sulfur gas was predominantly diatomic (> 800 °C). Extrapolation of sulfidation behavior to cooler temperatures relies on understanding the sulfidation mechanisms of longer chain sulfur gas molecules.

Meanwhile, the effectiveness of oxide-sulfide anion exchange can be measured by the subsequent ability to physically separate product phases. As discussed in Chapter 2, this begins with the ability to liberate product oxide and sulfide phases from one another. Larger grind sizes during comminution require less energy than ultrafine grinding and afford more opportunities for dry physical separation, such as magnetic methods. Separation of ultrafine particles requires more expensive and energy intensive wet methods, such as froth flotation. The sizes of these product phases are governed by nucleation and growth phenomena during oxide-sulfide anion exchange, which have not been extensively considered herein. Elucidating nucleation and growth behavior during sulfidation is an important avenue of future work for optimizing subsequent physical separation. Collectively, more informed kinetics, thermodynamics, and mass transport analyses may unveil new synergies between sulfidation, physical separation, and sulfide reduction to metal beyond those realized herein. Further implementation of irreversible thermodynamics is an attractive avenue to unify kinetic, transport, and thermodynamic considerations.

8.3 Conclusion

Decarbonization of materials production is difficult to achieve via currently deployed carbon and water intensive extraction, separation, and reduction chemistries. Processing dynamics are generally driven by the anions within the system: oxide, halide, aqueous, etc. Oxide-sulfide anion exchange was proposed to shift processing operations into chemical regimes where new minimums in cost, energy usage, and emissions could be realized. Three hypotheses were established:

- Selective oxide-sulfide anion exchange decreases the solubility of target cation elements in feedstock materials, supporting their selective extraction and physical separation.

- Increasing the selectivity of pyrometallurgical processes via oxide-sulfide anion exchange reduces the need for subsequent hydrometallurgical processing, lowering the cost and environmental impact of materials separations.

- Sulfidation of an oxide decreases the thermodynamic barrier to metal reduction, supporting the use of less reactive reductants or direct thermal decomposition for metal production.

An integrated classical thermodynamic, kinetic, and mass transport framework rooted in fundamental material properties was established to design oxide-sulfide anion exchange processes. This foundation enabled a single component of a mixed oxide to be sulfidized and precipitated as a distinct sulfide phase, enabling subsequent physical separation of the sulfide and carbon-free sulfide reduction to metal. Oxide-sulfide anion exchange was demonstrated to be highly effective across challenges ranging from rare earth element separation to lithium ion battery recycling to commodity mineral processing. Technoeconomic and life cycle assessment confirmed this separation approach to be of lower impact and cost than legacy processes deployed today. Sulfide products were subsequently found to be amenable to carbon-free vacuum thermal methods of reduction, providing a pathway to electrified materials processing.

In summary, pyrometallurgical oxide-sulfide anion exchange was found to enable improved materials separation over conventional approaches with reduced costs, lower environmental impacts, and less burdensome metal production. These innovations confirm the proposed hypotheses and establish sulfide-based metals processing as a new platform technology to enable a sustainable future in metals, mining, and recycling.

8.4 Gallery

The images of sulfidized samples on the following pages were acquired via optical microscopy.

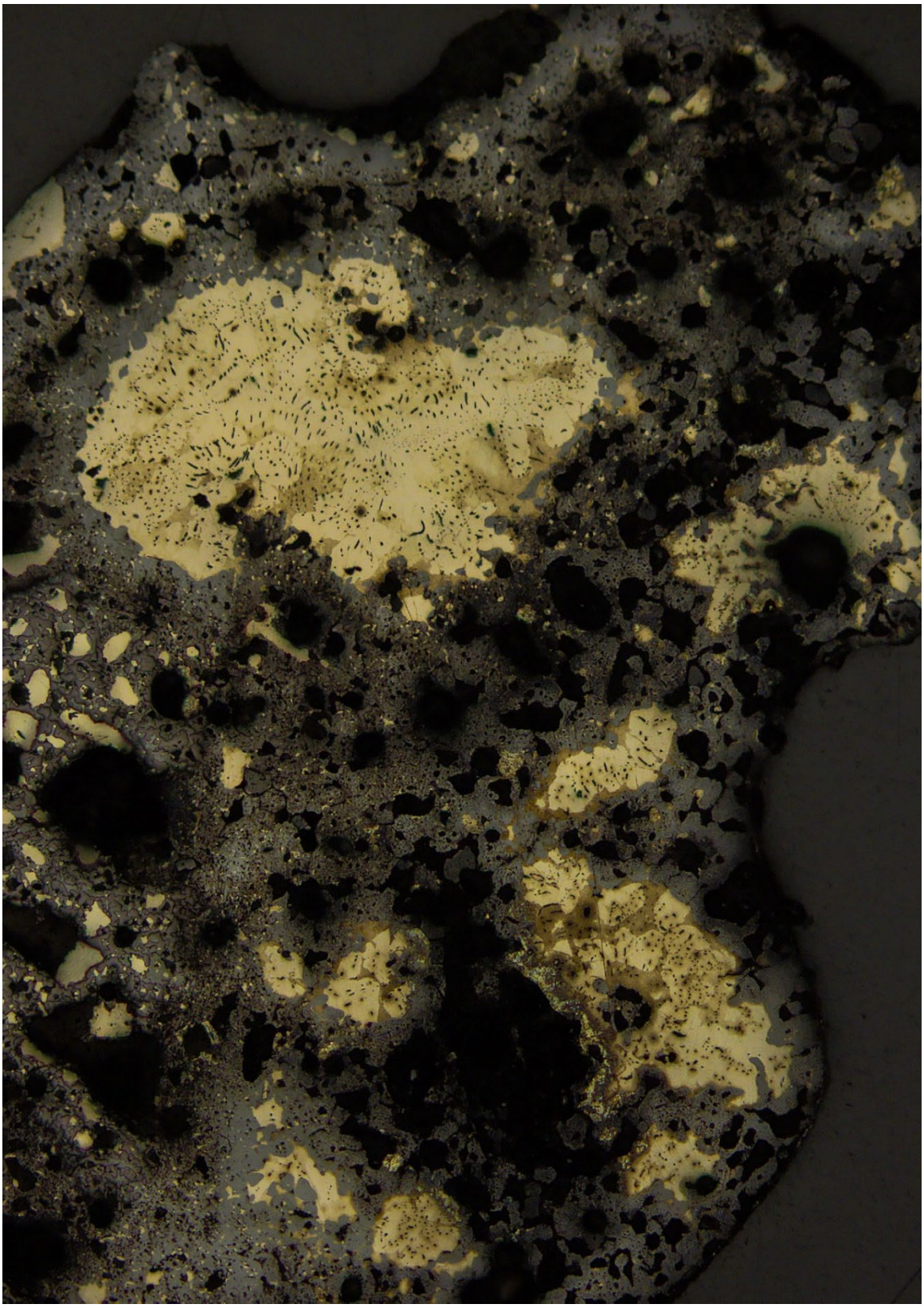

Sulfidized lithium ion battery cathode oxides

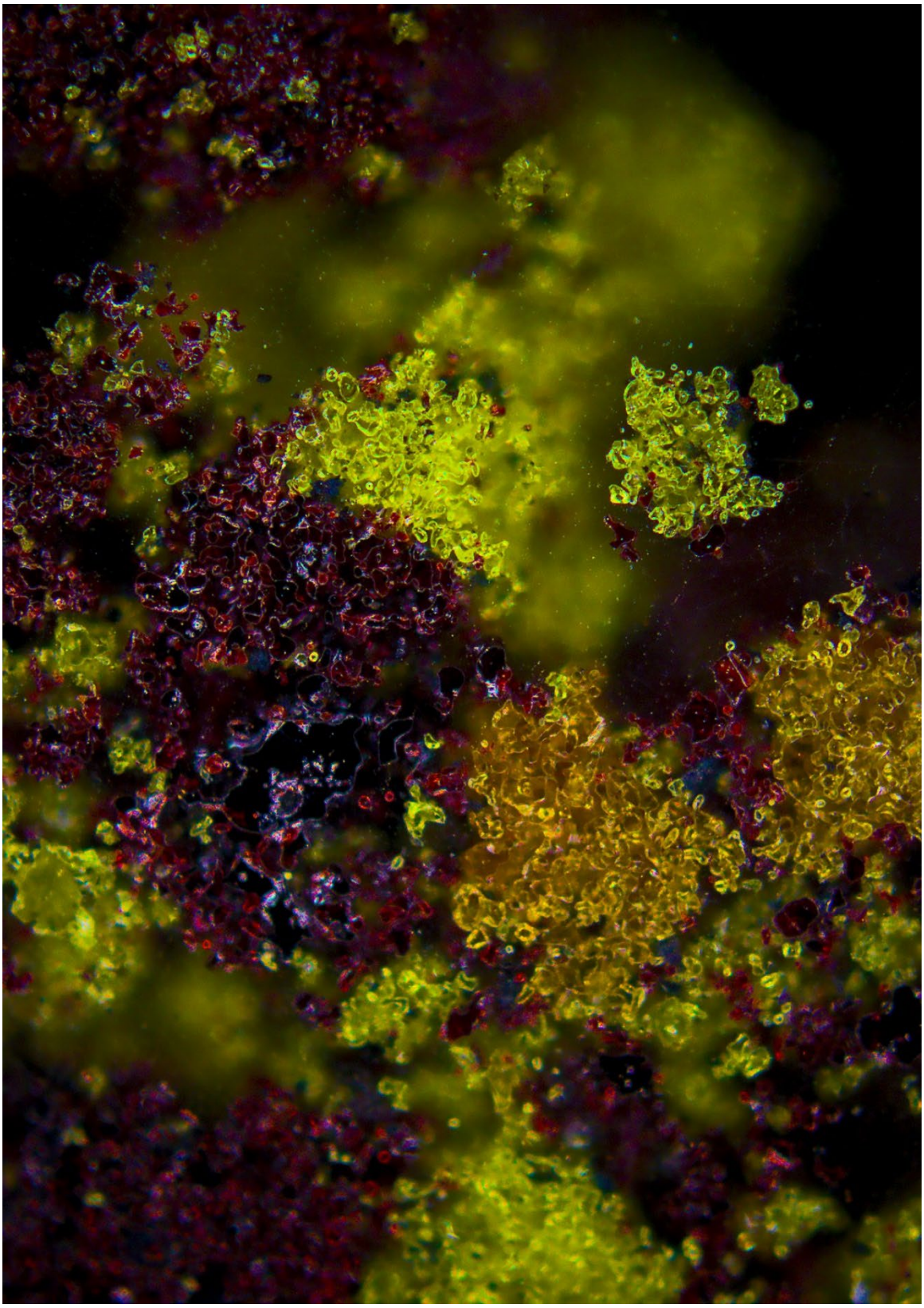

Sulfidized mixed rare earth oxides

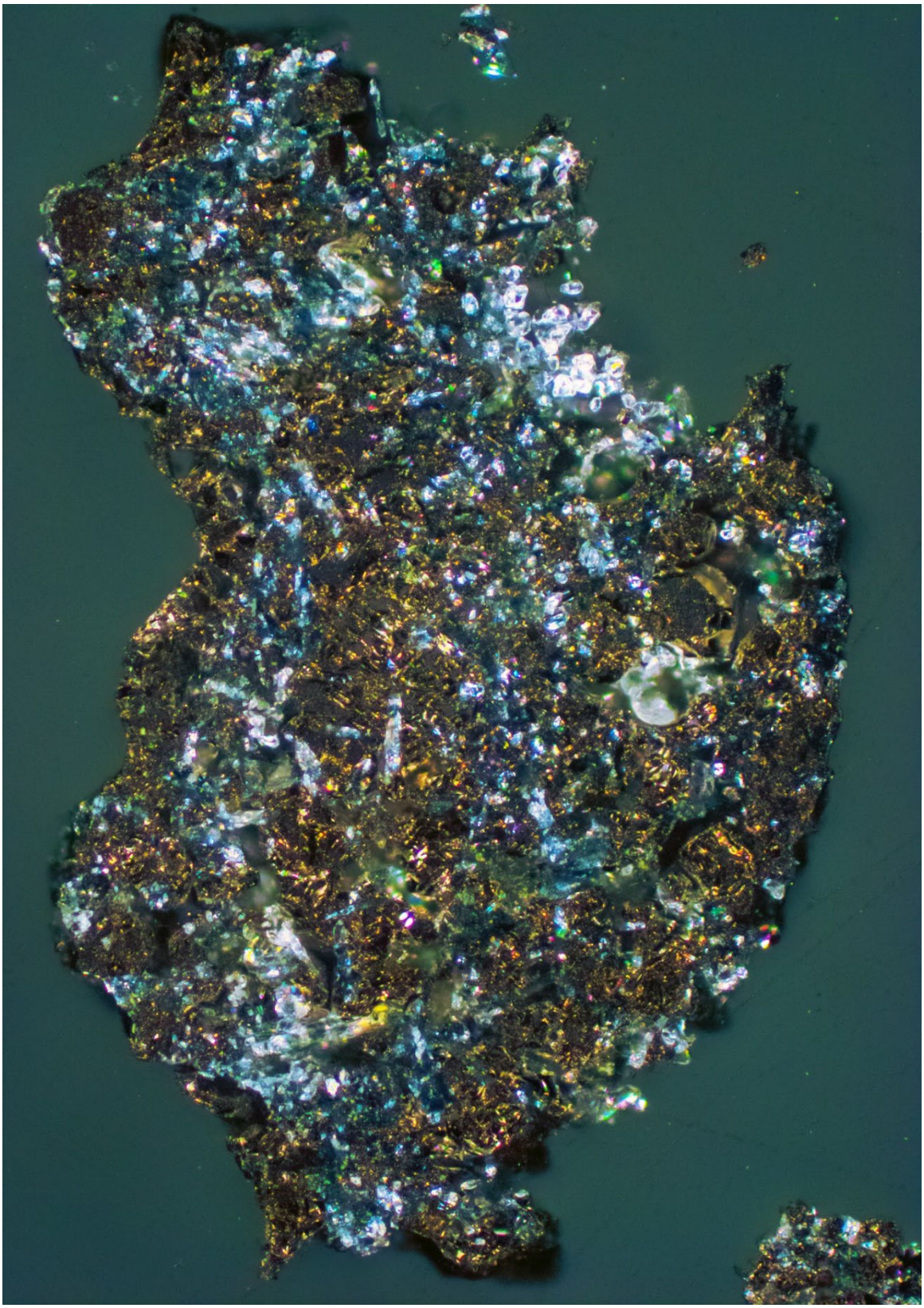

Calcined and sulfidized rare earth magnet

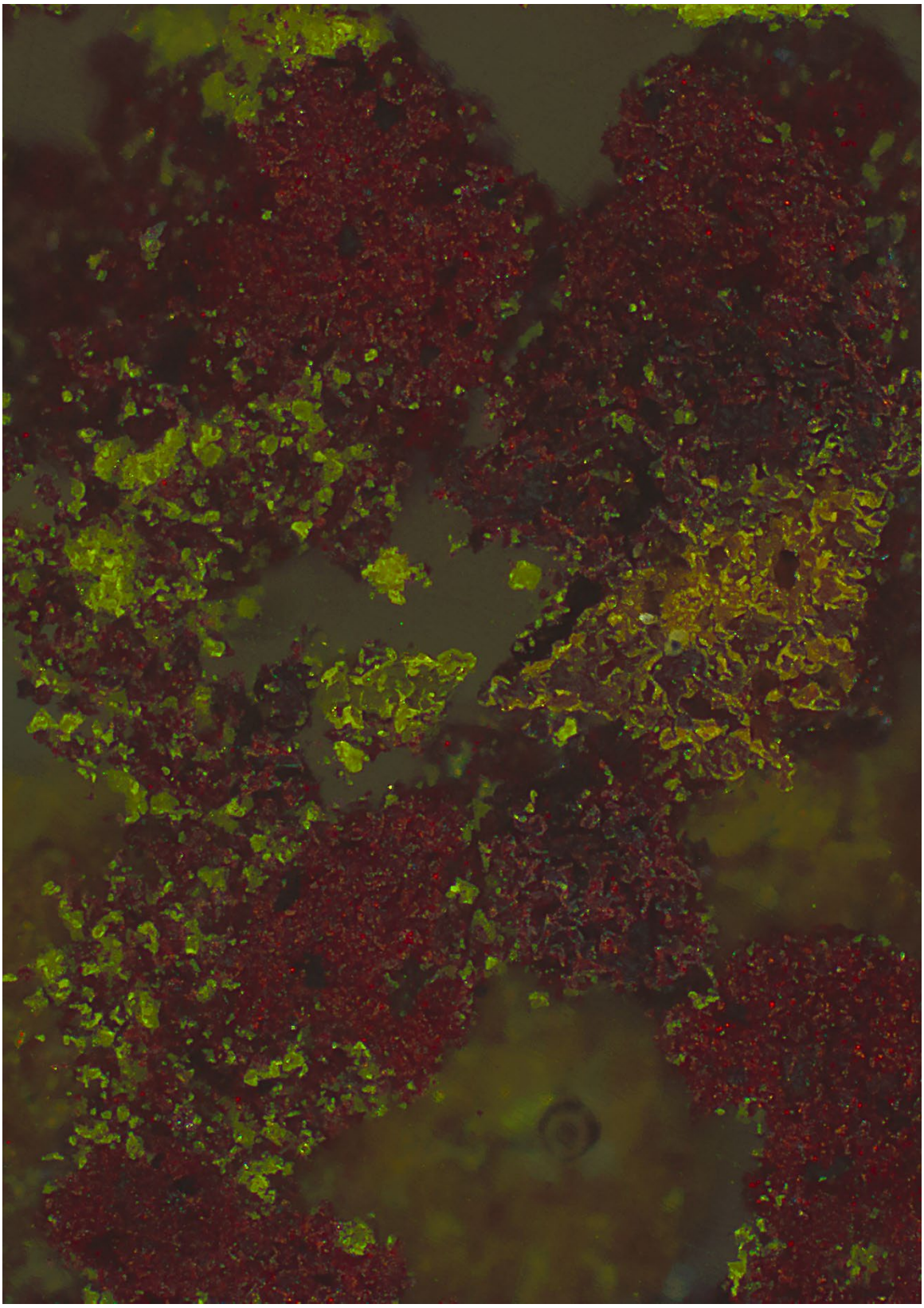

Sulfidized mixed rare earth oxides

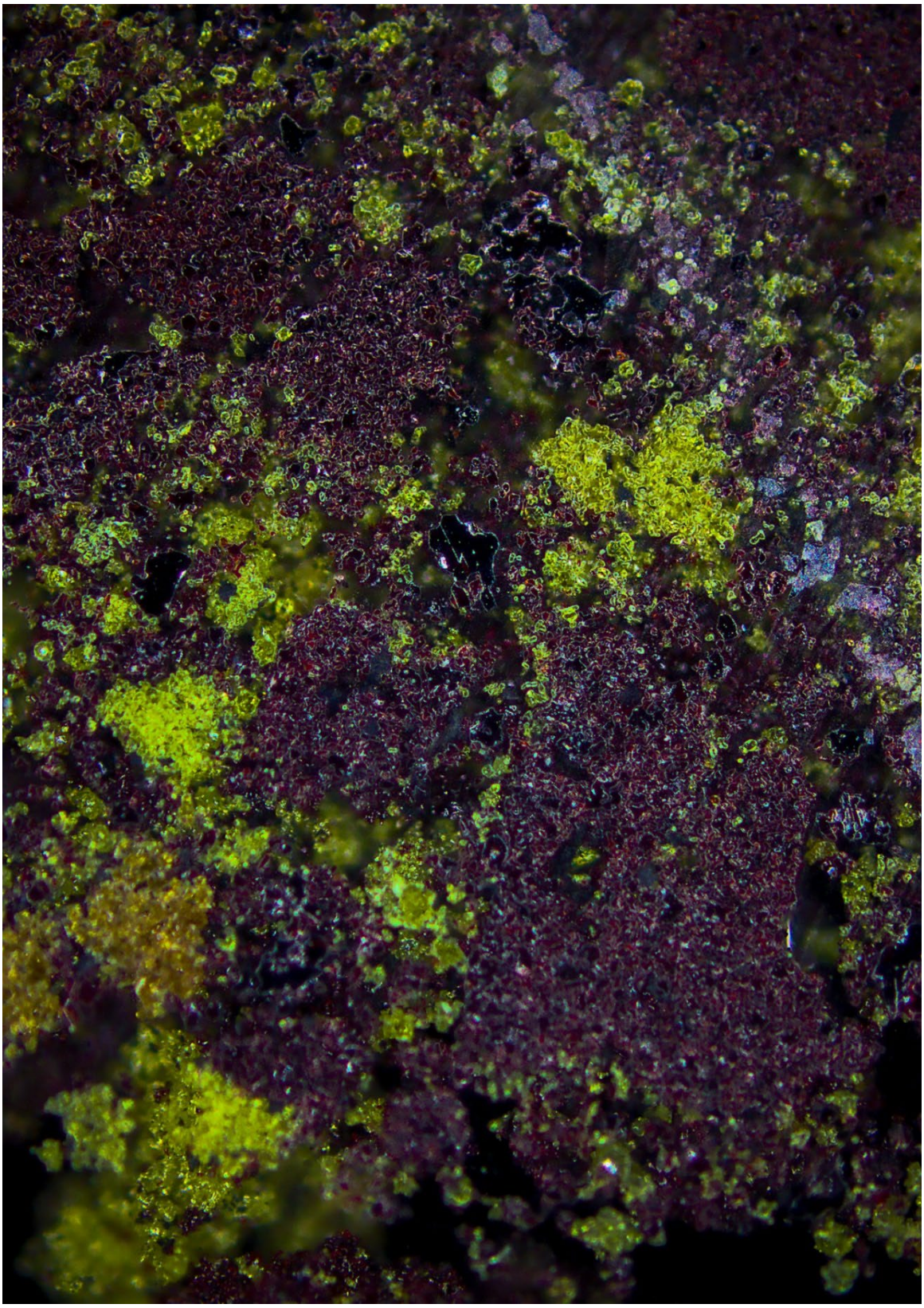

Sulfidized mixed rare earth oxides